CRANFIELD UNIVERSITY

G CREECH

MESOSCOPIC FINITE ELEMENT MODELLING OF NON-CRIMP FABRICS FOR DRAPE AND FAILURE ANALYSES

SCHOOL OF APPLIED SCIENCES

PhD THESIS

CRANFIELD UNIVERSITY

SCHOOL OF APPLIED SCIENCES

PhD THESIS

Academic Year 2002 – 2006

G CREECH

Mesoscopic Finite Element modelling of Non-Crimp Fabrics for drape and failure analyses

Supervisor: A K Pickett

April 2006

This thesis is submitted in partial fulfilment of the requirements
for the degree of Doctor of Philosophy

ABSTRACT

To date, macroscopic analysis methods have been invariably used to analyse textile composite structures for forming and mechanical performance. Techniques such as geometric ‘mapping’ for the draping of textile fabrics and classical laminate analysis combined with simplified failure criteria to determine mechanical performance have formed the basis of most of these methods. The limited accuracy of the physical laws applied is appropriate to macro- analysis methods in which the fibre-matrix composite is treated as homogeneous medium. Today, however, modern high performance computers are opening new possibilities for composites analysis in which far greater detail of the composite constituent materials may be made. This paper presents Finite Elements techniques for the draping simulation of textile composites, specifically biaxial Non Crimp Fabrics, in which the complex deformation mechanisms of the dry tows and stitching may be properly modelled at the individual tow and stitch mesoscopic level. The resulting ‘deformed’ Finite Element model is then used to provide a basis for accurate simulation of the impregnated composite structure. The modelling techniques for both draping and structural analysis are presented, together with validation results for the study of a relatively large scale hemisphere composite part.

ACKNOWLEDGEMENTS

I would first like to thank Anthony Pickett for his supervision and support all the way through this project. It is very much appreciated!

I would also like to thank all the people of the Composites Centre at Cranfield University who have been friends, colleagues and much more besides.

Special thanks have to go to my long-suffering office-mate Michel Fouinneteau, who has put up with me for these years. Thanks also go to Andrea Marasco, Harry Zervos, Ben Hopper and Andy Lamb and all the other students that I have shared an office, had the pleasure of working with or lived with during my time at Cranfield; Holger Ax, Niko Naumann, Loraine Vinot, Nak Seung Chung, Michael May and the guys from the Wilstead Manor.

I gratefully acknowledge the support of Faraday Advance and ESI Group, especially Patrick de Luca who has provided valuable guidance throughout this work.

Finally, to my family, who have always been there to support me and guide me in everything I have chosen to do. Thank you!

CONTENTS

9. Appendix

LIST OF FIGURES

LIST OF TABLES

LIST OF EQUATIONS

TERMINOLOGY

Term	Definition
Biaxial/bi-directional	A continuous fabric constructed of two fibre directions (usually 0°/90° or ±45°)
CAD	Computer Aided Design
CFRP	Continuous Fibre Reinforced Plastic
Digital Image Correlation (DIC)	The calculation of displacements, strains or fabric inter-fibre angles from digital images taken during mechanical testing
Drapeability	The ability of a continuous fibre fabric to deform to a three dimensional geometry
Finite Element (FE)	A numerical simulation method whereby the geometry approximated by smaller, finite volumes/surfaces/lines
Impaled stitching	A NCF stitching method whereby stitching passes directly through individual tows
Liquid Composite Moulding (LCM)	A general manufacturing term describing the use of dry fabrics requiring the infusion of a separate resin
Non-Crimp Fabric (NCF)	A continuous fibre fabric constructed of UD fibres in separate layers which are stitched together
Non-impaled stitching	A NCF stitching method whereby stitching is wrapped around individual tows
Preforming	The forming of a dry fabric to the three dimensional component geometry prior to the infusion of resin
Prepreg	A continuous fibre composite sheet in combination with a partially cured thermoset resin
Shear Bias	A term to describe a fabric which requires differing deformational forces in the separate directions of possible shear
Tow	A single bundle of fibres within a composite fabric
Warp/weft	Fibre directions in a composite fabric
Woven fabric	A continuous fibre fabric constructed by intertwining individual tows

NOTATION

Symbol	Description	Symbol	Description
α	Acute inter-fibre angle	F_c	Contact force
δ	Contact penetration depth	F_N	Normalised axial force
ε	Strain	F_S	Shear force
ϕ	Inter-fibre shear angle	G	Shear modulus
η	Resin viscosity	G_b	Flexural rigidity
μ	Friction coefficient	h	Characteristic stitch segment length
ν	Poisson's ratio	h_{cont}	Contact distance
ρ	Density	L_b	Overhang length
σ	Stress	l_b	Bending length
σ_s	Coulomb friction stress	$L_{be,0}$	Original bias extension coupon length
[C]	Stiffness matrix	$L_{be,1}$	Characteristic length of the bias extension test coupon
$_{be}$	Bias extension	L_{pf}	Edge length of the picture frame test equipment
c	Characteristic stitch segment length	l_{pf}	Edge length of the cruciform picture frame test sample
D	Axial displacement	P	Normal surface load
d	Characteristic stitch segment length	$_{pf}$	Picture Frame
d	Scalar damage factor	t	Fabric thickness
D_N	Normalised axial displacement	Vel	Velocity Relative surface sliding velocity
E	Elastic modulus	W_{be}	Bias extension test coupon width
e	Engineering strain	W_f	Fabric mass per unit area
F	Force	W_g	Simulated gap length between tows
F_A	Axial Force	W_t	Simulated tow width

1. INTRODUCTION

1.1. COMPOSITE MATERIALS AND SIMULATION

The drivers for all material scientists are to produce materials having improved performance while reducing design, manufacturing and material costs. This has inevitably led to the development of many new materials that further extend the envelope of potential material properties. Fibre based composites are one such classification of relatively new material that are proving particularly attractive for the aerospace and automotive sectors to lower component weight, increase performance and improve impact tolerance/crashworthiness; these are key factors in reducing fuel emissions and improving occupant safety, respectively.

The concept of combining two or more materials to produce a product of performance far exceeding those of the individual components has been used for many thousands of years in building materials. However, the current development of fibrous composites as a suitable engineering material was instigated with the development of carbon fibres in the UK, and boron fibres in the USA, in the early 1960's [2]. When combined with a suitable polymeric matrix, these fibres produce materials having significant performance improvements compared to the dominant materials of the time, such as glass fibre composites, metallic and polymeric materials. Other benefits include good fatigue properties, low thermal and electrical conductivity, good vibration damping, corrosion resistance and the ability to mould-in sensors [40].

The type of fibre reinforcement and manufacturing method used to produce composite components depends on a balance between the required material performance and cost. For example, the addition of short fibres can provide small increases in material performance when compared to the polymer alone. However, continuous fibres are required to provide significant performance increases, but inevitably at higher cost and with more complex manufacturing methods.

1. Introduction

The manufacturing technologies used for continuous fibre composites are predominantly hand, or automated, methods to lay unidirectional fabric plies, pre-impregnated with a partially cured thermoset resin to construct the composite part for subsequent curing in an autoclave. In-plane properties for this type of composite are excellent; however, the raw materials and production methods prove such ‘pre-preg’ materials to be overly costly for many medium to high volume manufacturing applications. Industrial attention has consequently focussed on the development of lower cost manufacturing methods using materials suitable for forming complex geometries.

Today, the use of dry engineered fabrics which are preformed to the required component shape and then injected with a thermoset resin (termed ‘Liquid Composite Moulding’ or LCM) are proving competitive. These materials are cheaper, because the resin and chemical hardener are mixed only as required, the fabrics can be mass produced using traditional textile technologies and the manufacturing methods can be easily automated.

Numerous 2D fabric architectures are available and can be generally classified as woven or Non-Crimp Fabrics (NCF). Woven fabrics consist of fibre bundles, called tows, woven into a 2D sheet. A variety of woven architectures such as plain, twill and satin weaves are common. Non-Crimp Fabrics differ from woven fabrics in that unidirectional layers of fibres are held together by through thickness stitching; consequently there is no interlocking of fibre tows. These Non-Crimp Fabric types are proving effective with regards to fabric drapeability (predominantly controlled by the through thickness stitching pattern), cost, impregnation and final mechanical properties, due to the absence of tow undulation, commonly termed ‘crimp’.

With any fabric style, prediction of the draped fabric architecture is an important step in the virtual design of the composite part. The draping analysis should, ideally, give reliable information on changes in the fibre angle, thickness redistribution and compaction. The identification of drapeability limits are also required, such as shear locking, fabric buckling and regions of excessive deformation. Prediction of these defects allows the designer to consider alternative draping processes, fabric restraints or fabric types without the requirement for expensive trial and error testing.

Methods for draping analysis can be broadly grouped into three categories; kinematic mapping, macroscopic Finite Element (FE) and mesoscopic FE modelling. The first methods, developed in the 1950's, were geometrical kinematic methods that essentially used mapping techniques to fit a pin-jointed net to the desired geometric component shape. These 'mapping' methods are fast, robust and require only minimal data input, but are of limited accuracy since material behaviour and process parameters are ignored.

The second group uses macroscopic FE methods, developed since the 1980's, to approximately represent the fabric as a homogeneous material using a fabric constitutive law and continuum Finite Elements. The inherent limitation is that the fabric is not a true continuum, but can be more closely likened to a structure comprising discrete tows, possibly intertwined, or loosely held together with stitching. Interaction of the tows via contact, with friction, and deformation of the stitching control the complex deformations of the fabric. This leads to the third group which are now starting to emerge and attempt to accurately represent the structural features of the fabric using FE techniques and meso-mechanical modelling methods. The potential of this approach is to capture the true deformation mechanisms of fabrics.

Whereas the macroscopic FE technique can be considered industrial and several commercial FE codes have been applied to fabric draping [4][5], the latter mesoscopic modelling methods are at the research level and are commonly restricted to the simulation of small unit- or representative-cells due to the long computation times required with such detailed models. However, the modelling detail of complete fabric forming problems inevitably increases in unison with available computing power. Consequently, it is now conceivable to model fabric deformation of comprehensive structures using an appropriate meso-mechanical FE fabric model within reasonable timescales and using relatively inexpensive computing resources. Development of such a mesoscopic fabric model has been the primary aim of the current work.

Accurate information on the deformed fabric architecture after draping is vital for subsequent analysis of permeability and component mechanical performance. Simulation packages which integrate these analyses are becoming commercially available [4][89] and are based upon simple mapping, or macroscopic FE methods. Although FE mesoscopic modelling of the preforming process is still at a research level, the FE method is inherently flexible and coupling of drape results to performance prediction of the final composite component is possible. A further aim of the present work is, therefore, to demonstrate this coupling of forming results with a mesoscopic failure model of the final composite component.

1.2. AIMS AND OBJECTIVES

The aims of this work are;

- To develop a mesoscopic Finite Element model that is capable of including all the important deformation mechanisms of biaxial Non-Crimp Fabrics. This model should be suitable for simulating forming of full-scale comprehensive fabric structures within reasonable timescales and be able to correctly predict the complex interaction between fibre tows and stitching, that can only be properly modelled at this mesoscopic scale.

- To demonstrate that accurate predictions of the deformed mesoscopic fabric architecture, obtained with preforming simulations, can be used as the basis for mesoscopic damage and failure modelling of complex composite components.

THESIS SUMMARY

The following summarises the contents of this thesis:

Chapter 2: Textile Drape and Composite Failure Literature Review

This chapter begins by considering textile fabrics, their deformation mechanisms and characterisation test methods. Progressive modelling approaches of increasing complexity are then described. Failure analysis of solid composites will then be considered. The aim will be to place the current work in context of current drape and failure simulation research, justifying the current research into mesoscopic modelling.

Chapter 3: Finite Element Mesoscopic Modelling of NCF

This chapter describes the modelling techniques developed, and applied, to both fabric and impregnated composite modelling in the present work. Descriptions of the principle fabric components, deformation mechanisms and respective modelling strategies are presented. Furthermore, reasons are presented for the test and simulation methods used in this work to characterise material properties and validate the simulation models.

Chapter 4: Experimental and Simulation Procedures and Results

This chapter first presents the experimental test methods and results used in the present work to characterise fabric and impregnated composite properties. Following this, the corresponding procedures, and results, of simulations used to verify/calibrate the simulated material properties are presented, in addition to results of simulation used to validate the developed fabric model.

Chapter 5: Discussion

This chapter presents the main finding of this work and discusses the limitations of the developed fabric, and impregnated composite, modelling scheme.

2. LITERATURE REVIEW

2.1. INTRODUCTION TO CONTINUOUS FIBRE FABRICS

The number of fabric styles, lay-up variations, reinforcement types and manufacturing techniques available to the designers of composite structures are numerous, providing a high degree of flexibility with regards to performance and cost.

The use of simple textile technology has produced a variety of 2D fibrous materials, as indicated in Table 2.1. As shown, composite materials can be distinguished by those pre-impregnated by a polymeric resin and those requiring a separate resin infusion process. The dominant materials used by industry will be discussed in the following sections.

Pre-impregnated	Woven thermoset pre-preg Unidirectional (UD) thermoset pre-preg Woven thermoplastic UD/multilayered thermoplastic
Dry fabric	Non-Crimp Fabric (NCF) Woven Braid Weft/warp knitted Resin bonded unidirectional Commingled resin/reinforcement fibres

Table 2.1. General classifications of continuous fibre fabrics

2.2. PRE-IMPREGNATED THERMOSET AND THERMOPLASTIC MATERIALS AND MANUFACTURE

Unidirectional fibre tapes or woven fabrics can be pre-impregnated with a partially cured thermoset resin to produce what is known as a ‘pre-preg’. These materials form the basis of most high performance structural composite components and have been used for many decades as the material of choice for high-end military, aerospace, motor-sport and increasingly, automotive and sports applications.

The manufacturing process for pre-preg based components requires consolidation at elevated temperatures and pressures. A number of manufacturing methods are available and usually require the use of an autoclave (a heated pressure vessel) to cure the part under a controlled high temperature and pressure.

The resulting structures made from pre-preg materials can show significant performance benefits compared to those made from alternative continuous fibre materials, with stiffness and strength increases of up to 30% being reported [1]. These advantages are attributable to a high nominal fibre volume fraction of 60% and the use of high-grade, fully impregnated, resins. However, such performance comes at a price; with higher material, equipment, storage and skilled labour costs. Nevertheless, for performance critical applications and low production volumes these materials are considered optimal.

Thermoplastic based composites were first used for structural components in the 1980's and are therefore relatively new in comparison to thermoset composites [40]. These materials comprise continuous fibres embedded in a thermoplastic matrix at a predetermined volume fraction. Thermoplastic composites are suited to automated and rapid manufacture, on the order of a few minutes for heating, forming and cooling of the polymeric matrix, which is substantially faster than most thermoset composites, which can require several hours for cure. The negative aspects of thermoplastic materials are a reduced range of operating temperatures (-40°C to 100°C for common thermoplastics) and problems associated with fatigue and moisture uptake, which can cause swelling, cracking or shape distortion [40].

Today, civil aviation and automotive industries are investing in the development of alternative cost effective production technologies suitable for medium volume manufacture, while maintaining good mechanical, fatigue and corrosion properties. Over the past decade this has led to increased research in the use of cheaper dry fabrics which are impregnated with separate thermoset resin systems. The most commonly used dry fabric materials and manufacturing techniques will be considered in greater detail in the following sections.

2.3. WOVEN AND NON-CRIMP FABRIC MATERIALS AND MANUFACTURE

Composites derived from dry fabrics and liquid infusion processing are being considered for applications in various low to medium volume structural components in the automotive, aerospace and other industries, where metals and pre-preg based composites once dominated. This change in materials choice has stemmed from the significant cost reduction offered by dry fabric composites and has led to continued investment into reliable production methods and automated manufacturing methods to produce low cost, highly reproducible components.

As Table 2.1 shows, continuous dry fibres can be manufactured in a variety of architectures and styles. However, research into fabric draping simulation is primarily of use for 2D continuous fibre fabric styles, with woven and Non-Crimp Fabrics being of greatest interest due to their good drapeability and excellent mechanical performance once infused. Consequently, both of these architectures will be considered in greater detail in the following sections.

2.3.1. Woven Fabric Architectures

Fabrics produced by directly interlacing separate bundles of fibres, or tows, are termed woven fabrics and are one of the most common fabric architectures used in industry. Production utilises relatively conventional weaving loom machinery with tows in the 0° 'warp' and 90° 'weft' directions, although other orientations of tows may be included. As with conventional textiles, the number of different weaving patterns available is numerous. Table 2.2 shows a summary of some common architectures.

The choice of woven architecture depends on a compromise between ease of handling during manufacture, drapeability (the ability to form a fabric to a three dimensional geometry) and mechanical performance. Considering Table 2.2, for example, the plain weave is highly stable during handling, due to the intertwined weave structure, but produces a composite with reduced in-plane strength and stiffness. This is a consequence of tow crimp which is a misalignment of fibres from the plane of the fabric which produce resin rich areas of limited performance benefit [12]. In contrast, the 5-

harness satin weave shown is the most drapeable example, with a weave pattern of reduced intertwining, and produces improved in-plane mechanical properties at the expense of stable handling.

Fabric style	Architecture	Example	Weave pattern elements (unit cell in bold)
Biaxial	**Plain weave** $N=2$ $S=1$	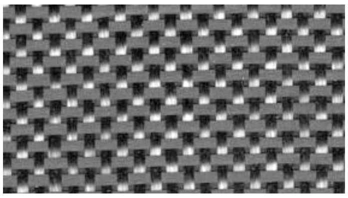	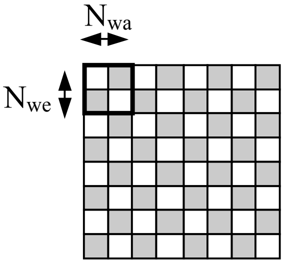
	Twill weave $N>2$ $S\pm1$	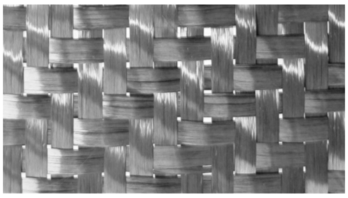 (2/2 weave)	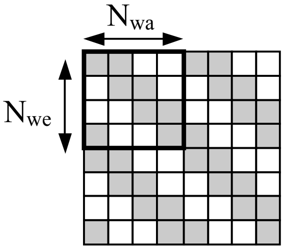
	Satin weave $N>5$ |S|>1	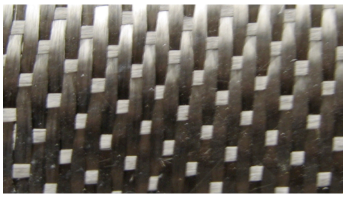 (5-harness weave)	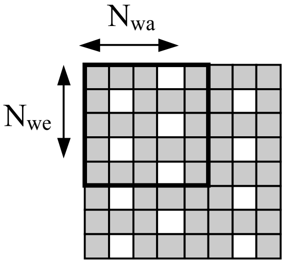
Multiaxial		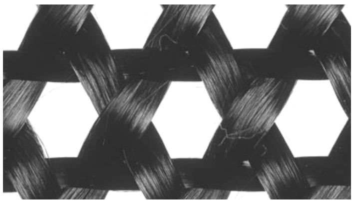	

N = unit-cell repeat size (N_{we} = weft repeat, N_{wa} = warp repeat)
S = shift in pattern of adjacent yarns

Table 2.2. The fundamental woven fabric architectures, based upon [55]

2.3.2. Non-Crimp Fabric Architectures

NCF’s differ from woven fabrics by using a separate through thickness stitching material to bind a number of unidirectional fibre layers; NCF manufacture and examples of a biaxial and unidirectional fabric style are shown in Figure 2.1.

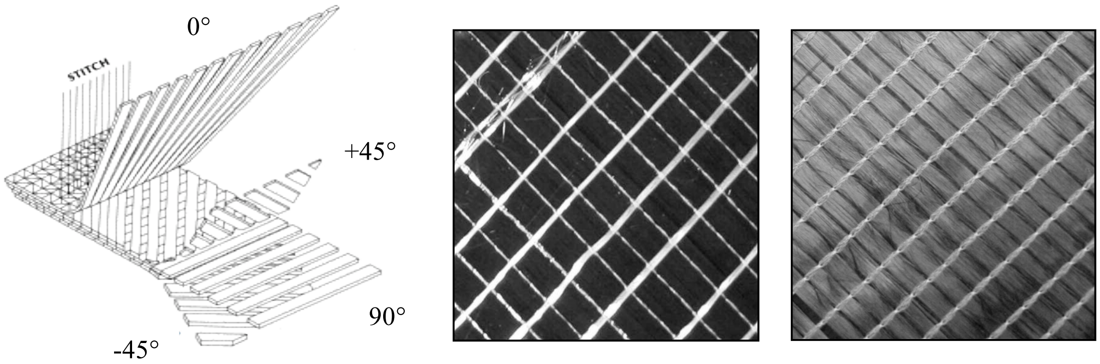

a) NCF architecture b) example of a biaxial NCF c) example of a UD NCF

Figure 2.1. NCF architecture and fabric examples

As with woven fabrics, a variety of fabric styles are available, leading to the requirement of a classification scheme, as detailed in Table 2.3 [10]. The mass per unit area is defined by the number of unidirectional layers in the fabric and the number of individual fibres contained in a single tow; these generally range from 3,000 to 48,000. The stitching mechanism is dependant on the machinery used during fabric production and two methods are used; namely, ‘impaled’ when the stitch passes through the fibre tows and ‘non-impaled’ when stitching is wrapped around individual tows.

Variable	Options
Number of fibre layers	1-7+
Tow fibre count	3-48k tows
Stitching geometry	Tricot, Chain, etc.
Stitching mechanism	Impaled, Non-impaled

Table 2.3. NCF classification scheme, based on [10]

The benefits of overlaying straight tows joined by stitching is that tow crimp may be avoided, which results in improved strength, stiffness and fatigue life compared to woven fabrics of equivalent weight [12]. Manufacture is simple, using conventional stitching machinery and the relative absence of tow crimp can produce composites of comparable mechanical performance to those derived from pre-pregs [13].

The cause for any performance reduction, when compared to pre-preg based composites, primarily results from lower fibre volume fractions (due to resin rich areas [13], as shown in Figure 2.2, and limitations of the manufacturing process) and the use of lower performance resins suitable for infusion. Studies also show some fibre crimp is present in NCF components, both from the nesting of tows [56][57], shown in Figure 2.2, and deviations in fibre path at through-thickness stitch points [12]. Both these factors are dependant on the tow spacing and stitching architecture and can be minimised during fabric manufacture with appropriate process control [12].

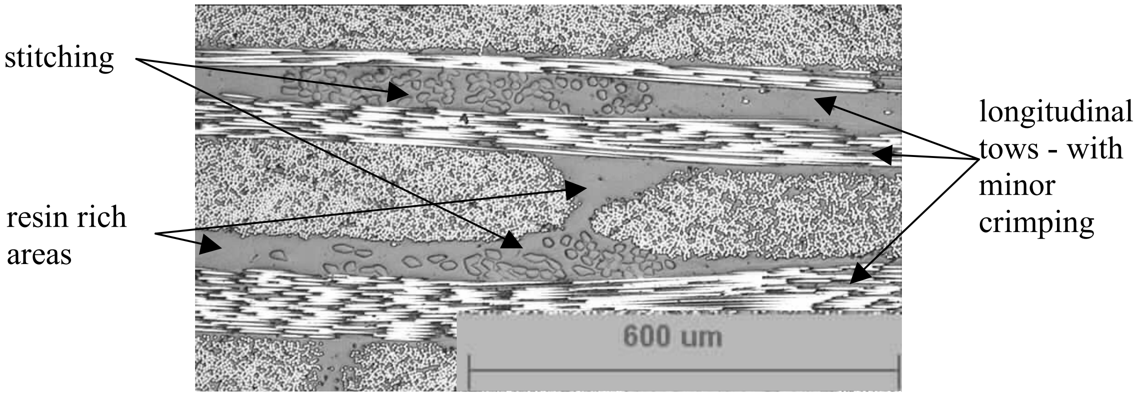

Figure 2.2. Cross-section of a NCF composite

The number and thickness of unidirectional layers used in a single fabric sheet also offer increased flexibility in both design and manufacture. Quadriaxial fabrics (0°/90°/±45°), for example, are considered in-plane quasi-isotropic materials but are comparatively stiff and generally limited to deformation over single curvature geometries; to summarise, the more fibre directions included in a single fabric ply, the fewer orientations of in-plane shear are possible, so limiting the drapeability of the fabric.

Stitched unidirectional fabrics are available and offer the same ability to tailor the fibre lay-up as pre-preg materials. However, care has to be taken in designing automated drape processes and tooling with such materials since the low flexural stiffness and strength offered by the stitching can inevitably lead to the occurrence of defects such as wrinkling and stitch tearing, as demonstrated in Figure 2.3.

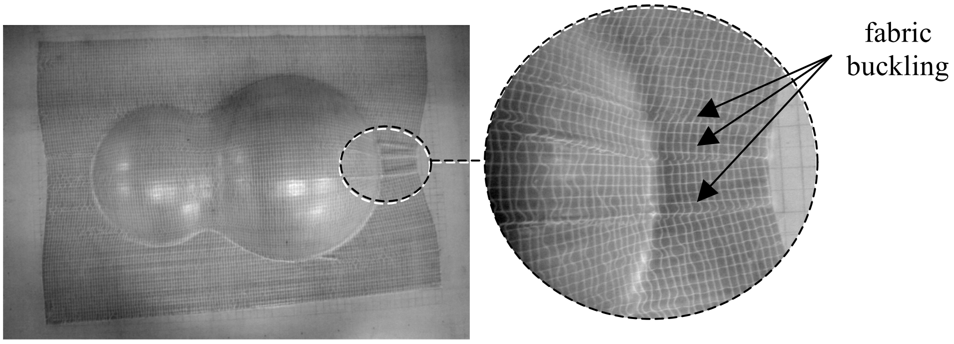

Figure 2.3. Example buckling of a unidirectional NCF sheet, preformed to a double dome using a membrane vacuum forming process

For both woven and NCF materials, biaxial fabrics (0°/90° or ±45°) are the most easily formable architectures due to an ability to shear easily in a high number of orientations. The two transverse fibre directions also stabilise the flexural rigidity and limit the occurrence of stitch tearing associated with unidirectional NCF’s. Consequently, biaxial fabrics are commonly used for complex parts where double curvature or re-entrant geometries are to be formed, such as automotive floor pans [128] and aerospace wing rib structures [14]. Consequently, it is for these biaxial fabrics that numerical drape models have been developed.

2.3.3. Composite Manufacture using Dry Fibre Reinforcements

LCM manufacturing methods have proved to be cost effective for the production of composite components in low to medium volumes and principally utilise Resin Transfer Moulding (RTM) or vacuum infusion techniques, as shown schematically in Figure 2.4. However, alternative methods are also available, such as Compression Resin Transfer Moulding (CRTM) and Resin Film Infusion (RFI). Each of these methods maintain the strict cost constraints, quality control and low rejection rates demanded by aerospace and automotive industries.

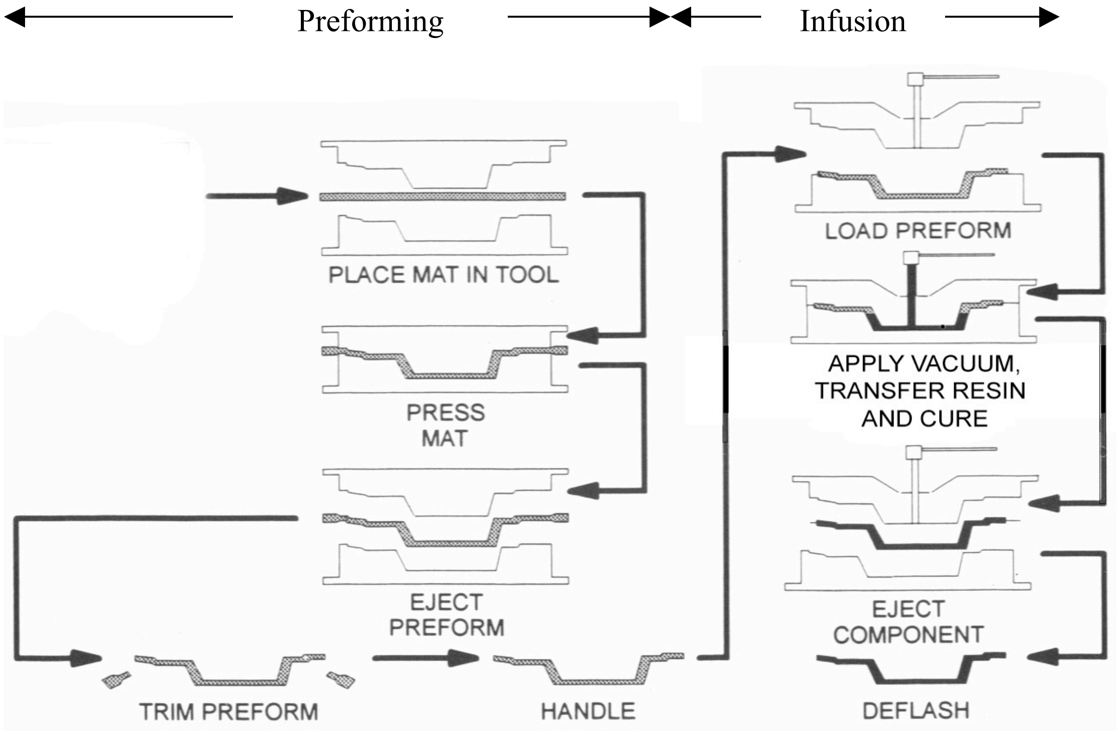

Figure 2.4. Schematic of a vacuum infusion process, adapted from [3]

The requirement to ‘preform’ the fabric sheet to the desired component geometry is common to all liquid moulding production methods and multiple fabric sheets can be formed in one draping process if required. These sheets can be pre-cut to net shape or, as denoted in Figure 2.4, the preform can be trimmed after draping. Pre-cutting of the preform requires initial knowledge of the pre-draped fabric shape, which can be obtained numerically, or experimentally, and permits the use of one set of tools for both preforming and resin infusion. However, due to the high cycle time of infusion and cure, in comparison to preforming, it is often preferential for preforming to be a separate process.

Forming complex geometries may also require the use of specific forming tools, with separate punch sections or blank holders. The aim of such tooling is to create tension within the fibres to control fabric deformation and therefore prevent excessive changes in fibre angle, fabric wrinkling or fibre breakage, since these are detrimental to resin infusion and final mechanical properties of the composite part. Figure 2.5 demonstrates an aircraft wing-rib that uses specific forming tools [14]. In this example, the surrounding blank holders create a state of fibre tension while separate internal punches form the required shape as a two-stage process; with a central punch followed by two outer punches.

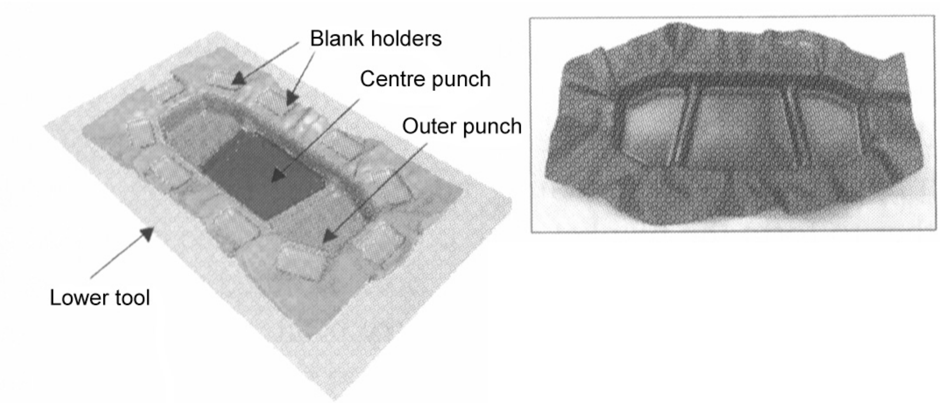

Figure 2.5. Demonstration fibre reinforced thermoplastic aircraft wing-rib during forming [14]

2.4. *FABRIC DEFORMATION MECHANISMS*

Before considering the problem of numerically simulating the preforming process it is necessary to define the deformation mechanisms by which a dry biaxial fabric will deform. In the current work the scales considered are either macroscopic or mesoscopic at a fabric sheet or tow/stitch level, respectively [3][28].

2.4.1. Macroscopic Deformation Mechanisms

Five principle deformation mechanisms have been identified from experimental draping and characterisation experiments of biaxial fabric sheets. These are shown schematically in Figure 2.6 [3][11][15].

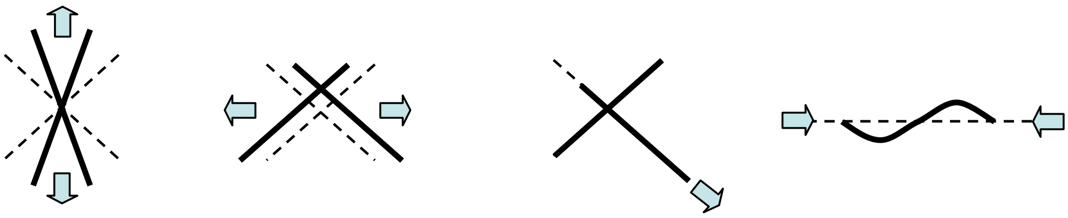

a) inter-tow shear b) cross-over sliding c) inter-tow sliding d) tow buckling

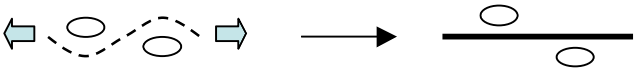

e) tow straightening (woven fabrics only)

Figure 2.6. Modes of fabric deformation during preform manufacture

a) In-plane shear is the dominant mechanism of fabric deformation, involving tow rotation around either a stitching point, or weave crossover, depending on the fabric type. Crossover rotation is predominantly limited by the ability of the fibre tows to become compacted and, for NCF, any stitching restraint.

b & c) Inter-tow and cross-over point sliding occurs when fibres move relative to each other. This is the main alternative deformation mechanism to in-plane shear and usually occurs as the fabric approaches limits of tow compaction and shear locking. Additionally, inter-tow slip is more common in NCF materials when compared to woven fabrics which are considerably stabilised by tow intertwining at the crossover points.

d) Tow buckling occurs due to local in-plane compression and leads to fabric wrinkling. This deformation occurs when the buckling resistance of the fabric is exceeded, usually at high inter-fibre shear angles of 60°-75°. This angle is generally termed as the ‘locking angle’ of a fabric.

e) Tow straightening occurs due to tension within fibre tows and is generally limited to woven fabrics since NCF utilises layers of unidirectional fibres of negligible crimp. The degree to which straightening can occur is controlled by the tow geometry [15][16], which is influenced by the fabric type, tow size and gap size between adjacent tows.

Fibre extension is generally considered negligible due to the high fibre moduli (approx. 160-290GPa for carbon fibres, 70-80GPa for glass fibres and 60-140GPa for aramid fibres).

2.4.2. Mesoscopic Fabric Deformation Mechanisms

At a mesoscopic scale the constituent deformation mechanisms differ between woven and NCF fabrics due to the influence of either tow intertwining or stitching constraints, respectively. For example, both architectures will deform primarily by in-plane shear, Figure 2.7b, with high strains achievable with low applied forces, but NCF materials also have an increased prevalence to deform by inter-tow frictional sliding mechanisms, as shown in Figure 2.7c. For any fabric architecture, progressive in-plane shear results in an increasing shear resistance as deformation limits are approached. The following seven deformation mechanisms have been identified for NCF materials [28][59]:

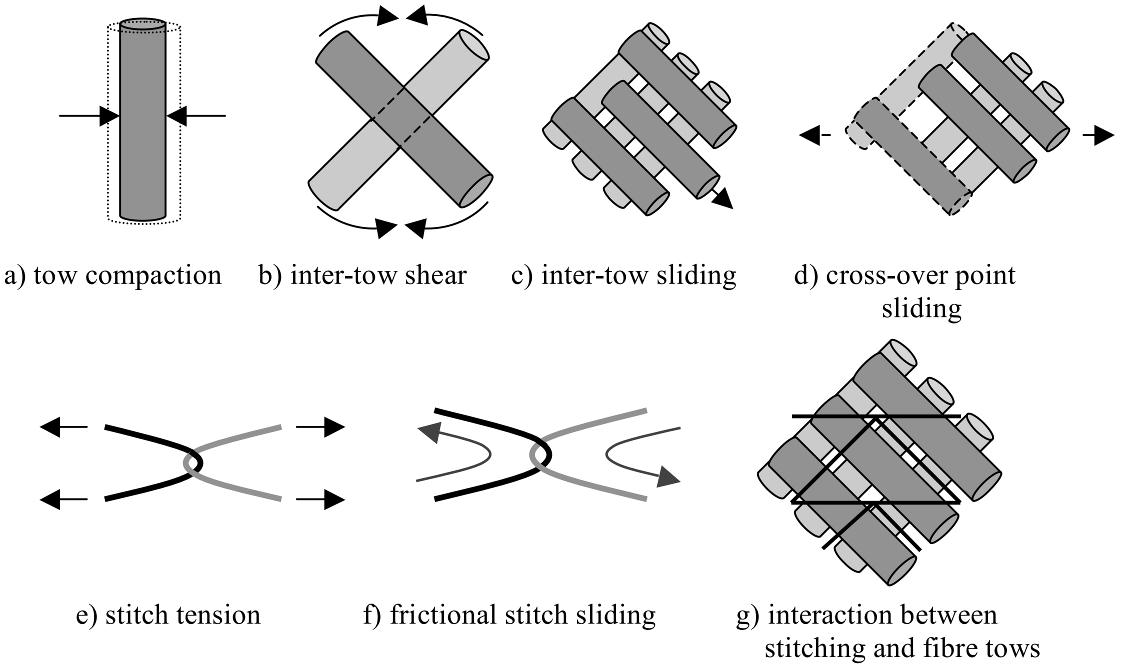
a) tow compaction
b) inter-tow shear
c) inter-tow sliding
d) cross-over point sliding
e) stitch tension
f) frictional stitch sliding
g) interaction between stitching and fibre tows

Figure 2.7. Mesoscopic fabric deformation mechanisms

a) In-plane tow compaction generally occurs during inter-tow shear and out-of plane tow compaction occurs when directly compacted by tooling restraints [41]. For both situations the result is in an increase of fabric fibre volume fraction, as the spacing between fibres is reduced [42].

b) During in-plane fabric shear the tows of separate fibre layers are subject to frictional contact about the point of rotation. The torque required to overcome such friction increases with additional fibre tension, stitch tension or external tooling compaction since all these factors increase loading transverse to the contact area.

c & d) Frictional inter-tow and cross-over point sliding may occur as an alternative deformation mechanism to in-plane shear and are prevalent in NCF materials due to an absence of tow intertwining. The extent to which slip can occur is limited by frictional interactions to surrounding tows and, from direct observation, by the degree of tow impalement, Figure 2.8.

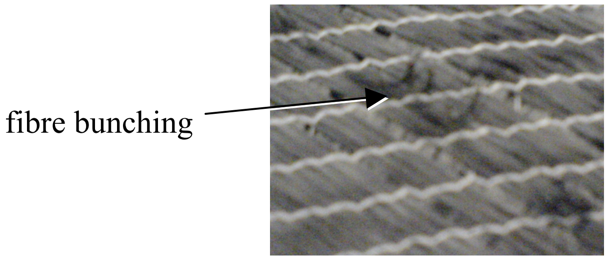

Figure 2.8. Fibre bunching due to slip of an impaled tow

e) During shear deformation the stitching of a NCF will inevitably have to deform to accommodate the in-plane shear deformation of the fibre tows and, consequently, will generate tension within sections of the stitching [28].

f) Frictional stitch sliding may occur at stitching loop points as a result of differing tensions in adjoining sections of the stitch geometry [28].

g) Each of the previously described deformation mechanisms is subject to coupling. For example, in-plane shear can generate stitch tension and sliding which leads to tow compaction and increased inter-tow shear friction.

In addition to the mesoscopic fabric deformation mechanisms described in this section are considerations of tow deformation significant to both testing and forming; specifically these are intra-tow shear and associated local tow buckling. Two modes of intra-tow deformation have been postulated [52]; namely, ‘clamped’ and ‘free’ deformation, Figure 2.9. Clamped deformation corresponds to a uniform shear strain within the tows and fabric, while free deformation corresponds to a state of negligible shear within individual tows, leading to localised compression and buckling. Observations of various woven and NCF fabric architectures indicate tow deformation is closer to the free shear state. Consequently, tow meso-buckling is observed in double curvature forming [52], as shown in Figure 2.10, and produces erroneous 'edge effects', associated with the clamping of tows, during picture frame tests [53].

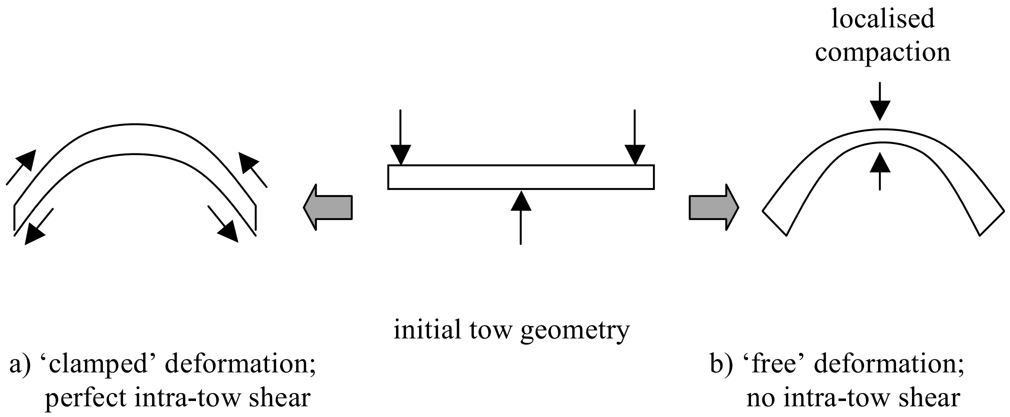

Figure 2.9. Schematic of the possible intra-tow shear deformation modes

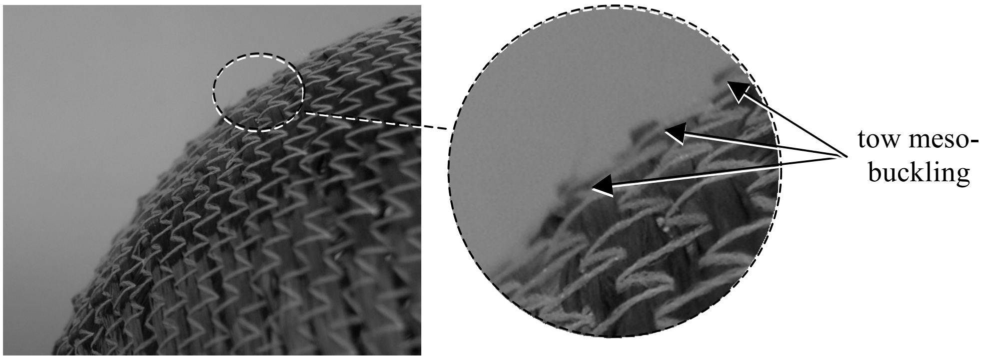

Figure 2.10. Meso-buckling of tows during double curvature forming trials

2.5. EXPERIMENTAL FABRIC CHARACTERISATION METHODS

As described previously, biaxial fabrics are the preferred choice of fabric for forming complex three-dimensional components and primarily deform by in-plane shear. Consequently, characterisation of this non-linear in-plane shear behaviour has received most consideration by researchers to date. Three tests have proved popular; the picture frame [44][67][69], bias extension [63][65][68] and 'Kawabata Evaluation System for Fabrics' (KES-F) [71][74].

The picture frame and bias extension tests have been used in the current work and are described in further detail in the following sections. The KES-F has been primarily developed for the textiles industry and is a complete fabric characterisation procedure for shear, tensile, bending, friction and compression. This test has yet to be widely accepted as a suitable tool to characterise engineering fabrics due to the low levels of deformation induced and limited availability of the costly test equipment [55][60]. Additional tests are available to characterise tow compaction [41][70], flexural rigidity [62], coupling of fibre tensions within woven fabrics [15][16], surface friction [61][103] and frictional tow removal properties [64][86][88]; tests relevant to the present work are described further in subsequent sections.

The difficulty with most test methods of engineering fabrics is the current lack of available standards. This is mainly due to the characterisation of engineering fabrics being a relatively recent endeavour. Standards are available for the textile industry, but these are generally unsuitable for engineering fabrics of defined fibre directions and large-scale deformability. Inevitably, separate institutions have developed 'in-house' test equipment and procedures. However, efforts are currently being made to improve on this inconsistency in a collaborative 'round robin' exercise between institutions with experience of testing engineering fabrics [142][148].

2.5.1. Picture Frame Shear Testing of Engineering Fabrics

The picture frame test, Figure 2.11, is preferred by many researchers for shear testing since a near pure state of strain can be imposed within the test specimen [55]. Shearing is induced by restraining the textile reinforcement in a rhomboid deformation frame with fibres constrained to move parallel to the frame edges. The frame is extended at diagonally opposing corners using simple tensile testing equipment.

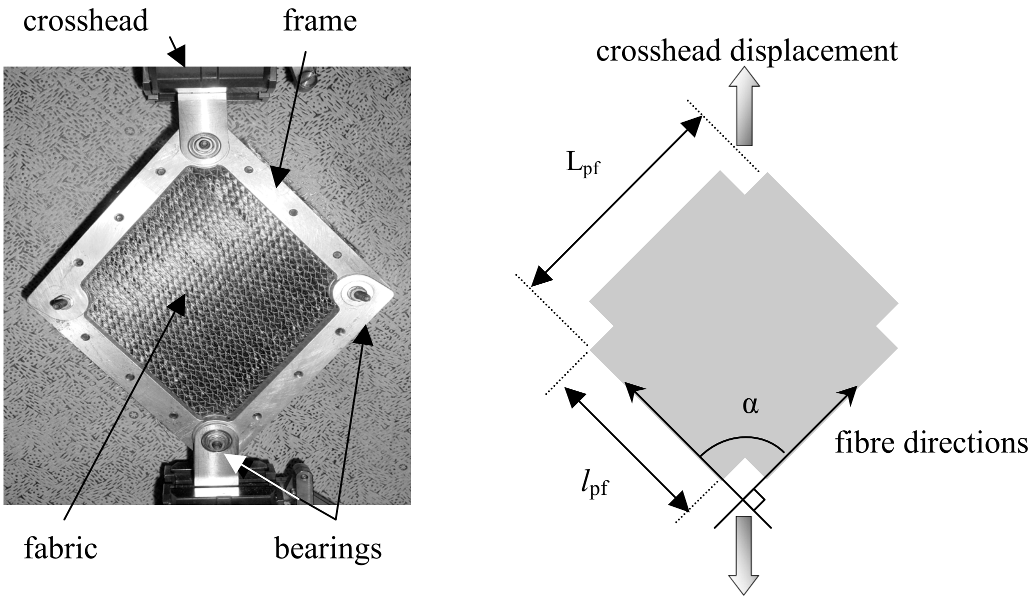

Figure 2.11. The picture frame test and a schematic of a cruciform picture frame fabric specimen

Tensile force data is recorded during the test and an indication of the shear limit is provided through recording the inter-fibre angle at which out-of-plane deformation (wrinkling) first occurs [55][73]. Typical non-linear shear data is shown in Figure 2.12. This figure also demonstrates the occurrence of shear bias with differing shear resistance in positive and negative shear, as defined schematically in Figure 3.2.

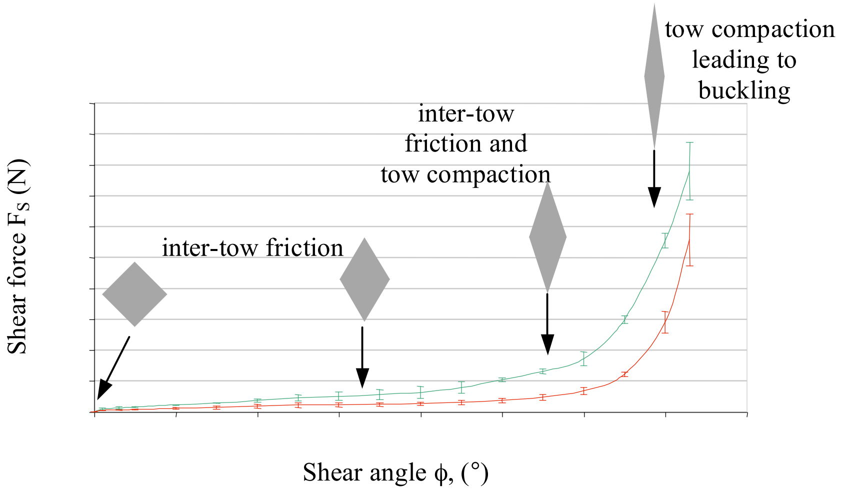

Figure 2.12. Typical NCF picture frame shear data; demonstrating differing shear resistance of positive and negative shear

The testing of complete square samples is possible, depending on the design of the picture frame equipment. However, the corners of each fabric specimen are commonly removed to permit free rotation of the frame bearings and prevent premature fabric wrinkling due to local over compaction. A schematic of such a cruciform fabric specimen is shown in Figure 2.11.

The method of constraining the fabric within the picture frame rig is an important consideration with respect to the fabric shear distribution and occurrence of experimental errors [72]. A common design utilises simple clamping plates along each edge of the frame. These plates can be bolted to the frame, and through the fabric sample [54][67][80]. or fixed to the frame with separate clamp mechanisms at each edge, to avoid possible fibre misalignment around the clamping bolts [69][70].

A consequence of clamping the fabric specimen is the possibility of introducing tensile fibre strains if fibres are misaligned; only small deviations will generate large errors in the measured tensile force due to the high fibre elastic moduli [67]. Careful fabric handling and alignment is therefore required during test setup. Specimen clamping can also contribute to the occurrence of ‘edge-effects’ which are visible as localised buckling of individual tows and result from high intra-tow shear stiffness [52][75], as shown in Figure 2.13. The consequence of this localised buckling is a slightly higher central shear angle and a possible increase in measured axial force.

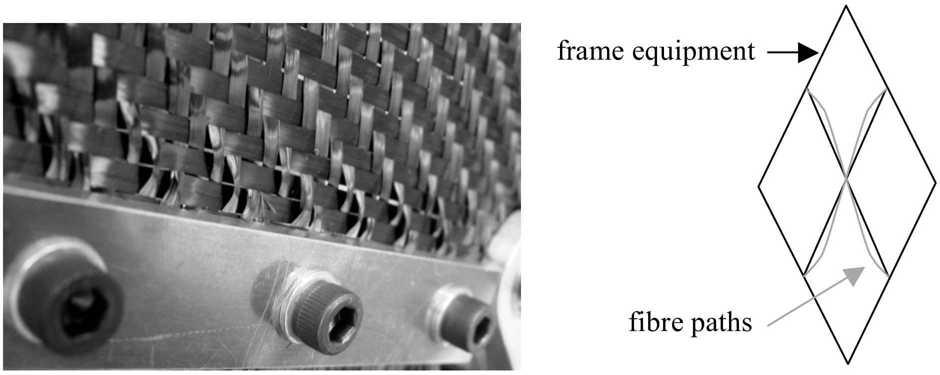

a) image of tow buckling 'edge effects' during picture frame testing of a woven fabric

b) schematic of the buckled fibre paths

Figure 2.13. Edge effects observed during picture frame testing of a woven fabric

Alternative frame designs have been investigated to reduce the effects of specimen clamping. Figure 2.14 shows two such designs, where a fabric specimen is loosely pinned to the frame with minimal clamping pressure, Figure 2.14a [55], or only small 'tabs' of fabric are clamped Figure 2.14b [58]. Such designs can improve the shear distribution and increase test repeatability; however, the lack of restraint can inevitably fail to induce the required deformation kinematics [55].

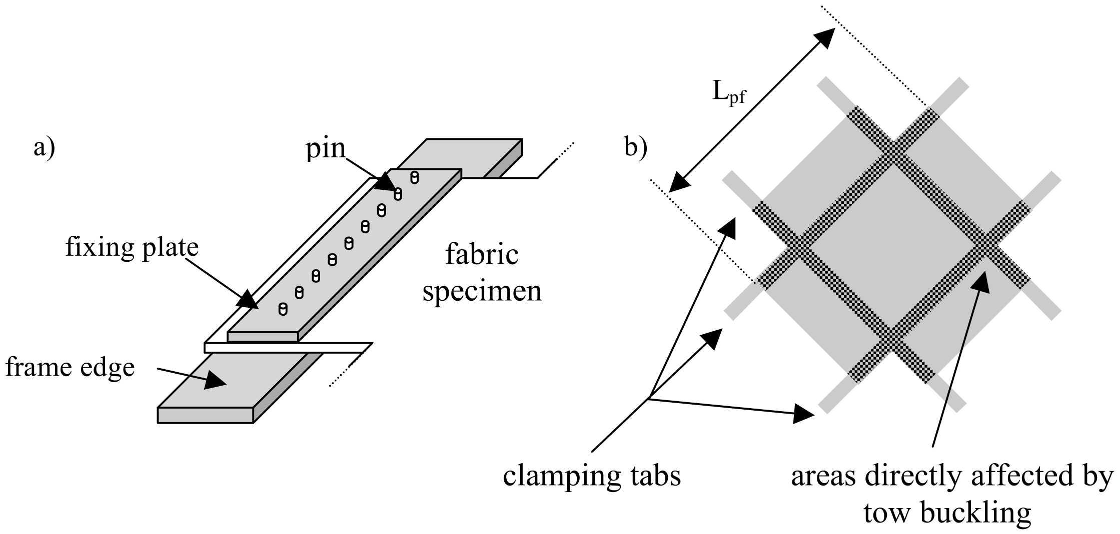

Figure 2.14. Schematic of a the alternative picture frame designs with; a) a pinned frame and, b) a tabbed specimen

Tensile test machines are most commonly used to apply a constant axial velocity, which produces an increasing rate of shear of the rhomboid picture frame and fabric sample.

This is a problem when testing rate dependant materials, such as resin pre-impregnated fabrics, for which a frame specific velocity profile is required to maintain a constant rate of shear. However, the resistance to intra-ply shearing of dry fabrics, like the NCF tested here, is not considered shear rate dependent [66][44] and a constant crosshead velocity can be used during testing.

During picture frame testing, the axial tensile force of the crosshead load-cell is recorded, from which the shear force produced by the fabric can be calculated, using the following equation, [55],

$$F_S = \frac{F_A}{2\cos\left(\frac{\alpha}{2}\right)}, \qquad \text{Eq. (1)}$$

where F_S is the shear force, F_A is the measured crosshead tensile force and α is the acute inter-fibre angle, as shown in Figure 2.11. The inter-fibre shear angle ϕ can be calculated from the acute inter-fibre angle α [81], as follows,

$$\phi = \frac{\pi}{2} - \alpha, \qquad \text{Eq. (2)}$$

where the inter-fibre angle α is measured from the fabric using manual visual methods or Digital Image Correlation (DIC) techniques. Alternatively, the inter-fibre shear angle may be obtained geometrically from the frame dimensions [81], using,

$$\phi = \frac{\pi}{2} - 2\cos^{-1}\left(\frac{1}{\sqrt{2}} + \frac{D}{2L_{pf}}\right), \qquad \text{Eq. (3)}$$

where D is the crosshead displacement and L_{pf} is the frame edge length as defined in Figure 2.11.

Ideally, physical tests should provide material data that is independent of the sample dimensions and test procedure. However, normalisation of picture frame results has proved problematic due to differences of equipment size and procedure. Recent studies have considered the energy required to shear a fabric and suggest normalisation of the measured axial force to the edge length of the picture frame shear specimen is required [59], as described using the following equation,

$$\frac{F_A}{L_{pf}} \approx \frac{f_A}{l_{pf}} = F_N, \qquad \text{Eq. (4)}$$

where F_A is the measured axial force when testing a square fabric specimen, f_A is the axial force measured when testing a smaller fabric specimen, F_N is the normalised axial force and Figure 2.15 defines the length parameters L_{pf} and l_{pf}. However, alternative studies have suggested normalisation of the axial force to the central sheared area (l_{pf}^2) is more accurate when comparing results obtained using cruciform shaped specimens, also shown schematically in Figure 2.15, due to only minor force contributions in deforming the specimen arms, [83]. Consequently, the normalisation of fabric shear force is a topic of active research and further work is required to define a standard procedure for analysing measured shear data.

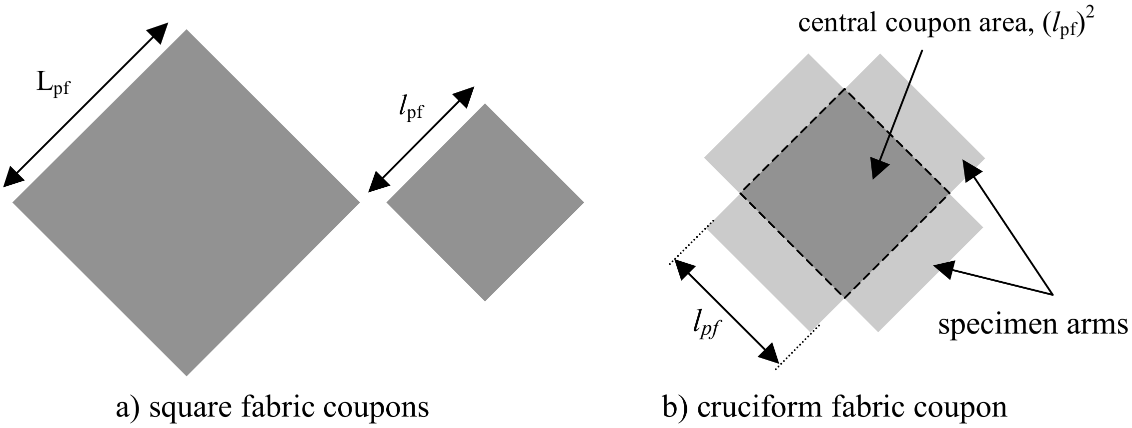

a) square fabric coupons b) cruciform fabric coupon

Figure 2.15. Picture frame force normalisation parameters

The normalised axial force from picture frame tests, F_N, can be compared to equivalent normalised bias extension shear test results by additional normalisation of the axial crosshead displacement, D, using the following equation,

$$D_N = \frac{D}{L_{pf}}, \qquad \text{Eq. (5)}$$

where D_N is the normalised displacement [59].

2.5.2. Bias Extension Textile Shear Testing

The bias extension test is commonly preferred to characterise fabric shear due to the simplicity of the test procedure and minimal equipment requirements [59]. Fabric coupons are tested with a ±45° fibre angle to the coupon edges. The coupon is clamped at each end of the specimen length in a tensile test machine and extended under displacement control. Large test coupons are preferable to maximise the induced shear area. The coupon length-to-width ratio should be at least 2:1 to give suitable shear deformation kinematics within the coupon centre (zone 1 of Figure 2.16) and prevent artificial increase in the measured resistance [55].

Although the test procedure is simple, the distribution of deformation over the sample is complex. Figure 2.16 demonstrates a schematic of the deformation zones induced, while Figure 2.17 highlights these zones for a NCF during testing [54][59].

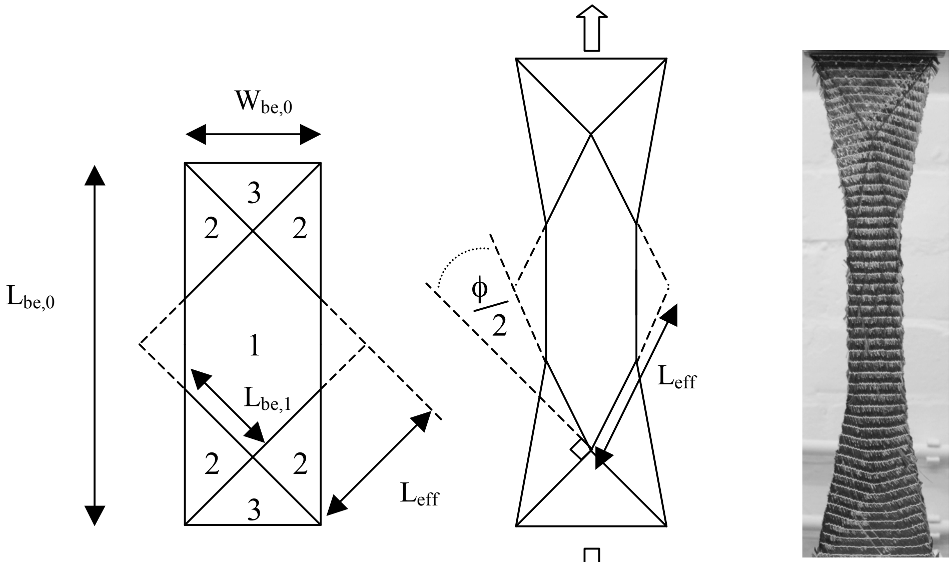

Figure 2.16. Kinematics of the bias extension test

As can be observed from the figure shown above, the clamping of each coupon end produces regions of minimal deformation, zone 3. Minor cross-over point and inter-tow slip may occur within this region, especially in NCF materials for which cross-over points are not stabilised by tow intertwining.

The central zone 1 area is commonly assumed to deform by pure shear at low fibre angles, comparable to a picture frame test of side length L_{eff}, [59], Figure 2.16. However, the inter-fibre shear angle is slightly reduced at the unclamped edges of the specimen compared to the centre of the specimen, due to resistance by tows to compaction.

Deformation in zone 2 acts as a transition between the constrained zone 3 and near pure shear zone 1. As such, cross-over and inter-fibre sliding occurs preferentially to accommodate this transition, observable in Figure 2.17.

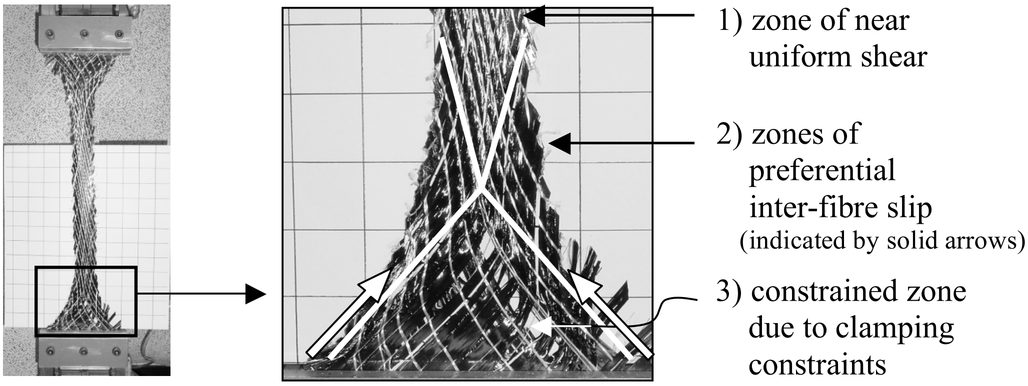

Figure 2.17. Bias extension deformation zones during testing

Example bias extension test results are provided in Figure 2.18, which also shows the dominant deformation mechanisms observed. In-plane shear is, initially, the dominant deformation mechanism and large strains are possible with low applied forces. As shear limits are approached, and the shear resistance of the material increases, alternative cross-over and inter-fibre slip mechanisms become dominant and can permit very high coupon strains before the sample loses integrity.

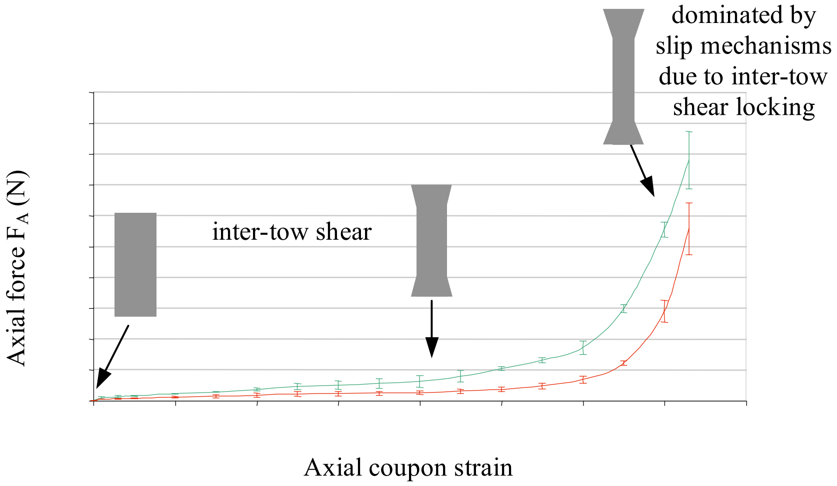

Figure 2.18. Example bias extension test results and main deformation mechanisms

A theoretical inter-fibre shear angle of the central shear zone (zone 1) can be calculated, using equation 3, by considering this shear area to deform similar to a picture frame shear test of edge length equal to L_{eff}, as shown in Figure 2.16. Consequently, this analysis assumes pure shear kinematics. Methods of treating inter-fibre slip between clamped and unclamped tows of the bias extension coupon have been developed [126], but are not based upon material properties. Instead, measurements of the central coupon width are used to directly reproduce the measured deformation and, therefore, this method is unsuitable for generic prediction of inter-tow slip.

The normalisation of bias extension test results has been investigated by considering the energy required to deform the separate deformation zones (1-3) within the specimen [59]. This is based upon an assumption of pure shear kinematics and is therefore only truly valid at low inter-fibre shear angles for fabrics of limited inter-fibre or cross-over slip, such as tightly woven architectures. The normalised axial force, F_N, is calculated using the following equations [59],

$$F_N = \frac{(\lambda - 1)F_A}{L_{eff}(2\lambda - 3 + 2X)}, \qquad \text{Eq. (6)}$$

for which,

$$X = \frac{1}{4}\left[\frac{\cos^2\phi\left(1+3\sin^2[\phi/2]\right)}{\cos^2(\phi/2)\left[1+3\sin^2\phi\right]}\right], \qquad \text{Eq. (7)}$$

$$\lambda = \frac{L_{be,0}}{W_{be,0}}, \qquad \text{Eq. (8)}$$

where ϕ is the inter-fibre shear angle of the central bias extension zone 1, calculated using equation 3, $L_{be,1}$ is a characteristic length of the bias extension test, shown in Figure 2.16, and subscripts '*be*' and '*pf*'' define the bias extension and picture frame tests respectively. Finally, the crosshead displacement, D_{be}, of the tensile test machine is also normalised using the following equation,

$$D_N = \frac{D_{be}}{L_{be,1}(\lambda - 1)}. \qquad \text{Eq. (9)}$$

2.5.3. Optical and Digital Image Correlation (DIC) of Textiles

Investigation of shear distribution in picture frame and bias extension test samples has led to the development of visual inter-fibre angle measurement techniques. Simple visual measurement of the inter-fibre angle is possible through manual analysis of images taken during testing [79], however, recent developments in digital image correlation (DIC) techniques are valuable to produce automated and complete shear maps of fabric specimens. DIC techniques have been extensively developed for measuring strain of solid materials but require special consideration to cope with textile materials deforming by inter-tow shear.

DIC equipment and software dedicated to quantifying full-field fabric deformation after forming is commercially available [76] as described in [78]. In addition, researchers have investigated the use of mesoscopic optical analysis of tows [75][111] and full-field analysis using low cost scanning equipment and proprietary analysis software [114] or commercially available optical strain measurement equipment [53][76], Figure 2.19. Results of picture frame tests with such DIC techniques indicate edge-effects can cause an increase of 5-10° shear angle when testing some woven and high-density fabrics. Results for similar NCF’s to that investigated in the current work, however, indicate minimal variation between fabric and frame shear angles [53].

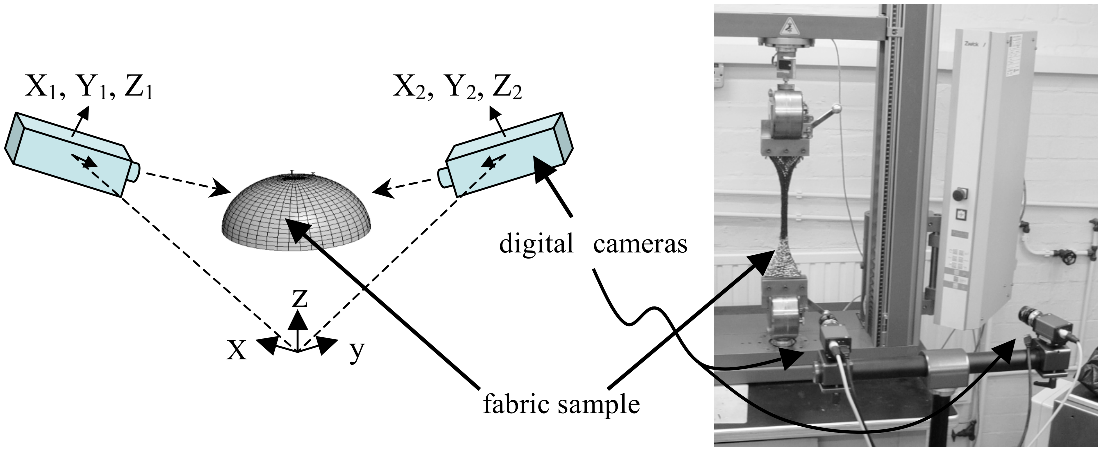

Figure 2.19. The full-field Digital Image Correlation (DIC) technique

2.5.4. Textile Friction Testing

Fabric preforming is a contact dominated operation with multiple fabric layers, blank-holders and punches. The contact pressure and friction forces generated at such surfaces are dominant factors that influence final fabric architecture and, consequently, require characterisation.

Surface friction test standards are currently available [151], although none are specifically designed for the testing of engineering textiles, particularly NCF’s. These materials introduce complexities, due to the surface stitching style and fibre orientations, which influence fictional properties.

Currently, the assumption that macro fabric friction obeys Amonton’s laws of friction is assumed by researchers, since the test methods are simple and equipment requirements are minimal. Considering Figure 2.20, Amonton’s law assumes,

- the measured friction force, $F\mu$, is proportional to the normal load, P,
- the measured friction force, $F\mu$, is independent of the surface contact area,
- the measured friction force, $F\mu$, is independent of the speed of surface sliding.

These assumptions lead to the following equation,

$$\frac{F_{\mu}}{P} = \mu, \qquad \text{Eq. (10)}$$

where, F_{μ} is the force parallel to the contact surface required to begin, or continue, relative surface displacement, P is the load normal to the contact surface and μ is the friction coefficient, to be determined. The friction coefficient, μ, can be defined as a static quantity, μ_S, if the force F_{μ} required to initiate movement between the contacting surfaces is measured, or a dynamic quantity, μ_D, if a constant velocity is maintained during the test.

Two commonly used examples of friction test setups are shown in Figure 2.20. Test (a) shows a static, or dynamic, test setup in which a force, F_{μ} , is applied to a moveable body [103]. Test (b) utilises a steadily tilting platform to ascertain the angle at which static friction is overcome and movement of the body is initiated [61]; the components of force normal and tangential to the inclined surface can then be calculated from simple statics.

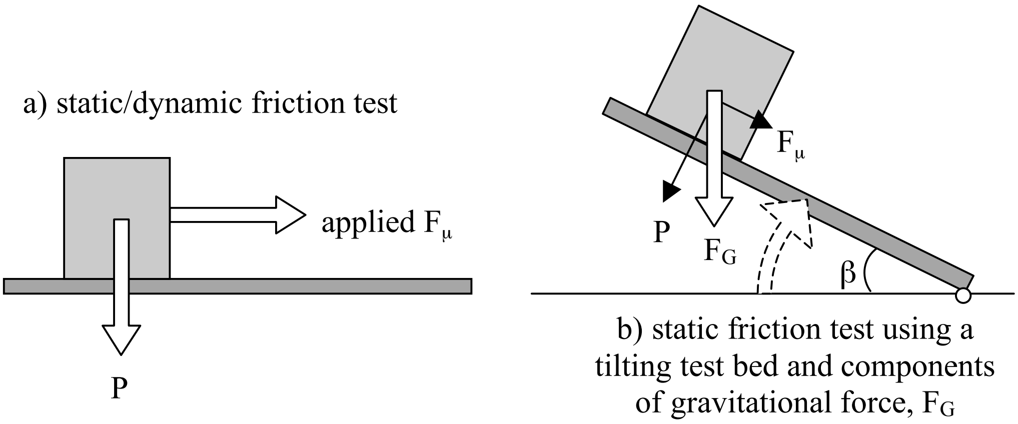
a) static/dynamic friction test

b) static friction test using a tilting test bed and components of gravitational force, F_G

Figure 2.20. Surface friction test methods

2.5.5. Textile Thickness Testing

The variations of fabric thickness and fibre volume fraction, caused by in-plane fabric shear, are important fabric properties that are required for predicting the fabric permeability and mechanical performance of the final composite part. Compaction of the fabric layers will reduce permeability and may lead to incomplete infusion. Equally, under-compaction may produce areas of high permeability that can lead resin ‘fast-tracking’ and incomplete infusion or, alternatively, produce resin rich areas that offer little performance benefit.

Standards for the measurement of textile thickness are available [91], but commonly involve static testing using a single value of load. The evolution of fabric thickness, or fibre volume fraction, with inter-fibre angle is not considered.

Thickness of dry engineering fabrics has previously been measured using a fabric micrometer during bias extension tests and found to be constant during shear [84]. However, the test method involved application of a low transverse load to the sample, which consequently permitted significant increase of fibre volume fraction. Conversely, thickness measurements of a sheared NCF with a higher pressure of 0.5kPa have indicated the fabric thickness closely approximates to a constant volume assumption, inferring the volume fraction remains approximately constant during shear [70]. A compaction model is inferred from these results and is summarised in Table 2.4, however, consideration should be given to the fabric architecture since, for example, shear induced thickness increase for woven fabrics would require elongation of the fibre tows [81].

Variable \ Model	*Plane-strain*	*Conservation of volume*
Transverse compaction pressure	low	high
Fabric thickness	constant	increases with shear
Volume fraction	increases with shear	constant

Table 2.4. Comparison of plane-strain and conservation of volume fabric thickness models

The assumption of constant volume fraction is advantageous in preforming simulation and arguably more representative of forming processes, where contact pressures can be significant. Constant volume is already assumed in commercial fabric models [85].

Fabric thickness progression can be inferred from mapping and macroscopic FE simulation results by simply relating fabric shear angle to a measured fabric thickness, however, mesoscopic modelling methods provide an opportunity to directly predict and account for fabric thickness increases during shear.

2.5.6. Preforming Trials

Experimental preforming trials of engineering fabrics are extensively used to validate fabric preforming models and simulation methods. Currently, no standards exist for characterising the drapeability of engineering fabrics and institutions have used a variety of test procedures, depending on the material and final application of the preforming model; for example, hydro-forming of thermoplastic pre-impregnated fabric is a very different process to the forming of dry fabrics using matched tooling and blankholders. Standards are available for characterising textile drapeability [143][144] but are not commonly used since these methods generally involve the fabric deforming under its own weight, which is not representative of preform manufacturing methods. Ideally a preforming test should approximate common industrial manufacturing techniques and cause sufficient fabric deformation to properly test the simulation, or analytical, fabric model.

Various mould geometries have been used to sufficiently deform engineering fabrics to validate forming simulation models, such as; cones [78], double-domes [31][64], sinusoidal-wave surfaces [35] and actual industrial component shapes [35][127][128]. Nevertheless, the most common geometry used for preforming trials is a single hemisphere [24][44][81][127]. The hemisphere surface geometry is popular because large fabric deformations are usually required. Furthermore, the symmetry of the hemisphere simplifies the analysis of fabric deformation mechanisms; for example, shear bias is known to occur as a result of the fabric properties and is not influenced by the geometry to which the fabric is formed.

Forming fabrics to the surface of a hemisphere has proven to be suitable for characterising fabric deformation, but is limited in representing the industrial forming of complex shapes, which commonly include re-entrant geometries, such as car floor-pans or aerospace wing-box structures. These structures can introduce additional defects, which are unlikely to occur when forming to a hemisphere, such as bridging across sections of the geometry [54] or even fibre breakage. Nonetheless, a hemisphere surface is still the popular choice of geometry for the majority of research into fabric preforming.

2.6. CONSTITUTIVE MODELLING OF FABRIC DEFORMATION RESISTANCE

The manufacture of CFRP materials in medium to high volumes requires efficient modelling tools to reduce design costs and time. Commercial codes to predict processing and final composite properties are available but commonly require significant quantities of fabric property data. Experimental methods are suitable to obtain such data but are time consuming and expensive, therefore, constitutive material models that predict textile properties have been developed. Such modelling should ideally account for contributions from individual deformation mechanisms of the tows, and any stitching [55], but this can prove complex to achieve due to the range of fabric deformation mechanisms possible.

In-plane shear resistance is the primary mechanism by which fabrics deformation and is controlled by frictional shear at tow crossover points [93]. A variety of constitutive models have been developed for woven fabrics, based upon a simplified mesoscopic models of the fabric geometry. Simplistic models treat woven tows as a network of trusses connected by pin-joints at tow cross-over locations [92]. Such models have been improved to include interactions of tow straightening between warp and weft tows [104][105]. However, the primary limitations of such models are that the true fabric comprises tows with oval cross-sections and smooth tow-path curvatures. Therefore, improved models have been based upon more realistic tow geometries using sinusoidal [41][84][112], or more general tow-path representations [67]. The mechanisms of deformation treated by these later works have also increased to include models of frictional contact at tow crossovers [92] and transverse tow compaction resistance [42].

NCF's differ from woven fabric through the absence of tow crimp and inclusion of binding stitching. The individual and coupled deformation mechanisms, of tows and stitching, inevitably increase the modelling complexity. Currently, only individual deformations of the tow and stitch have been investigated, based on a constitutive mesoscopic modelling scheme [94]; the effects of tow and stitch coupling require further investigation. Modelling of tow deformation is based upon the frictional torque resistance of each tow crossover and transverse compaction of tows with shear [28]. Deformation of a tricot stitch geometry has been investigated by considering the energy dissipated through tensile strains and frictional sliding of separate stitch segments [28], using a idealised stitch model shown in Figure 2.21.

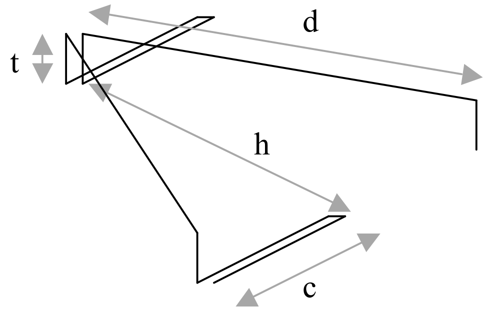

Figure 2.21. Model geometry of a tricot stitch, [28]

Consideration of pure shear deformation kinematics has resulted in the following relations between the lengths of the respective stitch constituents, c and d, and the fabric shear angle, ϕ, [28],

$$d(\phi) = \sqrt{2{c_0}^2 \cos^2\left(\frac{\pi}{4} - \frac{\phi}{2}\right) + 2{h_0}^2 \sin^2\left(\frac{\pi}{4} - \frac{\phi}{2}\right)}, \qquad \text{Eq. (11)}$$

$$c(\phi) = \sqrt{2} c_0 \cos\left(\frac{\pi}{4} - \frac{\phi}{2}\right). \qquad \text{Eq. (12)}$$

The total stitch length within a unit cell can now be calculated with the following equation and used for calculation of stitch strain during fabric shear,

$$L_s(\phi) = 2d(\phi) + 4c(\phi) + 4t(\phi), \qquad \text{Eq. (13)}$$

where the fabric thickness t(ϕ) can be obtained experimentally or with a suitable thickness model.

Predictions of shear resistance, using the NCF model described above and assuming constant fabric thickness, indicate stitch tension dominates at low inter-fibre shear angles, while in-plane tow compaction resistance becomes dominant at higher shear angles [28]. Predicted results are compared to experimental shear resistance data obtained using the picture frame test method [28]. Shear bias is predicted and occurs during tests, however, the fabric shear resistance is over-predicted at higher shear angles (>40°) [28]. This discrepancy can be attributed to excessive tow compaction resistance due to the assumption of constant fabric thickness, which has been based on experimental thickness results obtained in [41].

As previously described in section 2.5.5, the measurement of fabric thickness is highly dependent on the compaction load applied; an assumption of constant fabric thickness may be valid at low shear angles, but compares poorly at higher shear angles, for which fibre redistribution and fabric thickness increases occur. Experimental compaction tests, without the constraint of plane strain, have been undertaken for Kevlar and E-glass fibre tows and confirm that the tow compaction model used, and originally developed in [42], over-predicts the compaction resistance due to the assumption of plane strain [41]. A constitutive woven fabric model, originally developed in [41], has since been modified to include measurements of correct fabric thickness, from microscope analysis of fabric cross-sections, and shows improved results when compared to test [112].

In conclusion, the popular compaction model of [42] has been validated for the prediction of plane strain tow compaction stresses [41]. However, the tow volume and, thus, fibre volume fraction must be correctly accounted for if accurate predictions of in-plane tow compaction resistance are to be achieved.

The previous models have been based upon idealised theoretical geometries of the fabric structure and model the fabric with reference to a single initial state. This has proved suitable for simple weave structures [112], but does not account for changes in fabric geometry and is not ideally suited for complex 3D-woven structures, with which multiple interactions occur. An alternative modelling method is to generate 3D unit-cell geometries of textiles in what is termed a ‘textile geometry pre-processor’ for meso-mechanical modelling of textile composites [108]. This tool is not based on FE methods, but rather uses constitutive material models defining the axial compression/tension, bending and compaction of each unit-cell constituent.

Currently, this pre-processor is able to ascertain the equilibrium unit-cell geometry, based upon mechanical data of the virgin constituents [118], predict low-angle shear deformations [118], coupled fibre tensions of woven fabrics [51], the nested fabric geometry of multiple fabric plies [119] and out-of-plane compaction properties. FE meshes can be generated using the textile geometry obtained from these analyses, however, these detailed models are currently overly complex for the simulation of comprehensive parts and are only truly suitable for ascertaining localised properties of the fabric structure. Preforming simulation generally requires some simplification of the textile geometry or assumptions to be made regarding the deformation mechanisms treated. The methods most commonly used for preforming simulation are described in the following sections.

2.7. FABRIC PREFORMING NUMERICAL SIMULATION TECHNIQUES

The prediction of fabric draping is an important step in the virtual design of composites. The analysis should, ideally, give reliable information on changes in the fabric architecture such as tow and thickness redistribution, compaction and also identify drapeability limits such as fabric buckling, shear locking and regions of excessive deformation. Prediction of these defects allows the designer to consider alternative draping processes, fabric restraints or fabric types. Information on fibre reorientation is, for example, required for accurate stiffness analysis of a structural composite part. It is also important information for failure prediction and determination of orthotropic permeability models for resin impregnation analysis. A flow chart of a typical design process is shown in Figure 2.22.

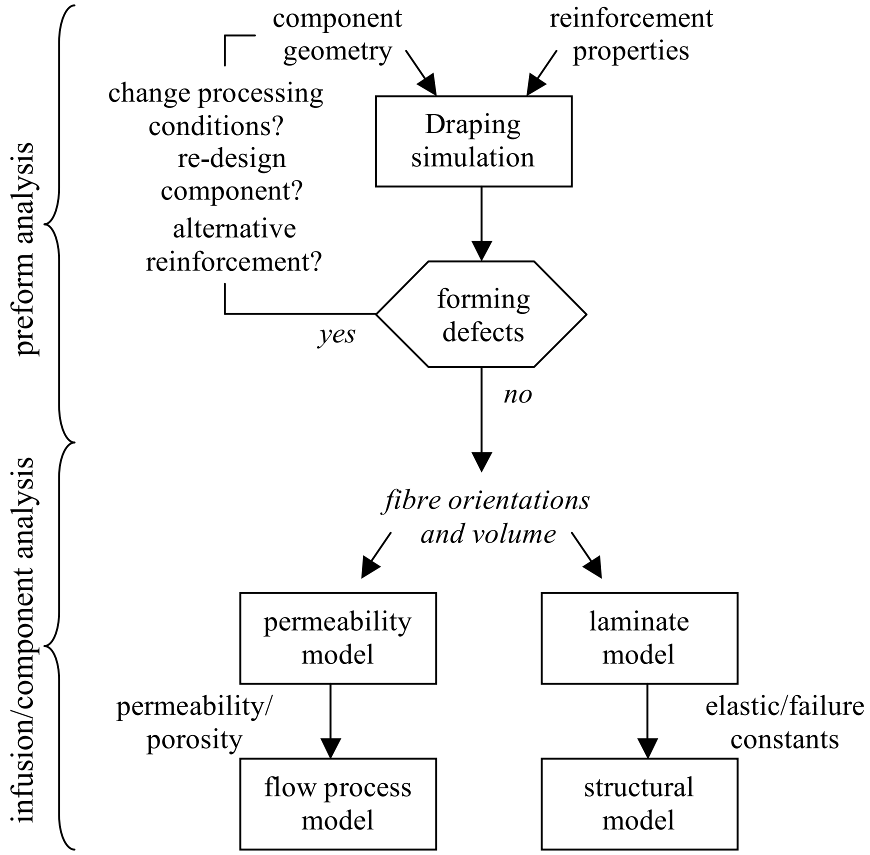

Figure 2.22. CAE approach to preform design, based on [3]

The definition of a forming defect is subjective and defined on an individual component basis. Generally, a selection from the following criteria is applied [18][35]:

- Freedom from wrinkling and bridging. Wrinkling can be caused by excessive in-plane fabric shear, or improper use of blank holders, leading to local in-plane fabric compression. Bridging may occur due to excessive friction between fabric plies and tooling or due to the inability of a fabric to deform fully to the required three-dimensional geometry.
- Minimum shear deformation in the greatest area.
- Satisfaction of fibre orientation tolerances in particular areas, if specified by the component design.

Methods for draping simulation can be broadly grouped into three categories; kinematic mapping algorithms, continuum Finite Element simulation and mesoscopic Finite Element simulation techniques. Each of these are described in the following sections.

2.7.1. Kinematic Mapping Algorithms

The first preforming simulation methods proposed were specifically developed to treat the deformation mechanics of biaxial fabrics and are called kinematic mapping algorithms. These mapping methods are fast, robust and able to provide useful information regarding the progression of inter-fibre shear during forming with minimal input data.

Kinematic methods are based on the original work of Mack and Taylor from the 1950's [29] and make the following assumptions about the fabric [29][16][3]:

- Fibres are inextensible.
- Fibre cross-over points are fixed and effectively treated as pin-joints.
- Fibre segments are straight between pin-joints.
- The fabric is infinitely thin.
- Uniform surface contact is achieved.
- Bending and shear stiffness are negligible.

In order to generate a deformed fibre pattern, the method requires two initial fibre directions (L_1, L_2), the edge length of the net segments (a,b) and a single starting point (P) to be specified, as shown in Figure 2.23.

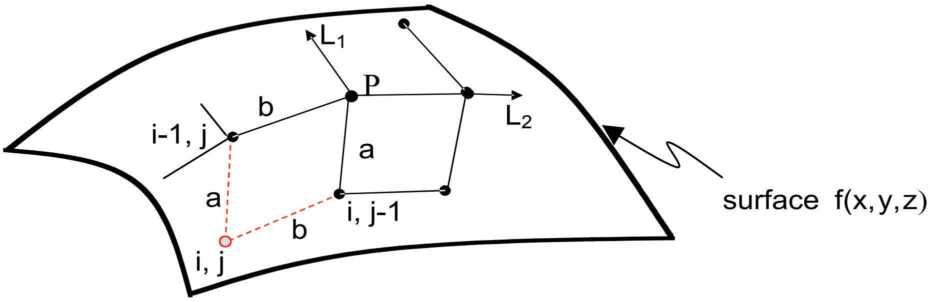

Figure 2.23. The kinematic mapping algorithm solution scheme

The technique works concentrically outward from an initial starting point that must be defined in addition to two initial fibre directions. The draped fibre pattern can then be found by solving the intersection of each pin-joint node, Equation 14, and the geometry surface, Equation 15.

$$\left(x_{i,j}-x_{i-1,j}\right)^2+\left(y_{i,j}-y_{i-1,j}\right)^2+\left(z_{i,j}-z_{i-1,j}\right)^2=a_i^2 \qquad \text{Eq. (14)}$$
$$\left(x_{i,j}-x_{i,j-1}\right)^2+\left(y_{i,j}-y_{i,j-1}\right)^2+\left(z_{i,j}-z_{i,j-1}\right)^2=b_j^2$$

$$f\left(x,y,z\right)=0\,. \qquad \text{Eq. (15)}$$

As Equations 14 and 15 suggest, the method can be idealised as the intersection of the required geometry surface with two spheres of radius (a) and (b), centred at points (i-1,j) and (i,j-1). This intersection can be solved explicitly if the required geometry is defined by a geometrical function, such as a hemisphere of known radius. For arbitrary surfaces the solution is numerical, with the surface defined as a grid of curved [18] or straight edged patches [17], using a polynomial or linear fit respectively. Linear patches simplify the computation greatly and small patches, with respect to lengths (a) and (b), can be used to ensure good accuracy. An example of a geometrical mapping result is shown in Figure 2.24, for the analysis of an automotive rear seat bench.

As can be inferred from the analysis data inputs, the results obtained from mapping methods are independent of the process and materials used; with tooling friction, interaction between multiple fabric sheets and shear locking being neglected. The basic method is intrinsically limited to analyse simple component geometries with few, or no, re-entrant surfaces; this is a consequence of the concentric solution scheme emanating from a single starting point [76].

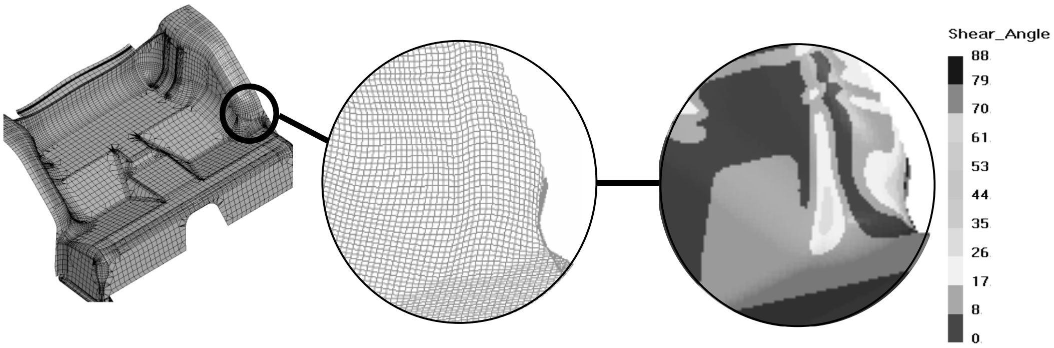

a) geometry mesh b) kinematic algorithm result c) inter-fibre angle data

Figure 2.24. Example results from a kinematic drape algorithm, [123]

Studies also indicate the fibre distribution to be dependent on the initial contact point and initial fibre paths chosen [36], which can be problematic to select when producing complex components, or considering parts that may have multiple initial contact points. Research considering these problems have developed optional ways of defining the initial fibre paths; the intersection of the geometry surface to two selected planes can be used [18] or, alternatively, geodesic lines can be specified for arbitrary geometries [17]. Comparisons between these methods indicate that the geodesic line method provides improved accuracy for complex geometries [35]. The planar method is found to produce excessive shear for fabrics draped on complex surfaces [35].

Algorithms have also been developed in an attempt to improve representation of the fabric deformation mechanisms. One simple improvement is to impose a maximum shear angle limit and thereby more evenly distribute shear [50]. The energy method [19] further enhances the simulated deformation kinematics by minimising the total shear energy in the mapped segments based upon the assumption that deformation energy is proportional to the shear angle. The treatment of fabric shear resistance is therefore improved and results have proven more accurate than the basic algorithm when forming complex geometries [35]. Results with such models are still, however, independent of material and processing conditions.

Further investigations on improving the mapping algorithm have considered the application of actual fabric shear test data [44]. A Hooke and Jeeves iterative minimisation method is used in conjunction with picture frame shear data to minimise the total shear energy of the simulated preform and so produce an optimised and material dependant solution. Shear data obtained in both positive and negative shear can be treated to consider directions of preferential shear bias; a condition required for many styles of NCF. The application of such an algorithm to NCF preforming is still, however, limited by the assumptions of pin-jointed deformation at tow cross-over points since complex deformation mechanisms such as tow slip cannot be treated.

As demonstrated in Figure 2.5, preforming processes commonly utilise blankholders to induce fibre tension, reduce the occurrence of fabric wrinkles and control shear angle variation in the final preform. Recent research has adapted the kinematic algorithm to model processing conditions by accounting for blankholder forces and thus produce process dependent results. The method uses the previously described iterative shear energy minimisation algorithm of [44], and calculates the frictional energy required to pull the fabric through the blankholder during forming, based on the surface contact area, pressure and Coulomb friction coefficient [43]. Mapping results presented in this work show that the effect of shear bias is reduced when the blankholder contact force is increased, as occurs experimentally [67]. However, this simple numerical method can only approximate the interaction between the fabric and simple blankholders. Therefore, this method is unsuitable for complex forming processes using separate punch sections or multiple blankholders, such as the example previously presented in Figure 2.5.

To summarise, despite the inherent limitations and modelling approximations, mapping methods do provide a popular initial design tool to indicate if any forming difficulties are likely to occur. A number of simple commercial codes are available [47][48][49][50] although, generally, the previously described improvements have not yet been implemented in these codes or been industrially validated.

As previously described, two other methods of fabric drape simulation are considered, namely; macroscopic Finite Element modelling and mesoscopic Finite Element modelling. These two methods are described in the following sections.

2.7.2. The Basis of Finite Element Modelling Techniques

Generally, two classes of Finite Element methods are available; either the Implicit or Explicit method [21]. The former, implicit method, is more widely available and used for a broad range of problems, including static and nonlinear stress analysis. The Explicit method has received increasing attention during the past two decades, particularly for dynamic, highly non-linear, contact dominated problems; for example, car crash and metal stamping simulation are applications particularly well suited to this technique. A brief description of these two techniques is given below.

Both techniques use conventional Finite Elements to discretise and represent the structure. The structural stiffness is provided by the assembly of the individual elements and any applied external loads, or boundary conditions, are imposed at the nodal points that join elements. In the Implicit method the global structure stiffness matrix [K] provides the relationship between applied nodal forces {F} and resulting nodal displacements {u},

$$\{F\} = [K]\{u\}, \qquad \text{or by inversion, } \{F\}[K]^{-1} = \{u\}. \qquad \text{Eq. (16)}$$

The nodal displacements are then used to compute individual element stresses and strains. Problems involving contact, buckling, large deformations and material nonlinearity yield a nonlinear stiffness matrix [K]; in this case a CPU intensive iterative solution is necessary to determine nodal displacements for a given applied loading. These phenomena are all present in fabric draping and an Implicit solution approach would present a formidable computational challenge.

The alternative Explicit algorithm uses a different solution strategy and poses the problem as a dynamic one, using the linearised equations of motion, from which a solution in the time domain is obtained. At each node the dynamic equation of motion is,

$$[M]\{\ddot{u}\}_n + [C]\{\dot{u}\}_n + [K]\{u\}_n = \{F_{ext}\}_n, \qquad \text{Eq. (17)}$$

where $\{u\}$, $\{\dot{u}\}$ and $\{\ddot{u}\}$ are vectors of nodal displacement, velocity and acceleration, n is the cycle number at time position T_n (after n.ΔT time steps); [M], [C] and [K] are the Mass, Damping and Stiffness matrices respectively and $\{F_{ext}\}$ is a vector of applied external nodal forces. Material damping can be neglected in short duration dynamic problems and, replacing the term $[K]\{u\}_n$ with the equivalent internal nodal force vector $\{F_{int}\}_n$ gives Newton's second law of motion,

$$[M]\{\ddot{u}\}_n = \{F_{ext}\}_n - \{F_{\text{int}}\}_n. \qquad \text{Eq. (18)}$$

If a lumped mass distribution is assumed the mass matrix [M] is diagonal and a solution for nodal accelerations $\{\ddot{u}\}$ is trivial,

$$\{\ddot{u}\}_n = [M]^{-1}(\{F_{ext}\} - \{F_{\text{int}}\})_n. \qquad \text{Eq. (19)}$$

The nodal velocities $\{\dot{u}\}_{n+1/2}$ and nodal displacements $\{u\}_{n+1}$ may then be obtained by integration in the time domain using the central finite difference operators,

$$\{\dot{u}\}_{n+\frac{1}{2}} = \{\dot{u}\}_{n-\frac{1}{2}} + \{\ddot{u}\}_n \Delta T_n, \qquad \text{Eq. (20)}$$

$$\{u\}_{n+1} = \{u\}_n + \{\dot{u}\}_{n+\frac{1}{2}} \Delta T_n. \qquad \text{Eq. (21)}$$

Finally, the updated displacements are used to compute element stresses and strains and the problem is advanced with a new time increment. Equations 20 and 21 are 'conditionally stable' and restrict the allowable integration time step to $\Delta T_{critical}$ which is dependent on the smallest element size and material properties.

To summarise, the Implicit method is superior for static, mildly nonlinear problems; whereas the Explicit method is advantageous for dynamic problems involving large scale deformation and material nonlinearity. Also, it is straightforward to treat sheet buckling and contact between surfaces using the dynamic integration scheme, both of which are important in draping analysis.

2.7.3. Macroscopic Finite Element Drape Simulation

As previously described in the section 2.7.1, mapping based algorithms are useful to provide a first approximation of the deformed preform fibre architecture. However, the inherent limitation of neglecting key fabric deformation mechanisms, such as wrinkling and accurate processing conditions, has led to adoption of the Finite Element (FE) simulation method for preform analysis.

Finite Element methods have been validated for the simulation of metal stamping [145], which involve similar contact problems to fabric forming, albeit using alternative constitutive material models. Compared to simple kinematic mapping methods, FE techniques offer improved modelling of fabric deformation and processing conditions by directly representing the fabric, tooling and any interactions by applying appropriate constitutive laws. The FE method is also inherently adaptable and new constitutive models can be easily implemented into existing FE codes. This has contributed to numerous constitutive fabric models being developed, as described in the following paragraphs.

The primary requirement of a macroscopic fabric law is to treat the high elastic stiffness in the fibre directions while also including nonlinear inter-fibre shear resistance. Membrane finite elements are capable of modelling fabric shear during preforming [152], but cannot transmit bending loads [137] and, therefore, are unable to correctly predict the occurrence of fabric buckling. Consequently, shell elements, which are capable of transmitting bending moments, are preferred for correct treatment of fabric buckling and contact forces during forming [4][30][109], despite requiring longer simulation times [138].

In-plane shear in macroscopic constitutive models is most commonly treated using constitutive material laws, to which experimental fabric shear data is usually applied or calibrated [54][138]. Research has shown that these material laws should correctly account for the varying orientation of the fibre directions during shear [24][25][26], as demonstrated in Figure 2.25. Recent developments of such non-orthogonal models have also included treatment of biased shear in NCF materials by separately accounting for fabric resistance to positive and negative orientations of shear [138]. Results of preforming simulations using this fabric model show improved treatment of NCF shear deformation with predictions of asymmetric fabric shear behaviour, despite forming to a symmetric hemisphere surface. However, inter-tow slip mechanisms of NCF are not included, therefore, excessive fabric deformation will be predicted at higher shear angles.

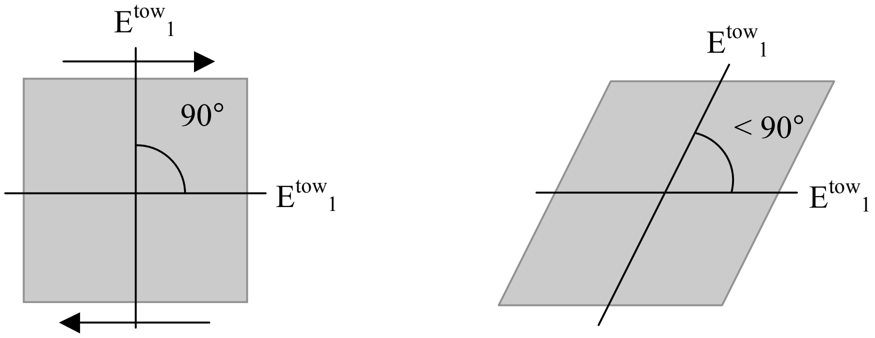

a) orthogonal fibre axes – pre-shear b) non-orthogonal fibre axes – post shear

Figure 2.25. Schematic of non-orthogonal inter-fibre angles in a biaxial fabric deformed by shear

The deformation of dry fabrics is considered rate independent [66][44]. However, preforming simulation of pre-impregnated fabrics requires consideration of the rate dependant viscoelastic contribution of resin by using appropriate constitutive laws [4][27][31]. Computationally efficient methods of treating inter-ply slip when thermoforming multiple fibre reinforced thermoplastic plies have also been developed [32]. However, current computing power permits the discrete simulation of multiple plies in reasonable timescales, using viscous-friction contact constraints and heat transfer models between plies [45].

As described in section 2.4.1, shear is the main mechanisms by which fabrics form to a surface, however, fabric specific deformation modes may also occur. Consequently, tied multi-ply models have been developed to treat the relative slip of unidirectional fibre layers in NCF [54]. Specific to the forming simulation of woven fabrics is coupled straightening of loaded fibre tows and methods of measuring, and including, these deformations are described in [15][16]. However, only small coupled strains are commonly possible in the fibre directions (typically <1%) and, therefore, this is not considered to be a dominant mechanism of fabric deformation.

Alternative approaches to fabric modelling have investigated the use of multiple element components, instead of computationally expensive constitutive material laws and continuum elements. For example, fabric representations using simple 1-D bar elements to treat the fibre stiffness and shear resistance have been investigated [34], as shown in Figure 2.26. These models are capable of treating the dominant fabric deformation mode of pure shear, but are unable to represent true fabric deformation or accurately treat tooling and fabric contact.

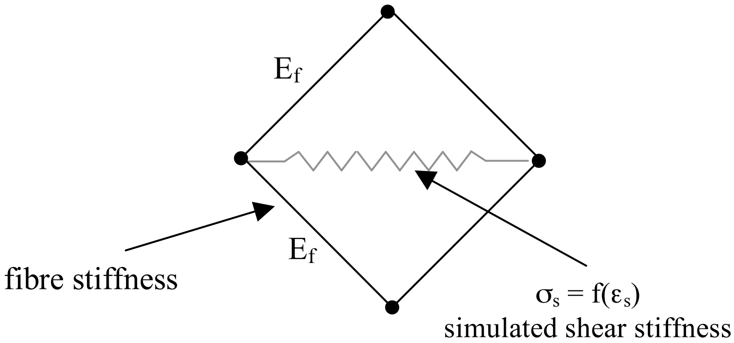

Figure 2.26. A simplified bar element fabric representation; using pin jointed bar elements to represent fibres and a single linked bar element to represent shear resistance [34]

Study into efficient methods of treating tow slip have investigated the use of bi-component fabric representations, in a specially defined pattern [33] to isolate the modelled fibres and, thus, attempt to treat inter-fibre slip. However, this approach does couple the fibre slip and membrane shear mechanisms and, consequently, is not truly representative of inter-tow slip deformation.

To summarise, although results obtained using FE methods are more accurate than previously described kinematic algorithms, the increase in material and process input data inevitably leads to greater demands on obtaining fabric test data, staff training and computation time to obtain a solution [55]. These factors have currently limited the widespread use of FE drape codes in industry, although dedicated forming software packages are increasing being adopted. One such commercial code, originally developed in a CEC funded Brite-Euram project [46], has led to the first commercial FE code, PAM-FORM [4], dedicated to thermoforming simulation of advanced fibre reinforced thermoplastics.

The above cited CEC project resulted in a validated methodology and constitutive model for modelling unidirectional and biaxial fabric sheets. The model includes a viscous contribution to treat pre-impregnated resin/thermoplastic component (considerations regarding the use of this model are described in [150]). The fabric model includes representation of uncoupled fibre stretching and fabric bending in addition to inter-fibre shear and locking via a designated locking angle at which point an associated increase in shear modulus is imposed to represent the 'locked' fabric, as shown in Figure 2.27.

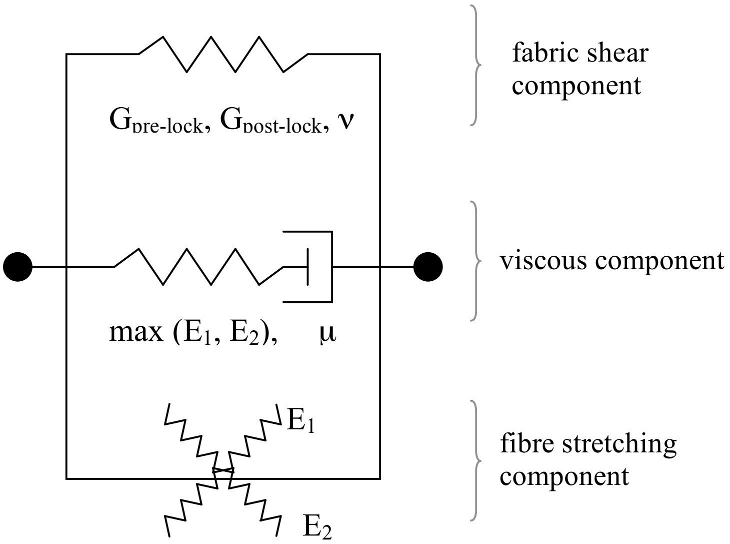

Figure 2.27. The fabric material model of PAM-FORM; a commercial FE draping code

Figure 2.27 shows the main features and constitutive laws used to simulate thermoplastic fabric sheets with PAM-FORM, using separate discretisation of individual fibre layers and a viscous-Coulomb friction law, σ_S, between adjoining sheets. The sliding resistance forces depend on the summation of dry friction $\mu.\Delta P$ and viscous friction $\eta_T.\Delta Vel$, where η_T is the resin viscosity, μ is the Coulomb friction, ΔP is the pressure difference between plies and ΔVel *is* the relative sliding velocity between plies. For the fabric ply an elastic fibres embedded in a viscous resin law is assumed, Equation 23. The first part of this equation is the elastic fibre contribution, whereas the second part is the rate dependant viscous resin contribution. Both resin longitudinal (parallel to fibres) viscosity η_L and transverse viscosity η_T are included which may be either constant in iso-thermal forming, or temperature dependant in thermoforming.

$$\sigma_S = f(\eta_T, \Delta Vel, \mu, \Delta P) \qquad \text{Eq. (22)}$$

$$\begin{pmatrix} \sigma_{11} \\ \sigma_{22} \\ \sigma_{12} \end{pmatrix} = \begin{pmatrix} E_{11}\varepsilon_{11} \\ E_{22}\varepsilon_{22} \\ G_{12}\varepsilon_{12} \end{pmatrix} + \begin{bmatrix} 4\eta_L & 2\eta_T & 0 \\ 2\eta_T & 4\eta_L & 0 \\ 0 & 0 & 2\eta_L \end{bmatrix} \begin{pmatrix} \dot{\varepsilon}_{11} \\ \dot{\varepsilon}_{22} \\ \dot{\varepsilon}_{12} \end{pmatrix} \qquad \text{Eq. (23)}$$

The main deficiency of the using macroscopic material models is that fabrics comprise separate tows and stitching, which can deform by inter-tow and crossover point slip mechanisms that are untreatable with homogenised continuum mechanics. Tow slip occurs at high inter-fibre shear angles, as the fabric approaches inter-tow shear ‘locking’, as an alternative mode of deformation from further shear or local buckling. Typically, areas of high fabric shear angle are essential to predict since the local permeability, and final composite mechanical performance, are greatly changed from that of the un-deformed fabric. Mesoscopic modelling techniques offer a method of directly treating these slip mechanisms, to improve the accuracy of inter-fibre angle prediction, and can be used to analyse any woven, NCF or three dimensional fabric architecture, by generating appropriate geometrical fabric models.

2.7.4. Mesoscopic Finite Element Drape Simulation

Numerical modelling of the mesoscopic fabric architecture is a relatively new research area that is increasingly being used as an alternative to conventional constitutive modelling to predict fabric properties; such as draping characteristics, permeability and stiffness tensors. The tows and stitches are modelled discretely and individually treated as a continuum at this mesoscopic scale. The explicit FE solution scheme is a suitable basis for mesoscopic fabric simulations due to its ability to handle large-scale element deformation, non-linear material models and contact. A further benefit of this approach arises from the possibility to correctly treat the complex interactions that occur between tows and stitching.

Analysing localised and repeatable fabric unit-cells first requires accurate geometrical models of the fabric structure. Numerous models of specific fabrics, or fabric types, have been generated [107][110][111], although generic software tools are also actively under development. Two such proprietary pre-processors of fabric geometry are described in [108] and [106]. These pre-processors aim to generate specific fabric geometrical models from inputs of the fibre tow and stitch geometry for both woven and Non-Crimp fabric architectures. Discretisation of the resulting CAD descriptions can be used to produce FE meshes. The meshing is relatively trivial, but inevitably leads to the use of many fine-scale elements, which are computationally expensive in explicit FE codes.

Simulations using detailed mesoscopic models have been used to investigate a number of key fabric deformation mechanisms. Intra-tow shear is the principle method by which fabrics deform and has been simulated for woven fabrics by inducing pure shear kinematics in unit-cell models [61][110][120], as shown in Figure 2.28. The material models used are generally orthotropic [110], to account for high fibre stiffness and low compaction stiffness of the tow, or have been further modified to incorporate an increasing compaction resistance when woven tows are in tension [15]. Results show reasonable prediction of pure shear force when compared to picture frame test results, however, the difficulty of defining boundary conditions which suitably replicate the fabric structure surrounding the single unit-cell has limited the accuracy of current unit-cell models [120].

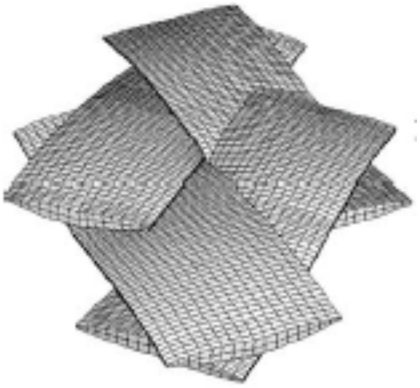

Figure 2.28. An example of a sheared, plain weave mesoscopic unit-cell, from [120]

Other deformation mechanisms modelled using FE fabric unit-cells include the biaxial tension properties of woven fabrics [111] and inter-tow slip of a woven fabric unit-cell during shear [61], which was found to be minimal, but is not representative of the deformation which could occur in large scale forming problems.

To the authors knowledge, the mesoscopic FE simulation of NCF's or larger comprehensive fabric layers has, as yet, only been published in work resulting from this current thesis [64][123] [124][125]. The large computational requirements for such analyses have, so far, severely limited work in this area. Consequently, the complex tow/stitch interactions and inter-fibre slip mechanisms of NCF's are currently untreated in forming simulation.

Large scale simulations of woven fabrics (typically comprising Kevlar fibres and up to approximately 90cm^2 in area) have proved useful for predicting the ballistic impact properties of defensive fabric layers, such as bulletproof vests or turbine engine fragment barriers [113][114][121][122]. This work is principally aimed at better understanding the deformation mechanisms which occur during ballistic impact and more accurately model tow straightening and separation; the later of these mechanisms being untreated in continuum macroscopic models.

The problem of impact simulation is considerably different to fabric forming since deformation occurs at very high strain rates and is principally concerned with the loading and damage evolution of fibre tows. Nevertheless, the principles of modelling the fabric geometry, tow deformation and inter-tow friction are similar to draping. Solid element models of woven fabrics have successfully been used to simulate ballistic impact using comparatively coarse (3 elements in each tow cross-section [113]) and fine (12 elements in each tow cross-section [121]) meshing schemes. The fibre tows, in these respective studies, have been modelled using an elastic constitutive law, calibrated against tensile tow tests, and an orthotropic constitutive law, which has a low transverse tow stiffness to account for tow compaction [15].

To summarise, the mesoscopic unit-cell models developed to date are overly refined for direct application to large structures and are consequently limited to analysing smaller Representative Volume Elements, which require careful consideration of the boundary conditions used to replicate the true fabric deformation. Nevertheless, Finite Element mesoscopic modelling of textiles has proved a valuable tool for predicting fabric properties, but has only been applied to the simulation of larger, comprehensive structures for ballistic impact analyses of woven fabrics. The Finite Element modelling of NCF stitching has not been considered. Inter-tow slip deformation mechanisms in NCF's are, therefore, untreated in current preforming simulation models, despite occurring in areas of high fabric shear, where correct prediction of the fibre architecture is critical to both the local permeability and final mechanical performance of the part. Consequently, the work presented in this thesis describes the development of a Finite

Element mesoscopic model for NCF, suitable for comprehensive preforming analysis and able to provide useful insight into the tow and stitch deformation mechanisms that occur during forming. Furthermore, the simulated Finite Element preform architecture has been directly applied to impact simulations of the final composite component to demonstrate the link between preforming and mechanical analyses and investigate the use of mesoscopic simulation methods as a tool for predicting the performance of composite components.

2.8. *FIBRE REINFORCED COMPOSITE FAILURE MODELLING*

Unlike homogeneous metallic materials, Continuous Fibre Reinforced Composite (CFRP) materials are anisotropic and comprise continuous cylindrical fibres embedded in a polymeric matrix. Discrete modelling at this microscopic (individual fibre) scale is impractical for performance analysis of complete structures. Therefore, a constitutive macroscopic approach is generally adopted in which each lamina is modelled as an orthotropic ply, with principal material directions defined as shown in Figure 2.29. The failure mechanisms of CRFP are complex due to the heterogeneous anisotropic composition. Modes of failure can include intra-ply (within a single ply) and inter-ply (between ply layers) mechanisms, as shown in Figure 2.31.

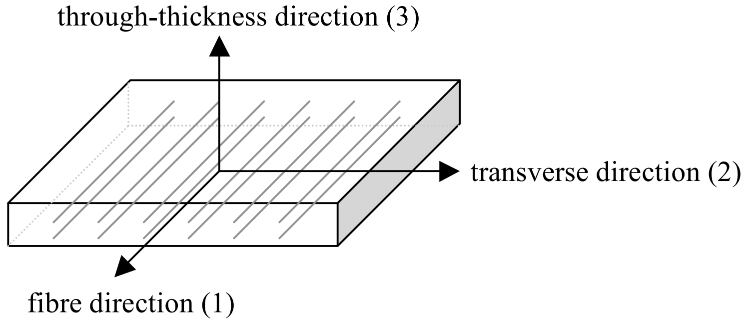

Figure 2.29. Macroscopic orthotropic ply definition

The prediction of composite failure strength has been a topic of substantial research and has led to the development of many failure criteria. Some of the most popular of these intra-ply criteria are summarised in Figure 2.30; briefly, the maximum stress criterion produces a non-continuous failure envelope [95]; the maximum strain criterion [97] *(not shown)* produces a similar failure envelope, but couples fibre-matrix failure using Poisson's ratio and the quadratic (Tsai-Wu) criterion [95] produces a continuous failure envelope which couples all fibre and matrix stresses. Each of these models is based on simple failure envelopes and is unable to predict the failure mode of the composite.

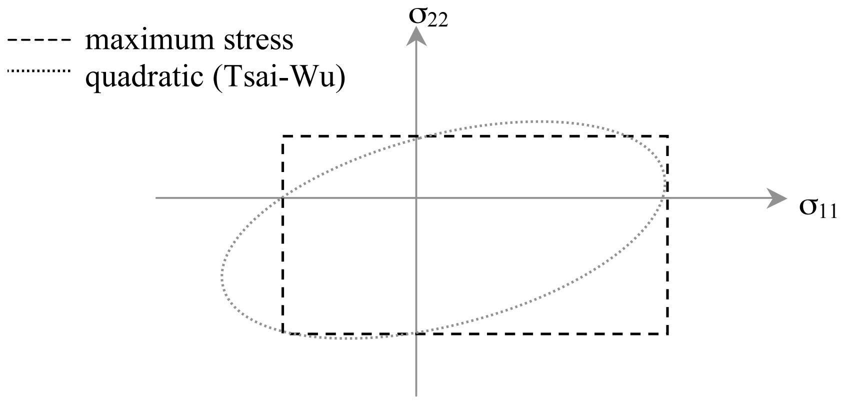

Figure 2.30. Comparison of common failure criteria applied to CFRP

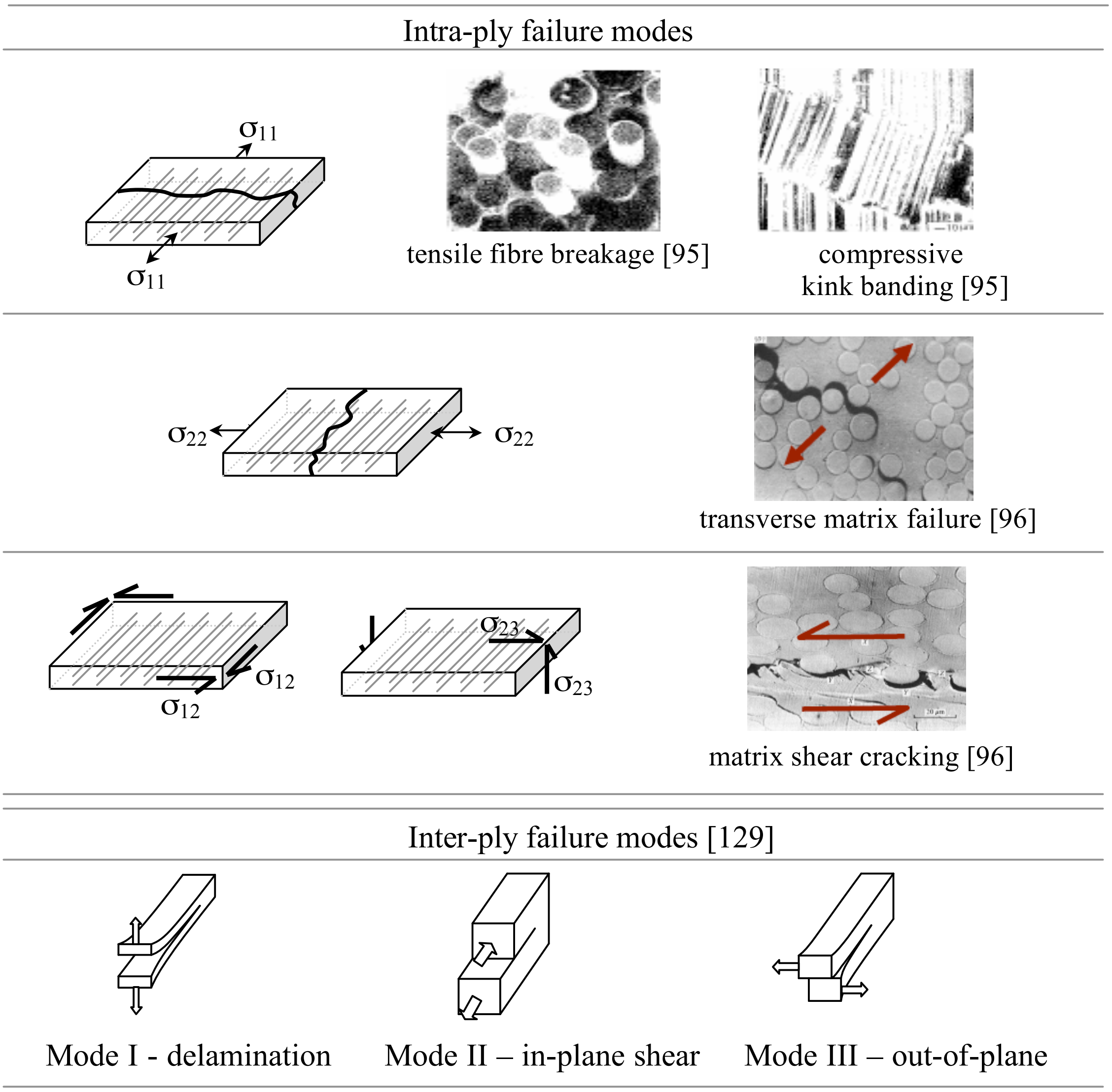

Intra-ply failure modes

tensile fibre breakage [95]

compressive kink banding [95]

transverse matrix failure [96]

matrix shear cracking [96]

Inter-ply failure modes [129]

Mode I - delamination

Mode II – in-plane shear

Mode III – out-of-plane

Figure 2.31. Modes of failure for unidirectional CFRP

A comparative study to test the accuracy of fourteen of the popular failure criteria was launched in 1995 [100] and compared the predicted failure strength of glass/epoxy and carbon/epoxy laminates to experimental data. From this study, a matrix failure criterion [99] was able to correctly predict the highest number of failures due to the ability to treat the different modes of matrix failure and predict the mode of final composite failure.

The models described in the previous paragraphs are appropriate to identify final material (ply) failure. For progressive failure, impact and crash problems the concept of material damage is more appropriate, which correctly treat the different damage and failure mechanisms that can occur in the materials. One model in particular is capable of treating tensile elastic damage and matrix plasticity [102] based on test data of cyclic sheared composite coupons. This constitutive model has been further developed and applied to failure prediction of braided textile composites [98] and has been combined with the previously defined matrix failure criterion [99] to improve treatment of transverse compressive matrix failure [101].

Microscopic [139][140] and mesoscopic [141] FE modelling of composite Representative Volume Elements (RVE) offers a direct method of predicting the stiffness, damage and failure mode of laminate plies. However, as with fabric unit-cell simulation, these methods are excessively detailed for practical analysis of complete structures. However, failure prediction of complete composite coupons has been researched using the same mesoscopic tow model developed in the current thesis [131]. In this work, tow elasticity has been modelled using an orthotropic heterogeneous fibre/matrix material law [90] and failure has been modelled using a Mode-I/Mode-II intra-ply damage and failure law between each modelled tow and ply layer [130]. Test and simulation results have compared results of tensile coupon test, with, and without, notches at the coupon edges. Fibre angles of ±35°, ±45° and ±55° to the loading direction have been investigated. The mesoscopic tow model shows good prediction of the failure stress and mode, which occurs by matrix cracking between tows as shown in Figure 2.32a and b. Furthermore, only minor variations in strength are correctly predicted between notched and un-notched samples, since failure occurs parallel to the fibre direction and not due to stress concentrations aligned between each crack tip [130].

Results from the above tests and mesoscopic simulations have also been compared to similar predictions using an implicit FE code and the maximum stress model, as shown in Figure 2.32c. The maximum stress model treats the composite as an orthotropic continuum and is unable to predict matrix cracking in the fibre direction. Consequently, this model predicts stress concentrations and coupon failure across the centre of specimen. Consequently, failure occurs at significantly lower stresses than occurs in practice.

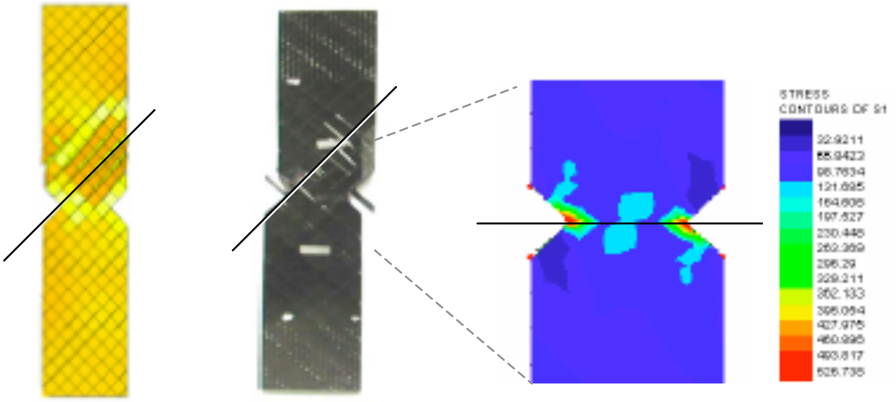

Figure 2.32. Mesoscopic modelling of failure in tensile tests of notched composite coupon; showing mesoscopic simulation, experiment and maximum stress results

2.9. SUMMARY OF THE LITERATURE REVIEW

CFRP materials are providing opportunities to reduce component weight and improve crash worthiness of aerospace and automotive components. Accurate prediction of the deformed fibre architecture of the final component is vital if a virtual design process is used to optimise composite components, which is, itself, a necessary process if the design time and costs are to be industrially acceptable. Preforming simulation methods have been proposed and validated but are currently unable to treat the more complex deformation mechanisms of popular Non-Crimp Fabric styles.

Early preforming simulation methods have been based on kinematic mapping algorithms. These are able to treat the dominant fabric deformation mechanism of pure shear, but are limited in representing any more complex fabric deformation mechanisms or process conditions.

More recent macroscopic FE drape simulation techniques offer improved treatment of both the processing conditions and fabric deformation mechanisms and generate good results when simulating woven fabrics. However, these are not truly representative of the deformation mechanisms possible by NCF architectures and cannot provide useful information on the interaction between stitching and fibre tows.

Mesoscopic FE representation of the separate tow and stitch constituents provides a simple method of directly representing the true fabric architecture and deformation mechanisms, but at the expense of long simulation times. Current research into mesoscopic modelling of fabric deformation has commonly used finely detailed FE fabric representations. These models are suitable for analysing only small representative areas of fabric, using current computing power, and are principally used to predict macroscopic deformation properties. However, it is now becoming reasonable to consider modelling the preforming of comprehensive structures using a mesoscopic fabric modelling scheme within acceptable timescales, therefore, this is the primary aim of this thesis.

Predictions of the deformed fabric architecture after preforming are necessary as the basis for permeability and performance modelling of the final impregnated composite component. Demonstrating the feasibility of using the simulated preform fibre architecture as the basis for mesoscopic damage and failure modelling of composite components is, therefore, another aim of this thesis. Composites components are most commonly modelled using orthotropic continuum material models that are often unable to predict the complex damage modes of loaded complex structures. Consequently, mesoscopic modelling methods offer the opportunity to predict, in detail, the complex inter-ply and intra-ply damage mechanisms that may occur. Furthermore, for preforming and damage modelling, the mesoscopic modelling scheme can be easily adapted to treat complex fabrics and 3D textiles, which are becoming popular in industry.

3. FINITE ELEMENT MESOSCOPIC MODELLING OF NCF

The present work continues from previous preforming research by developing a mesoscopic FE model, but differs by aiming to use the coarsest fabric FE model achievable that can capture the main deformation mechanisms of the true fabric architecture. This coarse modelling approach has been investigated to minimise computational requirements and permit direct simulation of full-scale, comprehensive structures within reasonable timescales. The possible benefits of using a mesoscopic fabric model for draping simulation are improved treatment of fabric deformation mechanisms, particularly cross-over and inter-fibre slip, since these are not treated using macroscopic FE or kinematic mapping methods.

The FE modelling technique is now a validated and widely used tool for industrial metal stamping simulation [145]. This has provided the basis for macroscopic FE simulation of composite forming and is also the basis for this research. As described in the literature review, explicit FE codes are able to efficiently treat buckling, material nonlinearity and contact, which are essential for fabric preforming. Therefore, the new mesoscopic fabric modelling methods developed in the present work have been implemented in the commercial explicit Finite Element simulation code, PAM-CRASH [22]. The model could, however, be readily applied to other explicit finite element codes.

3.1. MODELLING & VALIDATION STRATEGY

The development of a FE mesoscopic NCF model requires identification of the separate fabric constituents, the deformation mechanisms of these constituents during forming and how these mechanisms are to be modelled. In conjunction to producing a suitable fabric model are considerations of how to obtain suitable material data for the FE constitutive material models. Inevitably, this input data has to be obtained using suitable experimental or numerical methods, for input into the material and process constitutive models, or for calibration purposes using equivalent simulations. A detailed presentation of these considerations is included in this chapter and leads to the required experimental and simulation procedures, and results, presented in the subsequent chapter, *4. Experimental Procedures and Results*.

The development of a mesoscopic NCF model has been an iterative process with a number of different modelling approaches having been investigated that aimed to treat the complex stitch and coupled stitch/tow deformation mechanisms. Where useful, these techniques are defined in addition to the optimal modelling methods resulting from the current work.

Validation of the mesoscopic fabric model compares experimental and simulation results of bias extension tests and preforming trials over a hemisphere mould. The bias extension test has been chosen since the range of deformation mechanisms are complex and include cross-over and inter-tow slip, while the hemisphere draping trials are representative of industrial forming processes and is the most common geometry used to validate preforming simulation techniques.

The mesoscopic fabric model developed in the present work provides the opportunity to model the failure of complex composite components in the same detail as has been investigated for fabric preforming. This can be acieved by direct coupling of the preform fabric architecture to solid composite models. The deformed FE mesh geometry resulting from the hemisphere drape trials has therefore been used as a basis of composite failure simulation and the results compared to equivalent experimental tests. Consequently, the following chapter also includes descriptions of the composite manufacturing process, testing and simulation strategy for this failure work A summary of the work conducted in the next chapters is provided in the following flow diagram, Figure 3.1.

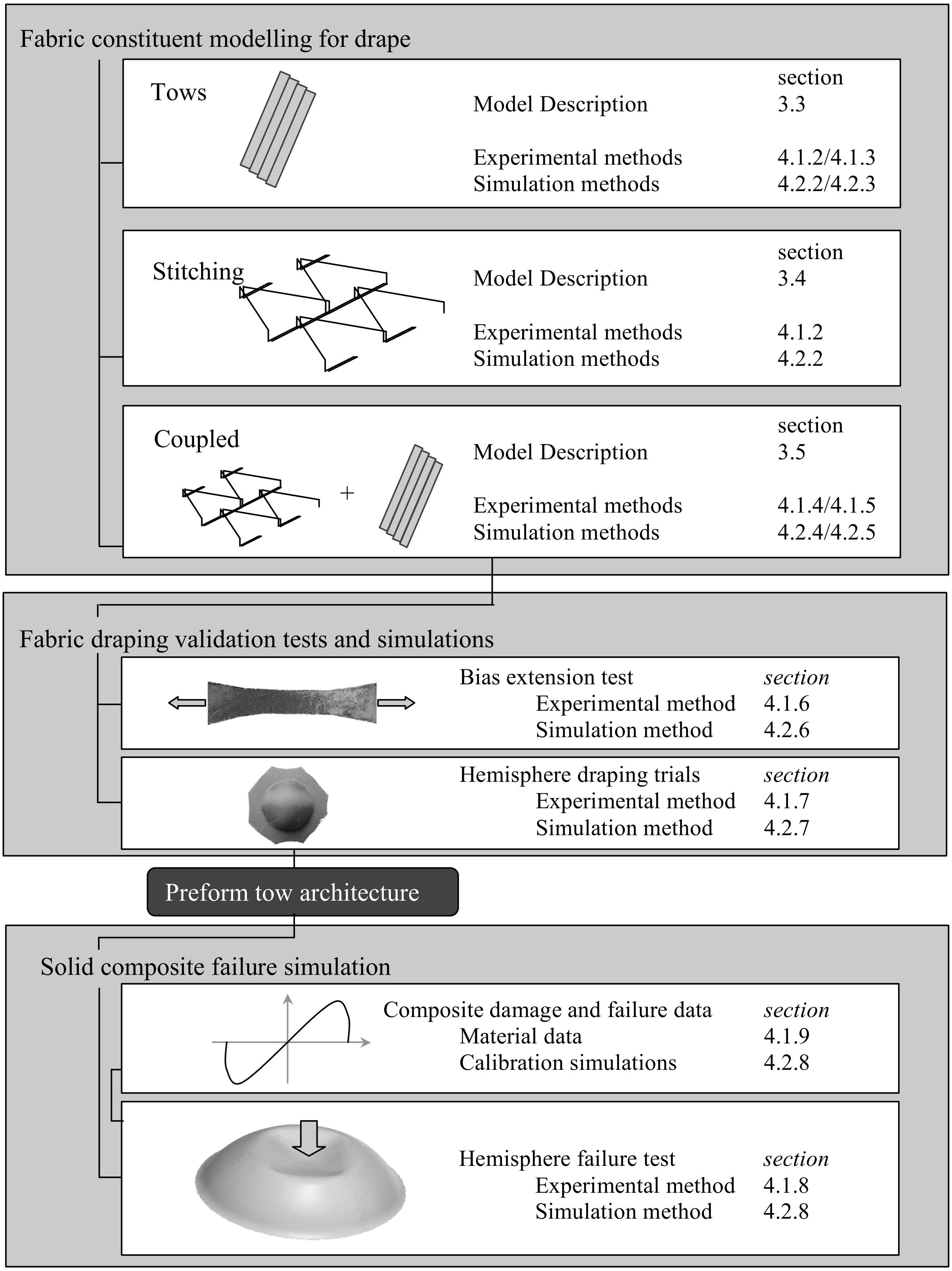

Figure 3.1. Modelling summary and flow chart for chapters 3 and 4

3.2. SPECIFICATION AND DEFORMATION MECHANISMS OF THE MODELLED NCF

The fabric studied in the present work is a biaxial NCF comprising two unidirectional layers of carbon fibre in combination with impaled tricot stiching at 45° to the fibre directions, Table 3.1. This fabric has been selected since the biaxial architecture is highly drapeable, popular in aerospace and automotive industries for the manufacture of complex component geometries and produces composites of improved mechanical properties compared to equivalent woven fabrics. The tricot stiching of the chosen fabric is a common style that allows good drapeability, but does produce relatively complex deformation mechanisms such as biased shear and tow slip mechanisms.

Tricot stitched biaxial Non-Crimp Fabric (NCF)	Specification
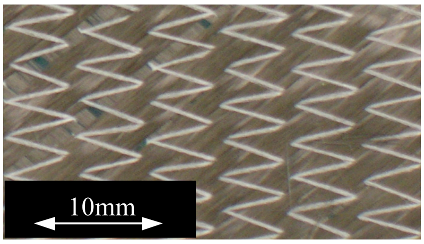	**Material:** Saertex V93813 **Fabric type:** Biaxial ±45° NCF **Weight:** 321 gm^{-2} **Fibre tow:** 12K Toray T700 carbon **Stitch:** PES 76 dtex (Tricot) **Stitch orientation:** 45° to fibres

Table 3.1. Specification of the NCF fabric studied in the present work

Shear bias produced in the studied NCF is due to the unbalanced geometry of the tricot stitching pattern and stitching orientation at 45° to the fibres. Definitions of positive and negative shear with respect to the stitch orientation are shown in Figure 3.2 and will be used when describing shear deformation throughout the current thesis.

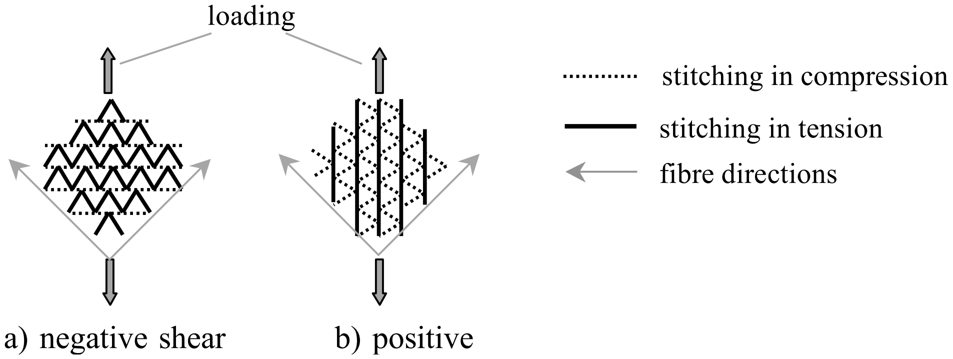

Figure 3.2. Schematic definitions of negative and positive shear, with relation to the stitch geometry

The studied biaxial NCF can be divide into two main constituents; namely, fibre tows and stitching. The principle deformation mechanisms of these two constituents, and their interaction, are summarised in Figure 3.3. It should be noted that the fabric studied here has been manufactured using an older variant of mutiaxial textile loom and, consequently, is of lower quality than those produced using modern Liba multiaxial loom technology [149]. The fabric studied here shows random carbon fibre tows missing from the fabric. As an indication of the scale of these defects, the missing tows are approximately 4mm in width and are estimated to occur every 100mm. Inevitably, these missing tows will contribute to the scatter in measured fabric and composite properties, but can be minimised by careful selection of the fabric area used when cutting specimens for testing.

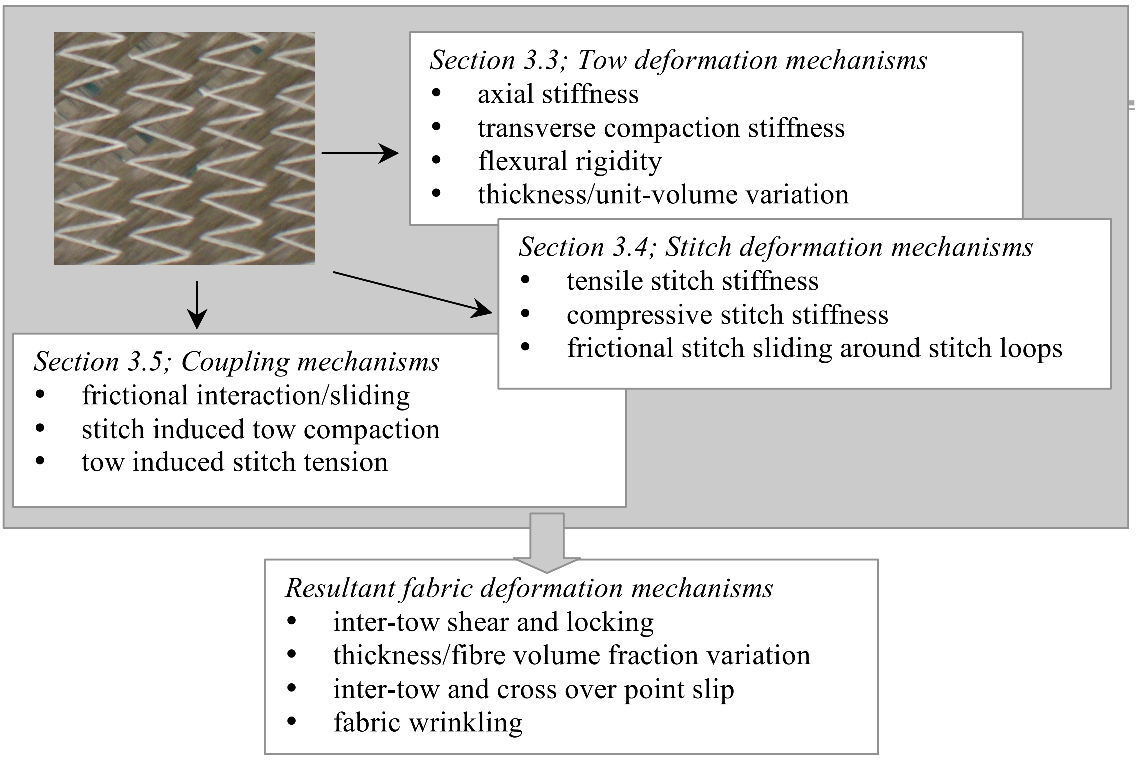

Figure 3.3. Mesoscopic model constituents, deformation mechanisms and resultant fabric deformation mechanisms

3.3. FINITE ELEMENT MODELLING STRATEGY OF DRY FIBRE TOWS

3.3.1. Dry Tow Deformation Mechanisms

Fibre tows consist of many individual fibres, usually between 3,000 and 24,000, which are characterised by high axial fibre stiffness. Therefore, axial strains are considered negligible in draping since the in-plane forces required to form most biaxial NCF's are low. Consequently, biaxial fabrics must predominantly deform by inter-tow shear, which induces lateral (in the fabric plane) compaction of tows, as shown in Figure 3.4. This compaction resistance to shear deformation is produced by the complex redistribution of many individual fibres as the tows are required to change their cross sectional shape.

Intra-tow shear of individual tows is minimal due to friction contact between fibres. This produces free tow-end rotation at fabric edges that are unconstrained, as shown in

Figure 3.4. The flexural stiffness of a tow is also low, since localised compression can easily result in tow buckling, as shown in Figure 3.5.

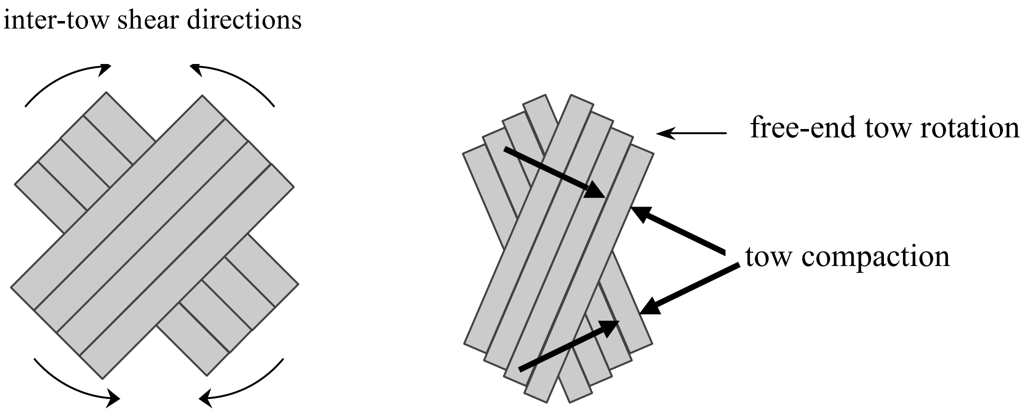

a) pre-shear tow architecture b) post-shear tow architecture

Figure 3.4. Schematic of tow deformations resulting from inter-tow shear deformation

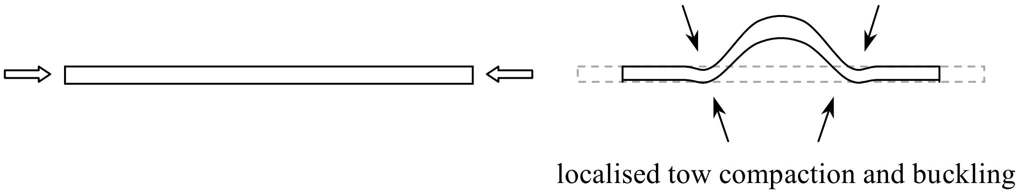

a) pre-flexure tow geometry b) post-flexure tow geometry

Figure 3.5. Schematic of localised tow buckling during flexure

3.3.2. Geometrical Finite Element Modelling of Fibre Tows

Geometrically, fibre tows normally exhibit a near oval shape in cross-section. Modelling of this geometry would require a detailed meshing scheme which is currently unsuitable for simulation of comprehensive parts. Hence, in the current work, each tow is simplified and represented in cross-section by a series of 8-node solid finite elements, as shown in Figure 3.6.

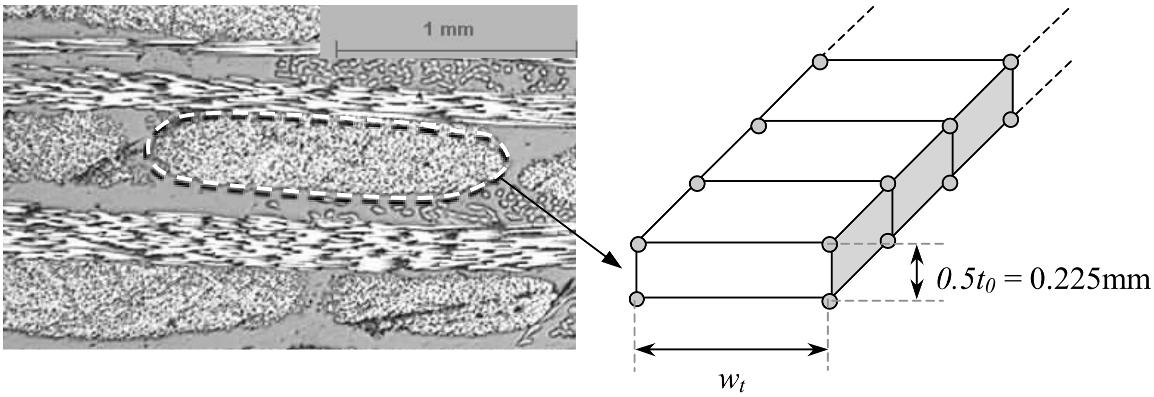

a) cross-sectional image of the infused NCF composite, showing oval tow geometry

b) a single modelled tow, constructed of 8-node solid elements

Figure 3.6. Comparison of actual and modelled cross-sectional geometries of a single tow

Considering the geometry of each solid tow element, the element width is defined by the location of the through-thickness stitch elements. Regular shaped elements are preferable in FE simulations therefore each element length is equal to the width. Finally, the combined thickness of elements within the two tow layers is equal to the measured fabric thickness, t_0.

The impaled fabric construction produces fibre voids around through-thickness stitch locations [116], as shown in Figure 3.7a, which is impractical to model using a coarse discretisation scheme. Hence, the tow geometry has been further simplified by including a constant separation gap between adjacent tows, Figure 3.7b. This separation is used to treat frictional contact between tows and permit cross-over and inter-tow slip mechanisms.

Contact of elements during preforming simulation, and solid composite impact simulation, is treated by efficient contact algorithms. These algorithms are defined between shell elements on each adjacent surface in contact. The required shell elements are included here by surrounding each separate tow element with four null-shell elements. These are joined to the solid elements by coincident nodes and contribute no stiffness or mass to the structure and, therefore, are used only for treatment of contact.

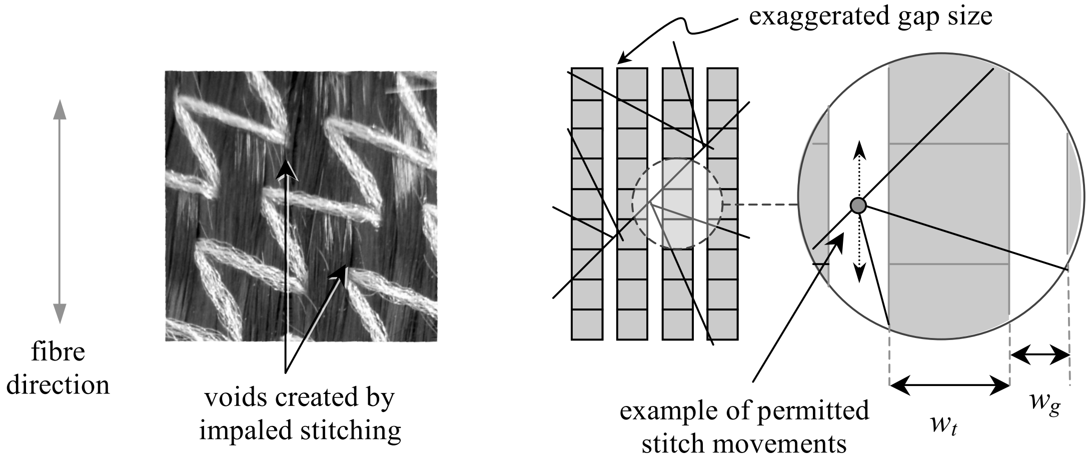

a) Image of stitch impaled tows   b) Mesoscopic tow model

Figure 3.7. True and modelled NCF tow architectures

3.3.3. Constitutive Material Modelling of Tow Deformation

The tow deformation behaviour must be characterised for axial, in-plane compaction and bending stiffness. To approximate tow behaviour an orthotropic ‘bi-phase’ fibre/matrix constitutive material model [90] has been used consisting of a separate fibre $[C]^f$ and matrix $[C]^m$ stiffness laws, the latter ‘matrix’ component being used to simulate the compaction resistance of the dry fibre tows,

$$[C]^{tow} = [C]^f + [C]^m = \begin{bmatrix} E_{11}^f & 0 & 0 \\ 0 & 0 & 0 \\ 0 & 0 & 0 \end{bmatrix} + \begin{bmatrix} E_{11}^m / N_m & \nu_{12}^m E_{22}^m / N_m & 0 \\ \nu_{21}^m E_{11}^m / N_m & E_{22}^m / N_m & 0 \\ 0 & 0 & G_{12} \end{bmatrix}, \qquad \text{Eq. (24)}$$

where,

$$E^{tow}_{11} = E^f_{11} V^f + E^m_{11} V^m \quad \text{and} \quad E^{tow}_{22} = E^{tow}_{33} = E^m_{22} = E^m_{33}. \qquad \text{Eq. (25)}$$

The suffixes f and m denote fibre and matrix respectively; E, G and ν are Young’s modulus, shear modulus and Poisson’s ratio in the fibre direction 1, transverse direction 2, or out-of-plane direction 3; N_m is the quantity $1-\nu_{12}^m \nu_{21}^m$ and V is the constituent volume fraction. This model is heterogeneous, for which material stresses are calculated independently in the resin and matrix. The orthotropic material directions are defined using local axes defined by the element numbering scheme, as shown in Figure 3.8.

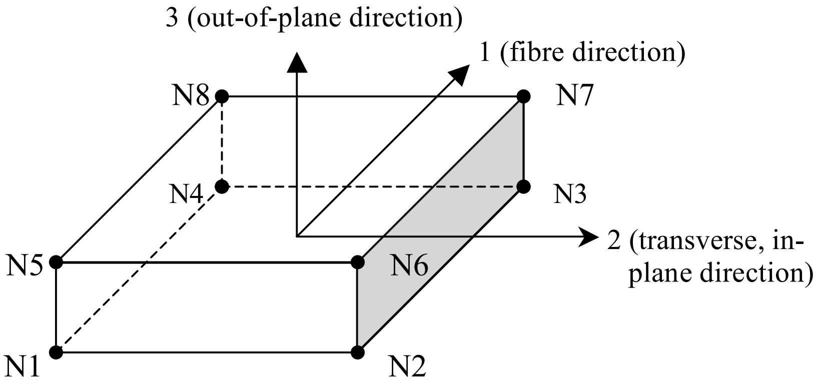

node order as listed in the PAM-CRASH input file = N(1-8)

Figure 3.8. Solid tow element local material coordinate system

In-plane tow compaction resistance is modified in this material model using a linear transverse stiffness, $E^m{}_{22}$. Both the axial and bending stiffness are modified using the tow axial moduli, $E^{tow}{}_{11}$. Lastly, the element volume is assumed to be constant, so Poisson's ratio, ν_{ij}, is set equal to 0.5.

This constitutive material model inevitably leads to certain limitations for the modelling of tow deformation. Firstly, the constant transverse modulus produces a linear relationship between compaction resistance and compaction strain. However, experimental tow compaction resistance is nonlinear and increases as fibres approach a close-packing arrangement [41][42]. Experimental procedures [41] and theoretical models [42] for characterising tow compaction resistance have been developed and are generally based upon plane strain deformation.

Compaction data obtained by plane strain methods are valid if the change in tow thickness with fabric shear is known. However, tows do compact at very low stress, which makes measurement of the tow thickness problematic. As described in section 2.6, an assumption of constant fabric thickness has been investigated, but led to the over-prediction of tow compaction forces at high shear angles, when modelling shear in NCF's [94]. Therefore, in the present work, an experimental technique has been proposed to measure in-plane tow compaction resistance, using the picture frame shear test. The procedure involves removing stitching from the fabric samples once clamped in the frame equipment and using the picture frame shear to compact the constricted tows. The results from this test have been used to calibrate the linear compaction modulus, E^{m}_{22}, of the tow constitutive model through simulation and calibration of an equivalent representative-cell of the picture frame test. The experimental test and simulation procedures, and results, for tow compaction are presented in sections 4.1.2 and 4.2.2 respectively.

The second main limitation of the constitutive tow model is that axial stiffness and flexural stiffness are coupled. As shown in Figure 3.5, the tow architecture can accommodate flexure by localised buckling under very low forces. This cannot be represented using the high axial fibre stiffness and, consequently, the axial tow modulus has been calibrated to represent experimental tow flexural stiffness, rather than the true axial fibre stiffness. This treatment to give correct flexure behaviour is preferred to properly account for buckling behaviour and fabric/tooling contact forces. It will be subsequently shown, using results from bias extension and hemisphere forming simulations, that the modelled tows do not exhibit excessive axial tow strains, which are possible by using this calibrated, and low, axial stiffness.

Adaptation of a testing standard, ASTM D1388 [62], has been used to experimentally characterise tow flexure and results from this test have been compared with an equivalent simulation in order to calibrate the axial modulus, E^{tow}_{11}, of tows for correct flexural stiffness. The test and simulation methods, and results, for flexural stiffness are described in sections 4.1.3 and 4.2.3 respectively.

Lastly, intra-tow shear deformation of tows is generally small has been estimated here from the calibrated axial tow modulus based upon equations of linear elasticity,

$$G_{ij} = \frac{E^{tow}_{11}}{2\left(1+\upsilon_{ij}\right)}. \qquad \text{Eq. (26)}$$

To summarise the modelling of fibre tows;

- the modelled axial tow stiffness is not representative of the fibre axial stiffness; instead, the tow axial stiffness is calibrated against experimental flexure results to ensure correct fabric bending behaviour,
- a linear transverse tow stiffness is calibrated using tow compaction results indirectly measured using the experimental picture frame shear test, with stitching removed from samples,
- intra-tow shear is calculated using a linear-elastic relation to the calibrated axial tow stiffness,
- constant tow volume is assumed and is treated using Poisson's ratio set equal to 0.5.

3.4. NCF STITCH MODELLING

3.4.1. Stitch Deformation Mechanisms

A schematic of the tricot stitch pattern is shown in Figure 3.9 and includes an enlarged view of the inter-linking between individual stitch unit-cells.

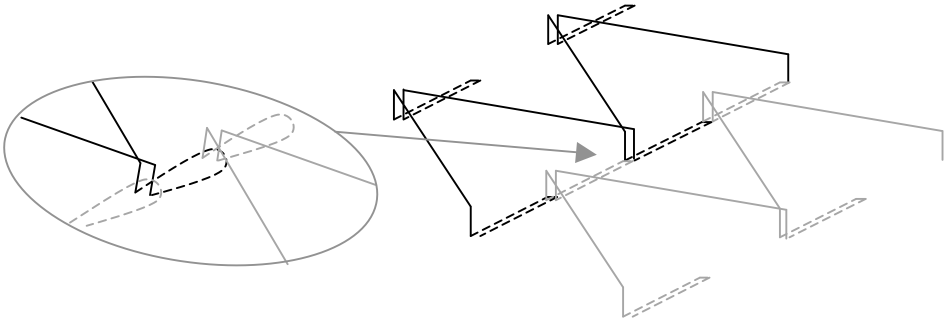

Figure 3.9. Schematic of the tricot stitch geometry and an enlarged view of the inter-linking between stitch unit-cells; stitch sections pass over tows where solid lines are drawn and under tows where dashed lines are shown; dashed lines are oreiented at ±45 ° to the fibres

Geometrically, the tricot stitch is a comparatively complex structure to model. Considering Figure 3.10, fabric shear requires sections of the stitch that are aligned to the shear extension direction to lengthen (solid black lines). Conversly, stitch sections transverse to shear extension become unloaded (dashed black lines), which permits frictional sliding of material in order to lengthen the stitch sections under tension.

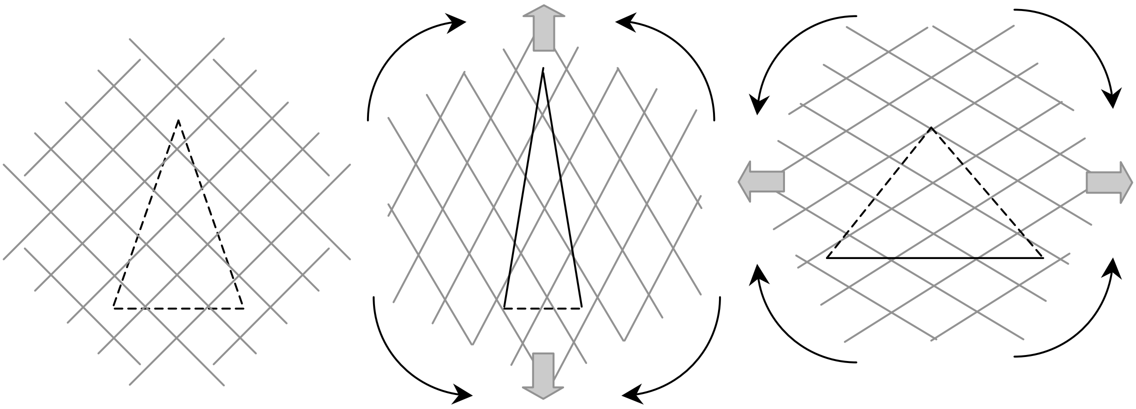

a) original geometry b) negative sheared geometry c) positive sheared geometry

Figure 3.10. Unit-cell stitch segments under tension (solid black lines), compression (dashed black lines) during positive and negative pure shear loading (fibre directions shown as grey lines)

3.4.2. Geometrical Finite Element Modelling of NCF Stitching

Investigation into methods to fully model the interlinked stitch geometry and frictional stitch sliding have been made, but have yet proved unsucessful. These methods are discussed in chapter 5. Nevertheless, stitching primarily constrains fibre tows, to form a stable fabric, and contributes to the shear resistance of the fabric. A simplified FE model of the tricot geometry has been developed which aims to satisfy these requirements. As shown in Figure 3.11, each stitch section is interconnected and comprises of a system of single 2-node bar elements; again, the modelling approach adopted is to use the minimum number of elements possible to capture the required deformation mechanisms.

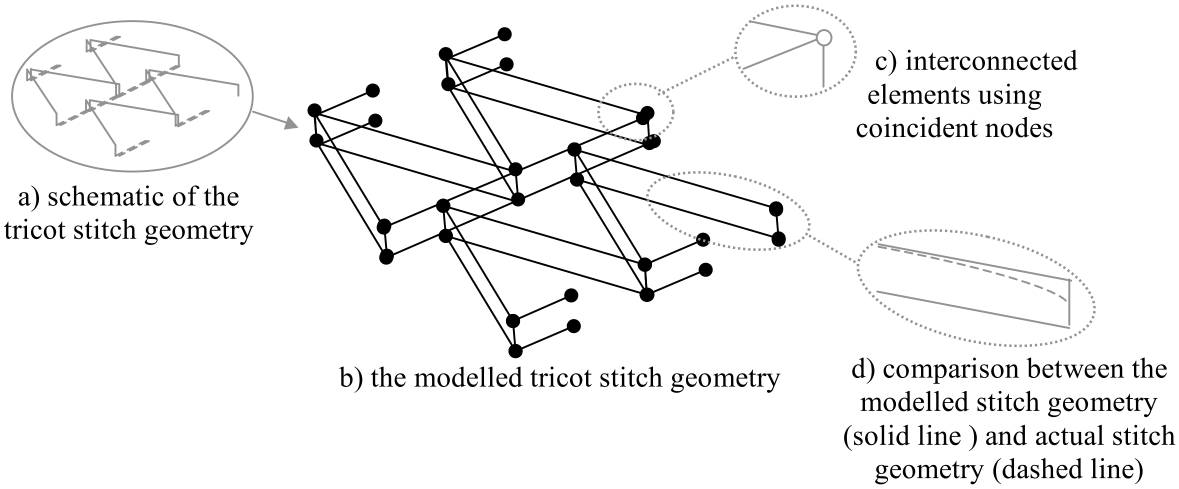

a) schematic of the tricot stitch geometry

b) the modelled tricot stitch geometry

c) interconnected elements using coincident nodes

d) comparison between the modelled stitch geometry (solid line) and actual stitch geometry (dashed line)

Figure 3.11. Geometry of the actual modelled tricot stitch pattern

The limitations of the simplified FE stitch model are:

- The modelled stitch elements are connected at common nodes and element lengths are uncoupled, Figure 3.11c; in that the slip of stitch material from one un-loaded cell to adjacent loaded cells, as stitch (element) forces try to equilibrate, is not possible. This may occur in practice and represents the main deficiency of the current stitch model.

- An additional through-thickness stitch component is necessary, Figure 3.11d; in practice, stitching is wrapped around the fibres to create a stable fabric. To achieve this, with respect to the coarse tow model currently used, additional through-thickness stitch element are required.

- The modelled geometry is symmetric about the fabric central plane, Figure 3.11d; the addition of a through thickness bar element is a simplification of the true stitch geometry and can lead to modes of deformation which may not occur in practice, unless symmetry is introduced.

In light of the limitations detailed above, stitch tension is the only mode of deformation that is treated by the current stitch model. Accordingly, the stitch elements require calibration to the global shear resistance contributed by the stitching to the fabric, during both positive and negative in-plane fabric shear. With this method, shear bias is treated in the current stitch model by applying the positive and negative shear resistance contributions to only the stitch elements under tension in each of these shear modes, as defined previously in Figure 3.10.

3.4.3. Constitutive Material Modelling of Stitch Deformation

The constitutive material model applied to stitch elements is a nonlinear elastic, tension only law [90], Figure 3.12. Using this material model, the stitches are assumed to have zero stiffness if they undergo compressive loading, which is a correct representation of a stitch thread. The non-linear tension response of the stitches are calibrated against appropriate test measurements, which are described below.

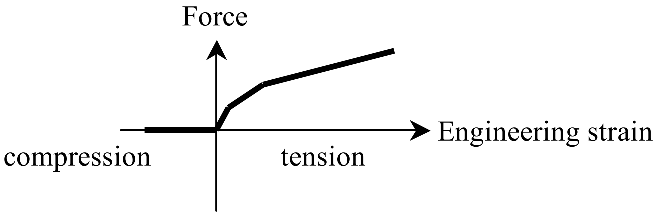

Figure 3.12. The non-linear elastic, tension only material model applied to stitch elements

In this work, the shear contribution produced by the fabric stitching in a NCF has been measured experimentally using the picture frame shear test. As demonstrated in the literature review, this is a common method for experimentally measuring fabric shear deformation and constrains the fabric to near pure shear. The shear resistance of only the stitching has been identified by comparing shear data of complete fabric specimens to data obtained with stitching removed from the tows. This is shown diagrammatically in Figure 3.13.

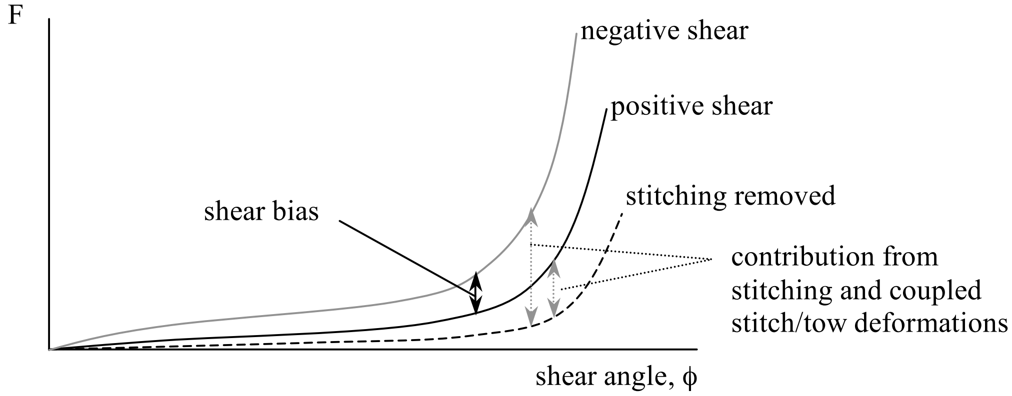

Figure 3.13. Example picture frame results; schematically showing the method used to obtain the shear resistance contribution from stitching

It should be noted that the resultant shear resistance obtained using the above method comprises of both stitch deformations and coupled stitch-to-tow frictional resistance contributions that occur during pure shear loading. The picture frame test methodology and results are presented in the experimental section of this thesis, section 4.1.2, while the methods of calculating and validating the stitch response to shear loading are presented in the simulation section 4.2.2.

3.5. MODELLING OF COUPLED TOW AND STITCH DEFORMATIONS

In practice, fibre tows and stitches are coupled by frictional contact, which is predominantly controlled by the state of tension in the stitching and the state of fibre compaction in the tows. In order to couple the modelled stitch and tow deformations, additional bar elements have been used which link stitch nodes to adjacent nodes of the solid tow elements. These additional bar elements are necessary since the stitch model is unable to reproduce the correct state of tension in the stitch threads and, therefore, account for frictional resistance to relative slip between the tows and stitches, Figure 3.14.

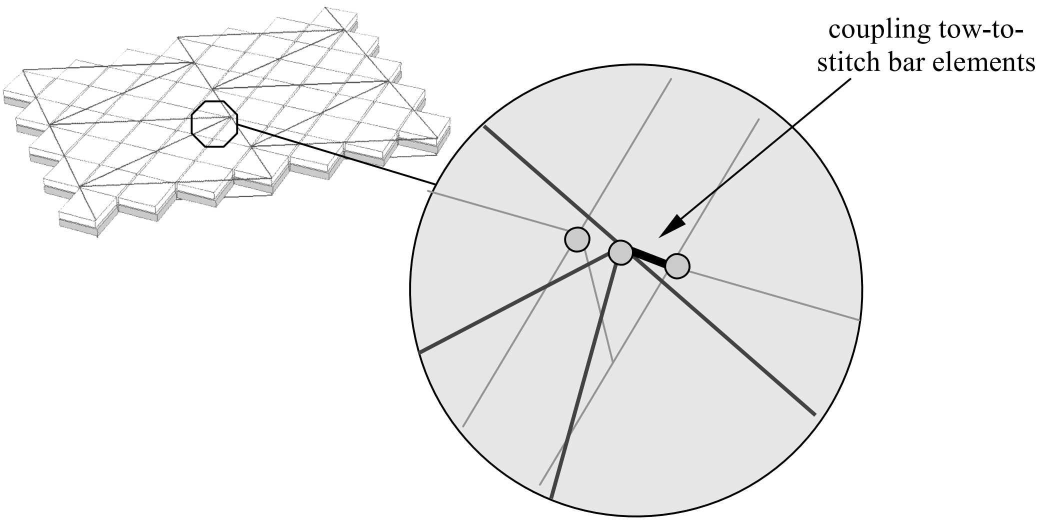

Figure 3.14. Modelling of bar elements between adjacent stitch and tow nodes

Experimental measurement of the friction resistance produced by tow slip has been performed using a tow pull-out test, in which a number of individual tows are pulled from a fabric sample using a simple tensile testing machine. The resistance data obtained can be directly applied to the coupling bar elements using the same tension only, non-linear elastic material model used for stitch elements, as shown schematically in Figure 3.12. The pull-out test methodology and results are presented in section 4.1.4. An equivalent simulation of this test is also performed to validate these results and is described in section 4.2.4. Finally, a contact algorithm is used between the stitch elements and tow elements to prevent interpenetration. Details of this algorithm are presented in section 4.2.5.

Tow-to-tow contact and friction is treated using a frictional contact algorithm based upon a single dynamic (constant velocity) Coulomb friction coefficient, μ. This coefficient is calculated experimentally in section 4.1.5.

3.6. MODELLING OF FABRIC-TO-TOOLING CONTACT

The treatment of friction contact between tooling and fabric plies is a prominent advantage of using the FE technique for fabric forming. The current mesoscopic model is able to treat these contacts through use of the previously described contact algorithm used between adjacent tows. This contact algorithm is applied between tows and tooling surface elements during preforming simulation. Coulomb friction for this contact uses the experimental data obtained and described in section 4.1.5.

Stitch-to-tool contact is treated using a frictionless contact algorithm and therefore only prevents interpenetration. Considering Figure 3.15, a reduced stitch-to-tool contact thickness, h_{cont}, is applied, when compared to the tow-to-tooling contact, to maintain stable tow deformation during draping. This issue occurs due to the simplified stitch geometry developed in the present work.

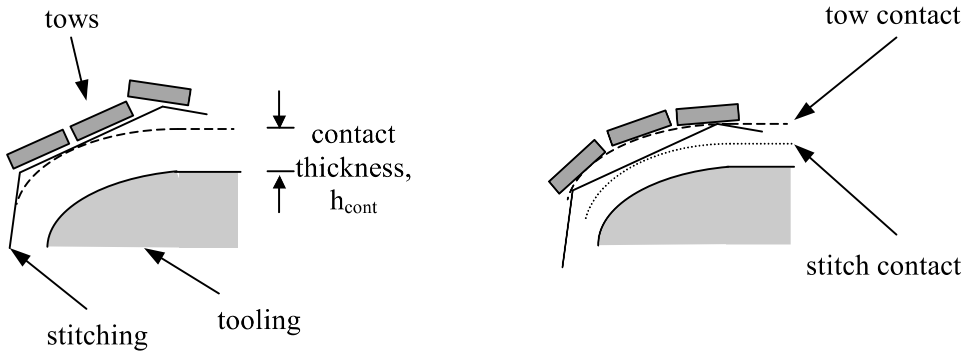

a) unstable tow deformation due to equal tow and stitch contact thickness a the tooling surface

b) improved tow deformation due to reduced contact thickness between the stitching and tooling surface

Figure 3.15. Simulation stability issues resulting from contact thickness of stitching, tows and tooling

Contact thicknesses used in explicit FE simulations are generally defined with consideration to the expected contact forces; generally, larger contact forces can require greater contact thickness to prevent interpenetration of elements. Therefore, the contact thickness, h_{cont}, applied to both stitch-tool and tow-to-tool contacts are low (<0.5mm) since contact forces are small. These thicknesses are defined in the appendix and are factored into the meshed geometry of the hemisphere tooling, since the contact thickness effectively increases the hemisphere radius by h_{cont}.

3.7. SUMMARY OF THE CONSTITUTIVE MATERIAL MODELS USED IN NCF DRAPE MODELLING

The following Table 3.2 summarises the constitutive material models and input data required for each of the fabric constituents.

Fabric model constituent	*PAM-CRASH model no.*	*(Numerical material model)*		*Experimental/ simulation methods and results section*
		Required numerical data	Fabric characterisation method	
Tow	MAT 30	*(Orthotropic fibre/matrix linear elastic)*		
		Elastic moduli - E^f_{11}, E^m_{11} Shear moduli - G^m_{ij}	Flexural rigidity test	4.1.3 / 4.2.3
		Elastic moduli - E^m_{22}, E^m_{33}	Picture frame test	4.1.2 / 4.2.2
		Poisson ratio - ν^m_{ij}	Constant volume assumption	-
Stitching	MAT 205	*(Tension only, non-linear elastic)*		
		Force response – $F(\varepsilon)$	Picture frame test	4.1.2 / 4.2.2
Coupling bar element links	MAT 205	*(Tension only, non-linear elastic)*		
		Force response – $F(\varepsilon)$	Tow pull-out test	4.1.4 / 4.2.4
Frictional contact; tow/tow, fabric/tooling	CNTAC 33	*(Coulomb frictional contact algorithm)*		
		Friction coefficient - μ	Friction test	4.1.5 / 4.2.5

Table 3.2. Summary of the mesoscopic model constituents, numerical material model requirements and associated fabric characterisation methods

3.8. MODELLING DAMAGE AND FAILURE OF COMPOSITE COMPONENTS USING THE DEVELOPED MESOSCOPIC FABRIC MODEL

As shown in the literature review, the mesoscopic fabric representation developed in this thesis has already been applied to the simulation of impregnated composite coupons during tensile shear loading. The results from this previous work have demonstrated that the model can produce realistic predictions of the composite failure stress and failure modes [131]. This thesis aims to continue this initial work by demonstrating the feasibility of coupling accurate preform fibre architectures to failure simulations of the final composite component. This has been straightforward to achieve using PAM-CRASH, by exporting the discretised FE mesh of the deformed preform fabric geometry into a new simulation model file to be used as a basis for failure analysis. Suitable material models and boundary conditions have then been applied to replicate the test of interest; specifically, the quasi-static loading of a draped composite hemisphere.

The following section describes the mesoscopic composite model and the constitutive material laws used to represent damage and failure of the impregnated composite part. Material data has been obtained from manufacturers datasheets of the separate fibre and matrix materials, therefore, no experimental methods have been used here to measure material properties. The material data and failure simulations for the hemisphere are presented in section 4.1.9.

3.8.1. Composite Material Modelling

The composite model uses the deformed tow mesh that has been generated by the hemisphere preforming simulation. Therefore, the FE representation of the fabric is similar to that previously described, where individual tows are represented by a series of inter-connected, 8-node solid elements. The bar elements that represent the stitching threads have been removed from the fabric model since they will have negligible influence on the predicted component performance using the current modelling scheme.

The constitutive material model used to represent damage and failure in impregnated tows is the same composite bi-phase fibre/matrix model used to treat dry tows during draping, as described by equation 24 and shown schematically here in Figure 3.16. However, mechanical composite properties of the dry tow are now replaced with fibre and matrix stiffness, damage and failure data obtained from manufacturers datasheets of these materials [146][147].

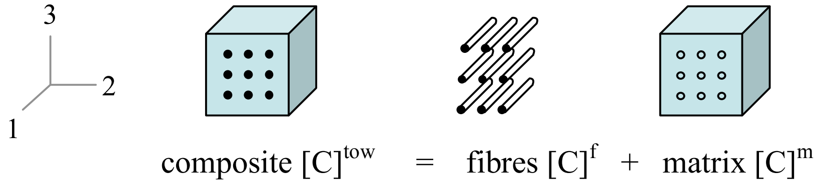

Figure 3.16. Schematic diagram of the composite bi-phase material law, [90]

The bi-phase material model is heterogeneous, whereby stiffness and strength are calculated by superimposing the fibre and matrix mechanical contributions. Consequently, both the fibres and matrix are able to independently undergo damage by the reduction of elastic modulus according to,

$$[C]_{(0)} = \frac{[C]_{(d)}}{1-d}, \qquad \text{Eq. (27)}$$

where; $[C]_{(d)}$, is the instantaneous stiffness matrix; $[C]_{(0)}$ is the initial (undamaged) elastic stiffness matrix and d is a scalar damage parameter. The damage function and equivalent stress vs. strain curve is shown schematically in Figure 3.17.

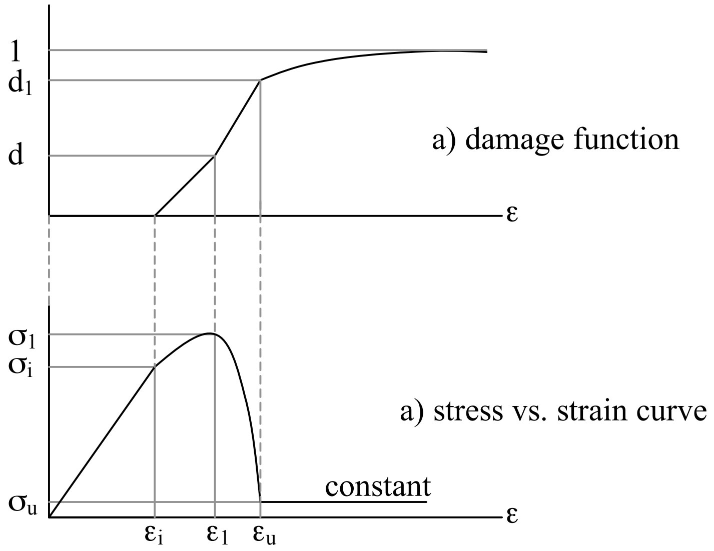

Figure 3.17. Schematic diagram of the modulus damage function and equivalent stress vs. strain curve used to model impregnated fibre tows, [90]

Damage and failure of loaded composite elements is based upon calculation of an equivalent scalar shear strain, ε_s, calculated using equation 28; the full derivation of this equation is provided in [90]. These effective shear strains, $\varepsilon_{s,1}$ and $\varepsilon_{s,u}$, and their corresponding scalar damage factors, d_l and d_u, are required input parameters for the material model to account for damage. At any instant, the effective shear strain is given by,

$$\varepsilon_s = \left(\frac{\varepsilon_{11}}{\sqrt{3}}\right). \quad \text{Eq. (28)}$$

The scalar damage parameter, d, is able to treat the main tow damage properties, specifically; fibre breakage and tensile, compressive and shear damage, and failure, of the resin matrix. CFRP materials may also behave differently if loaded in compression or tension. Elastic deformation properties may be symmetric, but the damage properties are not, therefore, all elastic and damage parameters can be defined independently for both tension and compression.

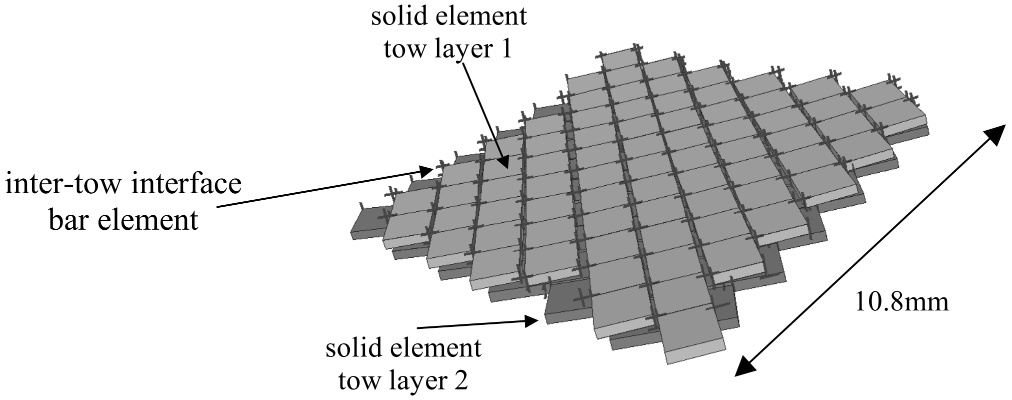

Figure 3.18. Mesoscopic composite modelling scheme

Inter-tow damage mechanisms are treated in the mesoscopic fabric representation, shown in Figure 3.18, using a delamination interface defined between separate tows within the same ply and between separate UD plies. The interface is applied between null-shell elements that surround the solid elements of the tow; these null shell elements have previously been described in section 3.3.2. The interface is defined by projecting a link element between the nodes of one surface onto the element of the second surface, as shown in Figure 3.19. Both Mode-I delamination, and Mode-II in-plane shear failure mechanisms are treated based upon the strain energy released during crack propagation [130].

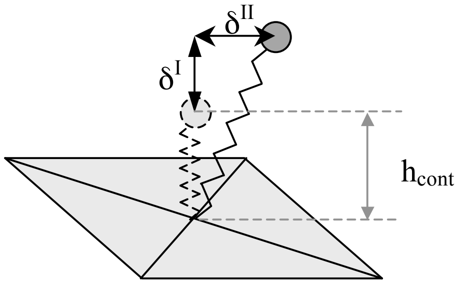

Figure 3.19. Schematic definition of the surface displacement scheme used in modelling inter-tow delamination

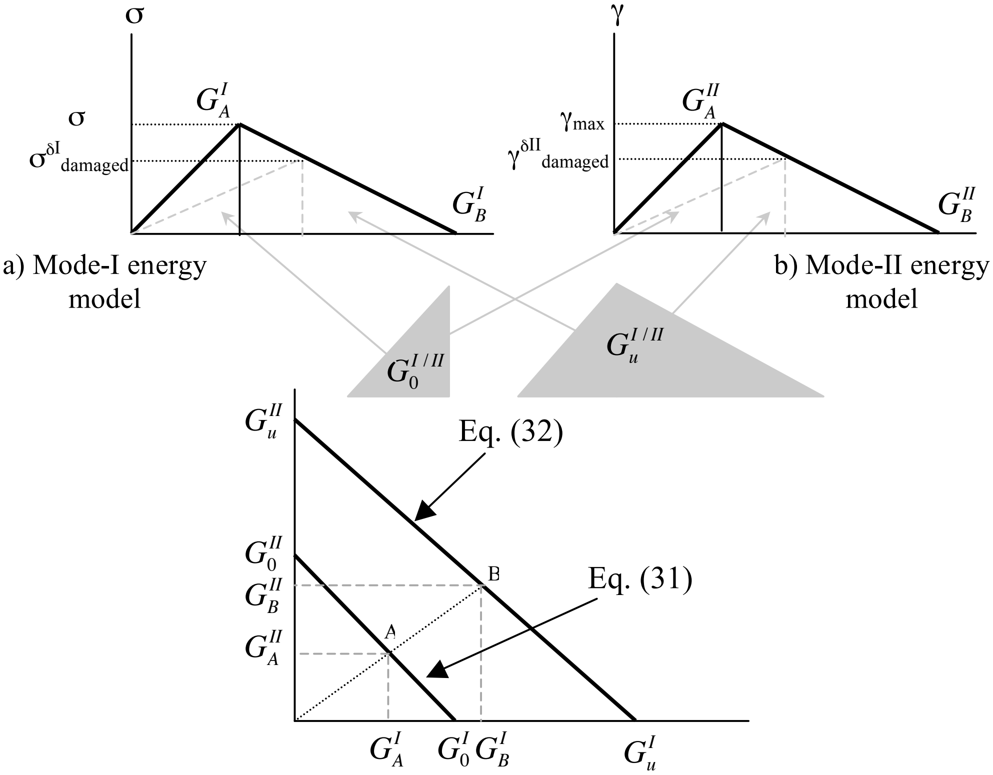

a) Mode-I energy model

b) Mode-II energy model

c) linear coupling of Mode-I and Mode-II failure mechanisms for arbitrary load cases

Figure 3.20. Curve definitions of the energy limits in Mode-I, Mode-II and coupled inter-tow failure

Failure of the defined interface will occur when the elastic strain energy within the structure exceeds $G_0^{I/II}$, which is calculated using the following equations,

$$G_0^I = \frac{\sigma_{\max}{}^2 h_{cont}}{2E_0}, \tag{Eq. (29)}$$

$$G_0^{II} = \frac{\gamma_{\max}{}^2 h_{cont}}{2G_0}, \tag{Eq. (30)}$$

where E_0 and G_0 are the normal and shear stiffness of the interface link element. Arbitrary loading of a practical structure will inevitably lead to a mixture of Mode-I and Mode-II strain deformations. Therefore, a linear coupling model has been used, as shown in Figure 3.20c, with which the initiation of failure will only occur once the following criteria has been met,

$$\frac{G_i^I}{G_0^I} + \frac{G_i^{II}}{G_0^{II}} = 1, \tag{Eq. (31)}$$

where, G_i denotes the instantaneous interface strain energy in the deformed link. After failure has initiated, the damage produces a linear reduction in stress up to an end limit as defined by the following criteria,

$$\frac{G_i^I}{G_u^I} + \frac{G_i^{II}}{G_u^{II}} = 1. \tag{Eq. (32)}$$

The connection between each node and element defined in the interface is individually eliminated once this total damage criteria is reached.

Considering Figure 3.19 and Figure 3.20, the required inputs of the inter-ply failure model are; the elastic normal stiffness, E_0, and shear stiffness, G_0, of the interface; the maximum normal stress, $\sigma_{\max}$, and shear stress, $\gamma_{\max}$, to initiate and propagate failure and the total energy release rate of pure Mode-I, G_u^I, and pure Mode-II, G_u^I, failure. Each of these parameters has previously been determined experimentally for a carbon NCF composite [134], using the Double Cantilever Beam (DCB) delamination test to obtain Mode-I failure data [135] and End Notched Flexure (ENF) shear test to obtain

Mode-II failure data [136]. This experimentally measured data is used here and is presented in Table 3.3.

Delamination model input parameter	Parameter value	Delamination model input parameter	Parameter value
G_{IU}	470J	G_{IIU}	2000J
Stress to initiate/propagate cracking, σ_{max}	0.002GPa	Stress to initiate/propagate cracking, γ_{max}	0.03GPa
Mode I normal stiffness, E^{I}	3.55GPa	Mode II shear stiffness, G^{II}	1.34GPa

Table 3.3. Delamination interface properties used to model inter-tow/ply failure, PAM-CRASH MAT303, [134]

3.9. SUMMARY OF THE FINITE ELEMENT MESOSCOPIC MODELLING SCHEME

This chapter has described a novel mesoscopic modelling approach for coupled drape and failure simulation of a biaxial NCF, comprising two unidirectional fibre tow layers and a tricot stitching. For draping the approach has been specifically developed to ensure that all principle deformation modes of the individual tows and stitches are represented and, importantly, that the technique is computationally efficient so that relatively large scale structures may be analysed.

For failure analysis of the impregnated composite, the draped mesoscopic Finite Element mesh obtained from preforming simulations is to be used with material models for the impregnated tows. The tow constitutive model accounts for elastic, damage and ultimate failure. Modelling strategies for the mesoscopic representation of NCF and procedures for identification of material parameters for drape and failure analysis have been presented, together with descriptions of the tests and simulations which are to be used in validating the models.

4. EXPERIMENTAL AND SIMULATION PROCEDURES AND RESULTS

Section 4.1 of this chapter describes the procedures and results of experimental tests used to characterise the NCF fabric studied in this thesis. Section 4.2 then describes the corresponding simulations used to confirm or calibrate the constitutive material models used to characterise fabric deformations.

4.1. EXPERIMENTAL FABRIC CHARACTERISATION PROCEDURES

4.1.1. Measurement of Fabric Geometry

The geometry of the mesoscopic fabric model is primarily defined by the stitch pattern and location of the impaled through-thickness stitch points. The dimensions of a stitch unit-cell have been ascertained by measuring the total width and length of 40 unit-cells and averaging the results to obtain the dimensions of a single unit-cell. Measurements have been taken using Vernier callipers, accurate to ±0.1mm. Results are presented in the appendix; the mean average dimensions of a single unit-cell are presented in Figure 4.1.

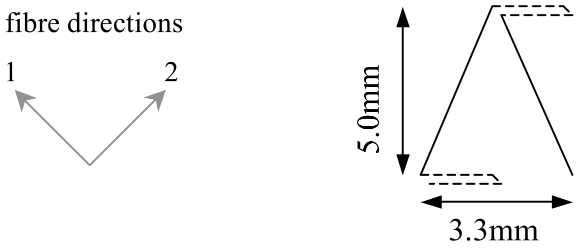

Figure 4.1. Tricot stitch unit-cell dimensions; shown perpendicular to the plane of the fabric

Fabric thickness tends to vary with inter-fibre shear and when sufficient compaction pressure is applied. The test method used here utilises the picture frame equipment, described in section 4.1.2, to impose a defined shear angle in increments of 5°. These increments are determined based on measured axial extension of the frame and the corresponding inter-fibre shear angle has been calculated using equation 3. The fabric thickness is measured to ±0.01mm accuracy with a micrometer, over a 20mm x 20mm area using metal plates. The attached plates are used to help distribute the transverse compaction load and avoid local fabric indentation, which would otherwise occur. Pressure is applied with a constant torque ratchet included as part of the micrometer. Three values of sample thickness are recorded at each shear angle and averaged, as presented in Figure 4.2. Measured data is provided in the appendix.

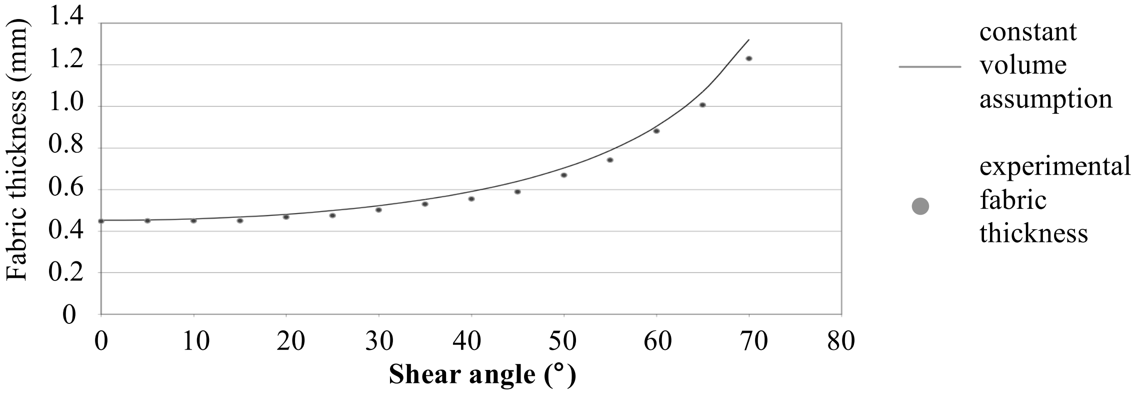

Figure 4.2. Fabric thickness results during shear

The results show that the experimental thickness measurements approximate well to the constant volume assumption. The un-deformed fabric thickness at 0° inter-fibre shear angle is 0.45mm.

4.1.2. Picture Frame Shear Test Procedure and Results

The picture frame test is a relatively simple method to characterise fabric shear resistance, that constrains the fabric to a state of near pure shear deformation. The test involves clamping of the fabric sample into a specific test frame, shown in Figure 4.3, with fibres aligned parallel to the edges of the frame. Significant care has been taken to ensure fibres are aligned correctly, since any misalignment would produce axial fibre strain and increase the measured axial force. Diametrically opposite corners of the frame are extended and the axial force is recorded. The results from this test have been used to calibrate both transverse tow compaction and the influence of stitching on shear resistance.

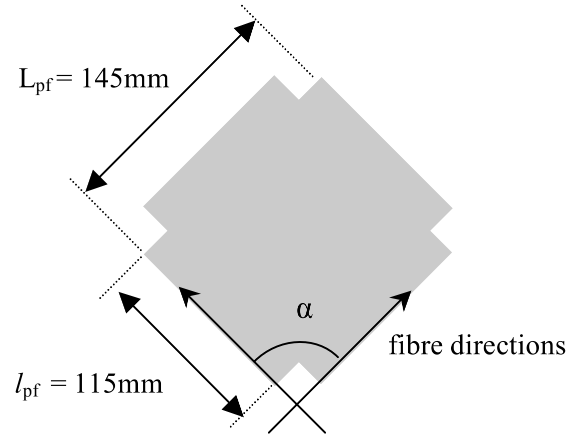

Figure 4.3. Schematic of the fabric samples tested in the present work

The dimensions of the cruciform fabric specimens are shown in Figure 4.3; the design specifications of the frame equipment are also provided in the appendix and are based upon the design used in [67]. The tensile test equipment used to perform this test is a Zwick Z010 with a 2.5kN load cell calibrated to 0.1% error. Dry fabrics are not influenced by strain rate effects and, therefore, the rate and variation of loading is not important. For this work a constant crosshead velocity of 20mm/min is used for all picture frame tests and induces the shear rate profile shown in Figure 4.4, calculated as follows.

$$\dot{\phi} = \frac{2\dot{D}}{\left(2L_{pf}^{\ 2} - 2\sqrt{2}L_{pf}D - D^2\right)^{1/2}}, \qquad \text{Eq. (33)}$$

where, $\dot{\phi}$ is the rate of shear, $\dot{D}$ is the axial displacement velocity, D is the measured axial displacement and L_{pf} is the picture frame edge length.

Three picture frame tests have been performed in each test case of positive shear, negative shear and with stitching removed, to check repeatability. Stitching has been removed from fabric samples, where necessary, by first clamping the complete specimens in the picture frame and then manually cutting away each stitch. This method ensures that fibre tows are correctly aligned and undergo minimal disturbance.

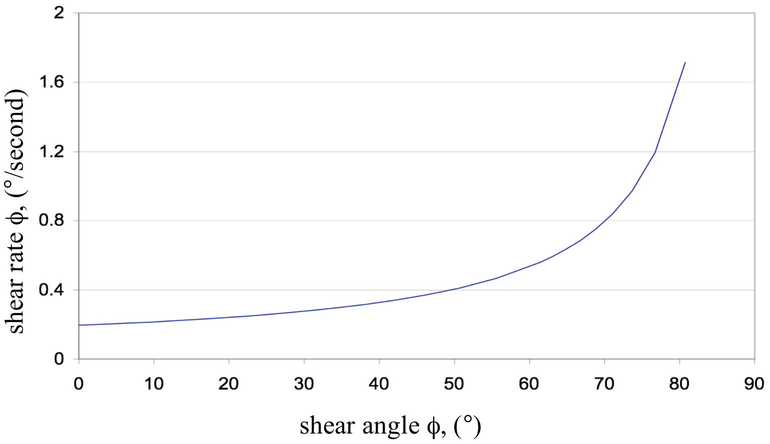

Figure 4.4. Picture frame shear rate profile using a crosshead velocity of 20mm/min

Clamping of picture frame specimen edges can lead to errors associated with edge-effects. as described in the literature review section 2.5.1. An initial set of picture frame tests have consequently been performed to quantify the magnitude of edge-effects by comparing the shear angle of the picture frame, calculated using equation 3, and the true measured inter-fibre angle of the fabric. Three tests have been performed and mean average results computed and presented in Table 4.1. Errors have been calculated based upon the range of values from these three tests. The fabric inter-fibre angle has been measured manually from images taken during picture frame tests and post processed using visual analysis software (CorelDraw [153]) over a 30mm fibre length at the coupon centre.

True fabric inter-fibre shear angle	*Picture frame shear angle*	*Resultant difference in fabric and frame inter-fibre angles*
0.0° (±0.1°)	0.0°	0.0°
12.2° (±0.2°)	11.8°	0.4°
25.5° (±0.1°)	25.5°	0.0°
41.9° (±0.2°)	41.3°	0.3°
53.6° (±0.1°)	53.5°	0.1°
60.8° (±0.1°)	61.0°	-0.2°

Table 4.1. Results comparing fabric inter-fibre angle to that determined by geometrical analysis of the frame

The results of Table 4.1 show that the differences in inter-fibre angle between the fabric and frame are small, <±0.4° and, therefore, demonstrate that edge-effects from edge clamping are minimal. The minor variations in shear angle that have been determined are attributed to experimental errors, produced by the visual measurement procedure and manual method of aligning fibres within the picture frame. Consequently, in this work the test procedure is simplified and calculated values of inter-fibre angle from the recorded crosshead displacement of the tensile test machine, using equation 3, are used instead of physical measurements. The effect of edge-effects on the measured force has not been investigated since this is deemed outside the scope of the current work.

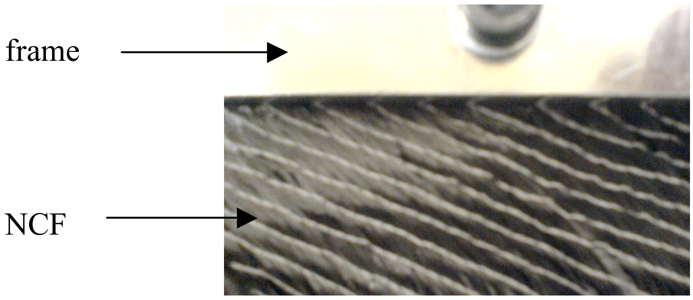

Figure 4.5. Negligible picture frame edge-effects of the NCF fabric studied

Picture frame test results are presented in two separate graphs. The first graph, shown in Figure 4.6, plots the measured axial force, F_A, against the shear angle, ϕ. This data is later used to calibrate both the tow and stitch shear resistance. Error bars have been calculated using a statistical student t-test analysis, which assumes the data approximates to a normal distribution of unknown variance to a defined confidence interval of 90%. A second graph, shown in Figure 4.7, plots normalised axial force, F_N, versus normalised axial displacement of the frame, D_N. This data allows a comparison with similarly normalised bias extension shear test results. The axial force is normalised here to the edge length of the picture frame test coupon, l_{pf}, as defined previously in Figure 4.3 and the displacement is normalised using equation 5. However, as described in section 2.5.1, the normalisation of fabric shear data is still a topic of active research and the latest literature should be considered before following any normalisation procedure.

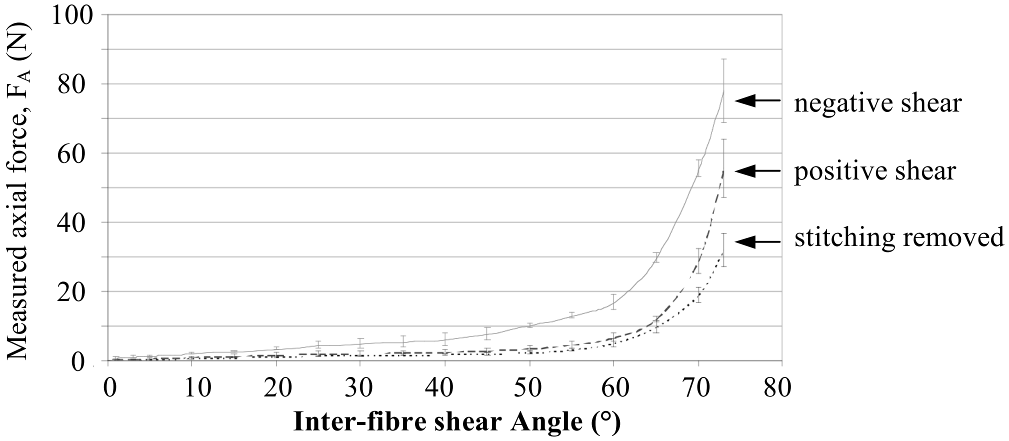

Figure 4.6. Picture frame shear test results, plot of axial force versus fabric shear angle

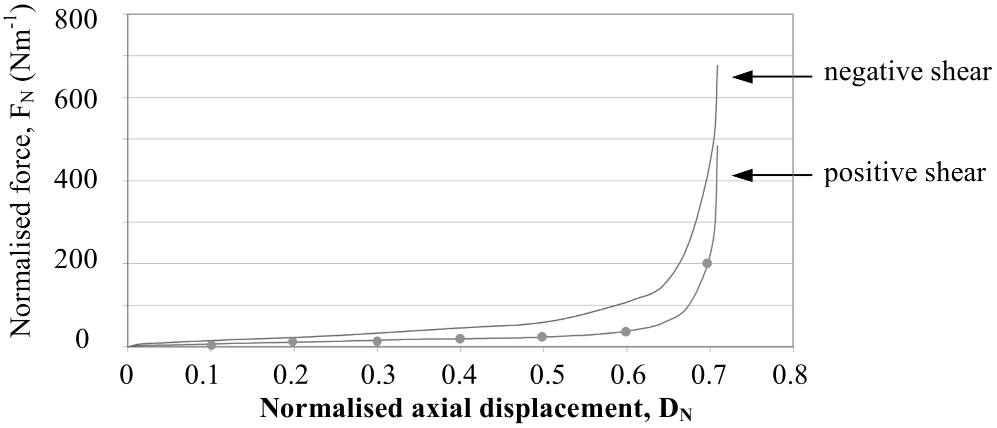

Figure 4.7. Picture frame shear test results, plot of normalised axial force versus crosshead displacement

The results show that negative shear exhibits greater resistance than positive shear, a consequence of the different loading mechanisms that occur in the tricot stitch.

4.1.3. Tow Flexural Rigidity Test Procedure

Flexural rigidity testing is based upon a standard originally developed for textiles, ASTM D1388 [62]. This test has been used here to calibrate the modelled tow flexural stiffness and aims to ensure that the developed fabric model correctly predicts fabric bending stiffness.

A schematic diagram of the experimental method used is shown in Figure 4.8 and is based on the 'cantilever beam' methodology of the test standard. The test involves sliding a coupon of material, parallel to the coupon length, over the edge of an inclined surface at 41.5°. The specimen is slid continuously and, under the action of its own mass and gravity, eventually contacts the inclined plane. The resulting overhanging tow length is measured and recorded. Specific machinery is available to automate this test procedure, however, in this work the coupon is slid manually using a slide rule.

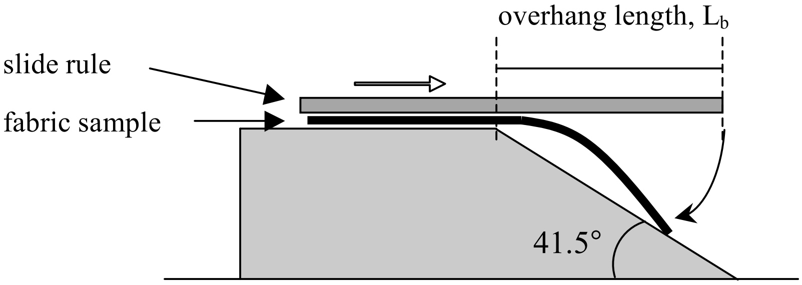

Figure 4.8. Tow flexural rigidity test procedure, [62]

The fabric coupon usually used for this standard test has been replaced here by a single tow that has been removed from the studied NCF. For completeness, the procedure has been analysed as defined by the ASTM standard, as follows,

$$l_b = \frac{L_b}{2}, \qquad \text{Eq. (34)}$$

where, l_b is the bending length and L_b is the measured overhang length. The flexural rigidity, G_b, is then given by,

$$G_b = W_f \times l_b^3, \qquad \text{Eq. (35)}$$

where W_f is the fabric mass per unit area.

Three tests have been performed from which a mean average overhang length, L_b, and flexural rigidity, G_b, is determined. These results are presented in Table 4.2.

Flexural rigidity, G_b	Overhang length, L_b	Variation in measured overhang length from 3 tests
7.3e-5	155mm	±1mm

Table 4.2. Tow flexural rigidity results determined using the ASTM D1388 [62] test methodology

Direct simulation of the flexural rigidity test has been used to calibrate longitudinal elastic modulus, E^t_{11}, of simulated tows, as described in section 4.2.3.

4.1.4. Tow Pull-out Test Procedure

The tow pull-out test provides a method of characterising the frictional coupling between tows and stitching that occurs during inter-tow slip. The test involves removal of a number of tows from a constrained fabric sample. No standards exist for this test procedure and methods differ between authors [64][86][88]; however, the test should ideally obtain friction data using a constant area of fabric through which the tows are pulled. Extracting several tows through a constant contact area helps to prevent an undulating force being measured, which can occur due to tows passing under NCF stitch loops, as observed in [86].

A cruciform fabric sample is used in the current work, in which the coupon sides are clamped and the protruding tows pulled using the crosshead of a tensile testing machine, Figure 4.9a. The cruciform specimen, shown in Figure 4.9b, demonstrates the axial tows left unconstrained, which have been pulled through a constant area of transverse tows, 2,880mm^2. A Zwick Z010 tensile test machine with a 2.5kN load cell calibrated to 0.1% error has been used for this test.

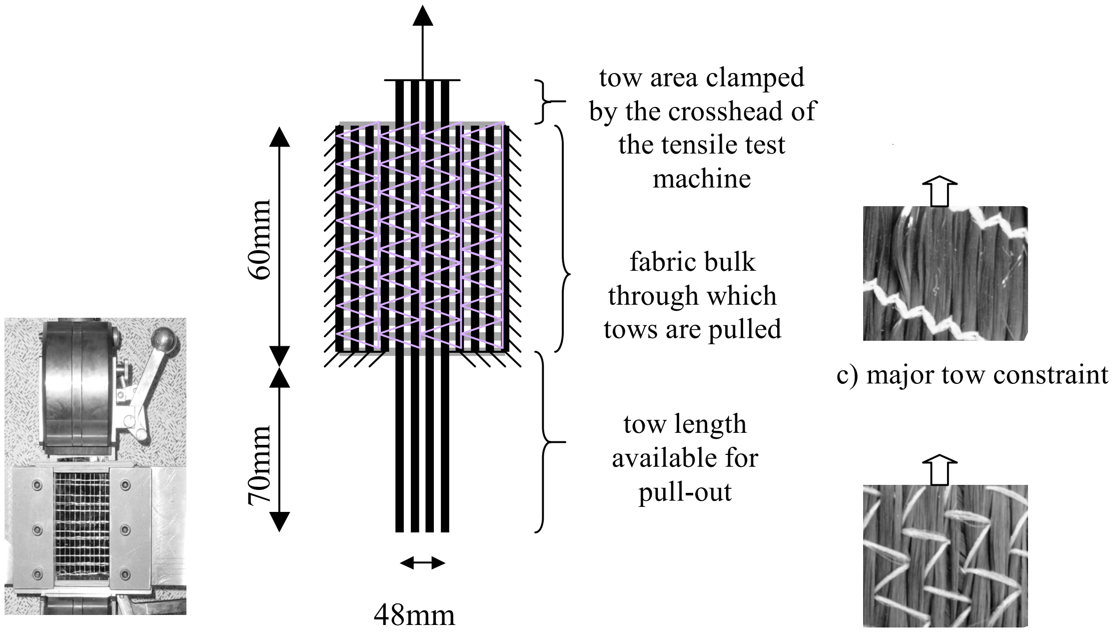

a) the tow pull-out test b) pull-out test specimen geometry c) major tow constraint d) minor tow constraint

Figure 4.9. The tow pull-out test, specimen geometry and definitions of stitch constraint

The NCF fabric studied is manufactured with impaled stitching making identification of individual tows difficult. Consequently, a defined 48mm width of fibres has been pulled. Pull-out tests have been performed in each of the two possible fibre directions, as illustrated in Figure 4.9c and d. The mean tensile force from three tests is normalised to the area of removed tows in contact with the specimen bulk (2,880mm^2) and plotted against tow displacement, Figure 4.10. Error bars are calculated from three repeated tests using a student t-test statistical method to a 90% confidence interval.

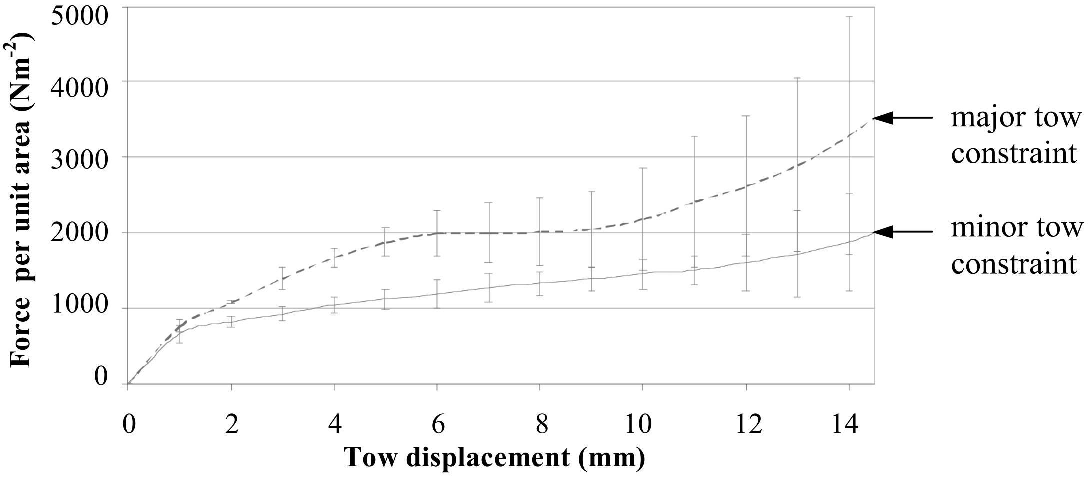

Figure 4.10. Experimental tow pull-out test results

The above results indicate that the smaller loops of stitch material, as shown in Figure 4.9c, produce greater frictional resistance to tow slip. The error bars indicate a large amount of scatter in results, which progressively increases with tow displacement. The scatter is due to the random nature of progressive buckling of individual fibres that is observed to occur at stitch locations; this buckling causes significant variation in tow pull-out resistance and leads to the general increase in measured tow pull-out force.

4.1.5. Fabric Friction Characterisation Procedure

Preforming is a friction, contact dominated, problem which has been modelled in the current work using suitable contact algorithms. The test setup used to obtain the Coulomb friction coefficient between two surfaces is shown in Figure 4.11. A tensile test machine is attached to the horizontal sliding surface via a pulley that translates a vertical machine displacement to the required horizontal displacement; the pulley contains roller bearings to minimise friction during rotation. The test equipment, Figure 4.11, measures dynamic friction and is based on the test setup shown in Figure 2.20a. A Zwick Z010 tensile test machine having a 2.5kN load-cell calibrated to 0.1% has been used for this test.

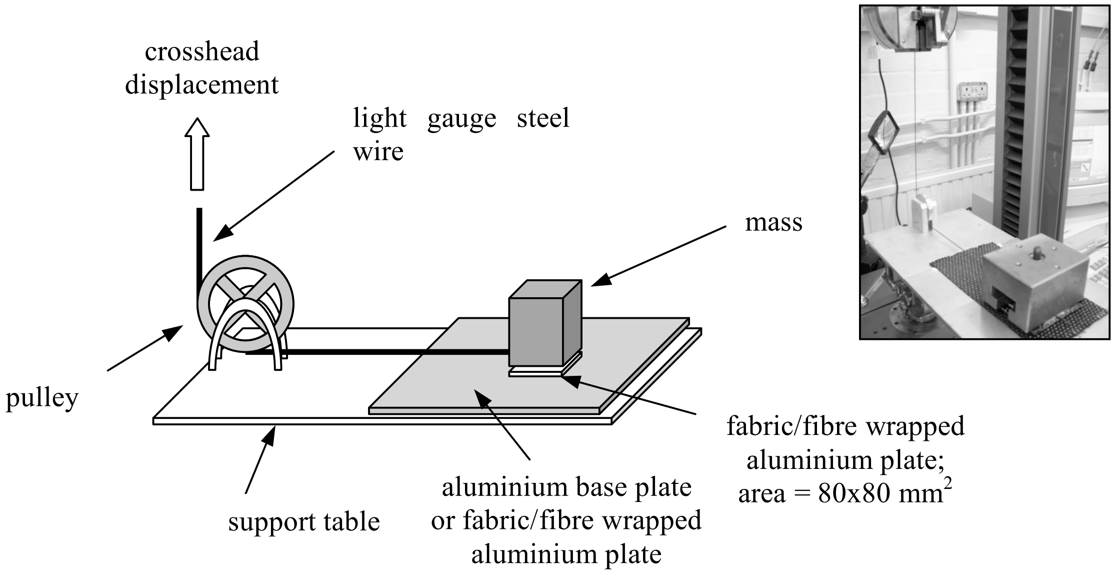

Figure 4.11. Fiction test equipment used in the current work

Tooling friction: Friction tests have been performed between an aluminium base plate and NCF fabric to quantify tooling contact during forming trials. Friction measurements have also been taken with two fibre orientations relative to the sliding direction, 0°-90°, 90°-0°, to ascertain the influence of fibre and stitching orientations on contact friction.

Tow-to-tow friction: Tests have also been preformed to characterise inter-tow friction. Two relative fibre orientations have been tested; 0°/0°, to characterise inter-tow frictional slip, and 0°/90°, to characterise inter-ply friction during in-plane shear and cross-over point slip. Testing of tow-to-tow friction with the equipment shown in Figure 4.11 requires two contact surfaces comprised of Toray T700 fibres. However, the complex impaled stitching of the NCF studied makes removal of fibres difficult. Consequently, Toray T700 carbon fibres from an alternative NCF, with easily removed stitching, has been adhered to flat aluminium plates. This procedure is advantageous since it maintains a consistent distribution of fibres over the contact surfaces.

The friction coefficient calculated for a pair of surfaces may vary, depending on the normal surface load and velocity. Therefore, three different displacement velocities, Vel, and normal loads, P, have been tested for each combination of contact surfaces. These variables and their values, as tested here, are summarised in Table 4.3. The normal load, P, includes contributions from both the added mass and fabric wrapped aluminium plate and has been normalised to the contact area, $0.0064m^2$, to obtain surface pressure.

Each combination of displacement velocity and surface pressure possible has been tested for each of the fibre, or fabric, surface combinations. The total relative surface displacement is 20mm for each test case. The displacement velocities, Vel, chosen vary between 25mm/min and 1000mm/min in an attempt to be representative of practical fabric preforming. The normal surface pressures have been also been selected to represent typical loads that may occur during fabric forming processes. A range of approximately 1,370 to 6,500Pa has been tested in the present work.

Variable		Tested parameter values		
Vel, Displacement velocities, mm/min		25	300	1000
Total pressure normal to contact surface, Pa (calculated to nearest 1Pa)		1,369	3,692	6,505
Fibre orientation relative to direction of movement	fibre/fibre	0° - 0°		0° - 90°
	fabric/aluminium	0°/90°		90°/0°

Table 4.3. Friction test velocities, applied pressures and fibre directions

The Coulomb coefficient of friction has been calculated for each test from the experimentally measured applied force, N, using equation 10. Comprehensive coefficient of friction data for each combination of surfaces is provided in the appendix. These results show that the calculated friction coefficient between two surfaces does not significantly vary with changing pressure or relative surface velocity, within the range of the values tested. Consequently, the mean average friction coefficient for each combination of surfaces has been calculated using results from each of the nine test combinations of normal pressure and velocity tested. These averaged values are shown in Table 4.4, in conjunction with the standard deviation from these nine test cases.

Contact interfaces	μ	standard deviation
Tow-to-tow 0° - 90°	0.18	0.006
Tow-to-tow 0° - 0°	0.35	0.019
Fabric–aluminium 0°/90° & 90°/0°	0.25	0.011

Table 4.4. Fabric and fibre friction coefficient test results

The results show significantly higher friction coefficients for aligned tows, 0°-0°, compared to perpendicular tows, 0°-90°, which is due to the nesting of fibres that occurs when fibres are aligned. The fabric-to-tooling friction coefficient is subject to both fibre and stitching contact on the relatively smooth aluminium surface and is found to be unaffected by fabric orientation.

4.1.6. Fabric Forming Validation: Bias Extension Test Procedure and Results

The bias extension shear test has been used to characterise fabric shear deformation and, unlike the picture frame test, does not impose pure shear. Therefore, combined inter-tow and cross-over point slip mechanisms can occur which makes the test ideal for validating the developed mesoscopic NCF model. This is performed by directly comparing the axial resistance force, inter-fibre shear angles and deformation mechanisms for both bias extension tests and simulations. A description of the experimental test procedure follows.

Fabric coupons, 250mm x 100mm and comprising ±45° fibres, have been clamped at each end of the coupon length and axially extended at a constant 10mm/minute velocity. The test is performed using a Zwick Z010 tensile testing machine with a 2.5kN load cell calibrated to 0.1% error. Four tests have been performed for both positive and negative shear to check repeatability and quantify any occurrence of shear bias in the material.

Bias extension test results are presented in two separate graphs. The first graph, shown in Figure 4.12, plots the measured axial force, F_A, versus the axial engineering strain.

An indication of test scatter is provided using error bars, calculated using a statistical student t-test analysis, which assumes the data approximates to a normal distribution of unknown variance to a defined confidence interval of 90% [82]. A second graph, shown in Figure 4.13, plots normalised axial force, F_N, (determined using equation 9), versus normalised axial displacement of the frame, D_N, (determined using equation 6), for comparison to normalised picture frame shear test data.

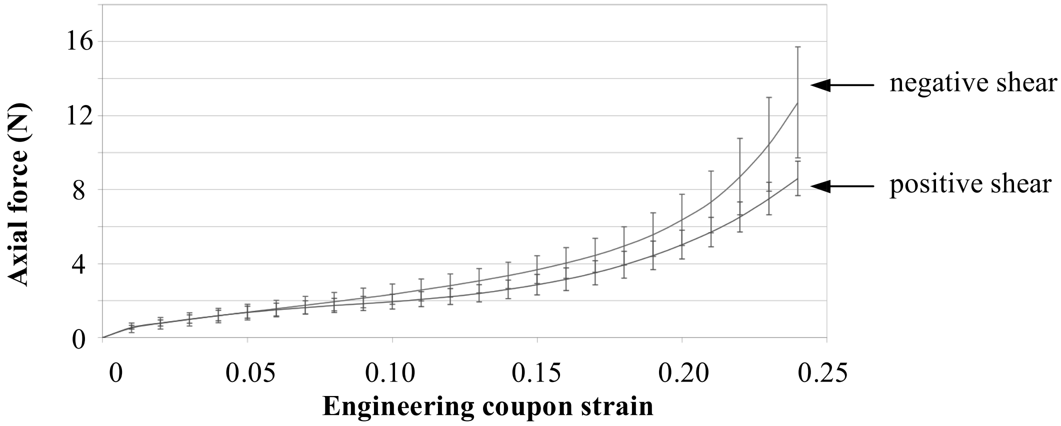

Figure 4.12. Bias extension shear test results, plot of axial force versus axial coupon engineering strain

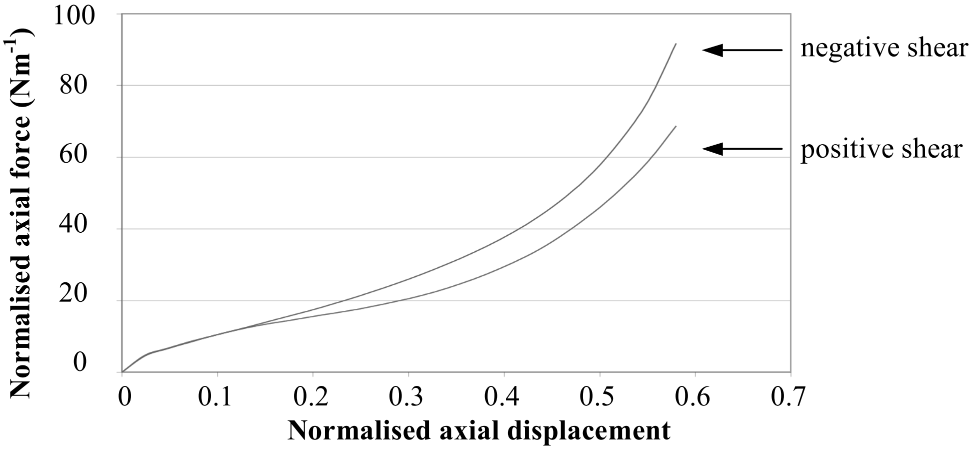

Figure 4.13. Bias extension shear test results, plot of normalised axial force versus normalised axial coupon displacement

The variation of inter-fibre shear angle produced by shearing of the bias extension coupon can be compared to the inter-fibre shear angle predicted by pure shear kinematic analysis, as described in section 2.5.1 [59]. This comparison is used here to quantify the effects of deformation mechanisms that occur, other than pure shear, in the fabric sample. DIC techniques are useful for this task by producing complete inter-fibre shear maps of the fabric coupon surface. However, dedicated fabric analysis techniques are required to account for mechanisms other than pure shear [53][76] and for the analysis of NCF, which has only one fibre direction visible on each surface of the specimen. A manual method of measuring inter-fibre shear angle has therefore been used here by analysing digital images of the fabric specimen taken during the bias extension test.

A coloured stitching thread has been sewn into the fabric to highlight the fibre directions, as shown in Figure 4.14. The inter-fibre shear angle highlighted by this coloured stitch is measured on the digital images using CorelDraw [153]. Measurements are taken at three points, distributed across the central plane of the coupon, Figure 4.14, at axial displacement intervals of 5mm.

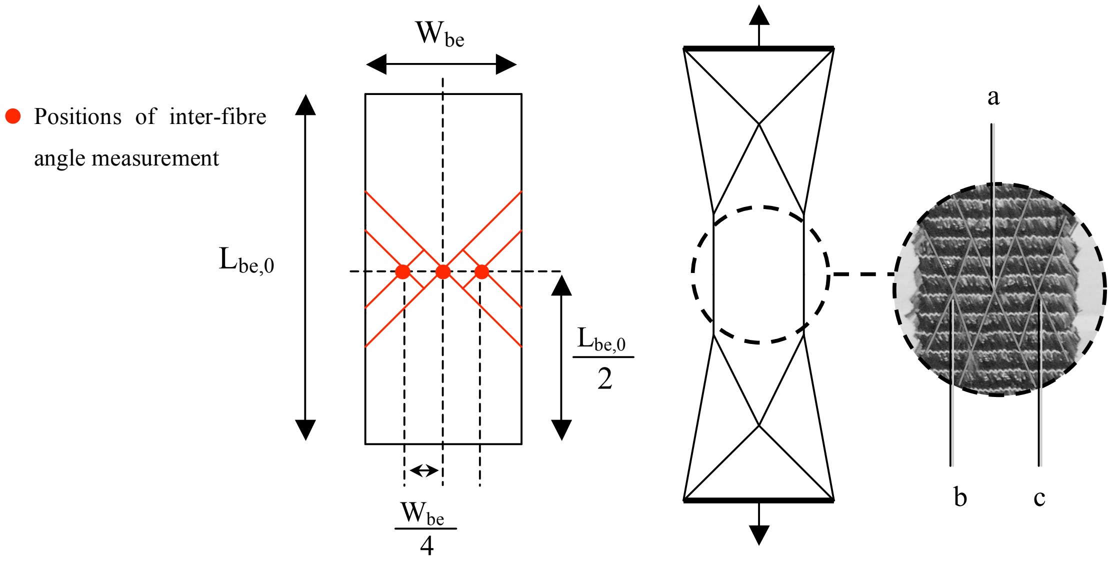

Figure 4.14. Location of points for measuring inter-fibre angle in a bias extension coupon

Figure 4.15 and Figure 4.16 show graphs of inter-fibre shear angle measurements versus engineering coupon strain, for both positive and negative sheared bias extension samples, respectively. These results are compared with the analytical shear angle based upon pure shear kinematics and calculated using equation 3. This model effectively regards the central shear zone of the bias extension test as a picture frame test which has a frame edge length of L_{eff}, as shown previously in Figure 2.16.

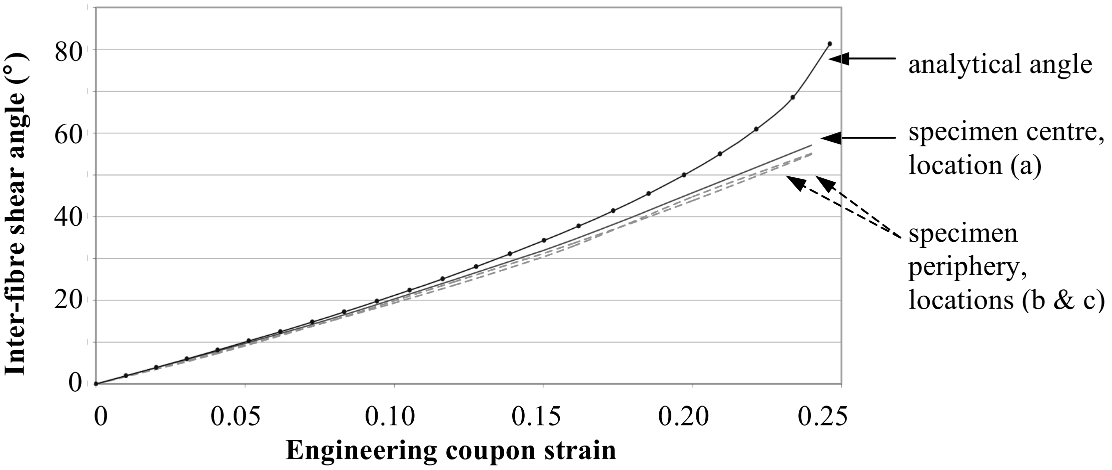

Figure 4.15. Inter-fibre shear angle variation during positive shearing of a bias extension test

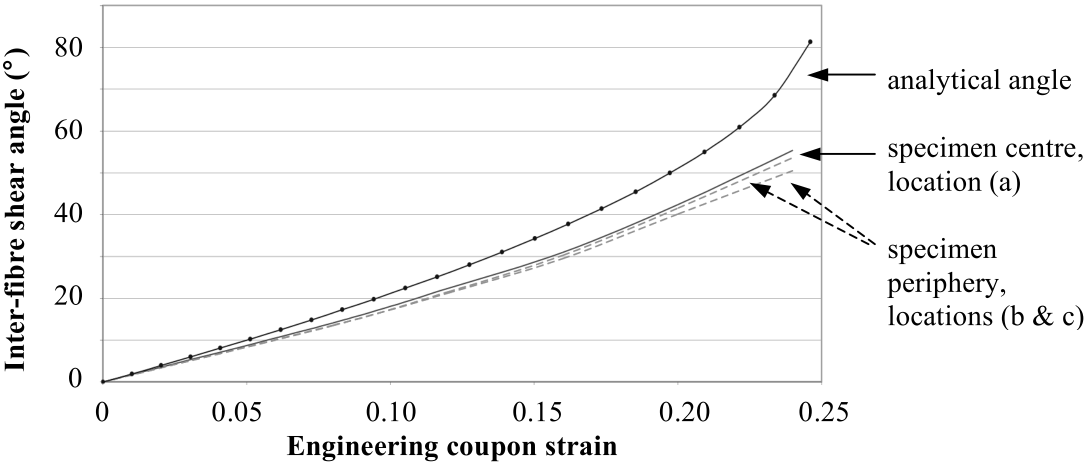

Figure 4.16. Inter-fibre shear angle variation during negative shearing of a bias extension test

From Figure 4.15 and Figure 4.16 it can be seen that the measured inter-fibre shear angles are less than that predicted using the analytical model for both positive and negative fabric shear, especially at higher shear angles. This is due to the increasing dominance of inter-tow and cross-over point slip that occurs in the test specimen, which the analytical model cannot treat since it is based upon pure shear kinematics. The shear angle measurements toward the free edges of the specimen, b and c, also show that the inter-fibre shear angle slightly relaxes towards the free edges of the specimens.

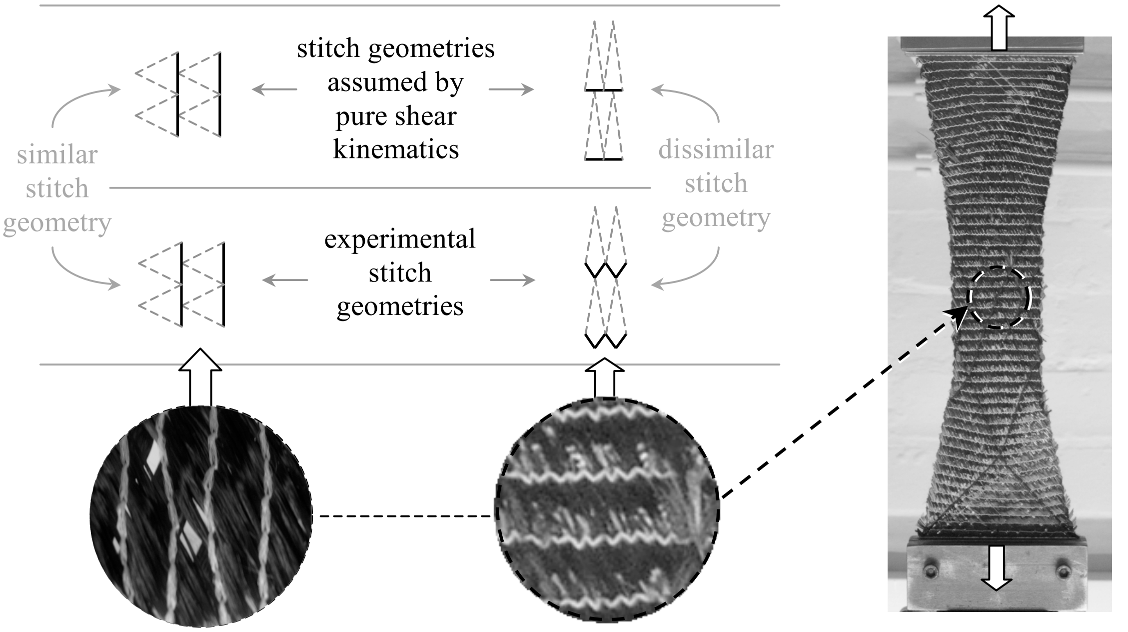

a) positive shear stitch deformation
b) negative shear stitch deformation
c) negative shear bias extension coupon at 22% axial engineering strain

Figure 4.17. Observations of experimentally deformed stitch geometries for bias extension samples at 22% axial engineering strain; showing schematics of the experimental and kinematic model stitch geometry during positive and negative shear

Experimental observations of the deformed stitch geometry are shown in Figure 4.17 and compared to the stitch geometry assumed by pure shear kinematic modelling. As this figure shows, the modelled stitch geometry correlates well to the true stitch geometry observed during positive fabric shear tests. However, during negative fabric shear the tensile stitch loads are distributed between all segments of the tricot stitch pattern, which is not predicted by pure shear kinematics; this presents a deficiency of the kinematic fabric model used here when determining the modelled stitch response to loading, as is to be discussed in chapter 5.

4.1.7. Fabric Forming Model Validation: Hemisphere Drape Trials and Results

Draping trials have been used to validate the mesoscopic fabric model developed in this thesis for a general, relatively large scale geometry. A hemisphere geometry, with a radius of 76mm, has been chosen for this task because areas of high shear are produced and the complete symmetry of the shape allows shear bias to be easily quantified.

A draping test assembly has been designed, as shown in Figure 4.18, which aims to replicate common industrial forming processes by incorporating fabric blankholding pressures around the hemisphere circumference; the design specifications of this assembly are included in the appendix. The blankholder comprises of two rings that clamp the fabric at a constant 3.35kPa (±5Pa) pressure, applied with three calibrated springs. A simple compression test machine is used to lower the blankholder assembly, and single fabric layer, over the male hemisphere mould. Axial forming force is measured using a Zwick 010 test machine with a 2.5kN load-cell calibrated to 0.1% error.

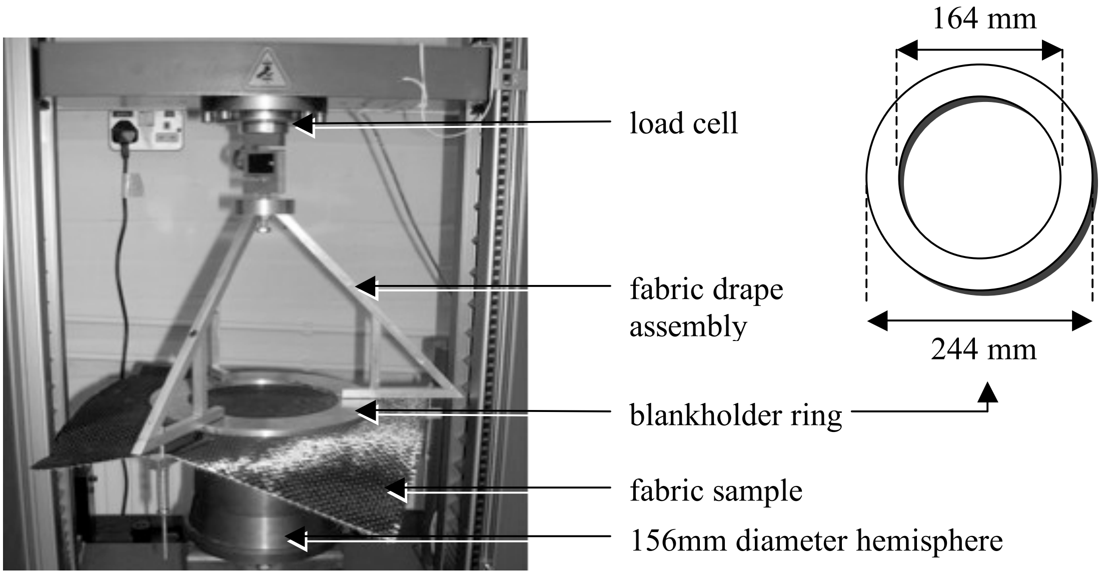

Figure 4.18. Hemisphere draping test assembly

The forming process and final fabric deformations are shown in Figure 4.19 and Figure 4.20. Stitch deformation is observed to be comparable to pure shear in areas of positive shear, but deviates from the pure shear geometry in negative sheared areas. These observations are comparable to the stitch deformation mechanisms identified during the bias extension tests, as shown in Figure 4.17.

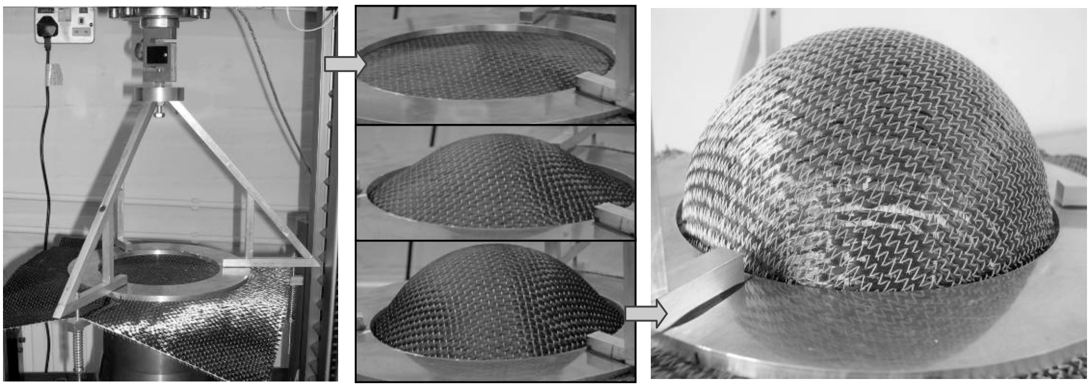

a) Test setup b) Forming stages c) Final fabric deformations

Figure 4.19. Forming of the biaxial NCF using a hemispherical metal punch and blankholder restraint

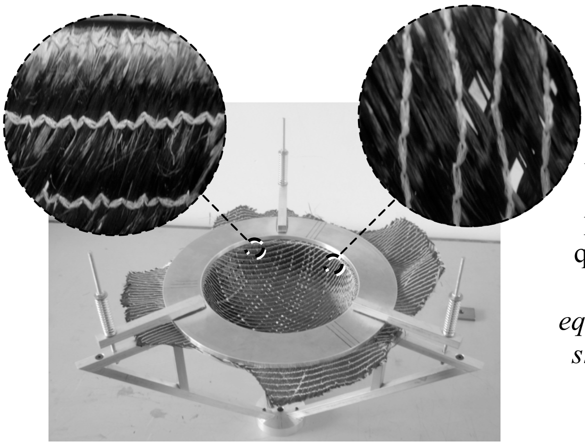

negative shear quadrant; *stitch deformation dissimilar to that assumed by pure shear kinematic modelling*

positive shear quadrant; *stitch deformation equivalent to pure shear kinematic modelling*

Figure 4.20. Underside view of the preformed fabric hemisphere showing details of fabric deformations

Visual inter-fibre shear angle measurements have been taken at two planes identified in Figure 4.21; measurement positions are shown for one quadrant only, whereas actual measurements have been taken around the full hemisphere circumference at heights relative to the hemisphere base as indicated.

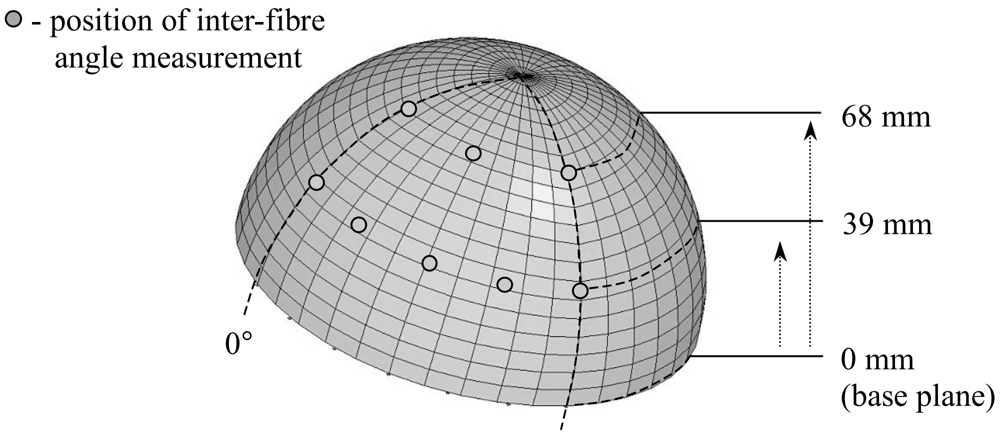

Figure 4.21. Locations of inter-fibre shear angle measurement for the experimental hemisphere preform

The results of the experimental shear angle measurements are presented in Figure 4.22. Significant bias of the fabric shear is visible as shown by the variation in maximum inter-fibre shear angle of adjacent fabric quadrants.

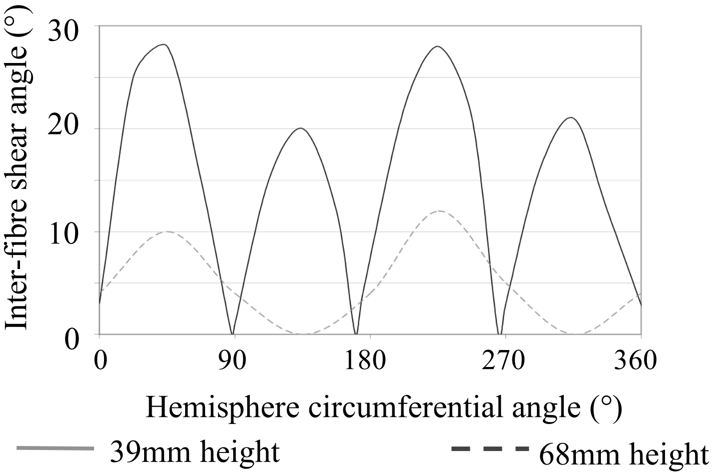

Figure 4.22. Results of experimental inter-fibre angle measurement of a hemisphere preform at heights from the hemisphere base as indicated

The force required to form the hemisphere is shown in Figure 4.23. The graph plots the axial force, measured with the compression test machine, versus the depth of the formed hemisphere into the fabric sheet; the fabric surface is in contact with the hemisphere mould surface at 0mm depth.

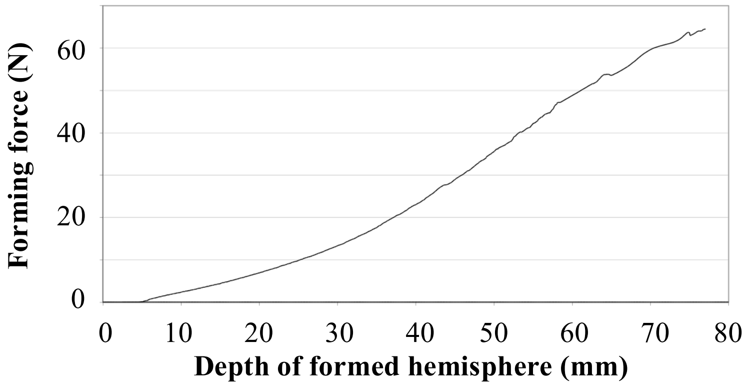

Figure 4.23. Results of experimental forming force of a 76mm radius hemisphere

4.1.8. Manufacture and Failure Testing of Hemispherical Composite Components

Preforming simulation is commonly used to obtain information of the fabric architecture for use as an accurate starting point for mechanical and process analyses. In the current work, the final fabric mesh produced by simulating the forming of the previously described hemisphere is used as a basis of quasi-static damage and failure simulation of composite materials. The simulated composite deformation mechanisms and failure modes are compared to equivalent experimental failure tests. This section describes the manufacture of the hemisphere components used for these tests.

A single NCF fabric sheet has first been preformed to the hemisphere geometry, using the same procedure as detailed in section 4.1.7. The deformed sheet is then transferred to the male infusion mould and impregnated with resin (Araldite LY3505/XB3404) using a vacuum assisted resin infusion process to obtain the final composite component. The resin has been de-gassed at full vacuum for 5 minutes after mixing of the resin and hardener to remove air pockets and minimise the occurrence of voids in the final part. The infusion process is shown schematically in Figure 4.24 and illustrates the location of the resin inlet and vacuum outlet, which are at the highest point of the hemisphere and near one corner of the base plate, respectively.

The resin, mould and base plate are placed on a hot plate and heated to approximately 40°C prior to infusion in order to reduce the resin viscosity and aid infusion. The NCF is fully infused in approximately 2-3mins, after which time the resin inlet is sealed and the hotplate temperature increased to 70°C for 3 hours for initial curing. The part is then allowed to cool, while still under full vacuum and de-moulded. Finally, the composite hemisphere is post-cured at 80°C for 3 hours to maximise the resin mechanical properties, as recommended by the manufacturers processing guidelines.

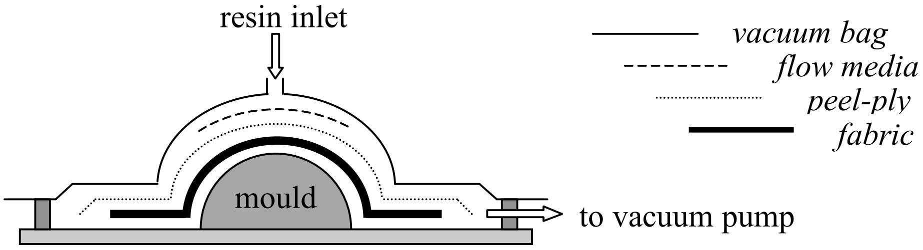

a) schematic of the infusion process

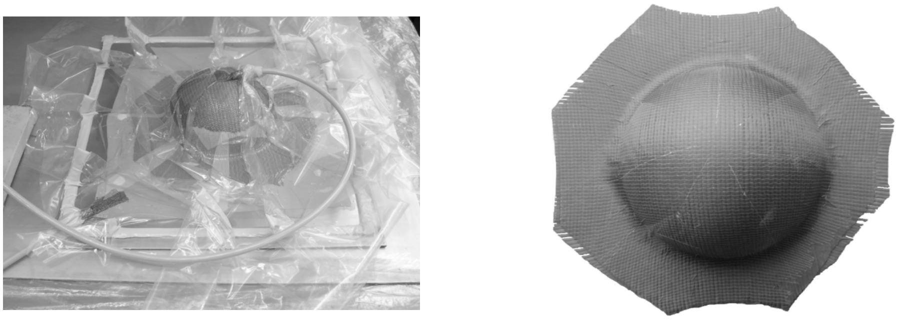

b) image of the infusion process c) the final hemisphere component

Figure 4.24. Manufacture of the composite hemisphere using vacuum assisted infusion processing

One of the most problematic issues for manufacturing composite components with LCM processing methods is achieving satisfactory quality. The vacuum assisted infusion process used here has produced good components that are completely infused and have excellent surface quality. However, visual inspection of the infused parts shows significant defects in the fabric, due to missing tows and inconsistent fibre distribution, as shown in Figure 4.25a. These defects are significant to the mechanical properties of the final impregnated component, since the large resin rich gaps between tows are prone to act as sources premature failure and crack propagation at low stresses.

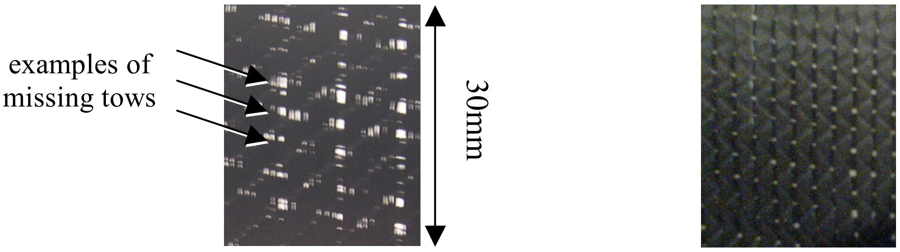

a) image of the studied Saertex fabric, showing significant fabric defects

b) image of the high quality fabric with improved fibre distribution

Figure 4.25. Comparison of the high and low quality fabrics used in manufacture of 76mm radius composite hemispheres

The mechanical performance of experimental hemisphere components manufactured with a low quality fabric will inevitably be lower than predicted using the current simulation model, since defects are not currently modelled. Ideally, the effects of fabric variability on composite performance, and methods of modelling this variability, should be included in the mesoscopic tow modelling scheme. However, this has not been possible to include in the time-scale of the current work. Therefore, an approach has been adopted to additionally compare hemisphere failure simulations to tests of components manufactured with an equivalent, but higher quality fabric to the Saertex material currently studied.

The high quality fabric chosen for this additional test has been produced using modern multiaxial looms from Liba [149], which are able to produce fabrics with consistent fibre distribution and spacing. Consequently, the quality of this fabric architecture is more comparable to that assumed by the current simulation model. The fabric style chosen is equivalent to the Saertex NCF studied in this work, comprising of a 312gm^{-2} biaxial NCF, with Toray T700 carbon fibres, which are held together with tricot stitching (no fabric grade is available for this fabric since it has been manufactured as part of a demonstrator batch). A single specimen of this fabric has been preformed and impregnated, as described previously, and is tested in addition to components manufactured using the original Saertex fabric. Images of the two infused fabrics are shown in Figure 4.25.

Testing the failure properties of the hemisphere components has involved quasi-static loading using a rigid steel hemisphere, ∅=50mm, applied to the centre of the specimen at 1mm/minute to a total depth of 60mm. This test setup is shown in Figure 4.26, together with a view of the specimen after testing. Two tests are performed to check repeatability. An Instron 5500 machine with a 5kN load-cell has been used for this test.

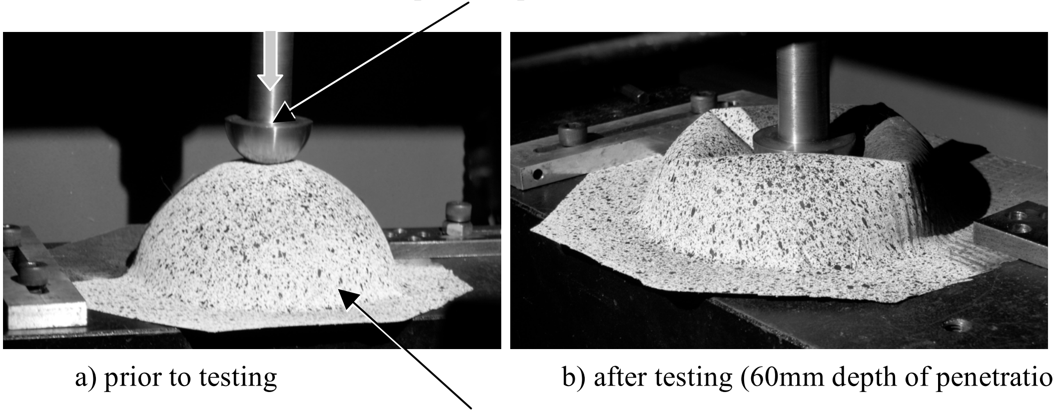

a) prior to testing b) after testing (60mm depth of penetration)

Figure 4.26. Quasi-static failure testing of the composite hemisphere components

Continuous loading of the hemisphere produces local buckling and development of four folds that grow outward in a cruciform pattern and are aligned to the fibre directions, as shown in Figure 4.27. Bending stress-related fibre breakage occurs at the tips of the cruciform fold pattern where compressive stresses are concentrated, as shown in Figure 4.27b. Furthermore, the failure path follows the resin rich areas between tows which, for the low quality fabric, corresponds to the closest fabric defect to the fold pattern.

The axial impactor load, measured by the load-cell of the compression test machine, shows reasonable repeatability from two impact tests of the low quality fabric, as shown in Figure 4.28; the small variation in load is attributed to differences of defect size and location in this fabric. A significant load increase of approximately 250% is produced by the hemisphere manufactured from the high quality fabric, despite being manufactured with an equivalent fabric architecture and fibre weight. To reiterate, the predicted deformation force of hemisphere failure simulations is expected to most closely correlate to the measured load obtained with this high quality fabric, since fabric defects are not treated using the current mesoscopic fabric model.

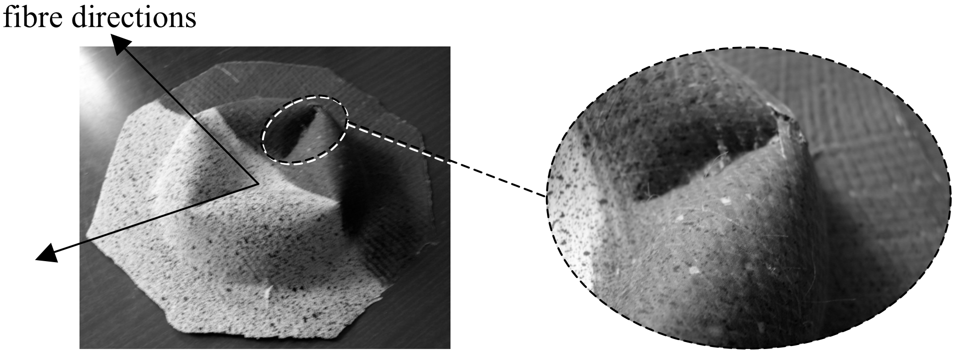

a) the impacted hemisphere

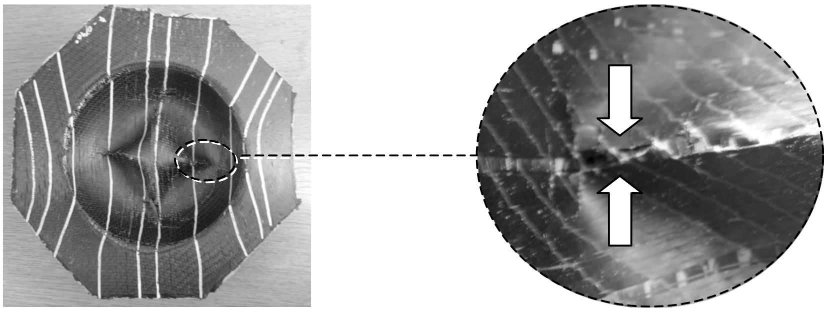

visible fibre direction
indicated by white lines

local compression failure
at areas of buckling

b) under-side of the impacted hemisphere

Figure 4.27. Images of the failed hemisphere componenents; sample manufactured using the lower quality Saertex fabric

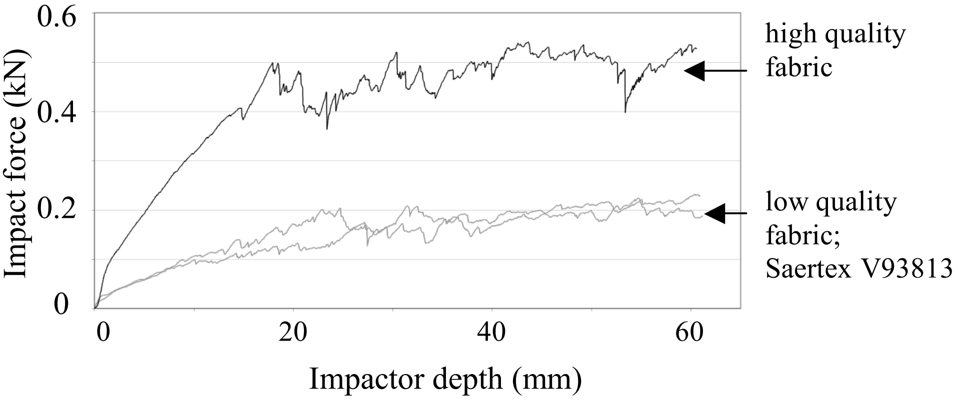

Figure 4.28. Axially measured loading force from the crushing of single ply hemispheres

4.1.9. Composite Material Data

The mechanical properties of the fibre and matrix material have been obtained from manufacturers datasheets, as provided in Table 4.5 (N.B. resin properties are provided in the datasheet as a range and, therefore, average values have been used here).

Fibre properties (Toray T700 [147])		Resin Matrix Properties (Araldite LY3505/XB3404 [146])	
Density, ρ^f	1.8 g/cm^3	Mix ratio (parts by weight)	LY3505 (100) XB3404 (35)
Longitudinal elastic modulus, E^f_{11}	210 GPa	Constituent densities	LY3505 – 1.18 g/cm^3 XB3404 – 0.98 g/cm^3
Tensile Strength, σ^f_u	4,900 MPa	Mixed density, ρ^m	1.13 g/cm^3
Strain at failure, ε^f_u	2.1%	Elastic modulus, E^m_{ij}	3.55 GPa
		Tensile strength, σ^m_1	84 Mpa
		Strain at tensile strength, ε^m_1	4.2%
		Ultimate Strength, σ^m_u	75.5 MPa
		Ultimate strain, ε^m_u	5.5 MPa

Table 4.5. Mechanical properties of the resin and fibre; obtained from manufacturers datasheets [146][147]

The additional material properties required have been obtained from literature [95] and are presented in Table 4.6.

Fibre properties (Generic carbon fibre)		Resin Matrix Properties (Generic epoxy)	
Transverse elastic modulus, E^f_{22}	22 GPa	Poisson's Ratio, ν^m_{ij}	0.3
Poisson's Ratio, ν^f_{12}	0.3		
Poisson's Ratio, $\nu^f_{23} = \nu^f_{13}$	0.35		

Table 4.6. Additional mechanical properties of the resin and fibre; obtained from [95]

The modelled fibre properties contribute to the mechanical properties of the composite in the fibre direction only, as defined previously in equation 24. Therefore, the mechanical properties of the modelled 'matrix' include contributions from the resin *and fibre* in the remaining transverse directions. Classical laminate analysis has been used to obtain the required transverse ply properties, but first requires the fibre volume fraction of the part to be a known quantity.

An average fibre volume fraction, V^f, of the hemisphere component has been calculated using the following rule of mixtures equation,

$$V_f = \frac{m_f}{\rho_f\left(\frac{m_f}{\rho_f} + \frac{m_c - m_f}{\rho_m}\right)}, \qquad \text{and,} \quad V_m = 1 - V_f, \qquad \text{Eq. (36)}$$

where, m and ρ are the mass and density, V is the constituent volume fraction and c, f and m denote the composite, fibre and matrix, respectively. This equation requires values of mass for the final composite component and the equivalent fabric within the composite part. The component mass has been obtained from the infused component with excess material removed, as shown in Figure 4.29, while the fabric mass within this hemisphere has been measured from a preform with excess material removed, as shown schematically in Figure 4.30. The resulting fabric mass is 9.6g and the component mass is 15.9g. Equation 36 is used in conjunction with these values of mass and fibre and resin density, provided in Table 4.5, to determine an average fibre volume fraction of 49% in the hemisphere component.

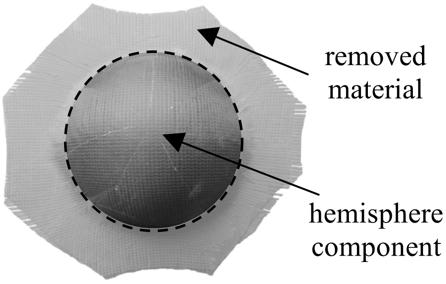

Figure 4.29. The hemisphere component; required for calculating fibre volume fraction

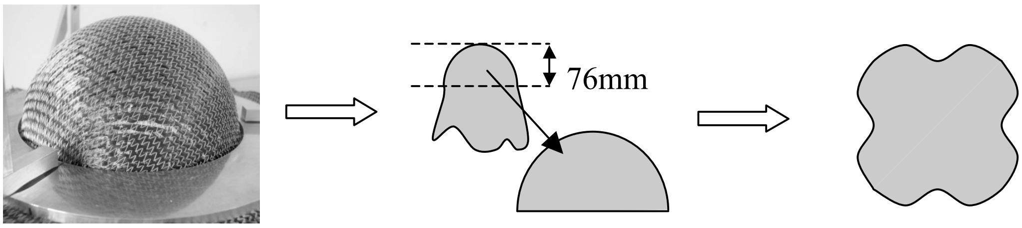

a) fabric preforming b) removal of unwanted fabric c) the hemisphere fabric sample

Figure 4.30. Methodology of obtaining the fabric hemisphere preform; required here to determine fibre volume fraction of infused components

Using the fibre/resin data presented in Table 4.6 and Table 4.5, the longitudinal and transverse elastic moduli of a unidirectional ply has been determined, using equations 37 and 38 respectively, with which, E_{11}^{UD} = 104.7 GPa and E_{22}^{UD} = 6.0 GPa.

$$E_{11}^{UD} = V^f.E_{11}^f + V^m.E_{11}^m. \qquad \text{Eq. (37)}$$

$$\frac{1}{E_{22}^{UD}} = \frac{V^f}{E_{22}^f} + \frac{V^m}{E_{22}^m}. \qquad \text{Eq. (38)}$$

The shear modulus of a unidirectional carbon fibre/epoxy matrix ply (V_f = 50%) has been obtained from the literature [95], $G_{ij}^{UD} = G_{ij}^{m}$ = 3.3GPa. The major and minor Poisson's ratios of the composite have been calculated using equations 39 and 40 based upon the Poisson ratio's of the individual constituents. Using these equations; ν_{1j}^{UD} = 0.3 and ν_{23}^{UD} = 0.33.

$$\nu_{1j}^{UD} = \nu_{1j}^f.V^f + \nu_{1j}^m.V^m. \qquad \text{Eq. (39)}$$

$$\nu_{23}^{UD} = \nu_{23}^{f}.V^{f} + \nu_{23}^{m}.V^{m}.$$ Eq. (40)

These results complete the mechanical data required for treating tensile loading in the constitutive composite model, as summarised in Table 4.7.

Damage due to loading is treated in the bi-phase constitutive model by a reduction of elastic modulus, based upon the effective shear strain in the material. Damage is modelled independently in the resin and fibres, however, fibre stiffness and damage only contribute to the material properties in the fibre direction. Consequently, damage transverse to the fibre direction is assumed to occur by matrix failure mechanisms, which is a reasonable approximation of what occurs in practice.

Elastic material properties as applied to the composite bi-phase material model *Properties of the unidirectional ply 'UD'* *are applied to the modelled 'matrix' 'm' as indicated*			
Fibre elastic modulus, E^{f}_{11}	210 GPa *	Resin longitudinal elastic modulus, E^{m}_{11}	3.55 GPa *
Fibre volume fraction, V^{f}	49% ***	Transverse elastic modulus, $E_{22}^{UD} = E_{33}^{UD} = E^{m}_{22} = E^{m}_{33}$	6.0 GPa ***
		Poisson's ratio, $\nu^{f}_{12} = \nu^{f}_{13}$	0.3 ***
		Poisson's ratio, ν^{f}_{23}	0.33 ***
		Shear Modulus, $G_{ij}^{UD} = G_{ij}^{m}$	3.3 GPa **

Table 4.7. Summary of the composite elastic material properties; (*) from datasheets [146][147]; (**) estimated from literature [95]; (***) determined using datasheet/assumed properties

The maximum and ultimate stress of the resin matrix are provided in Table 4.5, while the corresponding effective shear strains, used for modelling damage and failure, are calculated using the steps shown in Table 4.8. To summarise these steps; the values of strain obtained from the manufacturers datasheets are factored to account for the volume of fibres in the UD ply. The respective fibre strains at the maximum and ultimate stress have been added, assuming constant stress in the fibres and matrix, as determined using equation 41. The effective shear strains have subsequently been calculated, using equation 28.

$$\frac{\sigma^m_{1/u}}{E^f} = \varepsilon^f . \qquad \text{Eq. (41)}$$

The responses of composites differ if loaded in tension or compression. Here, the elastic properties are considered symmetric, but the damage is not; the effective shear strains in compression are factored to 60% of the tensile properties; this factor is consistent with typical tensile and compressive test results of unidirectional carbon composites [95]. Complete longitudinal and transverse load curves of the modelled tows are shown in Figure 4.31.

The values of elastic modulus damage, d, which correspond to the calculated effective shear strains, are calibrated using simulations presented in section 4.2.8, but are presented in Table 4.8 and Table 4.9 for completeness. The effective shear strains and corresponding scalar damage factors are the required input parameters for the tow material model.

Calculation steps used to obtain the effective shear strains required for damage modelling in the tow material model	Strain value at maximum stress (σ_1^m = 84 MPa)	Strain value at ultimate stress (σ_u^m = 75.5 MPa)
Original strain values, ε^m (from datasheet [146])	0.042 (4.2%)	0.055 (5.5%)
Factor resin failure strains to 51% due to fibre volume fraction	0.021	0.028
Assuming constant stress, add fibre strain, calculated using equation 41	0.024	0.031
Results	*Tow model damage parameters*	
Calculate effective shear strains, ε^t_s, for **tensile** loading, using equation 28	0.019	0.022
Multiply tensile effective shear strain by 60% for **compressive** effective shear strains, ε^c_s,	0.011	0.014
Corresponding values of damage	d_l	d_u
Scalar damage factor, d	0.58	0.99

Table 4.8. Calculation steps to obtain the effective shear strains used to model matrix damage

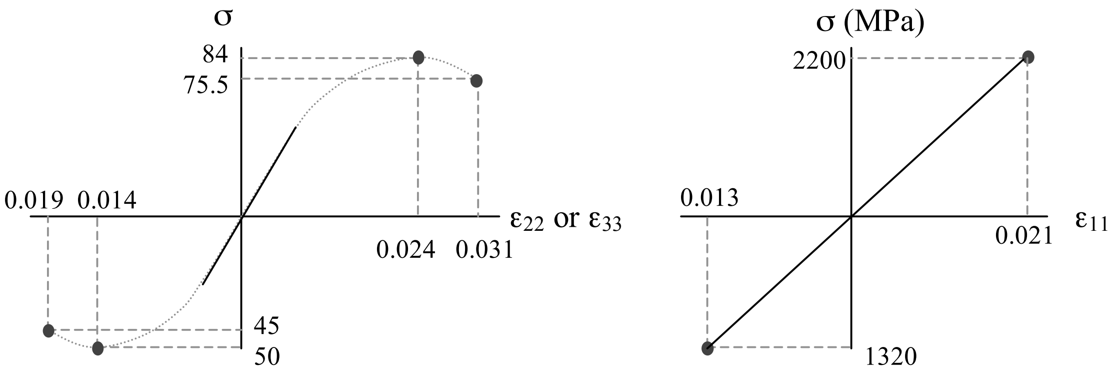

a) transverse matrix dominated failure b) longitudinal brittle fibre failure

Figure 4.31. Schematic load curves of the unidirectional composite mechanical properties

Figure 4.31 shows that in transverse loading the fibre tows undergo significant damage prior to failure, which is in contrast to the high stress brittle failure of fibres when loaded axially. Here, brittle failure is modelled by using high intermediate damage values, d_1, and negligible differences between the intermediate, $\varepsilon_{s,1}$, and ultimate effective shear strains, $\varepsilon_{s,u}$, as shown in Table 4.9.

Material property	Strain, 1	Strain, ultimate
Fibre strain at failure, ε^f (from datasheet [147])	0.021 (2.1%)	
Effective **tensile** shear strain, ε^t_s, calculated using equation 28	0.016	0.0163
Multiply tensile effective shear strain by 60% for **compressive** effective shear strains, ε^c_s,	0.0095	0.0098
Corresponding values of damage	d_1	d_u
Scalar damage factor, d	0.99	0.999

Table 4.9. Calculation of the effective shear strains used to model fibre damage

4.2. NUMERICAL FABRIC SIMULATION PROCEDURES AND RESULTS

The following section presents the simulation methods, and results, used here to confirm and calibrate the input data of the constitutive material models.

It should be noted that for all simulations the rate of loading is significantly faster than the experimental procedures described in section 4.1; this is necessary to reduce the computation time and is standard practice when using an explicit Finite Element code.

4.2.1. Dimensions of the Modelled Fabric Geometry

The dimensions of the modelled tows and tricot stitching are defined with respect to the measured dimensions of the stitch unit-cell, described in section 4.1.1. The dimensions of the modelled tow element, stitch unit-cell and tow separation are shown in Figure 4.33. The stitch unit-cell dimensions used are the closest match possible to the measured dimensions, to the nearest 0.01mm that satisfy the requirement for a consistent tow width and ±45° fibre angle. Manually generating the mesh of this detailed model is overly time-consuming using current Finite Element Pre-processors and, therefore, would be unsuitable for industrial applications. Here, a simple program has been produced in FORTRAN programming language, which is capable of producing a square fabric model from inputs of the fabric specimen size, as shown schematically in Figure 4.32.

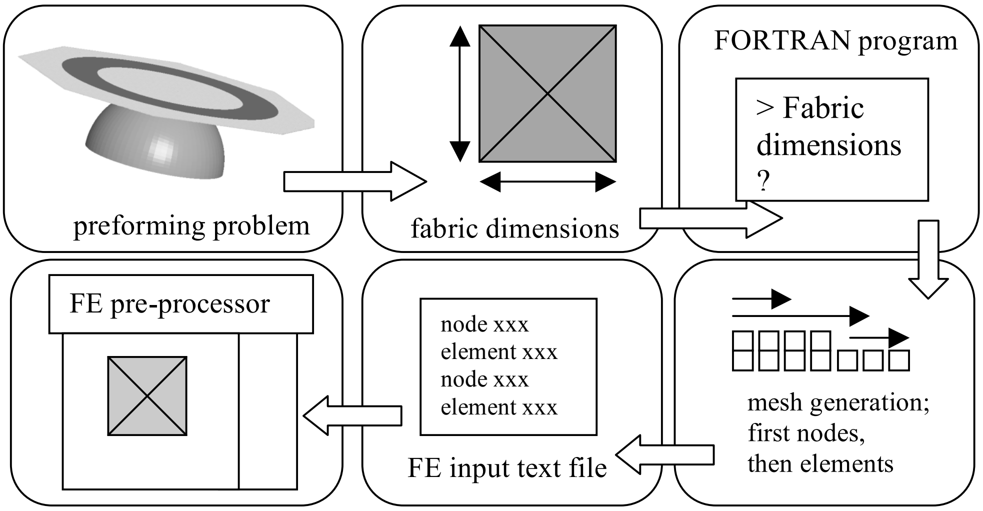

Figure 4.32. Schematic of the programming process used to generate un-deformed fabric meshes

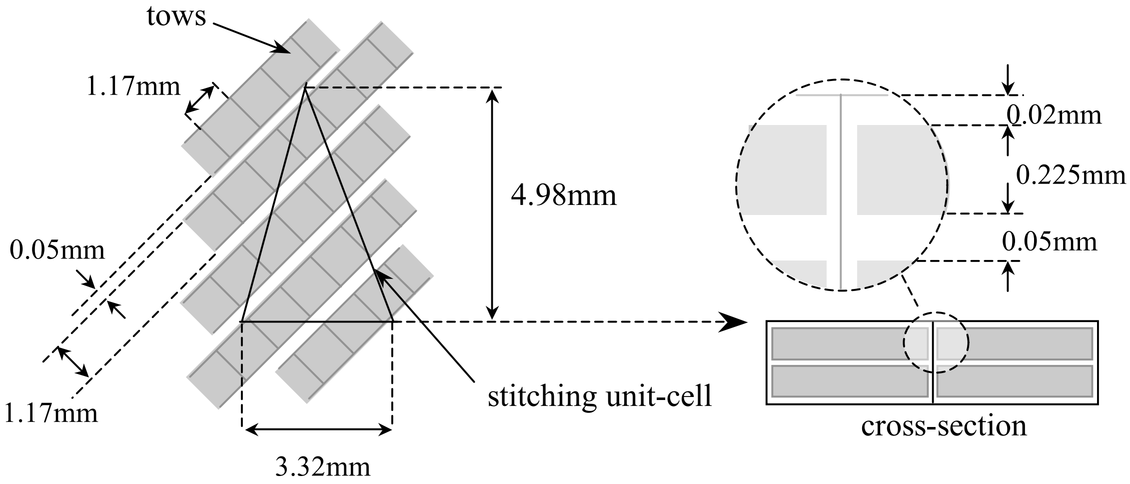

Figure 4.33. Geometrical specification of the modelled tows and stitching

The total thickness of the two tow element layers is equal to the measured fabric thickness at 0° shear angle, t_0 = 0.45mm. The through-thickness stitch elements are located centrally within the 0.05mm separation gap between tow elements.

4.2.2. Modelling of Transverse Tow and Stitch Stiffness using Picture Frame Test Results

The following section describes the calibration simulations that make use of material data obtained with experimental picture frame tests; this includes shearing simulations of a representative area of modelled tows, which is used here to calibrate tow compaction stiffness, and calculation of the force response of the bar elements used to approximate stitching threads.

Shear modelling of a representative tow area

The simulation setup used to shear a representative tow area is shown in Figure 4.34. A simple supporting frame made of beam elements has been used to induce pure shear deformation in the modelled tows, as shown schematically by Figure 4.34c. Individual edges of the frame are pin-jointed using coincident nodes to permit free rotation and thus approximate the bearings of the experimental frame, as shown by Figure 4.34b.

Experimental observations of fabric deformation have shown intra-tow shear is minimal during picture frame shear testing. This deformation is replicated in the simulation using a series of FE boundary conditions and constraints. Firstly, the end of each modelled solid tow is linked to a shell element using a sliding contact algorithm (PAM-CRASH contact no.1) that prevents both inter-penetration and separation. Each of these shell elements is rigid and able to rotate independently about the frame by tying a central coincident node to that of the frame beam element, as shown in Figure 4.34a. Each pair of tied nodes act as a pin-joint. These constraints ensure that tows remain within the frame during shearing and permit the entire length of the modelled tow to deform with free end rotation, which occurs in practice.

Additional shell elements are rigidly tied to the length of the beam elements that constitute the frame, as shown by Figure 4.34d. These shell elements represent boundary conditions for the representative cell model and approximate the loading of adjacent tows outside this region.

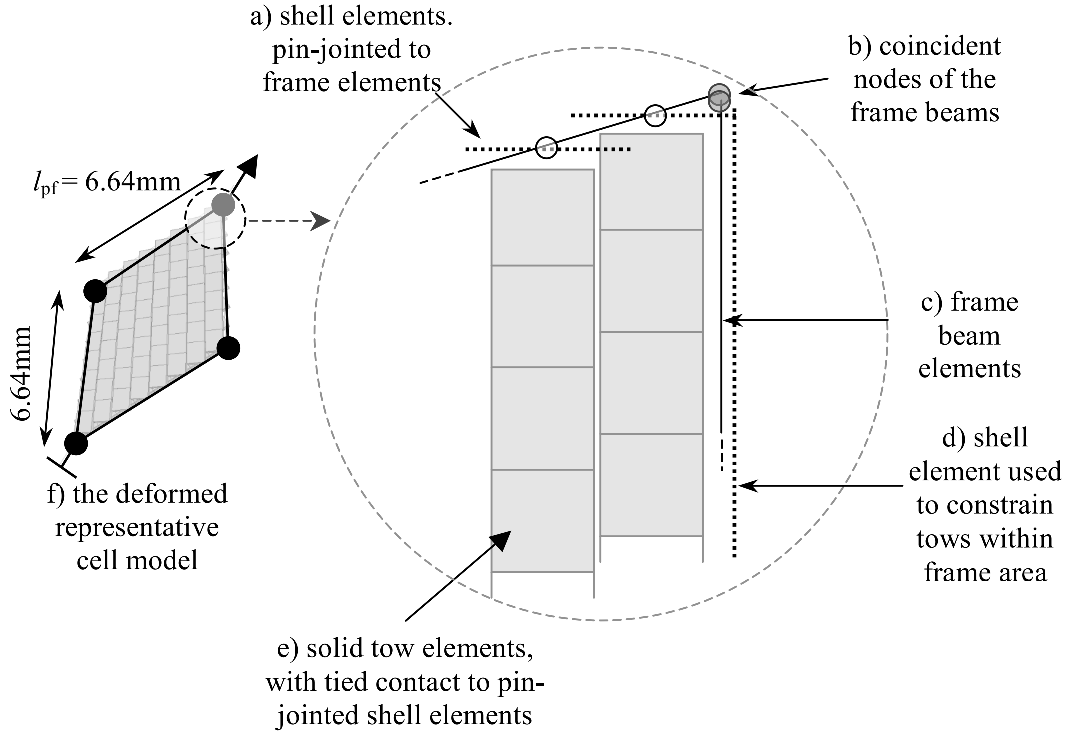

Figure 4.34. Simulated shearing of a representative tow area that is used to calibrate tow compaction stiffness

Shear deformation is produced in the representative tow cell by fixing the nodes at one frame corner and axially displacing the nodes of the diametrically opposite corner nodes at a velocity of 0.1ms^{-1}, shown by Figure 4.34f. The reaction force required at the support nodes is recorded and normalised with respect to the unit-cell edge length, (l_{pf}). The transverse tow stiffness, E^{m}_{22}, has been calibrated so that the normalised axial force of the simulation approximates the similarly normalised experimental picture frame test data. These results are presented in Figure 4.35, which plots normalised axial force versus the shear angle for the respective experimental and simulated picture frames, calculated using equation 3.

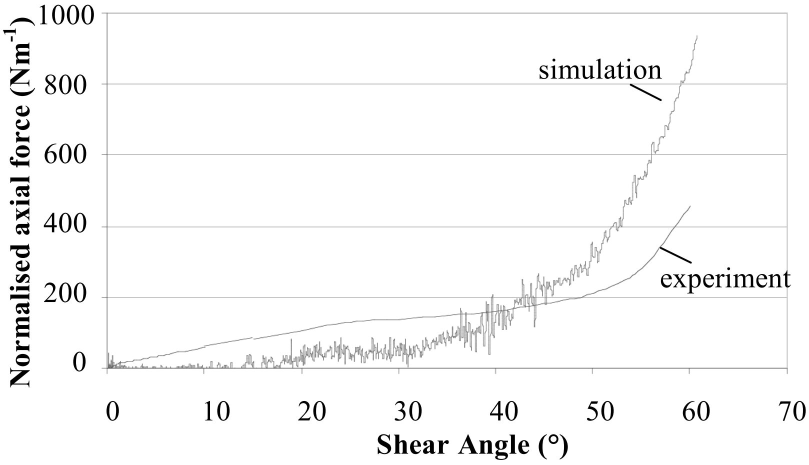

Figure 4.35. Simulation results of a representative tow-cell used to calibrate transverse tow compaction

As shown by the simulated axial force of Figure 4.35, the linear compaction stiffness of the numerical tow model is not ideal to reproduce the experimental compaction response, therefore a best-fit approach has been used and corresponds to an E^m_{22} of 700Pa.

Calculation of stitching force response using picture frame test data

The modelled stitching is used to constrain tows and contribute to the global shear resistance of the modelled NCF. As previously shown in section 3.4.3, this fabric shear resistance has been determined using experimental picture frame test results; the measured axial force obtained from samples with stitching removed has been deducted from the measured axial force obtained from complete samples, as previously shown in Figure 3.13.

The calculated stitch resistance, F_{stitch} is normalised to the number of stitch elements under tensile loading in the picture frame width, using equation 40, since these effectively deform as parallel springs. The fabric dimensions used in this calculation are shown schematically in Figure 4.38,

$$F_{stitch} = \frac{F_c . l_{uc}}{W_{pf}}, \tag{42}$$

where, F_{stitch} is the contribution of axial force from the stitching component; F_c is the determined force contribution of the stitching (during either positive or negative shear); l_{uc} is the characteristic width of the stitch unit-cell and W_{pf} is the width of the central deformation area of the tested cruciform picture frame sample.

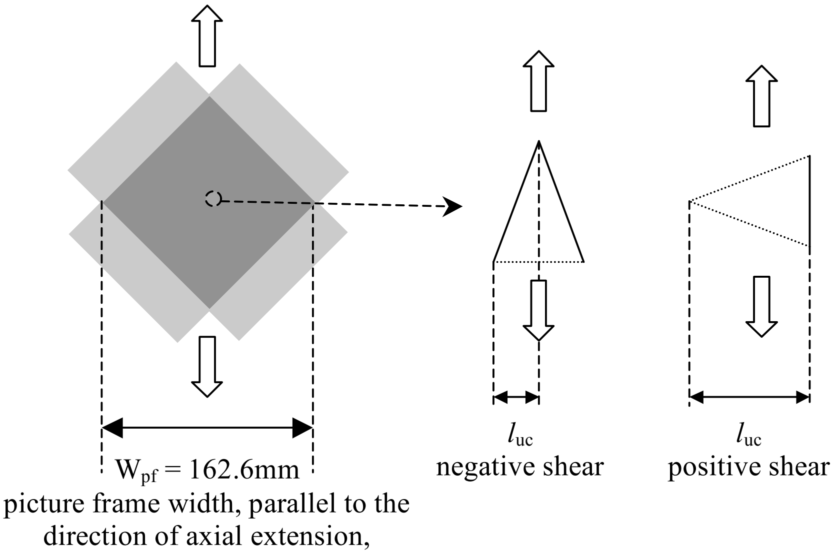

Figure 4.36. Schematic drawing of stitch and picture frame specimen dimensions required to calculate the stitch element force response

This stitch element force response, F_{stitch}, is correlated to an inter-fibre shear angle, ϕ, calculated using equation 3, which is based upon pure shear kinematics of the picture frame test. This force response can then been correlated to a tensile engineering strain of the stitch segment, using the following equations, and input into the constitutive stitch model.

$$e_d = \frac{d(\phi) - d(0)}{d(0)}, \tag{43}$$

$$e_c = \frac{c(\phi) - c(0)}{c(0)}, \tag{44}$$

where, d and c are characteristic lengths of the tricot stitch shown previously in Figure 2.21, e is the stitch engineering strain, ϕ is the inter-fibre shear angle and $c(\phi)$ and $d(\phi)$ are determined using equations 11 and 12, respectively.

4.2.3. Tow Flexural Rigidity Calibration Simulation Procedure

Direct simulation of the tow flexural rigidity test has been used to calibrate the axial tow stiffness, E^{tow}_{11} and shear stiffness, G_{ij}, of the bi-phase tow material model. The simulation involves applying gravitational acceleration, $9.81 ms^{-2}$, to a length of tow equal to the experimentally measured overhang length, L_b, as shown in Figure 4.37. The overhanging tow length deflects due to the mass of the tow.

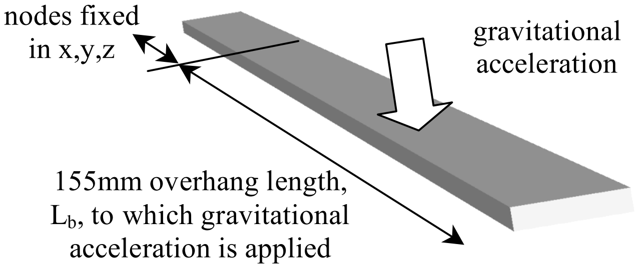

Figure 4.37. Simulation of the tow flexure test

Numerical viscous damping is applied to the tow elements to obtain a steady state of tow deflection. The axial tow stiffness, E^{tow}_{11}, has been varied until the angle between the horizontal and inclined plane, to which the tow deflects, is equal to the required 41.5° defined in the experimental method, Figure 4.38. Linear elastic bending theory has been used to obtain a first approximation of the correct axial stiffness, as provided in the appendix. The shear moduli, G_{ij}, have been calculated using a linear elastic relation to the calibrated axial tow elastic modulus, since this proves suitable to minimise intra-tow shear during forming. As shown in Figure 4.38, the calibrated axial stiffness and shear moduli are; $E^{tow}_{11} = 0.068GPa$ and $G_{ij} = 0.027GPa$.

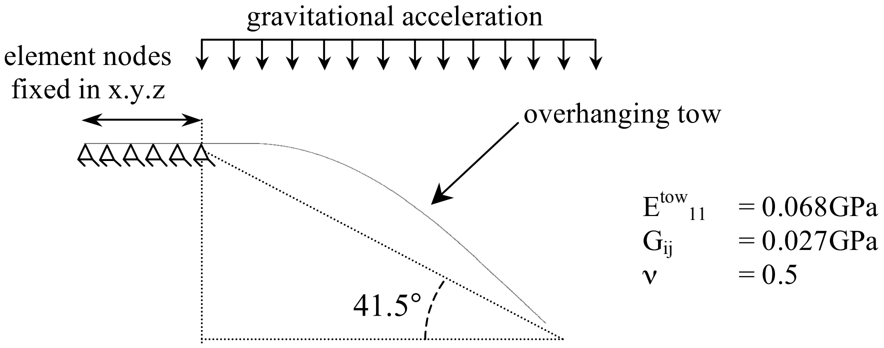

Figure 4.38. Simulation of the tow flexure test; boundary conditions, calibration and results

4.2.4. Tow Pull-out Simulation Procedure

The force response of each bar element which link tow and stitch elements has been determined using results of the experimental tow pull-out test. The measured force per unit area has been distributed equally amongst the link elements within the unit area. Direct simulation of the tow pull-out test has, consequently, been used to validate the force response of the linking elements, as shown in Figure 4.39. The dimensions of the simulated test coupon are identical to the experimental method.

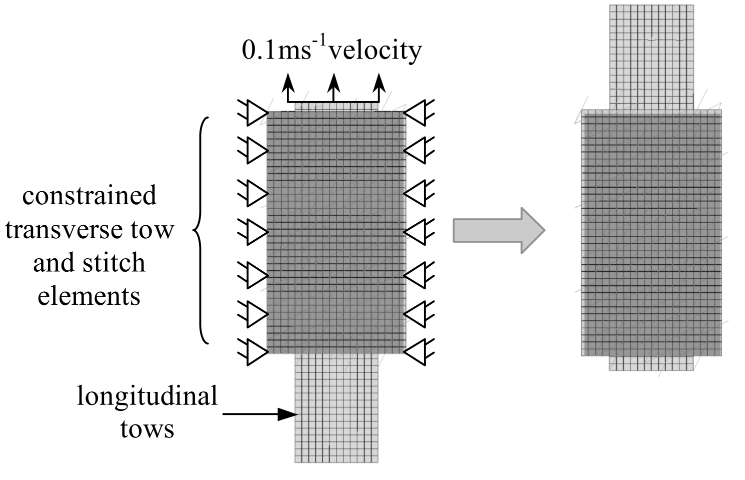

a) pull-out model *(initial state)*

b) pull-out model *(final state)*

Figure 4.39. The tow pull-out simulation model; mesh and boundary conditions

Longitudinal tows have been pulled at a velocity of 0.1ms^{-1}. All nodes of the modelled transverse tows and stitching are constrained in x,y,z to prevent all displacements and, therefore, duplicate the experimental test conditions. The reaction force required to maintain this boundary condition has been recorded and normalised with respect to the 2,880mm^2 contact area between pulled and transverse tows. These results are presented in Figure 4.40, in conjunction with experimental results. As shown by this graph, the simulation and mean averaged experimental results correlate exactly.

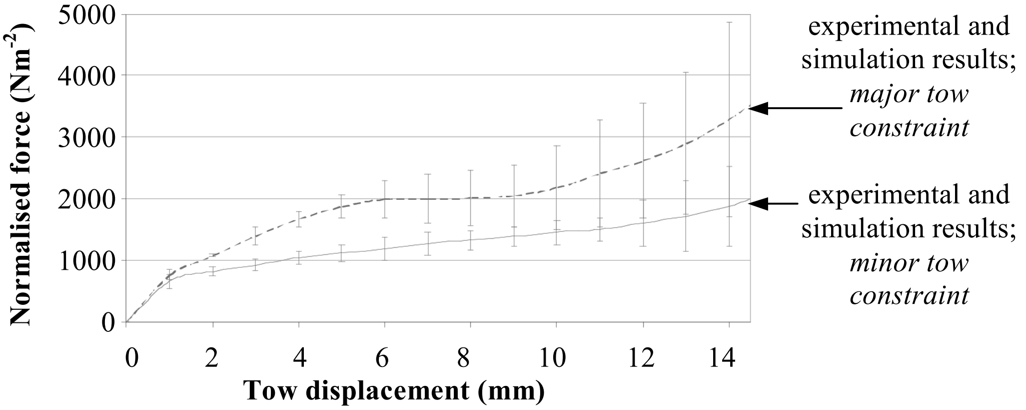

Figure 4.40. Simulated and experimental pull-out test results; simulation results correlate exactly; experimental data include error bars based on analysis of three tests

4.2.5. Treatment of Fabric Constituent and Tooling Contact

Contact between individual tows, stitch segments and the process tooling is treated using appropriate contact algorithms. Two algorithms are used in the present work; a master/slave algorithm (PAM-CRASH contact type 33) and a self-penetrating algorithm (PAM-CRASH contact type 36).

The master/slave contact algorithm prevents penetration of adjacent elements by declaring one object (the master surface) to be impenetrable by the other (the slave surface). This contact algorithm is used for the tow-to-tow and tow-to-tooling interfaces. This symmetric contact acts by checking for penetrations of nodes from each surface within a specified contact distance, h_{cont}, from the other surface [90]. Contact is prevented through the addition of a temporary external force, F_c, to the penetrated slave nodes within the explicit solution scheme, equation 18. This external force acts normal to the master segment and is determined based upon the nodal mass and stable FE time step [90]. In the current work this contact force increases non-linearly by a factor of 10 with respect to the depth of penetration, δ, Figure 4.41. Friction is treated using the

Coulomb friction model, defined by equation 10. The resistance to (sliding) friction force acts parallel to the master segment surface and is equal to the normal penetration force multiplied by the friction coefficient.

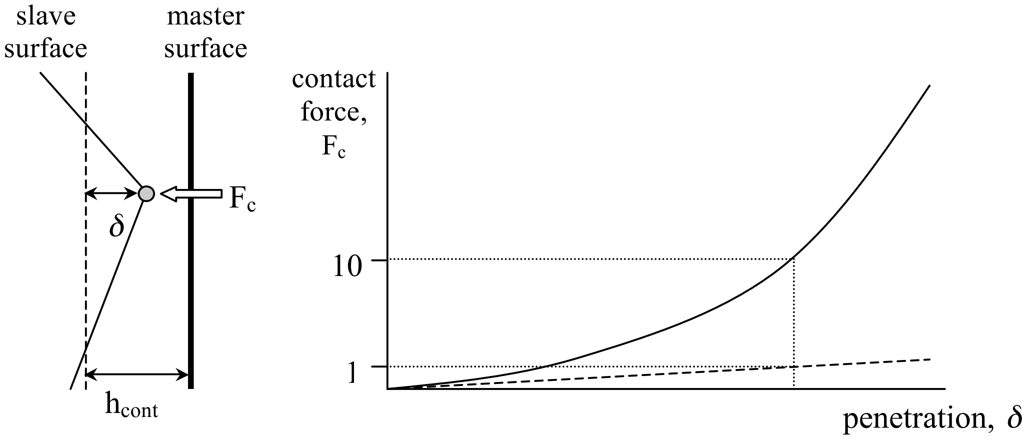

Figure 4.41. Contact treatment using the explicit finite element modelling technique

Stitch-to-tow and stitch-to-tooling contacts are treated using the self-penetrating algorithm. This is similar to the master/slave algorithm, as shown in Figure 4.41, but requires definition of a slave surface only. Each node/edge is checked for penetration to all other the segments/edges of the remaining slave elements. The treatment of friction has not been used for stitch-to-tow contact because additional bar elements, linking stitch elements to tow elements, account for this friction. Also, the modelled stitch-to-tooling contact is frictionless since the experimentally measured *fabric*-to-tooling friction coefficient includes friction contributions from both the stitches and tows.

4.2.6. Validation Simulation Procedure: Bias Extension Simulation

The bias extension test provides a simple, yet challenging test to evaluate the proposed mesoscopic fabric model due to the wide range of deformation mechanisms that occur. This validation study involves direct simulation of the test, using a 250mm by 100mm coupon of biaxial NCF, loaded axially with fibres in ±45° directions. Both positive and negative sheared coupons have been simulated. Images of the deformed coupon have been shown in Figure 4.17 (negative shear load case), which illustrate the different deformation zones that occur that must be captured by the mesoscopic NCF model.

The FE mesh, together with loading and boundary conditions used to replicate the test coupon are shown in Figure 4.42. A total of 36,000 solid and 21,000 bar elements are used to model the tows and stitching respectively. The simulation takes 30 hours to achieve a coupon strain of 28% using a twin, 2.2GHz Opteron™ processor computer.

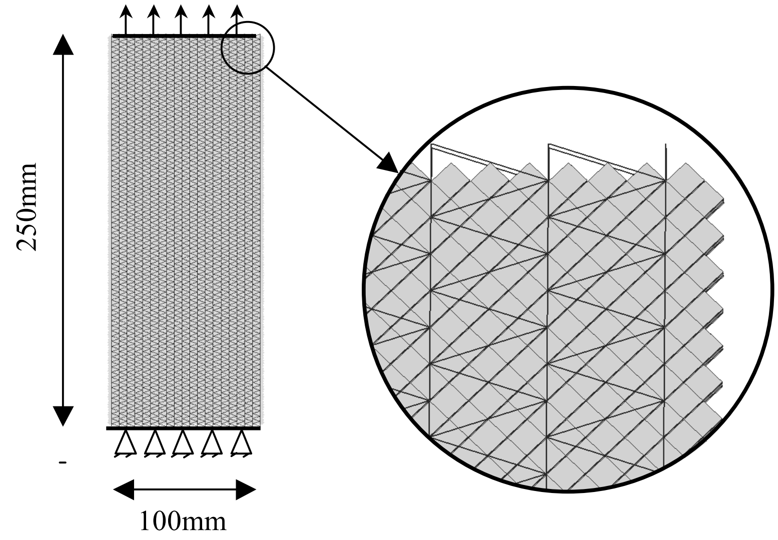

Figure 4.42. The bias extension simulation model: mesh, dimensions, boundary conditions and loading for the positive shear case

The velocity of axial extension applied to the simulated coupon is shown in Figure 4.43; an initial period of acceleration helps to minimise inertial effects from affecting the simulated fabric deformations and measured axial force. This axial deformation force is measured here as a support reaction of all the constrained nodes at the coupon base.

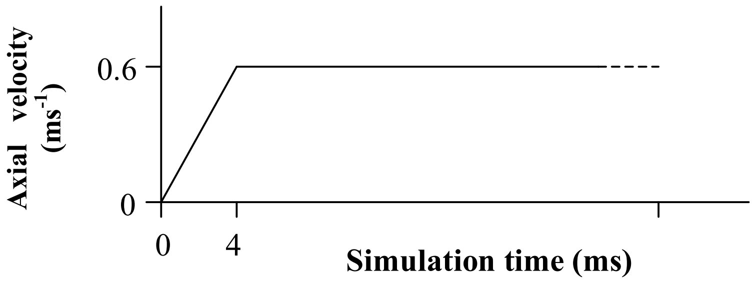

Figure 4.43. Axial displacement velocity curve of the simulated bias extension test

Figure 4.44 compares the inter-fibre shear angle measurements of bias extension simulations, showing results from the experiment, simulation and analytical kinematic model, for both positive and negative shear load cases. The kinematic model is based upon a pure shear deformation of the test coupon, using equation 3, and over-predicts the inter-fibre shear angle since tow slip deformation mechanisms, which occur in practice and comparatively relax the inter-tow shear angle, are not treated. Furthermore, the analytical kinematic model incorrectly gives identical results for both shear cases, since the method does not consider material behaviour as is based on geometrical considerations only. In comparison to the kinematic model, the mesoscopic model shows better agreement to test results. This is most significant at higher coupon strains as limits of tow compaction are reached, causing the inter-fibre shear angle to become effectively ‘locked’ and alternative slip deformation mechanisms dominate.

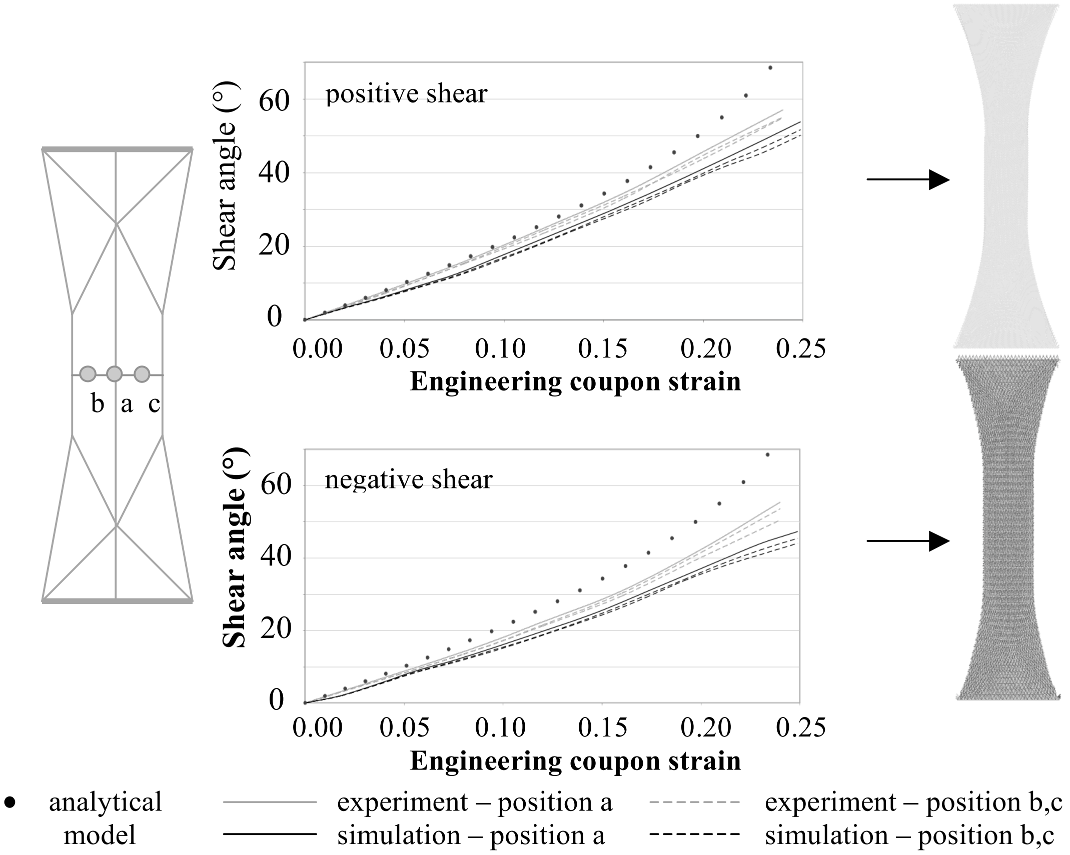

Figure 4.44. Comparison of the central inter-fibre angle of bias extension coupons for positive and negative shear; showing test, simulation and analytical prediction results and images at 25% axial coupon strain

Figure 4.45 compares the measured axial force of bias extension simulations and tests. The simulation under-predicts the axial force required to deform the fabric coupon in both positive and negative shear load cases. For this reason an alternative approach of calculating the stiffness of stitch elements has been investigated, as is described in the following paragraphs.

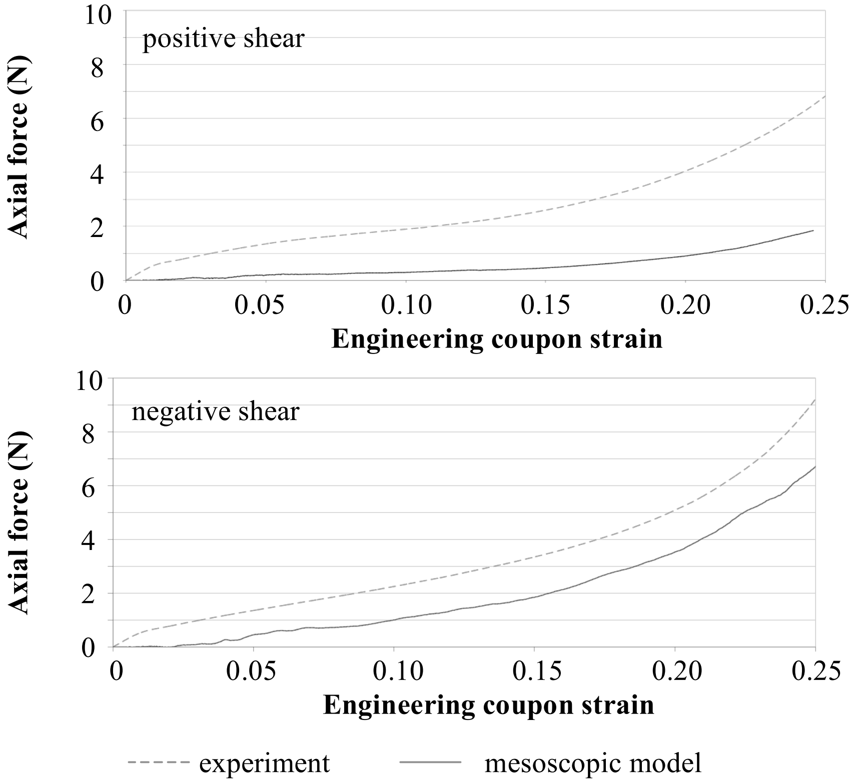

Figure 4.45. Comparison of the axial bias extension force from experimental tests and simulations

The shear resistance of a fabric, and any shear bias, contributes to the final fabric architecture of the preform and the force required to deform the fabric. Calibration of the tow and stitch constitutive material models using picture frame shear results has resulted in the under-prediction of the fabric shear resistance in the case of the bias extension simulations. This force is under-predicted because the bias extension test does not limit the fabric to pure shear deformation, which is, arguably, more representative of fabric deformation during practical preforming. This represents a significant limitation of the current material calibration strategy. Improving the correlation between test and simulated fabric shear resistance has been investigated by directly applying the bias extension axial force results to the stitch material model. The material data calculated in this way replaces the stitch material data determined from picture frame tests; the tow compaction data remains unchanged.

The force response of the modelled stitching has been calculated using a the same method as described in section 4.2.2, but substitutes the picture frame test data with bias extension test data. Consequently, the axial force of bias extension tests, F_A, has been distributed over the number of stitch elements under tension in the coupon width, (equal to, W_{be}/l_{uc}, where W_{be} is the width of the bias extension coupon and l_{uc} is the width of the unit cell in either positive or negative shear, as defined previously in Figure 4.36). The inter-fibre shear angle of the bias-extension test has been calculated using equation 3, which is based on the kinematic model presented previously in Figure 2.16, and then the corresponding stitch strains are calculated using equations 43 and 44. The stitch force response produced by calibration to bias extension data is shown in Figure 4.46 and is compared to the stitch force response that has been calibrated to picture frame data. The consequences of this calibration method are discussed further in chapter 5.

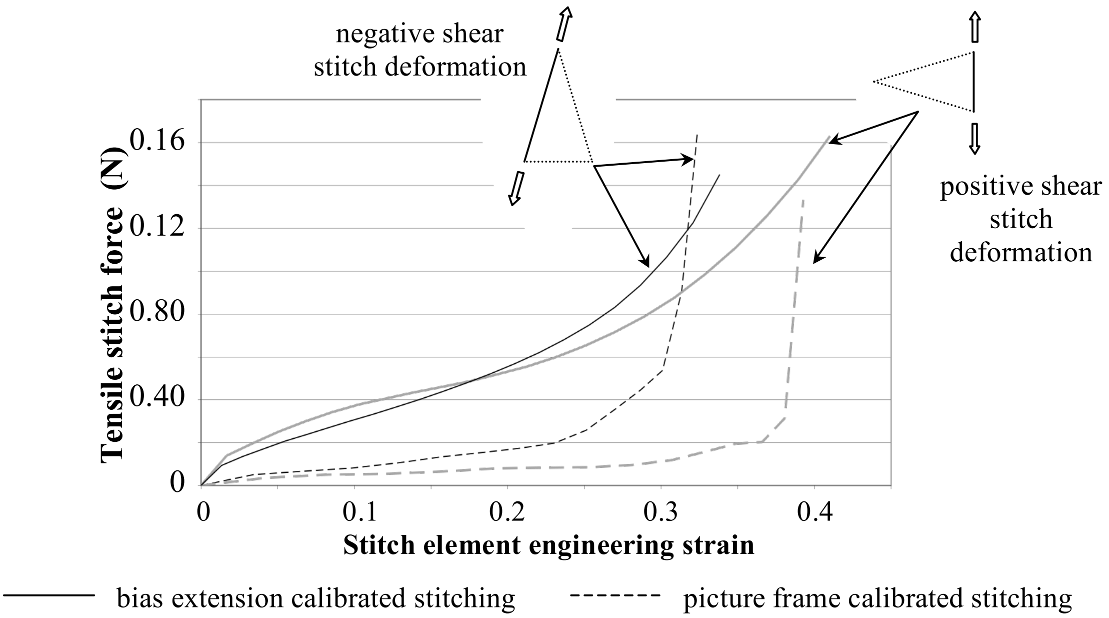

Figure 4.46. Simulated stitch element force response to loading

Calibrating stitch resistance to results of the bias extension test alters both the force required to deform the fabric and the distribution of inter-fibre shear, therefore, bias extension simulations have been repeated to investigate what influence the stitching resistance imparts on the fabric deformation. The axial force and inter-fibre shear angle measurements from these simulations are shown in Figure 4.47 and Figure 4.48 respectively; these figures compare experiment and simulation results, with stitch data calibrated using both the picture frame and bias extension test results. Bias extension simulations, with stitch data calibrated to bias extension test results, show a greatly improved correlation of axial force when compared with experimental results, but remain under-predicted for all shear angles tested and for both positive and negative shear.

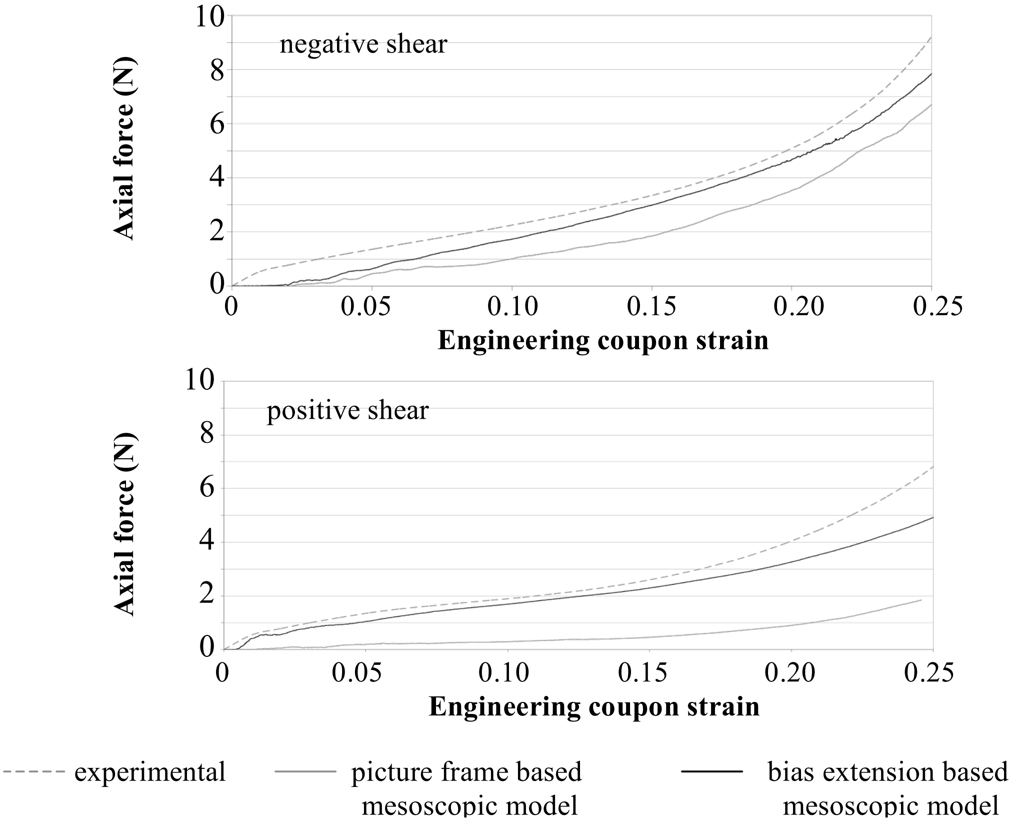

Figure 4.47. Comparison of bias extension axial forces for experiment and simulation, in both positive and negative shear load cases; simulation results shown for both picture frame and bias extension based stitch calibrations

Figure 4.48 shows the inter-fibre shear angle results of measurements across the central coupon plane for the fabric model using bias extension calibrated stitch data; this figure compares experiment, simulation and analytical model results for both positive and negative shear. The results show there is minimal difference of inter-fibre shear angle between the picture frame and bias extension calibrated stitch models during positive shear loading. However, the bias extension based model shows a reduced inter-fibre shear angle during negative shear loading due to the distribution of stitch tension over all stitch segments, as occurs in practice and has previously been shown Figure 4.17.

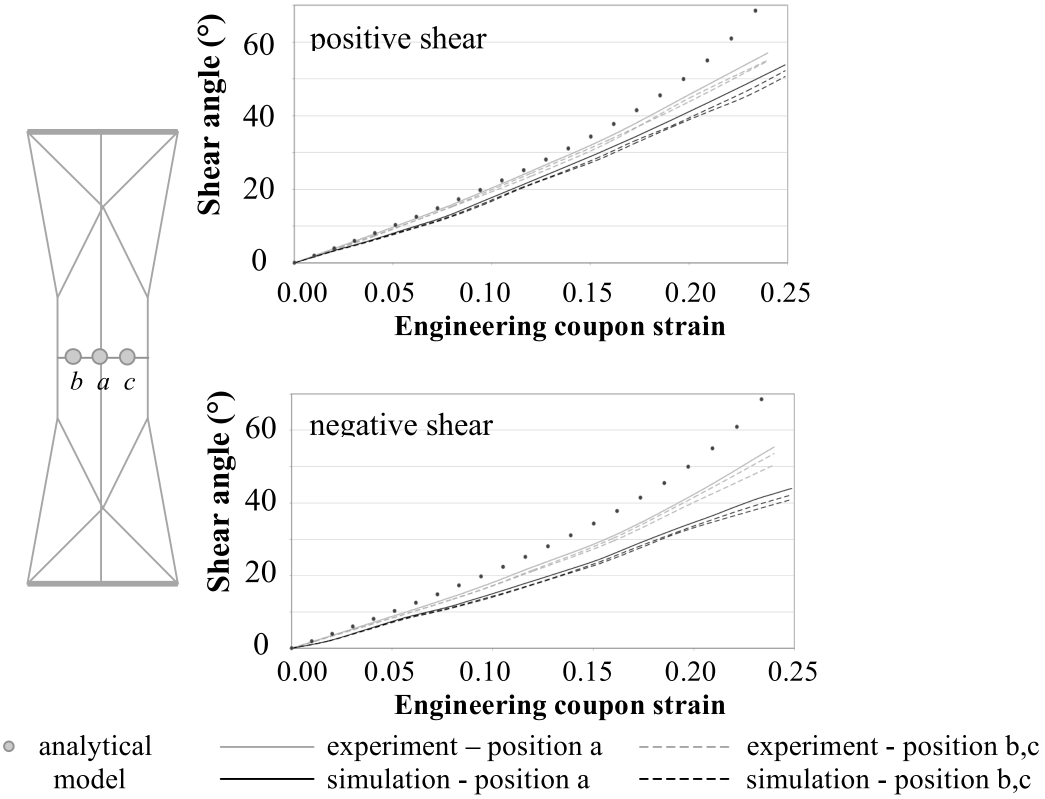

Figure 4.48. Comparison of bias extension central inter-fibre angle for positive and negative shear; test, simulation and analytical prediction; model based upon bias extension shear data

Regarding Figure 4.49 and Figure 4.50, the simulation shows a good agreement between the deformation mechanisms produced in the test coupon and the mesoscopic fabric model, for both positive and negative shear. The numerical model correctly predicts the three distinct deformation zones, identified from previous experimental tests in Figure 2.17, and inter-tow slip between clamped and un-clamped areas of the fabric.

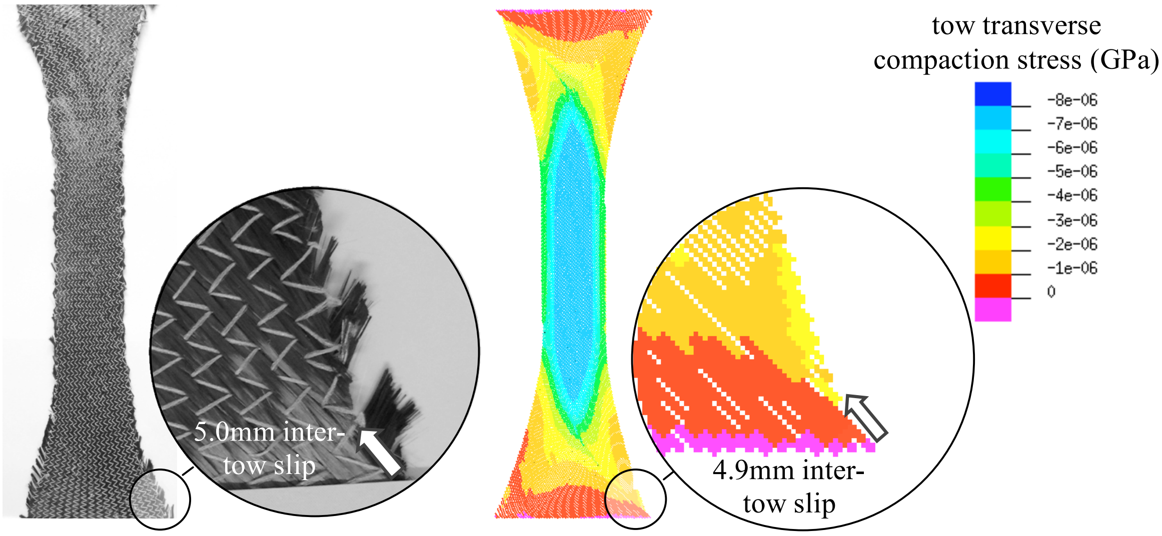

a) bias extension test b) bias extension simulation

(direction of inter-tow slip shown by solid white arrows)

Figure 4.49. Comparisons of global and local deformations for the test and simulated bias extension coupons (positive shear case, loaded to 28% axial engineering strain)

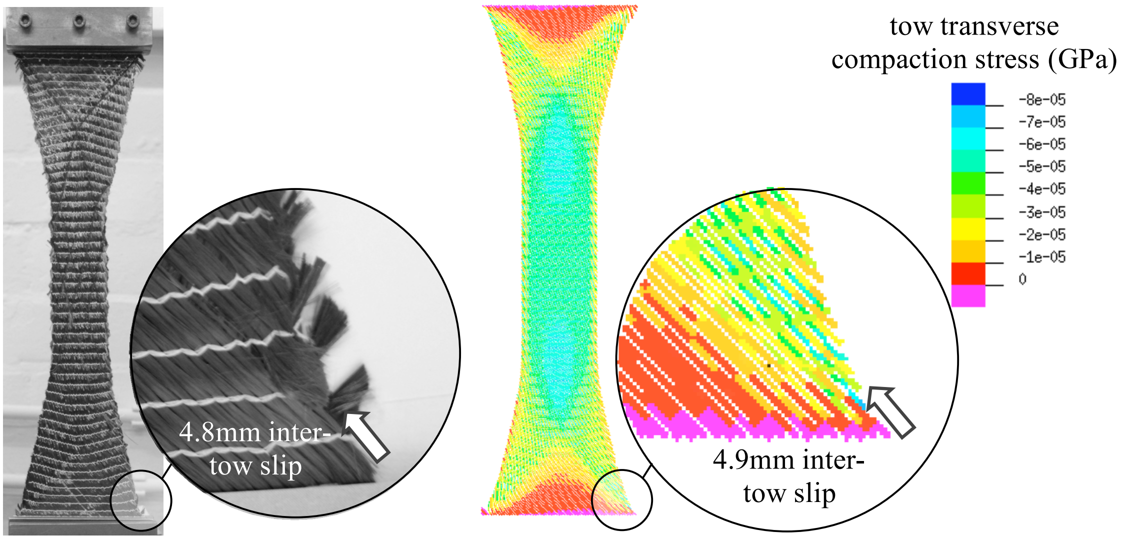

a) bias extension test b) bias extension simulation

(direction of inter-tow slip shown by solid white arrows)

Figure 4.50. Comparisons of global and local deformations for the test and simulated bias extension coupons (negative shear case, loaded to 28% axial engineering strain)

The bias extension simulation results presented above show that the highest tow compaction stresses are induced in the central shear region and that compaction is reduced at the unconstrained specimen edges, which is a good representation of the experimentally observed fabric deformation. It is also observable that the positive shear simulation does not show axial symmetry in the distribution of tow compaction within each modelled fibre layer. This non-symmetry is due to the occurrence of inter-tow slip, which creates non-symmetric deformation of the negative sheared stitching and, thus, the non-symmetric distribution of tow compaction.

A useful indication of relative stitch/tow slip is provided by the length, and orientation, of the bar elements that link the tow and stitch elements, as shown in Figure 4.51. These relative stitch/tow displacements indicate that the simulated fabric deformations deviate from pure shear. Results for the positive sheared coupon show significant relative tow/stitch slip between the clamped and unclamped tows, (zones 3 and 2, respectively), and between the central shear area (zone 1) and transitional areas (zones 2). Similar results are produced for negative shear loading; however, the relative tow/stitch displacements are more evenly distributed and smaller in magnitude; this is due to the applied loads being redistributed into the stitch elements which, as shown previously, deform in a different manor to those predicted by pure shear kinematics.

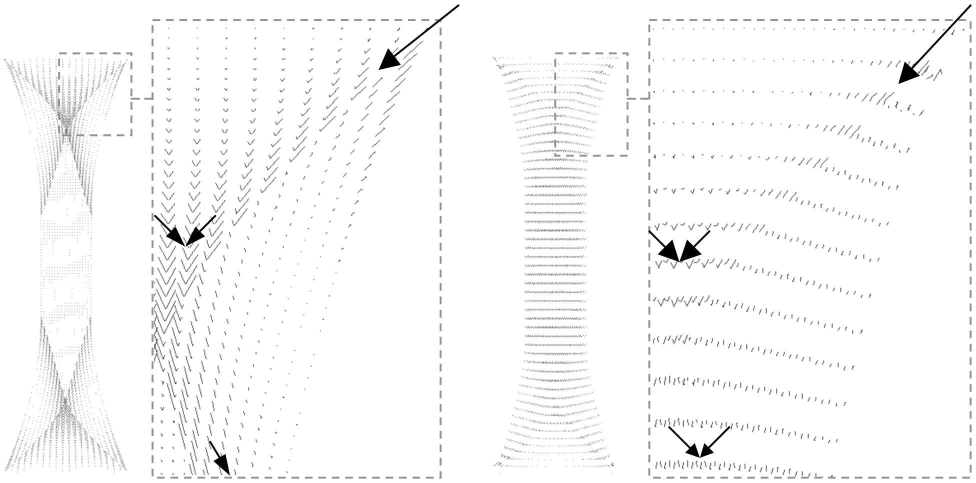

a) positive shear   b) negative shear

Figure 4.51. Deformation of the bar elements linking tows and stitching in simulated bias extension samples; loaded to 28% axial engineering strain.

4.2.7. Validation Simulation: Hemisphere Drape Trial Simulation

A Finite Element simulation of the hemisphere forming process was performed using 120,000 solid and 70,000 bar elements for the tows and stitching respectively. The set-up of the preforming simulation is shown in Figure 4.52, detailing the fabric, hemisphere mould and blankholder rings. The hemisphere and blankholder rings are simulated using shell elements that are treated as individual rigid bodies. The simulation first involved loading the fabric with the blankholder to the required 3.35kPa pressure prior to forming with the metal hemisphere at a velocity of 1ms^{-1}. Contact damping has been applied to the blankholder-to-fabric tow contact algorithms to maintain a stable and constant pressure during the forming process; the lower ring is fixed in all directions. The simulation takes 30 hours to form 76mm displacement of the hemisphere using a twin, 2.2GHz Opteron™ processor computer.

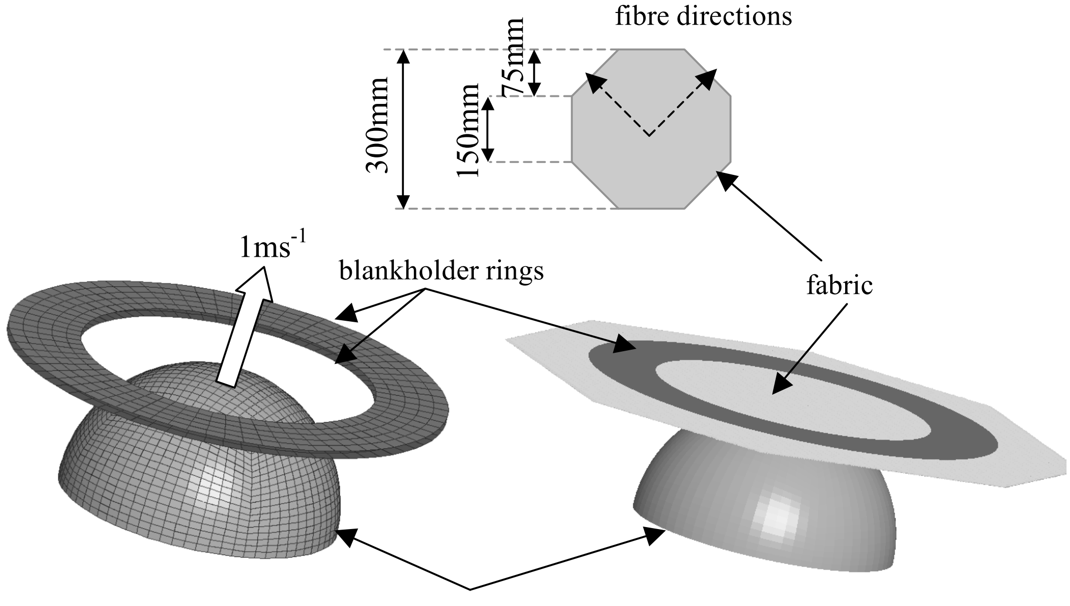

Figure 4.52. Set-up of the performing simulation and dimensions of the un-deformed fabric specimen

The final preformed fabric mesh is shown in Figure 4.53. The two insert figures show the tow and stitch architecture after preforming at two locations for both experiment and simulation. The deformation of the stitch geometry deviates from that predicted by pure shear and inter-tow/crossover point slip is minimal. The simulated stitch deformation is additionally shown in Figure 4.54, which demonstrates that where positive fabric shear occurs, only the stitching aligned to the shear direction is elongated. Furthermore, in negative sheared areas of fabric the stitch elongation is comparatively reduced and distributed between all the stitch segments, which is observed to occur in practice.

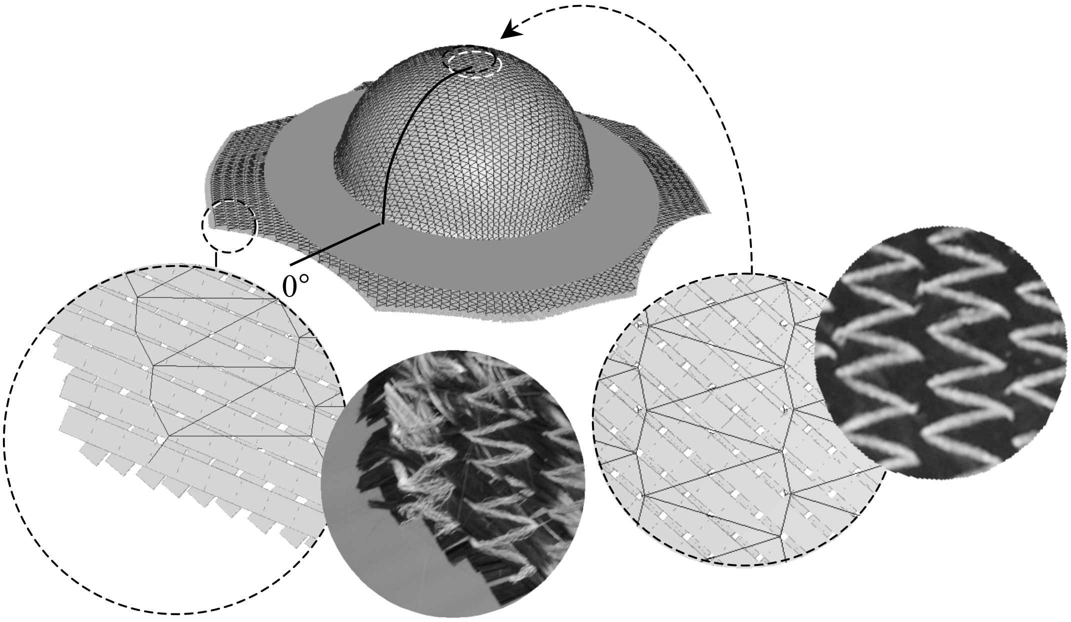

Figure 4.53. Final preformed fabric sample and blankholder; showing detailed areas of the simulated, and experimental, fabric edge and centre; and showing the starting point, 0°, of circumferential inter-fibre angle measurements

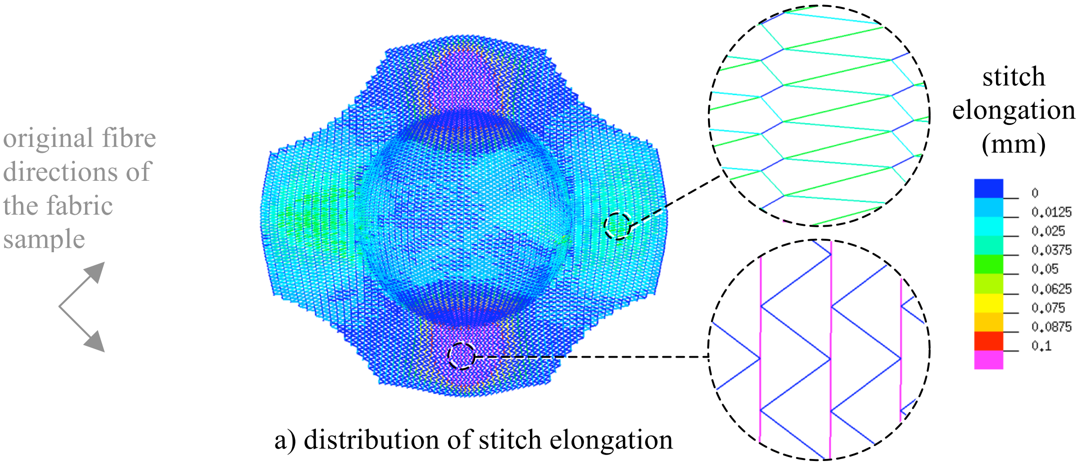

a) distribution of stitch elongation

Figure 4.54. Details of the stitch deformations present in the simulated hemisphere preform

Simulation results show the blankholder rings induce tension within the fabric during forming, which causes separation of the modelled tows over the hemisphere surface, as occurs in practice. Consequently, Figure 4.55 shows that there is minimal transverse compaction of the modelled tows over the hemisphere geometry. The simulated hemisphere preform shows transverse tow compaction principally occurs in areas of fabric under the blankholder rings, where inter-tow shear angles are high. Figure 4.55 also shows that the tensile fibre stress is minimal and is not a significant mode of deformation, despite using a low axial tow stiffness that has been calibrated to fit experimental tow flexural data, as described in section 3.3.3.

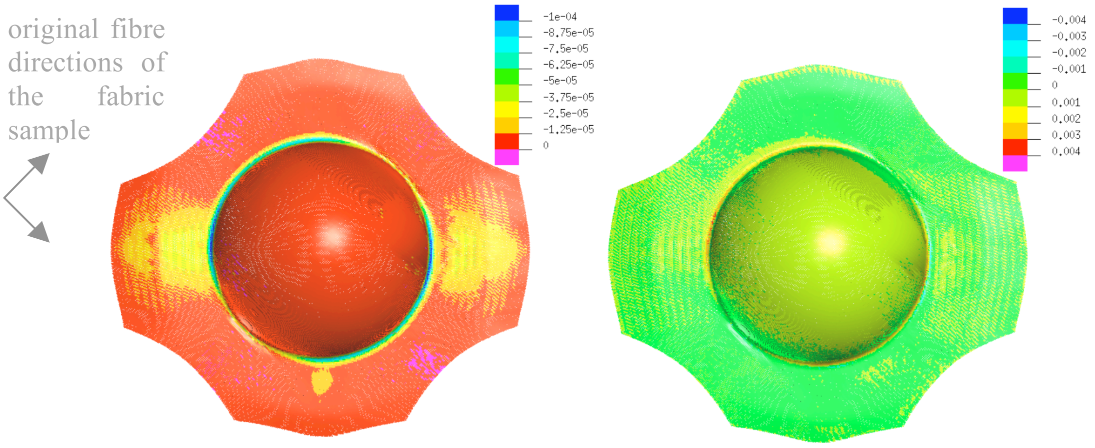

a) transverse tow compaction strain b) longitudinal fibre strain

Figure 4.55. Fibre and transverse tow strain distribution in the simulated hemisphere preform

Figure 4.56 and Figure 4.57 show the variation of inter-fibre shear angle around the hemisphere at 39mm and 68mm height respectively (measured from the base of the hemisphere), for test, macroscopic and mesoscopic FE simulations. The test and mesoscopic simulation show an excellent agreement of shear distribution and, importantly, the numerical model correctly predicts differences of maximum shear angle in each quadrant of the hemisphere, which is an effect of fabric shear bias. The macroscopic FE model results [76] have been obtained using the commercial PAM-FORM software [4] using shell elements and a homogenised anisotropic constitutive fabric law, previously shown in Figure 2.27, and cannot currently detect this non-symmetric shear.

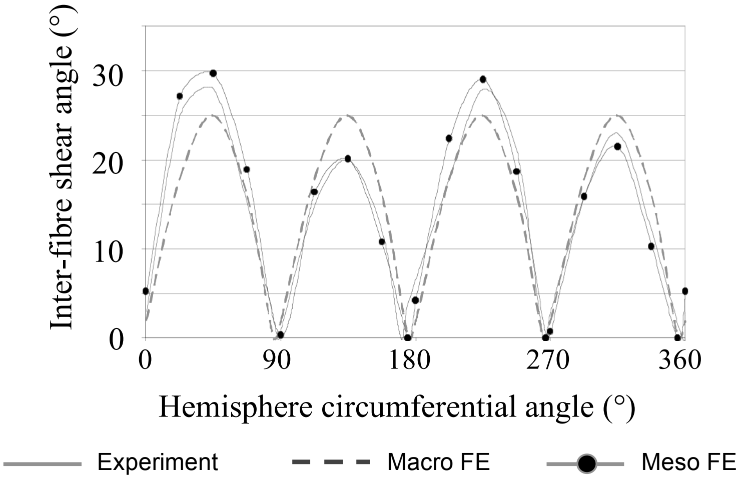

Figure 4.56. Fabric shear angle results at 39mm height using test, macroscopic FE and the developed mesoscopic FE models

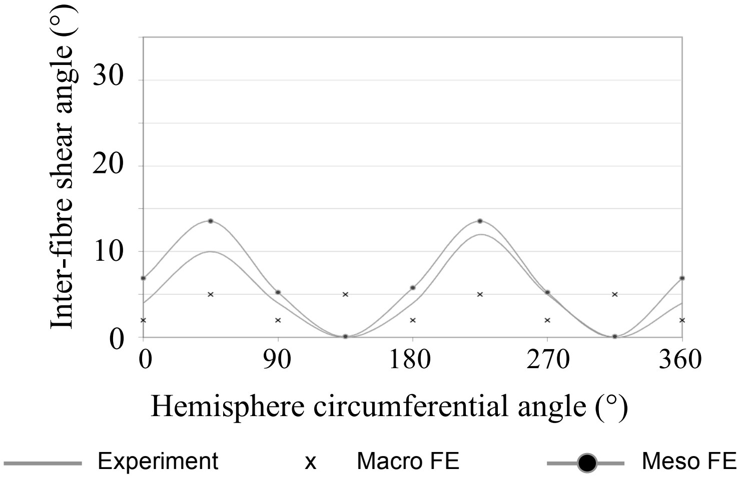

Figure 4.57. Fabric shear angle results at 68mm height using test, macroscopic FE and the developed mesoscopic FE models

The force required to preform the fabric sheet to the hemisphere mould is under predicted by the mesoscopic simulation model, as shown in Figure 4.58, but shows a good correlation to the general trend of the experimental curve. This result is to be expected considering the shear resistance of the modelled fabric is known to be lower than that measured experimentally, as previously discussed for results of the bias extension simulation; section 4.2.6. The oscillations in the simulated forming force occur due to minor local variations in contact pressure and friction of the many contact interfaces in the forming simulation; these oscillations are common when using the dynamic explicit Finite Element solution scheme.

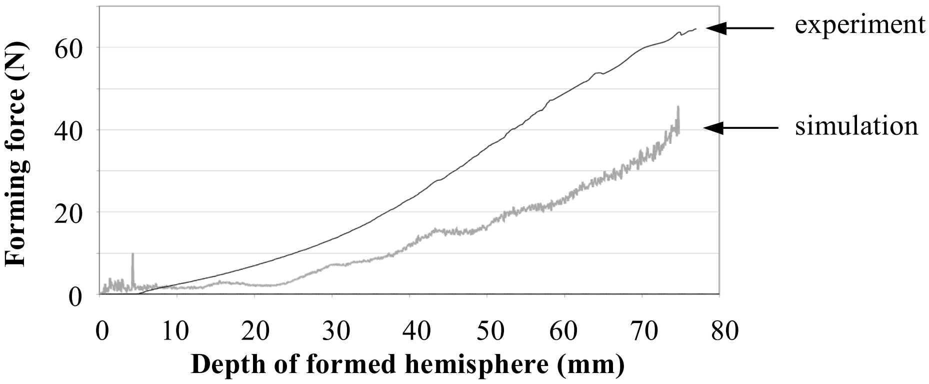

Figure 4.58. Forming force results of a 76mm radius hemisphere; test and simulation

4.2.8. Calibration of the Composite Damage Model and Simulation of the Hemisphere Failure Tests

Simulations have been performed to calibrate the damage and failure values, d_l and d_u, of the constitutive bi-phase material model applied to tow elements. The calibration simulation has involved axial, and transverse, extension and compression of a representative tow. Figure 4.59 shows a schematic representation of the FE models used for these calibration simulations, with tows loaded axially, and transversely, to the fibre direction. These models represent the simulated fabric architecture used in the hemisphere simulations, therefore, the axially loaded FE model comprises two conjoined elements, while the transversely loaded model comprises two tow elements that are tied using an inter-tow delamination model. In each case, the reaction force of the supporting nodes is recorded for calculation of stress in the loading direction. This is then plotted against strain and compared to the required material data, previously provided in section 4.1.9, as shown in Figure 4.60.

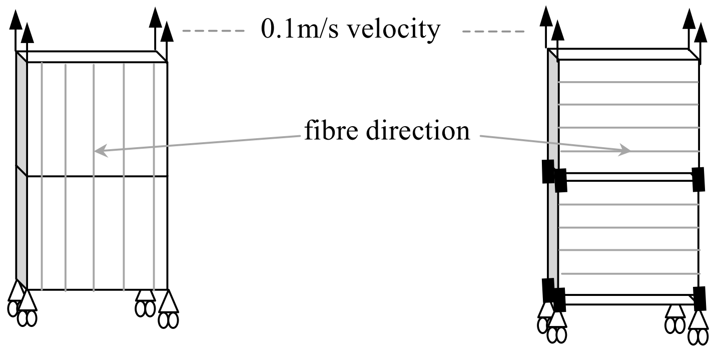

a) axial simulation model b) transverse simulation model

Figure 4.59. Schematic of the FE tow meshes, used to calibrate tow plasticity and damage

The damage values calibrated using the above tow simulations have been included with the material data provided in section 4.1.9. The simulation results, after calibration, compare very well to the required data, as shown in Figure 4.60.

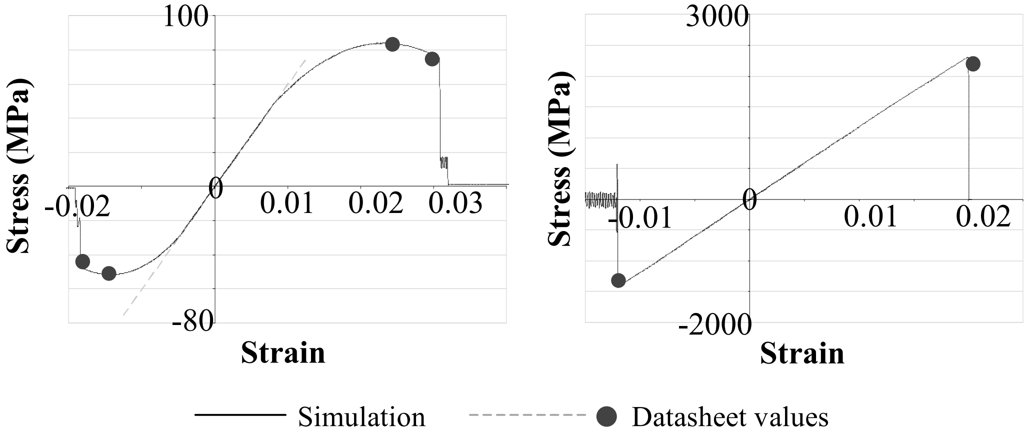

a) transverse matrix damage and failure b) longitudinal fibre failure

Figure 4.60. Results of composite failure calibration simulations

The crushing simulation of the hemispheres is performed using a rigid 49mm radius impactor at 1.5m/s velocity (a 4ms period of linear acceleration to 1.5m/s is used to prevent inertial effects from being measured in the recorded impactor loads). Figure 4.61 shows the simulated composite hemisphere, impactor and boundary conditions. The hemisphere impactor surface comprises shell elements that are defined as a rigid body and constrained to move only in the vertical direction. The crushing force is measured using the reaction force at the hemisphere base.

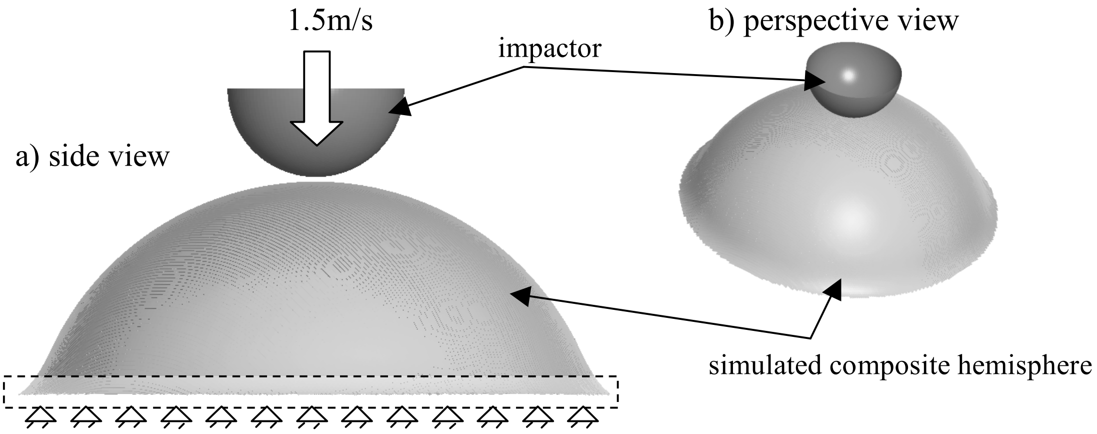

Figure 4.61. Loading and boundary conditions applied to simulations of the hemisphere impact test; a) side view, and b) perspective view

Comparison of the experimentally measured and simulated impact forces, presented in Figure 4.63, show that the simulation model compares poorly with experimental results for the low quality fabric, but compares well with the experimental crush force of the high quality fabric. This result is encouraging and to be expected, since the simulation model does not currently account for the fabric defects that are present in the low quality fabric. The simulation model is capable of only ~40mm impactor displacement due to numerical instabilities induced by excessive deformation of the highly damaged, and therefore low stiffness, solid elements.

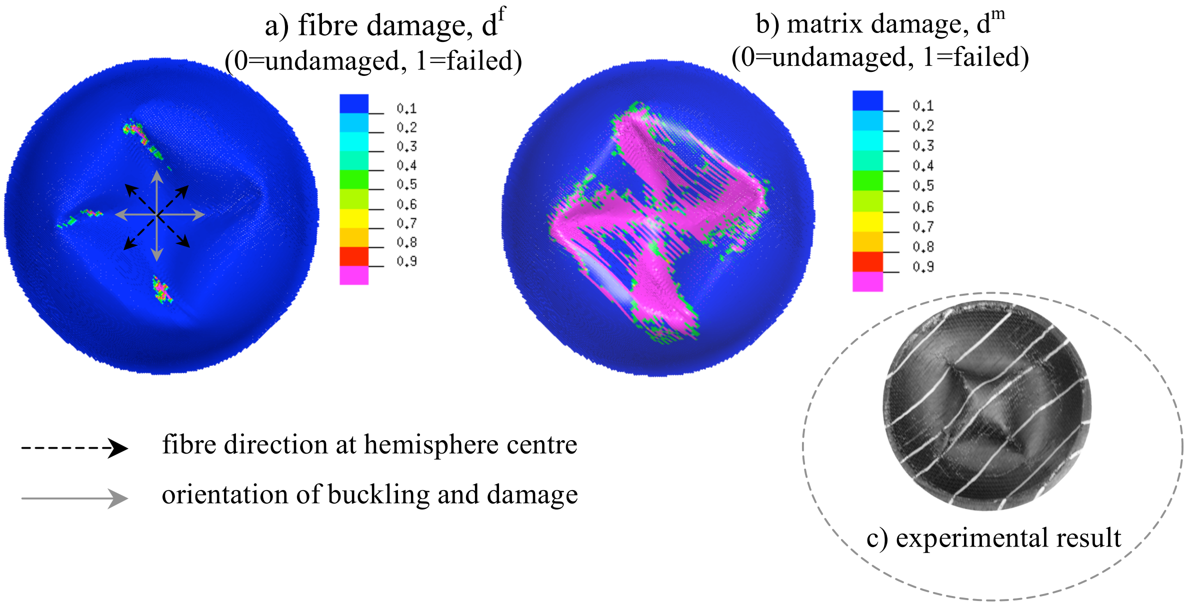

Figure 4.62. Fibre and matrix damage in crush simulations of an impregnated composite hemispshere

Closer inspection of the simulated damage modes, as shown in Figure 4.62, show differences in comparison to test. Failure in the simulated hemisphere occurs by shear damage of the resin matrix. Consequently, the characteristic cruciform shaped pattern of folding is reproduced, but folds are induced at approximately 45° to the fibre directions due to the modelled damage. This deformation compares poorly to the experimental folding, which is aligned to the fibre directions and induces damage by bending related fibre compression failure at the fold tips.

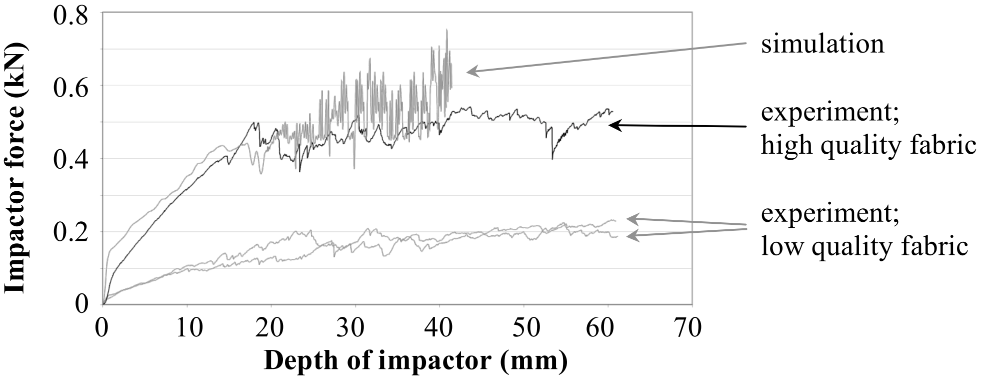

Figure 4.63. Comparison of experimental and simulated impactor forces produced during impactor loading of a 76mm radius hemisphere

4.3. SUMMARY OF THE EXPERIMENTAL AND SIMULATION WORK

This chapter has described the procedures and results of tests, and simulation, used to calibrate and validate the mesoscopic material model developed in this thesis. For fabric modelling, fibre tow compaction and flexural rigidity have been sufficiently calibrated using experimental fabric data. A method of ascertaining the stitch resistance loading using picture frame shear tests has been described, however, this has produced certain limitations, which have been defined and are further discussed in the following chapter. Consequently, bias extension results have been used to calibrate stitch resistance and improve the fabric response to deformation.

Validation of the fabric model has involved comparing tests and simulation results of bias extension tests and fabric preforming to a 76mm radius hemisphere, the *procedures and results of which have been presented. Good predictions of the deformed fabric architecture are produced, especially for the preforming analysis for which non-symmetric shear is well represented.*

The deformed fabric architecture of preforming simulations has been used as the basis for damage and failure simulations of impregnated composite hemispheres to demonstrate the feasibility of coupling these analyses. Methods of calibrating the material response to loading have been presented and simulation results have shown a good correlation. Hemisphere failure simulations show good predictions of deformation force, however, limitations of the failure mode have been observed and are discussed further in the next chapter.

5. DISCUSSION

To reiterate, current preforming simulation tools are based on either fast kinematic mapping methods, solved in the order of seconds, or macroscopic FE simulation models, which offer improved treatment of fabric deformation mechanisms and process conditions, but are solved in tens of minutes and require greater material data and user skill. Both of these preforming simulation methods are commercially available but are not able to fully capture complex tow deformation mechanisms or provide information regarding the coupled tow/stitch interactions that occur in engineering textiles, such as NCF. In the current work a mesoscopic modelling scheme has been developed which has improved the range and accuracy of fabric deformation mechanisms treated in preforming simulations while managing to keep computation times within reasonable limits. This model has not only been used to model fabric preforming, since the deformed fabric architecture has been coupled to mechanical performance simulations of impregnated composite components. To the authors knowledge, the work presented in this thesis is the first published attempt of applying a mesoscopic FE modelling technique to NCF preforming simulation of relatively large structures. The following section discusses the main findings of this work, including the main limitations of the model developed.

5.1. DISCUSSION OF FABRIC SHEAR DEFORMATION

As described in the literature review, biaxial engineering fabrics principally deform by inter-tow shear mechanisms and large strains are achievable with minimal applied force. A number of different test methods are available to characterise fabric shear and two practical test methods have been used in the present work; namely, the picture frame and bias extension shear tests.

The picture frame and bias extension shear tests are both popular methods of characterising fabric shear; the picture frame test induces near pure-shear kinematics while the bias extension test requires minimal equipment and set-up. The normalised axial resistance of NCF measured during these tests have been presented previously in Figure 4.7 and Figure 4.13. The normalisation scheme used here is based upon pure shear kinematics [59] and has been shown to produce good correlation between bias extension and picture frame results for woven fabrics [59]. However, this section compares the normalised results of tests performed on NCF in this work, to obtain Figure 5.1, and shows that significant differences are produced between the picture frame and bias extension results of the studied NCF.

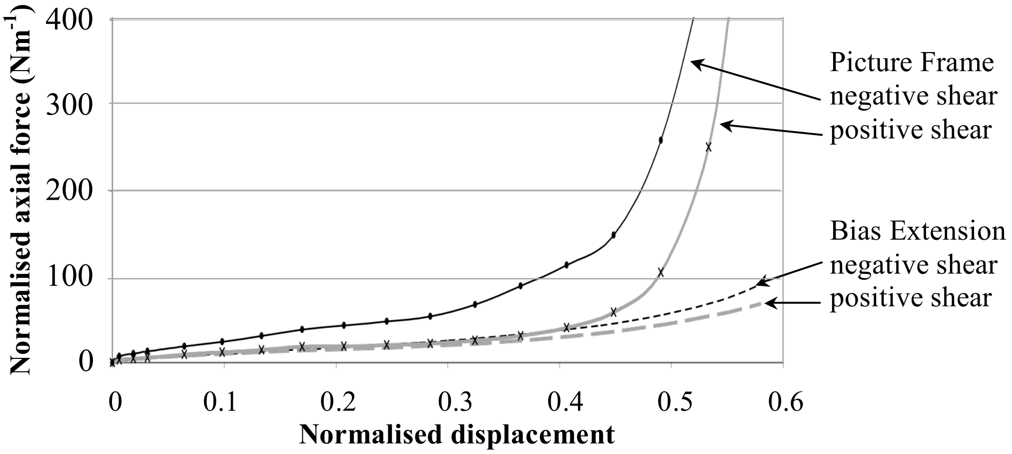

Figure 5.1. Comparison of normalised experimental picture frame and bias extension shear results

Normalised results of the picture frame test show a significant increase in normalised axial force above ~0.4 normalised displacement, which occurs due to shear locking as tow compaction limits are approached. However, these results are not reproduced in bias extension tests since alternative tow slip mechanisms occur once shear stresses become sufficiently high. Prior to shear locking of picture frame samples, the positive sheared fabric samples do show a good correlation between picture frame and bias extension tests; this is attributed to the respective stitching deformation being similar for both tests, as previously shown in Figure 4.17. However, in negative fabric shear, the normalised resistance determined for bias extension tests is significantly lower than for picture frame tests; this is attributed to reduced stitch tension during bias extension tests, which are caused by differences in stitch deformation kinematics, as shown previously in Figure 4.17.

5.2. MODELLING OF THE FABRIC CONSTITUENTS AND DEFORMATION MECHANISMS

NCF materials comprise individual layers of unidirectional fibre tows, which are held together by separate stitching. These constituents have been discretely modelled in the present work to capture the complex interactions that occur between the stitching and tows, a discussion of which is presented in this section.

5.2.1. Discussion of the Mesoscopic Tow Modelling Scheme

Fibre tows comprise of many aligned fibres, which are individually modelled here as a continuum by a series of 8-node solid elements. An orthotropic, heterogeneous fibre/matrix material law has been applied to these solid elements, which separately treats the axial stiffness and transverse compaction resistance of the tow. The use of this material law has resulted in two limitations, which have been defined in section 3.3.3. Firstly, experimental transverse tow compaction resistance is non-linear and increases with compaction strain [42]. This response has been modelled here using a linear elastic stiffness that has been calibrated by using a ‘best-fit’ approach to picture frame shear test results of NCF samples with stitching removed. This calibration gives rise to two considerations that are discussed in the following paragraphs; namely, the suitability of the picture frame test to measure transverse tow compaction and the treatment of the non-linear tow compaction response in the numerical model using a linear stiffness law.

The picture frame test has been used here to measure transverse tow compaction because current theoretical [42] and experimental [41] methods are based upon plane strain deformation, which is invalid at higher shear angles due to fabric thickness increases. Therefore, plane strain compaction data can be used if the change of fabric thickness during fabric shear is accurately measured, but this is difficult to achieve since fabric thickness can easily be modified during the measurement process due to the low compaction stress of dry tows. The picture frame shear test, as used here, is a simple method to measure in-plane tow compaction, while allowing fibre redistribution and, consequently, the fabric thickness to increase freely.

The main limitation of the picture frame test to measure tow compaction is that inter-ply friction, between the unidirectional fibre layers, contributes to the measured axial force. Figure 5.2 plots the normalised axial force for the experimental picture frame test (described in section 4.1.2), the simulated representative tow cell (described in section 4.2.2) and the previously described plane strain constitutive tow compaction model [42] (based on compaction data for aligned E-glass fibres presented in [41]). The presence of inter-ply friction in the experimental picture frame results is evident from higher measured compaction resistance at low shear angles <35°, in comparison to the constitutive tow compaction model data. At higher shear angles, tow compaction and fibre redistribution mechanisms dominate and a significant increase in compaction resistance is measured above ~55° inter-fibre shear.

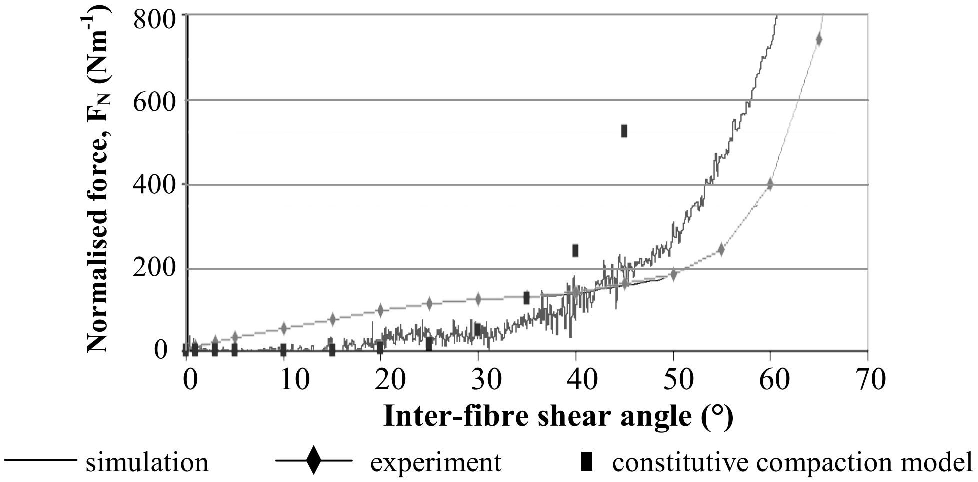

Figure 5.2. Normalised picture frame axial force, showing results of the representative tow cell, picture frame experiments with stitching removed and a constitutive tow compaction model from [42]

Figure 5.2 shows that the linear elastic tow compaction stiffness used in the current simulation model is unable to reproduce the experimental results, but correlates well to the predictive model at low shear angles (<30°). At higher angles of inter-fibre shear, the simulated tow model is unable to predict the rapid increase in experimental compaction resistance. However, the simulation shows significant improvement upon the results obtained using the plane strain constitutive model, which indicate a rapid increase of compaction resistance at very low shear angles of approximately 35°.

The second limitation of the tow model used in the present work is that the axial and bending tow stiffness cannot be independently defined. The simulated tows are currently calibrated to experimental tow flexure tests and do not represent the true, and significantly higher, axial fibre modulus. Nevertheless, the fibre strains predicted in both the bias extension and hemisphere preforming simulations are negligible (<0.4% in the simulations presented), which is representative of fibre deformation during tests.

5.2.2. Discussion of the Mesoscopic Stitch Modelling Scheme

The stitching of NCF is complex in terms of both the stitch pattern and deformation mechanisms that occur during preforming. The tricot stitching of the studied NCF comprises threads of PES, which are impaled through unidirectional carbon fibre layers in a complex arrangement of inter-linked loops. Deformation of this inter-linked stitching during fabric shear involves a combination of tensile strain and frictional sliding of threads around stitch loops; mechanisms that are particularly difficult to model without using highly detailed models of the stitch pattern.

Currently, a simplified stitch model has been used, which does not treat tensile stitch strain or sliding, but attempts to capture the shear resistance contribution of the stitching to the fabric as a whole. This approach has contributed to good predictions of the fabric architecture after preforming, as shown in section 4.2.7. Nevertheless, an attempt to fully model the inter-linked stitch geometry and frictional stitch sliding has been investigated by applying an algorithm which permits re-meshing of bar elements from one segment of the stitch geometry to another [90]. This re-meshing scheme has originally been developed for seat-belt applications in simulations of occupant safety tests. Element re-meshing occurs once a predefined threshold element length has been reached based on the condition that sufficient stitch tension is applied to overcome inter-stitch friction, as shown schematically in Figure 5.3. Bar element lengths are exchanged based on the pulley rim friction formulation,

$$F_1 - F_2.e^{\alpha\mu} > 0 , \qquad \text{Eq. (45)}$$

where, F_1 and F_2 are the tensile forces in adjoining bar elements, α is the angle between the bar elements and μ is the friction coefficient. The true stiffness of the PES thread material is represented using the same non-linear elastic, tension only law previously presented in Figure 3.12.

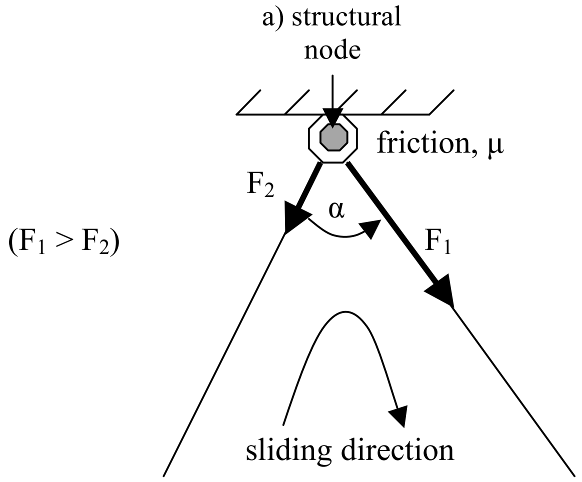

Figure 5.3. Schematic of the bar element modelling scheme used in an attempt to model frictional stitch sliding, [90]

Simulations of fabric deformation, using the bar element re-meshing option described above, highlighted a significant limitations of this re-meshing approach. The scheme requires bar elements to be tied to a main structural element, as shown at Figure 5.3a, at which frictional forces can be calculated. With respect to the fabric model, this has involved directly linking the bar elements to solid tow elements. During fabric deformation the coincident tow and stitch nodes prevent relative stitch/tow slip mechanisms. Therefore, the element re-meshing scheme has not been used in the final stitch model since relative stitch/tow slip is an important deformation mechanism that must be represented; results of the bias extension test show significant strains are achievable with low forces due to tow slip mechanisms, as shown previously in Figure 5.1. Nevertheless, the treatment of frictional stitch slip using a pulley-rim friction coefficient and stitch element re-meshing is likely to be a good approach to modelling the true stitch deformation kinematics that is worthy of further research.

Since methods of modelling stitch tension and frictional slip of stitch elements have yet to be validated, a simplified modelling scheme of the tricot stitch has been implemented in the developed mesoscopic NCF model. This simplified stitch model constrains the modelled fibre tows and is calibrated to reproduces the global shear resistance contribution of stitching to fabric deformation. Initially, picture frame tests have been used to obtain suitable fabric shear data by comparing the results of tests with stitching present and with stitching removed from the fabric samples. However, subsequent simulation of bias extension tests have shown that the mesoscopic fabric model under-predicts fabric shear resistance when not constrained to pure shear. These results infer three consequences regarding the current simplified stitch model:

- *Fabric shear properties obtained using the picture frame test are only truly valid for pure shear fabric deformation;* calibration of stitch deformation resistance with picture frame shear test results is not sufficient to reproduce the axial resistance of bias extension tests. This has been demonstrated by the difference of normalised axial force from these two tests, as shown in Figure 5.2.

- The calibrated stitch deformation is determined using stitch strains based on a kinematic model of fabric shear, which does not accurately represent stitch deformation; the kinematic model used to determine stitch strains, previously described in section 2.5.2, assumes pure fabric shear. However, Figure 4.17 shows that stitch deformation deviates from pure shear, especially during negative fabric shear.

- *The length of connected stitch segments are uncoupled;* consequently, the complex frictional resistance of stitch material sliding is not properly treated and the level of tow compaction which occurs in practice is not fully induced, as signified by the lower inter-fibre shear angles predicted for bias extension simulations, as shown in Figure 4.48.

An attempt at addressing the first limitation described above has involved using experimental bias extension axial force results to re-calibrate the stitch force response; a comparison of the stitch data has been shown in Figure 4.46. Results of the measured axial resistance from bias extension shear simulations with stitch data calibrated in this way show improved correlation with test measurements, as shown in Figure 4.45, but the model continues to under-predict fabric shear resistance due to the second and third limitations described above.

Regarding the second limitation defined above, the deviation of stitch deformation from pure shear, during bias extension tests, is demonstrated by comparing the simulated stitch strains to the theoretical stitch strains determined using a kinematic analysis, previously presented in section 2.5.2. Four different stitch segments at the centre of the simulated positive, and negative, sheared bias extension coupons are examined, as shown in Figure 5.4; this figure additionally shows the geometry of the stitch unit-cell for the simulated and kinematic models in positive, and negative, shear.

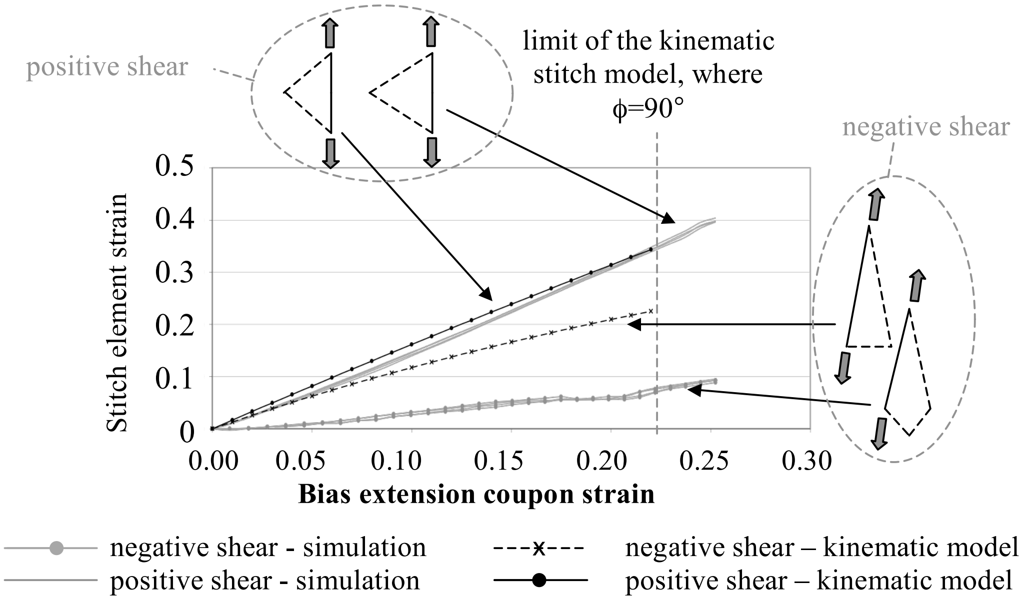

Figure 5.4. Stitch strains of the bias extension test obtained with the mesoscopic simulation model and theoretical kinematic model; the respective stitch deformation patterns are shown, with the stitch sections measured for strain indicated by loading arrows

Figure 5.4 confirms that the kinematic analysis is sufficient to determine the strain of modelled stitch segments under tension during positive shear. However, the strain of stitch segments under tension during negative shear is significantly lower in the mesoscopic simulation than predicted by pure shear kinematic analysis. In this respect, the mesoscopic simulation is more representative of the true fabric deformation with loading distributed over all the stitch segments.

5.2.3. Discussion of the Coupled Stitch/Tow Deformation Modelling Scheme

In practice, fabric deformation resistance is principally controlled by a complex interaction of stitch tension and tow compaction. The present stitch model is unable to fully represent the true state of stitch tension, since the lengths of connected stitch elements are uncoupled, and, consequently, friction between stitching threads and tows during fabric deformation is not properly treated. Additional bar elements have been used to account for the friction between stitch threads and tows by linking adjacent nodes of the stitch bar elements and solid tow elements. Relative stitch/tow slip causes strain in these linking bar elements, which have been calibrated to experimental tow pull-out results, as shown in section 4.2.4.

Calibrating the force response of the tow/stitch link elements to experimental pull-out results, has produced a good prediction of inter-tow and cross-over point slip in simulations of bias extension tests, demonstrated in Figure 2.17. The mesoscopic NCF model has also predicted differing distributions and magnitudes of relative stitch/tow slip between positive and negative sheared specimens, which are caused by differences of load distribution in the stitching, as demonstrated in Figure 4.17. The bias extension simulation results indicate that:

- Crossover point slip occurs in the constrained region of tows (zone 3) and is significant in areas close to the central shear region (zone 1). Therefore, the clamped region of tows (zone 3) cannot be assumed to remain un-deformed during bias extension tests.

- The central shear region (zone 1) does not deform by pure shear, since lower inter-fibre angles are measured at the free edges of the coupon than at the centre. Therefore, the unconstrained areas of fabric at the coupon edges contribute less to the measured axial resistance in bias extension tests.

- At higher axial coupon strains, the fabric predominantly deforms by inter-tow and cross over point slip mechanisms, which are well represented in the current mesoscopic NCF model.

It is worth noting that relative stitch/tow slip is currently only treatable using mesoscopic modelling techniques of relatively large fabric specimens. Unit-cell simulations of NCF would be unsuited for investigation of coupled stitch/tow deformations since the boundary conditions required to constrain unit-cell models are generally not representative of the constraint produced by the fabric outside the simulated cell.

5.3. DISCUSSION OF SIMULATIONS USED TO VALIDATE THE DEVELOPED MESOSCOPIC NCF MODEL

5.3.1. Discussion of the Bias Extension Shear Test Simulation Results

Simulation of the bias extension test has proved useful and valid approach to investigate the deformation mechanisms of the modelled fabric, since different deformation mechanisms occur within the specimen. Results of bias extension simulations show that the developed NCF model is capable of producing good predictions of tow/stitch slip mechanisms, as demonstrated in Figure 4.49, and is able to improve prediction of inter-tow shear deformation and shear bias, in comparison to pure shear based modelling methods.

The limitations of the mesoscopic NCF model have been elaborated previously in section 5.2.2, regarding the under-predictions of inter-fibre shear angles and axial resistance. Nevertheless, the results are very encouraging and demonstrate sufficient reproduction of the experimentally measured shear bias. These results could be improved with correct treatment of stitch tension and frictional stitch sliding. Therefore, compared to kinematic and macroscopic FE simulation methods, the current mesoscopic fabric model is able to improve the range of fabric deformation mechanisms treated and with further development should produce accurate predictions of fabric deformation beyond limits of tow compaction and inter-tow shear.

5.3.2. Discussion of the Hemisphere Draping Simulation

Hemisphere preforming simulations have shown that the mesoscopic model developed in the current work is sufficiently capable, and stable, for accurate prediction of the deformed NCF architecture after preforming. These results are significant since the hemisphere mould used here has induced large displacements and deformations in stitch and tow elements, which can cause instabilities in explicit FE codes, such as contact inter-penetrations and unstable element deformations. Nevertheless, the element deformations and contact integrity, simulated here between tooling, tows and stitching, remain stable throughout forming simulations. Results also show the mesoscopic model has successfully predicted un-symmetric fabric deformation, which is caused by biased shear resistance.

The limitation that stitch element segments are uncoupled has been shown to cause under-prediction of inter-fibre shear angles during experimental bias extension tests. However, a similar under-prediction of inter-fibre shear is not produced during hemisphere preforming simulations because the fabric loading mechanisms are significantly different, for the following reasons:

- During bias extension simulation of biaxial NCF, the fabric is only loaded axially: therefore, the overall deformation response of the fabric is controlled by the fabric, and constituent, properties, such as the state of stitch tension and tow compaction.

- During hemisphere preforming, the surrounding blankholder ring induces tensile stitch loading in *all* in-plane directions. Despite the use of un-coupled stitch element lengths, the mesoscopic NCF model responds better to this loading condition and produces good results of inter-fibre shear distribution in hemisphere preforming simulations, as shown in section 4.2.7.

The preforming process has produced only minor inter-tow slip. Tow slip mechanisms generally occur between constrained and unconstrained tows, or where inter-fibre shear angles are high, neither of which have occurred during preforming trials. The mesoscopic FE model has been able to accurately predict this lack of inter-tow slip.

However, results of bias extension test simulations indicate some discrepancy of fibre architecture would occur if the draping process involved more complex loading conditions, or underwent greater inter-fibre shear.

The force required to form the simulated fabric is compared to test measurements in Figure 4.58 and shows an under-prediction of approximately 50%. The forces required to preform a fabric are primarily due to fabric shear resistance, blankholder friction and tooling friction. In the current work, the shear resistance of the modelled fabric is known to be under-predicted, as shown in Figure 4.46, and it is felt that this contributes to the discrepancy between test and simulation. However, further investigation into the effects of tooling friction, blankholder pressure and fabric shear resistance on the required forming force is required. The effect of varying blankholder pressure on fibre shear has been investigated experimentally, where increased blankholder pressures have suppressed shear bias and induced a more symmetrical preform architecture [67]. Consequently, these effects require further investigation, with respect to the mesoscopic NCF model developed here.

The previously discussed hemisphere preforming results have been produced using a stitch model calibrated to experimental bias extension shear test results, as determined in section 4.2.6. However, as previously described in section 3.4, the stitching had also been calibrated to picture frame test results, but proved insufficient to reproduce the fabric shear resistance during bias extension tests. Nevertheless, a preforming simulation has been performed which uses stitching calibrated to experimental picture frame results to investigate the importance of correctly treating fabric shear resistance. The simulation procedure is identical to that described in section 4.2.7 and the results of inter-fibre angle at 39mm height from the base of the hemisphere are shown in Figure 5.5.

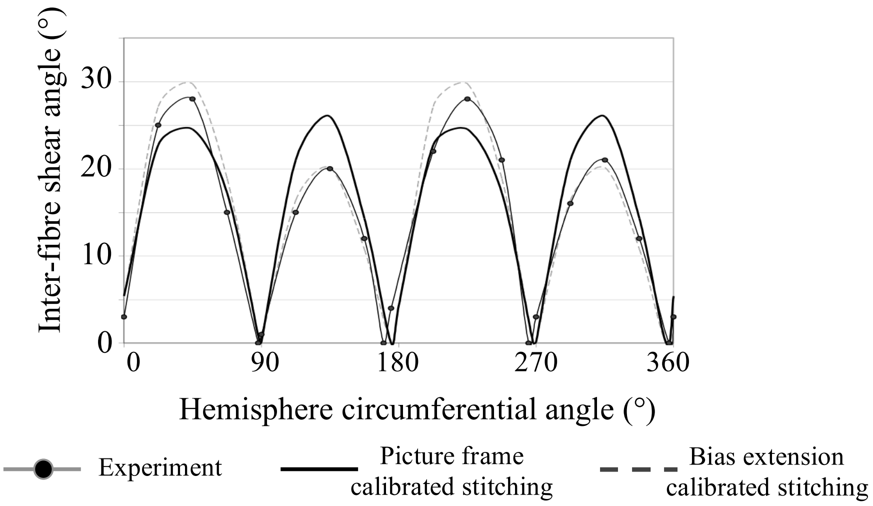

Figure 5.5. Fabric shear angle results at 39mm height using test, mesoscopic FE calibrated to bias extension shear data and mesoscopic FE calibrated to picture frame shear data

Figure 5.5 shows that the effect of shear bias is not correctly predicted when the stitch deformation resistance has been determined using experimental picture frame results and, therefore, the model shows poor correlation to experimental results. These results emphasise the importance of correctly treating fabric shear resistance and show that calibrating the modelled stitch resistance to bias extension test results has been sufficient to do this.

5.4. DISCUSSION OF THE MESOSCOPIC MODELLING OF IMPREGNATED COMPOSITE MATERIALS

As previously described, fabric preforming simulation is an important step in the virtual design of composite components, since the reorientation and distribution of the fibres can significantly influence fabric permeability during manufacture and mechanical properties of the final composite part. The ability to easily couple accurate fabric preforming simulation results to mechanical analyses of the final component is an important step that is usually simplified, or ignored, in complex shaped composite parts. This procedure has been demonstrated in the present work for the case of the hemisphere part, as shown in Figure 5.6.

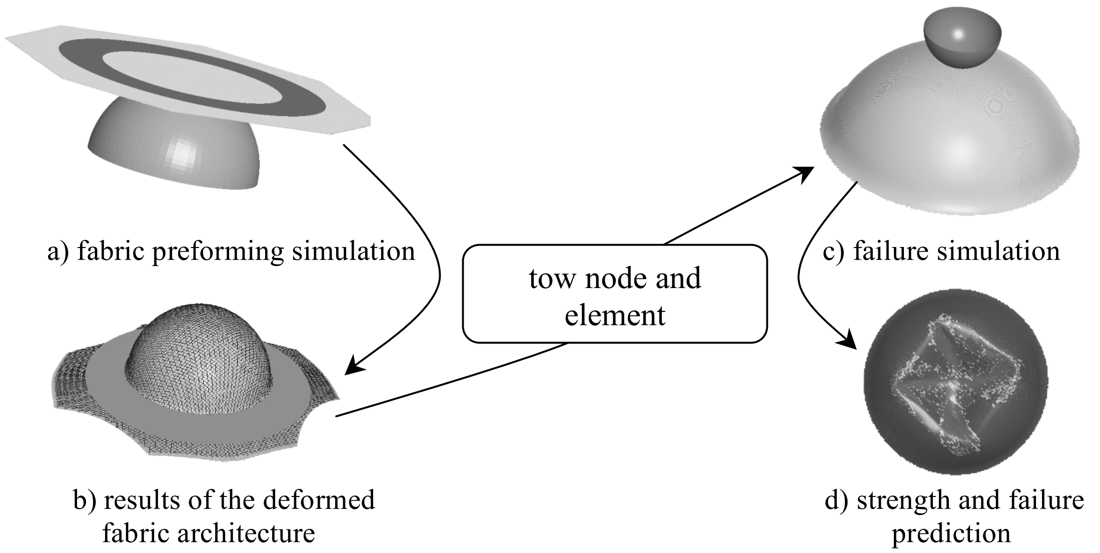

Figure 5.6. The coupling of fabric preforming and impregnated composite failure simulations, as demonstrated in the present work

As demonstrated in Figure 5.6, the deformed tow architecture of a hemisphere has first been obtained by performing a preforming simulation; this is then used as the basis for failure simulation of impregnated hemisphere components. Material data of the dry fibre tows has been replaced with mechanical data for resin impregnated tows. Both inter-ply delamination and intra-ply resin/fibre damage models have been used to properly account for the different modes of composite failure that may occur, as described in section 2.8. Simulations to calibrate the tow damage behaviour reproduce well the required composite behaviour, as shown in 4.2.8. Subsequent simulation of a composite hemisphere, loaded with a central punch, has been compared to equivalent experimental test failure modes and loads, from which two main conclusions can be drawn:

- The current mesoscopic fabric model does not account for fabric variability, which has been observed in an older Non-Crimp fabric style from Saertex. Therefore, the mesoscopic composite model only predicts well the deformation forces required when loading components manufactured with high quality fabrics having minimal imperfections. As described in section 4.1.8, hemisphere components have been manufactured using two different fabrics; a low quality fabric, with defects such as missing tows, and a high quality fabric, with a constant fibre distribution. Deformation and failure prediction of hemisphere components manufactured using the low quality fabric require comparatively lower forces, since missing tows reduce the composite mechanical properties and localise failure. These effects are not currently accounted for in the mesoscopic composite model.

- Whilst the general force levels and failure loads agree well, with tests it has been seen that the simulated mode of damage and failure in loaded hemisphere are different. As Figure 4.62 has shown, experimentally loaded hemispheres deform with folds aligned parallel to the fibre directions, which cause localised bending related fibre compressive failure at the fold tips. However, the current hemisphere simulation fails by matrix shear damage mechanisms, which produces similar folds to test, but are oriented between the fibre directions.

Further work would be required to account for the discrepancy of predicted and experimental damage mechanisms. The aim of the present work has been to demonstrate the feasibility of coupling mesoscopic preforming simulation to mechanical failure simulation of composite structures and, therefore, not to fully validate mesoscopic composite modelling. Nevertheless, initial findings suggest the treatment of shear damage is a likely problem of the tow modelling scheme and is discussed further in the following paragraphs.

The shear damage behaviour of tows has been characterised here by simulating the shear of a single tow element, a schematic of which is shown in Figure 5.7a. The axial support force of the constrained nodes, F_A, and the axial displacement, D, are measured to allow a shear stress, σ_s, and shear strain, e_s, to be calculated as follows,

$$\sigma_s = \frac{F_A}{2ld.\cos\left(\frac{\alpha}{2}\right)}, \qquad \text{Eq. (46)}$$

$$e_s = l.\sin\left(\frac{\pi}{2} - \alpha\right), \qquad \text{Eq. (47)}$$

where, *l* and *d* are the edge lengths of the simulated element and α is the acute angle between the element edges, which is calculated from the axial displacement, D, using equation 3.

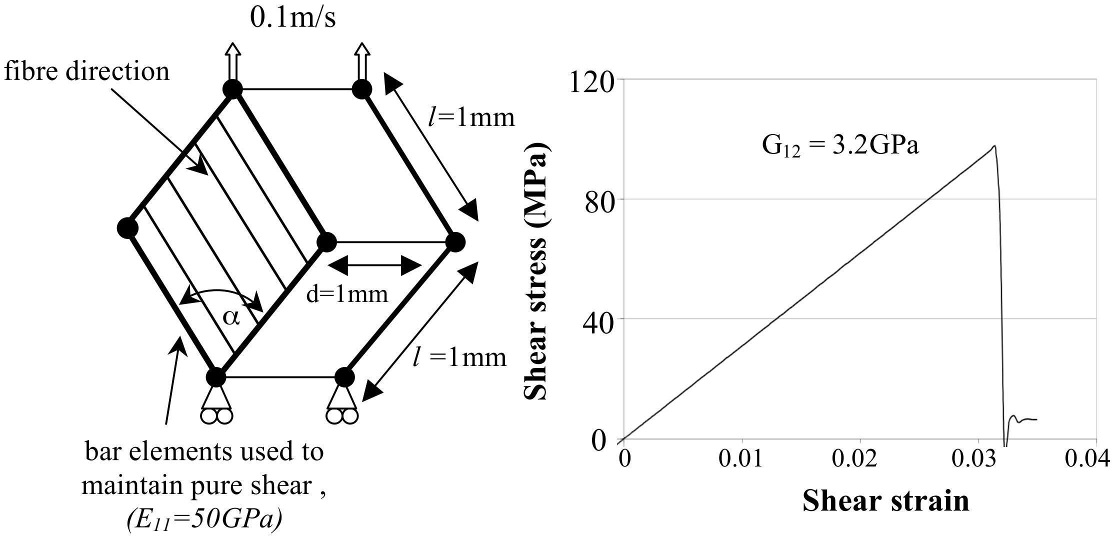

a) element shear simulation set-up and boundary conditions

b) shear element simulation results

Figure 5.7. Shear element simulation of the impregnated composite tow

Shear failure of continuous fibre composites occurs by progressive matrix damage [101]; however, a brittle mode of failure is simulated using the current tow material, as shown in Figure 5.7b. Consequently, the modelled shear strain at failure is low, at 3.14%, in comparison to published results of sheared NCF coupons, which fail at shear strains of approximately 6% to 8% [101][131]. The under-prediction of the tow shear strain at failure may be a contributing factor to the discrepancy between simulated and experimental hemisphere failure modes. However, as stated, further investigation into this tow modelling scheme is required, possibly combined with improvement to the damage and failure models available in PAM-CRASH [22].

6. CONCLUSIONS

A novel, and stable, mesoscopic Finite Element model for drape simulation of textile (NCF) fabrics has been presented that includes all the important fabric deformation mechanisms, including shear bias and relative tow/stitch slip. Tow and stitch slip mechanisms are especially important in Non-Crimp Fabrics, compared to equivalent woven fabrics, as demonstrated here with results of bias extension shear tests. Mesoscopic modelling has involved discretisation of the individual tow and stitch threads that comprise NCF sheets. Individual fibre tows have been modelled as a homogeneous continuum, using an orthotropic material law which is capable of treating all the main tow deformations, including low transverse compaction stiffness, low axial strain during fabric deformation, low flexural rigidity, tow buckling and inter-tow friction.

NCF stitch deformation is complex, due to inter-linked thread loops which include tension and frictional sliding mechanisms. Methods of accurately modelling these mechanisms have been investigated but have proved unsuccessful. Consequently, a simplified stitch model has been developed to represent the main shear resistance contribution. Initial calibration of the stitch resistance to results of the popular experimental picture frame shear test produced a model that is only truly valid for pure shear deformation. Subsequent calibration of stitch resistance to experimental bias extension test results has been found to improve the modelled fabric shear response and produce good predictions of the deformed fabric architecture of preformed hemispheres.

Some limitations in the current modelling scheme have been noted; in particular, improved constitutive modelling of tows is required to decouple axial and bending stiffness and represent non-linear transverse compaction stiffness. Furthermore, techniques to allow redistribution of local stitch forces due to thread slip mechanisms, which occur in practice, would improve accuracy. Nevertheless, the model has proven successful for complex preforming of hemisphere components and provides far greater information on fabric deformations than previously possible using mapping techniques, or homogenised material laws and continuum shell (or membrane) Finite Elements. In particular, the distinct and complex deformation zones of deformed bias extension coupons have been well represented and information on the distribution of tow and stitch slip can be obtained, which alternative modelling techniques would neglect. Furthermore, the mesoscopic model has been able to correctly capture shear bias for the preforming analysis of a hemisphere surface geometry.

The preform fabric model also provides a unique basis to perform failure analysis of impregnated composite parts, using accurate representation of the deformed fabric architecture. Coupling of preforming simulation and mechanical performance prediction is readily achieved by using the deformed fabric FE mesh with alternative stiffness-failure material data to represent the impregnated composite material. This methodology has been demonstrated for the failure analysis of the hemisphere part and predictions of the required deformation force show promising results. Some limitations of the failure model have been observed; in particular the mode of simulated composite failure requires further investigation. Nevertheless, the mesoscopic modelling scheme is a valid approach to predict composite performance and provides the opportunity to investigate the occurrence of individual inter-ply and intra-ply deformation mechanisms of complex components.

7. FUTURE WORK

Limitations of the current fabric modelling scheme have highlighted some areas requiring further work; these include:

- *Improved constitutive modelling of tows is required to decouple axial and bending stiffness:* In the present work a low axial tow stiffness has been calibrated so as to produce good bending stiffness. Axial tow strains have been negligible in the bias extension and preforming simulations investigated here, however, this may not be true for more complex preforming problems.

- *Techniques of modelling stitch sliding friction and tension are required to improve the accuracy of the predicted fabric deformations:* The current simplified stitch model is unable to induce the true level of tow compaction that occurs in practice since stitch lengths are uncoupled. Finely discretised, and detailed, stitch modelling could be used in conjunction with a suitable contact algorithm to treat stitch sliding friction, but this would be impractical for analysis of large structures. Therefore, methods of improving the stitch modelling require investigation and could be based on a pulley friction model, as discussed in section 5.2.2.

In addition, the fabric preforming work presented here highlights additional considerations, described as follows:

- *The influence of fabric quality requires further investigation;* the fabric studied in the present work contains defects, such as missing tows and fibre misalignment, which affect mechanical and infusion properties of the fabric and performance of the impregnated composite. The effects of quality are a topic of recent research [132][133] and can readily be treated using mesoscopic modelling schemes with direct representation of defects.

- *The influence of blankholder location and pressure on fabric deformation has yet to be determined:* The preforming experiments and simulations performed here have used a blankholder ring at a single pressure. However, the blankholder pressure is known to influence the symmetry of the preformed fabric architecture, when forming fabrics with biased shear, and also affect the required forming force.

Regarding the simulation of impregnated composite parts, limitations of the mesoscopic failure modelling scheme includes issues of fabric quality, as described above, and additional considerations, as follows:

- *The mode of simulated composite failure requires further investigation:* Failure of simulated hemisphere components show preferential matrix shear damage which does not occur in practice. Initial work suggests that the simulated shear failure mode and strain at failure are possible causes of this incorrect prediction, but further research is required to properly understand and improve the mesoscopic failure model for such applications.

8. REFERENCES

[1] Cox B.N., Flanagan G., NASA Contractor Report 4750. Handbook of Analytical Methods for Textile Composites. 1997.

[2] Matthews F.L., Rawlings R.D., Composite Materials: Engineering and Science. 1999. Woodhead Publishing, Cambridge, England.

[3] Rudd C.D., Long A.C., Kendall K.N., Mangin C.G.E., Liquid Moulding Technologies. 1997. Woodhead Publishing, Cambridge, England.

[4] PAM-FORM™ 2G, *ESI Group*, 99 Rue des Solets, Silic 112, 94513 Rungis-Cedex, France.

[5] ABAQUS™, *ABAQUS Europe BV*, Gaetano Martinolaan 95, 6201 BP Maastricht, Netherlands.

[6] Tong L., Mouritz A.P., Bannister M.K., 3D Fibre Reinforced Composite Materials. 2002. Elsevier Publishing, London, England.

[7] Yi H.L., Ding X., Conventional Approach on Manufacturing 3D Woven Preforms Used for Composites. Journal of Industrial Textiles, vol. 34, no. 1, 2004, pp 39-50.

[8] Rudov-Clark S., Mouritz A.P., Bannister M.K., Fibre Damage in the Manufacture of Advanced Three-Dimensional Woven Composites. Composites: Part A, vol. 34, 2003, pp 963-970.

[9] Birch S., Cranfield's 'Third Way' Car. Automotive Engineering International, vol. 111, no. 9, 2003, pp 17-18.

[10] Pastore C.M., Whyte D.W., Soebruto H., Ko F.K., Design and Analysis of Multiaxial Warp Knit Fabrics for Composites. Journal of Industrial Fabrics, vol. 5, no. 14, 1986, pp 4-14.

[11] Souter B J, Long A C, Robitaille F, Rudd C D., The influence of Fabric Mechanics on Draping. 6th International Conference on Advanced Composites (ICAC-99). September 1999. United Kingdom, Bristol, pp 55-62.

[12] Backhouse R., Multiaxial Non-Crimp Fabrics: Characterisation of Manufacturing Capability for Composite Aircraft Primary Structure Applications. Eng.D. Thesis, Cranfield University, United Kingdom, 1998.

[13] Dexter H.B., Hasko G.H., Cano R.J., Characterisation of Multiaxial Warp Knit Composites. First NASA Advanced Composites Technology Conference, Part II, NASA Langley Research Centre, Hampton, Virginia, USA, 1991.

[14] Pickett A.K., Review of Finite Element Simulation Methods Applied to Manufacturing and Failure Prediction in Composite Structures. Applied Composite Materials, vol. 9, 2002, pp 43-58.

[15] Gasser A., Boisse P., Hanklar. S., Mechanical Behaviour of Dry Reinforcements. 3D Simulations Versus Biaxial Tests. Computational Materials Science, vol. 17, 2000, pp 7-20.

[16] Boisse P., Gasser A., Hivet G., Analyses of Fabric Tensile Behaviour: Determination of the Biaxial Tension-Strain Surfaces and their use in Forming Simulations. Composites: Part A, vol. 32, 2001, pp 1395-1414.

[17] Long A.C., Rudd C.D., A Simulation of Reinforcement Deformation during the Production of Preforms for Liquid Moulding Processes. Proceedings of the Institute of Mechanical Engineers, Part B: Journal of Engineering Manufacturing, vol. 208, no. 4, 1994, pp 269-278.

[18] Van West B.P., Pipes R.B., Keefe M.J., Simulation of the Draping of Bidirectional Fabrics Over Arbitrary Surfaces. Journal of the Textile Institute, vol. 81, no. 4, 1990, pp 448-460.

[19] Bergsma O.K., Computer Simulation of 3D Forming Processes of Fabric-Reinforced Plastics. Proceedings of the 9th International Conference on Composite Materials (ICCM 9), Madrid, Spain, 1993, pp 560-567.

[20] Long A.C., Souter B.J., Robitaille F., Mechanical Modeling of In-Plane Shear and Draping for Woven and Non-Crimp Reinforcements. Journal of Thermoplastic Composite Materials, vol. 14, 2001, pp 316-326.

[21] Cook R.D., Malkus D.S., Plesha M.E., Concepts and Applications of Finite Element Analysis. 1989, Wiley Publishing.

[22] PAM-CRASH™, *ESI Group*, 99 Rue des Solets, Silic 112, 94513 Rungis-Cedex, France.

[23] LS-DYNA™, *Livermore Software Technology Corp.*, 7374 Las Positas Road, Livermore, CA94551, United States of America.

[24] Dong L., Lekakou C., Bader M.G., Processing of Composites: Simulations of the Draping of Fabrics with Updated Material Behaviour Law. Journal of Composite Materials, vol. 35, no. 2, 2001, pp 138-163.

[25] Yu W.R., Pourboghrat F., Chung K., Zampaloni M., Kang T.J., Non-Orthogonal Constitutive Equation for Woven Fabric Reinforced Thermoplastic Composites. Composites: Part A, vol. 33, 2002, pp 1095-1105.

[26] Peng X.Q., Coa J., Chen J., Stamping Simulation of Woven Composites Using a Non-orthogonal Constitutive Model. The 6th International ESAFORM Conference on Material Forming, Salerno, Italy, 2003, pp 827-830.

[27] Pickett A.K., Review of Finite Element Simulation Methods Applied to Manufacturing and Failure Prediction in Composite Structures. Applied Composite Materials, vol. 9, 2002, pp 43-58.

[28] Wiggers J., Long A., Harrison P., Rudd C., The Effects of Stitch Architecture on the Shear Compliance of Non-Crimp Fabrics. The 6th International ESAFORM Conference on Material Forming, Salerno, Italy, 2003, pp 851-854.

[29] Mack C., Taylor H.M., The Fitting of Woven Cloth to Surfaces. Journal of the Textile Institute. vol. 47, no.8, 1956, pp 477-488.

[30] Danial J.L., Soulat D., Boisse P., Shear and Tension Stiffness Influence in Composites Forming Modeling. The 7th International ESAFORM Conference on Material Forming, Trondheim, Norway, 2004, pp 301-303.

[31] Lamers E.A.D., Wijskamp S., Akkerman R., Fibre Orientation Modelling for Rubber Press Forming of Thermoplastic Laminates. The 5th International ESAFORM Conference on Material Forming, Krakow, Poland, 2002, pp 323-326.

[32] Lamers E.A.D., Wijskamp S., Akkerman R., Drape Modelling of Multi-Layered Composites. The 6th International ESAFORM Conference on Material Forming, Salerno, Italy, 2003, pp 823-826.

[33] Sidhu R.M.J.S., Averill R.C., Riaz M., Pourboghrat F., Finite Element Analysis of Textile Composite Preform Stamping. Composite Structures, vol. 52, 2001, pp 483-497.

[34] Sharma S.B., Sutcliffe M.P.F., A Simplified Finite Element Model for Draping of Woven Material. Composites: Part A, vol. 35, 2004, p 637–643.

[35] Wang J., Paton R., Page J.R., The Draping of Woven Fabric Preforms and Prepregs for Production of Polymer Composite Components. Composites: Part A, vol. 30, 1999, pp 757–765.

[36] Andrews P., Paton R., Wang J., Rudder Tip Drape Trials. Proceedings of the 11th International Conference on Composite Materials (ICCM-11). Gold Coast, Australia, 1997.

[37] Long A., Rudd C.D., Blagdon M., Smith P., Characterizing the Processing and Performance of Aligned Reinforcements During Preform Manufacture. Composites: Part A, vol. 27A, 1996, pp 247-253.

[38] Keilmann R., Innovative processing techniques for carbon-fibre materials. JEC Composites, no. 5, 2003, pp 81-82.

[39] Potluri P., Kusak E., Reddy T.Y., Novel Stitch-Bonded Sandwich Composite Structures. Composite Structures, vol. 59, no. 2, 2003, pp 251-259.

[40] Wijskamp S., Shape Distortions in Composite Forming. PhD Thesis, University of Twente, Enschede, Netherlands, 2005.

[41] McBride T.M., The Large Deformation Behaviour of Woven Fabric Microstructural Evolution in Formed Textile Composites. PhD Thesis, Boston University, United States, 1997.

[42] Cai Z., Gutowski T., The 3D Deformation Behavior of a Lubricated Fiber Bundle. Journal of Composite Materials, vol. 26, no. 8, 1992, pp 1207-1237.

[43] Long A.C., Wiggers J., Harrison P., Modelling the Effects of Blank-Holder Pressure and Material Variability on Forming of Textile Preforms. The 8th International ESAFORM Conference on Material Forming, vol. 2, Cluj-Napoca, Romania, 2005, pp 939-942.

[44] Long A.C., An Iterative Draping Simulation Based on Fabric Mechanics. The 4th International ESAFORM Conference on Material Forming. Liege Belgium, 2001, pp 99-102.

[45] Pickett A.K., Cunningham J.E., deLuca P., Johnson A.F., Lefebure P., Mallon P., Sunderland P., Ó Brádaigh C.M., Vodermeyer A., Werner W., Numerical Techniques for the Pre-Heating and Forming Simulation of Continuous Fibre Reinforced Thermoplastics. SAMPE, Basel, Switzerland, 1996.

[46] BE-5092: Brite-Euram Project: Industrial Press Forming of Continuous Fibre Reinforced Thermoplastic Sheets and the Development of Numerical Simulation Tools. 1992-1996.

[47] FiberSIM™, *VISTAGY Inc.*, 486 Totten Pond Road, Waltham, MA 02451-1917, USA.

[48] MSC Laminate Modeller™, *MSC.Software Corporation*, 2 MacArthur Place, Santa Ana, CA 92707, USA.

[49] QUIK-FORM™, *ESI Group*, 99 Rue des Solets, Silic 112, 94513 Rungis-Cedex, France.

[50] CATIA™ CPD Draping Module, Composites Part Design, Producibility Analysis Module, *Dassault Systèmes*, 9 Quai Marcel Dassault, 92150 Suresnes, France.

[51] Lomov, S.V., Huysmans G., Luo Y., Parnas R.S., Prodromou A., Verpoest I., Phelan F.R., Textile Composites: Modelling Strategies. Composites: Part A, vol. 32, 2001, pp 1379-1394.

[52] Harrison P., Clifford M.J., Long A.C., Rudd C.D., Constitutive Modelling of Impregnated Continuous Fibre Reinforced Composites Micromechanical Approach. Plastics, Rubber and Composites, vol. 31, no. 2, 2002, pp 76-86.

[53] Lomov S.V., Willems A., Barburski M., Stoilova Tz., Verpoest I., Strain Field in the Picture Frame Test: Large and Small Scale Optical Measurements. The 8th International ESAFORM Conference on Material Forming, vol. 2, Cluj-Napoca, Romania, 2005, pp 935-938.

[54] Creech G., Experimental and Finite Element Draping Simulation for Non Crimp and Twill Fabrics. MRes Thesis, Cranfield University, United Kingdom, 2001.

[55] Long A.C. (Editor), Design and Manufacture of Textile Composites. 2005, Woodhead Publishing and CRC Press LLC, ISBN 9781855737440.

[56] Miller A.J., The Effect of Microstructural Parameters on the Mechanical Properties on Non-Crimp Fabric Composites. M.Phil Thesis, Cranfield University, United Kingdom, 1996.

[57] Drapier S., Wisnom M.R., Finite-Element Investigation of the Compressive Strength of Non-Crimp-Fabric Based Composites. Composite Science and Technology, vol. 59, 1999, pp 1287-1297.

[58] Lebrun G., Bureau M.N., Denault J., Evaluation of Bias-extension and Picture-frame Test Methods for the Measurement of Intraply Shear Properties of PP/Glass Commingled Fabrics. Composite Structures, vol. 61, 2003, pp 341-352.

[59] Harrison P., Clifford M.J., Long A.C., Shear Characterisation of Viscous Woven Textile Composites: a Comparison Between Picture Frame and Bias Extension Experiments. Composites Science and Technology, vol. 64, 2004, pp 1453-1465.

[60] Mohammed U., Lekakou C., Dong L., Bader M.G., Shear Deformation and Micromechanics of Woven Fabrics. Composites: Part A, vol. 31, 2000, pp 299-308.

[61] Page J., Wang J., Prediction of Shear Force and an Analysis of Yarn Slippage for a Plain-weave Carbon Fabric in a Bias Extension State. Composites Science and Technology, vol. 60, 2000, pp 977-986.

[62] ASTM D1388-96^{E1}. Standard test for Stiffness of Fabrics, revised in 1996.

[63] Potter K.D., The Influence of Accurate Stretch Data for Reinforcements on the Production of Complex Structural Mouldings. Composites, July, 1979, pp 161-173.

[64] Creech G, Pickett A.K., Greve L., Finite Element Modelling of Non Crimp Fabrics for Draping Simulation. The 6th International ESAFORM Conference on Material Forming, Salerno, Italy, 2003, pp 863-866.

[65] Kong H., Mouritz A.P., Paton R., Tensile Extension Properties and Deformation Mechanisms of Multiaxial Non-crimp Fabrics. Composite Structures, vol. 66, 2004, pp 249-259.

[66] Sharma S.B., Sutcliffe M.P.F., Chung S.H., Characterisation of Material Properties for Draping of Dry Woven Composite Material. Composites: Part A, vol. 34, 2003, pp 1167-1175.

[67] Souter B.J., Effects of Fibre Architecture on Formability of Textile Preforms. PhD Thesis, Nottingham University, United Kingdom, 2001.

[68] Yu X., Zhang L., Mai Y., Modelling and Finite Element Treatment of Intra-ply Shearing of Woven Fabric. Journal of Materials Processing Technology, vol. 138, 2003, pp 47-52.

[69] Liu L., Chen J., Gorczyca J.L., Sherwood J.A., Modeling of Friction and Shear in Thermostamping of Composites – Part II. Journal of Composite Materials, vol. 38, no. 21, 2004, pp 1931-1947.

[70] Lomov S.V., Barburski M., Stoilova Tz., Verpoest I., Akkerman R., Loendersloot R., ten Thije R.W.H., Carbon Composites Based Upon Multiaxial Multiply Stitched Preforms. Part 3: Biaxial Tension, Picture Frame and Compression Tests of the Preforms. Composites: Part A, vol. 36, 2005, pp 1186-1206.

[71] Lomov S.V., Barburski M., Verpoest I., Masajtis J., Laperre J., Deformability of Multi-axial Textile Reinforcements: KES-F Testing. The 6th International ESAFORM Conference on Material Forming, Salerno, Italy, 2003, pp 843-846.

[72] McGuiness G.B., O'Bradaigh C.M., Characterisation of Thermoplastic Composite Melts in Rhombus-shear: The Picture Frame Experiment. Composites: Part A, vol. 29A, 1998, pp 115-132.

[73] Prodromou A.G., Chen J., On the Relationship Between Shear Angle and Wrinkling of Textile Composite Preforms. Composites: Part A., vol. 28A, 1997, pp 491-503.

[74] Kawabata S., The Standardisation and Analysis of Hand Evaluation. Textile Machinery Society of Japan, Osaka, Japan, 1975.

[75] Hivet G., Dumont F., Launay J., Maurel V., Vacher P., Boisse P., Optical Analysis of Woven Fabric's Shear Behavior. The 7th International ESAFORM Conference on Material Forming, Trondheim, Norway, 2004, pp 353-356.

[76] Vinot L., Advanced Textile Fabrics Draping. MSc Thesis, Cranfield University, United Kingdom, 2005.

[77] Automated Strain Analysis and Measurement Environment. *ASAME Technology LLC*, 1903 Wickett Way, Cedar Park, TX 78613, United States.

[78] Crookston J.J., Long A.C., Jones I.A., Modelling Effects of Reinforcement Deformation During Manufacture on Elastic Properties of Textile Composites. Plastics, Rubber and Composites, vol. 31, no. 2, 2002, pp 58-65.

[79] Harrison P., Clifford M.J., Long A.C., Rudd C.D., Constitutive Modelling of Shear Deformation for Impregnated Textile Composites. The 6th International ESAFORM Conference on Material Forming, Salerno, Italy, 2003, pp 847-850.

[80] Milani A.S., Nemes J.A., Pham X.T., Lebrun G., The Effect of Fibre Misalignment on Parameter Determination using Picture Frame Test. Proceedings of the 14th International Conference on Composite Materials (ICCM-14), San Diego, United States, 2003.

[81] Long A.C., Souter B.J., Robitaille F., Rudd C.D., Effects of Fibre Architecture on Reinforcement Fabric Deformation. Plastics, Rubber and Composites, vol. 31, no. 2, 2002, pp 87-97.

[82] Krevszig E., Advanced Engineering Mathematics, 8th Edition. 1999. John Wiley & Sons, United Kingdom.

[83] Peng X.Q., Cao J., Chen J., Xue P., Lussier D.S., Liu L., Experimental and Numerical Analysis on Normalisation of Picture Frame Tests for Composite Materials. Composites Science and Technology, vol. 64, 2004, pp 11-21.

[84] McBride T.M., Chen J., Unit-cell Geometry in Plain Weave Fabrics During Shear Deformation. Composites Science and Technology, vol. 57, 1997, pp 345-351.

[85] PAM-FORM™ – Solver Notes Manual 2002, *ESI Group*, 99 Rue des Solets, Silic 112, 94513 Rungis-Cedex, France, 2002.

[86] Kong H., Mouritz A.P., Paton R., Tensile Extension properties and Deformation Mechanisms of Multiaxial Non-crimp Fabrics. Composite Structures, vol. 66, 2004, pp 249-259.

[87] Ten Thije R.H.W., Loendersloot R., Akkerman R., Material Characterisation for Finite Element Simulation of Draping with Non-crimp Fabrics. The 6th International ESAFORM Conference on Material Forming, Salerno, Italy, 2003, pp 859-862.

[88] Bazhenov S., Dissipation of Energy by Bulletproof Aramid Fabric. Journal of Material Science, vol. 32, 1997, pp 4167-4173.

[89] PAM-RTM™. *ESI Group*, 99 Rue des Solets, Silic 112, 94513 Rungis-Cedex, France.

[90] PAM-CRASH™ – Solver Notes Manual 2005, *ESI Group*, 99 Rue des Solets, Silic 112, 94513 Rungis-Cedex, France, 2005.

[91] BS EN ISO 5084:1997. Textiles – Determination of Thickness of Textiles and Textile Products, 1997.

[92] Kawabata S., Niwa M., Kawai H., The Finite-Deformation Theory of Plain-weave Fabrics Part III: The shear-Deformation Theory. Journal of the Textile Institute, vol. 64, no. 2, 1973, pp 61-85.

[93] Skelton J., Fundamentals of Fabric Shear. Textile Research Journal, 1976, pp 862-869.

[94] Harrison P., Wiggers J., Long A.C., Rudd C.D., Constitutive Modelling Based on Meso and Macro Kinematics for Woven and Stitched Dry Fabrics. Proceedings of the 14th International Conference on Composite Materials (ICCM), San Diego, United States, 2003.

[95] Danial I.M., Ishai O., Engineering Mechanics of Composite Materials, 1994, Oxford University Press. ISBN 0195075064.

[96] Hull D., Clyne T.W., An introduction to Composite Materials, 2nd Edition, 1996, Cambridge University Press. ISBN 0521388554.

[97] Hart-Smith L.J., Predictions of the Original and Truncated Maximum-Strain Failure Models for Certain Fibrous Composite Laminates. Composites Science and Technology, vol. 58, no. 2, 1998, pp 1151-1178.

[98] Pickett A.K., Fouinneteau M.R.C., Material Characterisation and Calibration of a Meso-mechanical Damage Model for Braid Reinforced Composites. Composites: Part A, vol. 37, 2006, pp 368-377.

[99] Puck A., Schürmann H., Failure Analysis of FRP Laminates by Means of Physically Based Phenomenological Models. Composites Science and Technology, vol. 62, no. 12-13, 2002, pp 1633-1662.

[100] Hinton M.J., Kaddour A.S., Soden P.D., A Comparison of the Predictive Capabilities of Current Failure Theories for Composite Laminates, Judged Against Experimental Evidence. Composites Science and Technology, vol. 62, no. 12-13, 2002, pp 1725-1797.

[101] Greve L., Damage and Failure Modelling of Carbon/Epoxy Non Crimp Fabric Composites. PhD Thesis, Cranfield University, United Kingdom, 2005.

[102] Ladevèse P., Le Dantec E., Damage Modelling of the Elementary Ply for Laminated Composites. Composites Science and Technology, vol. 43, no. 3, 1992, pp 257-267.

[103] Gorczyca J.L., Sherwood J.A., Chen J., A Friction Model for use with Commingled Fibreglass-Polypropylene Plain-Weave Fabric and the Metal Tool During Thermostamping. Revue Européenne des Éléments finis (REEF), vol. 14, no. 6-7, 2005, pp 729-751.

[104] King M.J., Jearanaisilawong P., Socrate S., A Continuum Constitutive Model for the Mechanical Behavior of Woven Fabrics. International Journal of Solids and Structures, vol. 42, 2005, pp 3867-3896.

[105] Boubaker B., Haussy B., Ganghoffer J.F., Discrete Models of Woven Structures: Stability and Draping Analysis. C.R. Mecanique, vol. 330, pp 871-877.

[106] Robitaille F., Long A.C., Jones I.A., Rudd C.D., Automatically Generated Geometric Descriptions of Textile and Composite Unit Cells. Composites: Part A, vol. 34, 2003, pp 302-312.

[107] Sun W., Lin F., Hu X., Computer-Aided Design and Modeling of Composite unit Cells. Composites Science and Technology, vol. 61, 2001, 289-299.

[108] Lomov S.V., Gusakov A.V., Huysmans G., Prodromou A., Verpoest I., Textile Geometry Preprocessor for Meso-Mechanical Models of Woven Composites. Composites Science and Technology, vol. 60, 2000, pp 2083-2095.

[109] King M.J., Socratte S., A Mesostructurally-Based Shell Formulation to Model the Deformation Response of Woven Fabrics. Submitted to; Journal of Applied Mechanics, 2005.

[110] Peng X., Cao J., A Duel Homogenization and Finite Element Approach for Material Characterization of Textile Composites. Composites: Part B, vol. 33, 2002, pp 45-56.

[111] Boisse P., Zouari B., Gasser A., A Mesoscopic Approach for the Simulation of Woven Fibre Composite Forming. Composites Science and Technology, vol. 65, 2005, pp 429-436.

[112] Liu L., Chen J., Gorczyca J.L., Sherwood J., Modeling of Friction and Shear in Thermostamping of Composites – Part II. Journal of Composite Materials, vol. 38, No. 21, 2004, pp 1931-1947.

[113] Gu B., Ballistic Impact of Conically Cylindrical Steel Projectile into Plain-woven Fabric Target – A Finite Element Simulation. Journal of Composite Materials, vol. 38, no. 22, 2004, pp 2049-2074.

[114] Potluri P., Perez Ciurezu D.A., Ramgulam R.B., Measurement of Meso-scale Shear Deformations for Modelling Textile Composites. Composites: Part A, *In press, Accepted 2005.*

[115] Duan Y., Keefe M., Bogetti T.A., Powers B., Finite Element Modeling of Transverse Impact on a Ballistic Fabric. International Journal of Mechanical Sciences, vol. 48, 2006, pp 33-43.

[116] Loendersloot R., Lomov S.V., Akkerman R., Verpoest I., Carbon Composites Based on Multiaxial Multiply Stitched Preforms. Part V: Geometry of Sheared Biaxial Fabrics. Composites: Part A, *In press, accepted 2005.*

[117] Robitaille F., Long A.C., Rudd C.D., Geometric Modelling of Textiles for Prediction of Composite Processing and Performance Characteristics. Plastics, Rubber and Composites, vol. 31, no. 2, 2002, pp 66-75.

[118] Lomov S.V., Verpoest I., Model of Shear of Woven Fabric and Parametric Description of Shear Resistance of Glass Woven Reinforcements. Composites Science and Technology, vol. 66, 2006, pp 919-933.

[119] Lomov S.V., Verpoest I., Peeters T., Roose D., Zako M., Nesting in Textile Laminates: Geometrical Modelling of the Laminate. Composites Science and Technology, vol. 63, no. 7, 2002, pp 1171-1183.

[120] Boisse P., Zouari B., Jean-Luc D., Importance of In-plane Shear Rigidity in Finite Element Analysis of Woven Fabric Composite Preforming. Composites: Part A, *In press, accepted 2005.*

[121] Duan Y., Keefe M., Bogetti T.A., Cheeseman B.A., Modeling Friction Effects on the Ballistic Impact Behavior of a Single-Ply High-Strength Fabric. International Journal of Impact Engineering, vol. 31, 2005, pp 996-1012.

[122] Shockey D.A., Erlich D.C., Simons J.W., Improved Barriers to Turbine Engine Fragments. US Department of Transportation, Federal Aviation Authority (FAA), report no. DOT/FAA/AR-99/8 III, 2001.

[123] Pickett A.K., Creech G., de Luca P., Simplified and Advanced Methods for Prediction of Fabric Draping. Revue Européenne des Éléments finis (REEF), vol. 14, no. 6-7, 2005, pp

[124] Creech G., Pickett A.K., Meso-mechanical Modelling of Non Crimp Fabrics for Drape and Impact Analysis. The 7th International ESAFORM Conference on Material Forming, Trondheim, Norway, 2004, pp 349-351.

[125] Creech G., Pickett A.K., Meso-modelling of Non-Crimp Fabric Composites for Coupled Drape and Failure Analysis. Submitted to; Journal of Materials Science, 2005.

[126] Harrison P. Tan M.K., Long A.C., Kinematics of Intra-ply Slip in Textile Composites During Bias Extension Tests. The 8th International ESAFORM Conference on Material Forming, vol. 2, Cluj-Napoca, Romania, 2005, pp 987-990.

[127] Chernouat A., Borouchaki H., Billoët J., Geometrical and Mechanical Draping of Composite Fabric. Revue Européenne des Éléments finis (REEF), vol. 14, no. 6-7, 2005, pp 693-707.

[128] TECABS, Framework V Project G6RD-CT2001-00636, 'Technologies for Carbon Fibre Modular Automotive Body Structures'. *http://www.tecabs.org,* 1998-2002.

[129] Anderson T., Fracture Mechanics – Fundamentals and Applications, 2nd Edition. 1995, CRC Press LLC, Boca Raton, Florida, ISBN 0849342600.

[130] Pickett A.K., Johnson A.F., Rozicky P., Computational Methods for Predicting Impact in Composite Structures. Composites Science and Technology, vol. 61, 2001, pp 2183-2192.

[131] Caron O., Meso Mechanical Failure Modelling of Non Crimp Fabric Composites. MSc Thesis, Cranfield University, United Kingdom, 2004.

[132] Endruweit A., Long A.C., Influence of Stochastic Variations in the Fibre Spacing on the Permeability of Bi-directional Textile Fabrics. Composites: Part A, vol. 37, 2006, pp 679-694.

[133] Schneider M., Endelmann K., Tiltmann U., Quality Analysis of Reinforcement Structures for Composites by Digital Image Processing. The 25th International SAMPE Europe Conference, Paris, France, 2004.

[134] Fedolliere C., Delamination Failure and Crash Modelling of Composite Structures. MSc Thesis, Cranfield University, United Kingdom, 2004.

[135] ISO International Standard DIS15024. Fibre-reinforced Plastic Composites – Determination of Mode I Inter-laminar Fracture Toughness, GIC, for Unidirectionally Reinforced Materials.

[136] ASTM Draft Standard D30.06. Protocol for Inter-laminar Fracture Testing, End-Notched Flexure (ENF), revised April 24, 1993.

[137] Fagan M.J., Finite Element Analysis,1992, Longman Group UK Ltd. ISBN 0582022479.

[138] Yu W., Harrison P., Long A., Finite Element Forming Simulation for Non-Crimp Fabrics using a Non-orthogonal Constitutive Equation. Composites: Part A, vol. 36, 2005, pp 1079-1093.

[139] Barbero E.J., Lonetti P., Sikkil K.K., Finite Element Continuum Damage Modeling of Plain Weave Reinforced Composites. Composites: Part B, vol. 37, 2006, pp 137-147.

[140] Bonora N., Ruggiero A., Micromechanical Modeling of Composites with Mechanical Interface – Part II: Damage Mechanics Assessment. Composites Science and Technology, vol. 66, 2006, pp 323-332.

[141] Edgren F., Mattsson D., Asp L.E., Varna J., Formation of Damage and its effects on Non-crimp Fabric Reinforced Composites Loaded in Tension. Composites Science and Technology, vol. 64, 2004, pp 675-692.

[142] Cao. J., Cheng H.S., Yu T.X., Zhu B., Tao X.M., Lomov S.V., Stoilova Tz., Verpoest I., Boisse P., Launay J., Hivet G., Liu L., Chen J., de Graaf E.F., Akkerman R., A Cooperative Benchmark Effort on Testing of Woven Composites. The 7th International ESAFORM Conference on Material Forming, Trondheim, Norway, 2004, pp 305-308.

[143] DIN 54 306, Bestimmung des Fallvermögens von Textilen Flächengebilden (Prüfung von Textilien), 1979.

[144] BS 5058, Method for the Assessment of Drape of Fabrics, 1973.

[145] Haug E., Di Pasquale E., Pickett A.K., Ulrich D., Industrial Sheet Metal Forming Simulation using the Explicit Finite Element Method. International VDI Conference, Zurich, Switzerland, 1991.

[146] *Huntsman LLC*, Advanced Materials, Composites, Datasheet; Warm Curing Epoxy Systems based on Araldite® LY3505 /Harderers XB 3403/ XB 3404/ XB 3405, March 2004.

[147] *Toray Carbon Fibers America.Inc*, Datasheet; No. CFA005, Torayca® T700S Datasheet

[148] http://www.gtwebsolutions.com/nwbenchmark (viewed on the 12th January 2006).

[149] *LIBA Maschinenfabrik* GmbH. PO Box 1120, D-95112, Naila, Germany.

[150] Yu X., Ye L., Mai W., Finite Element Spurious Wrinkles on the Thermoforming Simulation of Woven Fabric Reinforced Composites. The 7th International ESAFORM Conference on Material Forming, Trondheim, Norway, 2004, pp 325-328.

[151] ASTM D1894-01, Standard Test Method for Static and Kinetic Coefficients of Prediction of Plastic Film and Sheeting, 1973.

[152] Boisse P., Borr M., Buet K., Cherouat A., Finite Element Simulation of Textile Composite Forming Including the Biaxial Fabric Behaviour. Composites: Part B, vol. 28a, 1997, pp 453-464.

[153] CorelDraw©, *Corel Corporation*, 1600 Carling Avenue, Ottawa, Ontario, Canada, K1Z 8R7.

9. APPENDIX

- ***Fabric, draping and failure simulation contact thicknesses;***

Interface	Contact thickness, h_{cont}	Interface	Contact thickness, h_{cont}
Tow-to-tow	0.055mm	Tow-to-stitch	0.02mm
Hemisphere mould-to-tow	1.3mm	Hemisphere mould-to-stitch	1.15mm
Blankholder-to-tow	0.4mm	Blankholder-to-stitch	0.4mm
Impactor-to-tow	1mm	Impactor-to-stitch	1mm

- ***Stitch unit-cell measurement data***

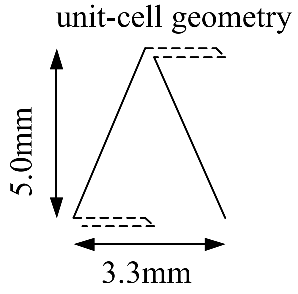

Length measurement data of 40 unit-cells		
66.7mm	66.4mm	66.9mm

Length measurement data of 40 unit-cells		
44.2mm	43.9mm	43.9mm

- ***Fabric thickness measurement data***

Fabric shear angle (°)	Measurement data of fabric thickness (mm)			Average (mm)
0	0.44	0.46	0.45	0.45
5	0.47	0.45	0.44	0.45
10	0.47	0.45	0.45	0.46
15	0.45	0.45	0.49	0.46
20	0.47	0.49	0.46	0.47
25	0.48	0.51	0.49	0.49
30	0.53	0.51	0.50	0.51
35	0.52	0.53	0.56	0.54
40	0.57	0.60	0.56	0.58
45	0.61	0.64	0.61	0.62
50	0.66	0.70	0.71	0.69
55	0.76	0.78	0.74	0.76
60	0.84	0.89	0.86	0.86
65	0.101	0.107	0.98	0.40
70	1.21	1.25	1.29	1.25

- ***Picture frame design specifications (and quantity of each part required).***

dimensions in mm

a) clamping plate (x4)

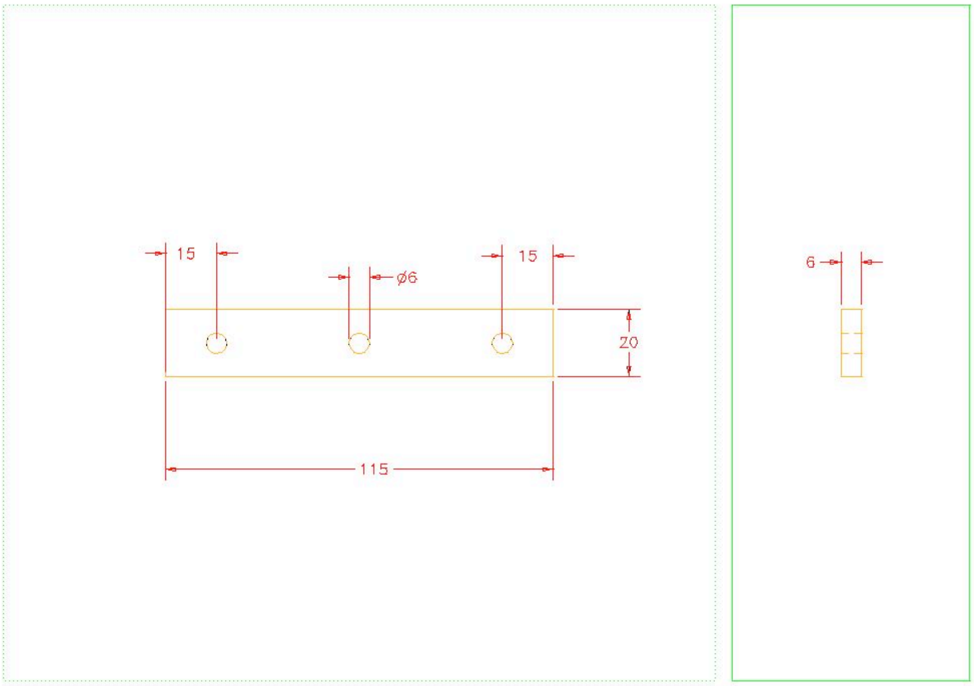

b) Clamp hanger (x2)

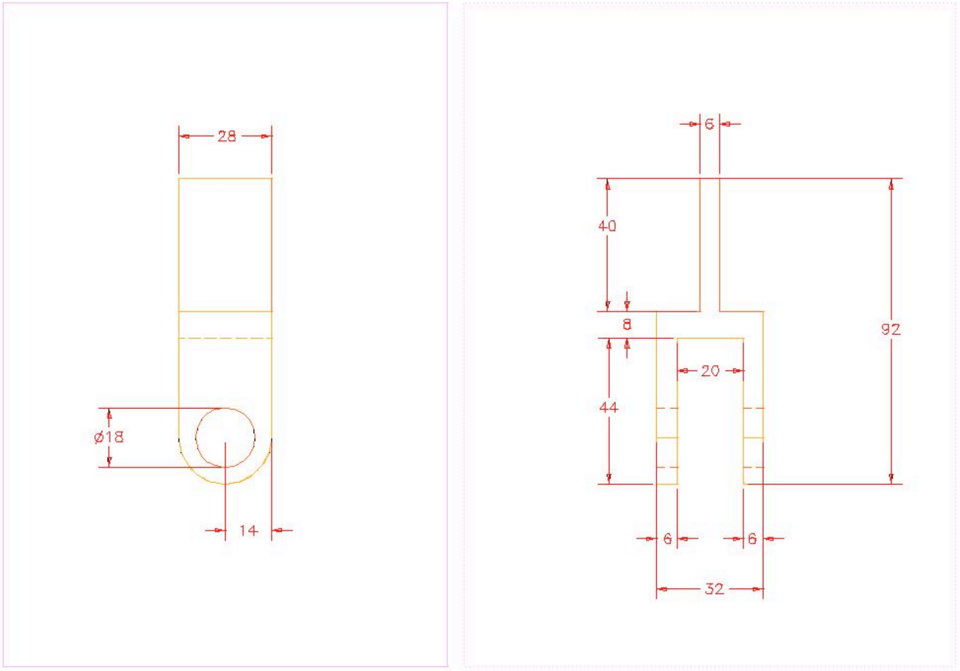

c) Frame edge no.1 (x2)

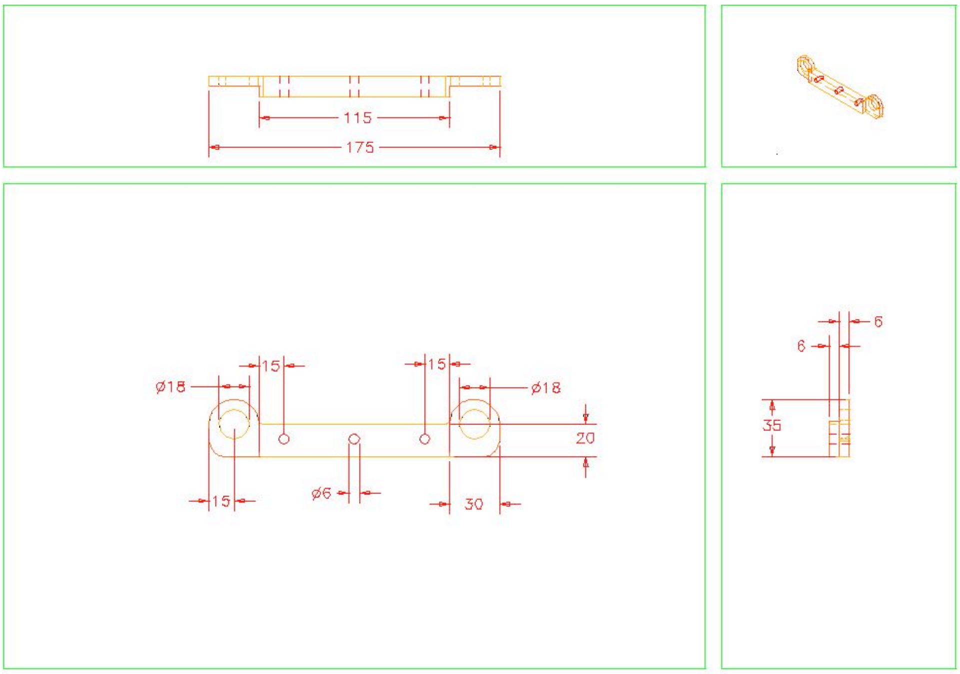

c) Frame edge no.2 (x2)

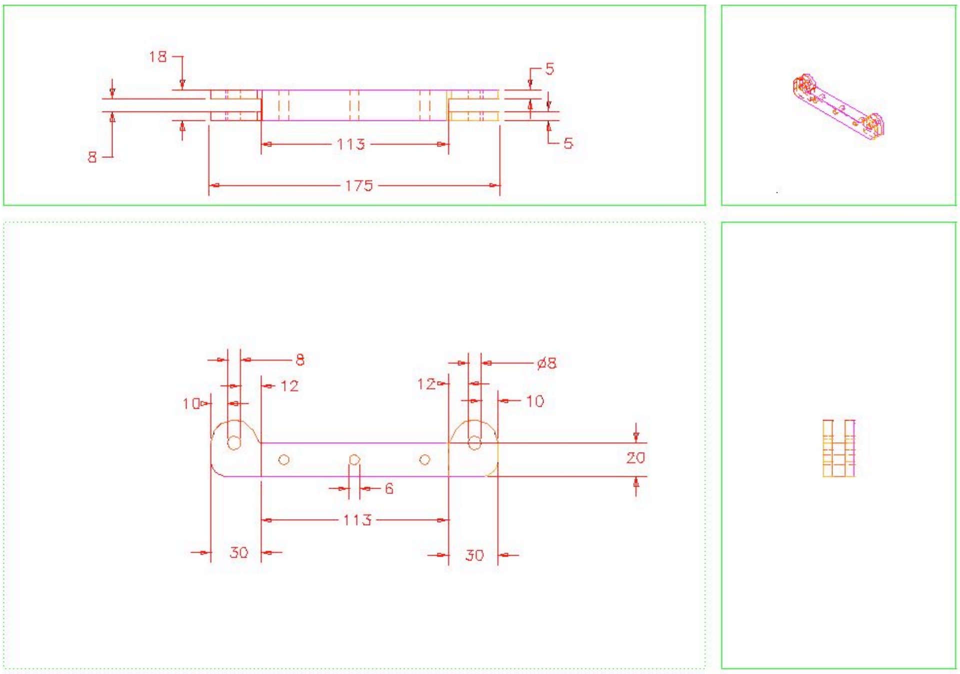

- ***Dynamic coefficient of friction data***

a) Tow-to-tow, 0°-0°.

Coefficient data summarised by surface pressure

Low pressure (1,369 Pa)	
Relative surface velocity	Dynamic friction coefficient from 3 tests
25mm/min	0.35 (±0.2)
300mm/min	0.34 (±0.1)
1000mm/min	0.38 (±0.2)
Average	0.36

Medium pressure (3.692 Pa)	
Relative surface velocity	Dynamic friction coefficient from 3 tests
25mm/min	0.34 (±0.1)
300mm/min	0.32 (±0.1)
1000mm/min	0.35 (±0.1)
Average	0.34

High pressure (6,505 Pa)	
Relative surface velocity	Dynamic friction coefficient from 3 tests
25mm/min	0.34 (±0.1)
300mm/min	0.34 (±0.2)
1000mm/min	0.34 (±0.1)
Average	0.34

b) Tow-to-tow, 0°-90°.

Coefficient data summarised by surface pressure

Low pressure (1,369 Pa)

Relative surface velocity	Dynamic friction coefficient from 3 tests
25mm/min	0.18 (±0.0)
300mm/min	0.18 (±0.2)
1000mm/min	0.17 (±0.2)
Average	0.18

Medium pressure (3.692 Pa)

Relative surface velocity	Dynamic friction coefficient from 3 tests
25mm/min	0.19 (±0.3)
300mm/min	0.18 (±0.1)
1000mm/min	0.19 (±0.1)
Average	0.19

High pressure (6,505 Pa)

Relative surface velocity	Dynamic friction coefficient from 3 tests
25mm/min	0.18 (±0.1)
300mm/min	0.19 (±0.1)
1000mm/min	0.19 (±0.2)
Average	0.19

c) Fabric-to-aluminium tooling. Results show an average of three tests for both 0°/90° and 90°/0° fabric orientations.

Coefficient data summarised by surface pressure

Low pressure (1,369 Pa)

Relative surface velocity	Dynamic friction coefficient from 6 tests
25mm/min	0.25 (±0.1)
300mm/min	0.26 (±0.1)
1000mm/min	0.25 (±0.2)
Average	0.25

Medium pressure (3.692 Pa)

Relative surface velocity	Dynamic friction coefficient from 6 tests
25mm/min	0.27 (±0.2)
300mm/min	0.24 (±0.1)
1000mm/min	0.26 (±0.1)
Average	0.26

High pressure (6,505 Pa)

Relative surface velocity	Dynamic friction coefficient from 6 tests
25mm/min	0.24 (±0.2)
300mm/min	0.24 (±0.1)
1000mm/min	0.26 (±0.2)
Average	0.25

d) typical test data obtained with friction tests (3 test curves shown, for a tow-to-tow test (0°-0°), with 1,369 Pa surface pressure and 300mm/min relative surface velocity)

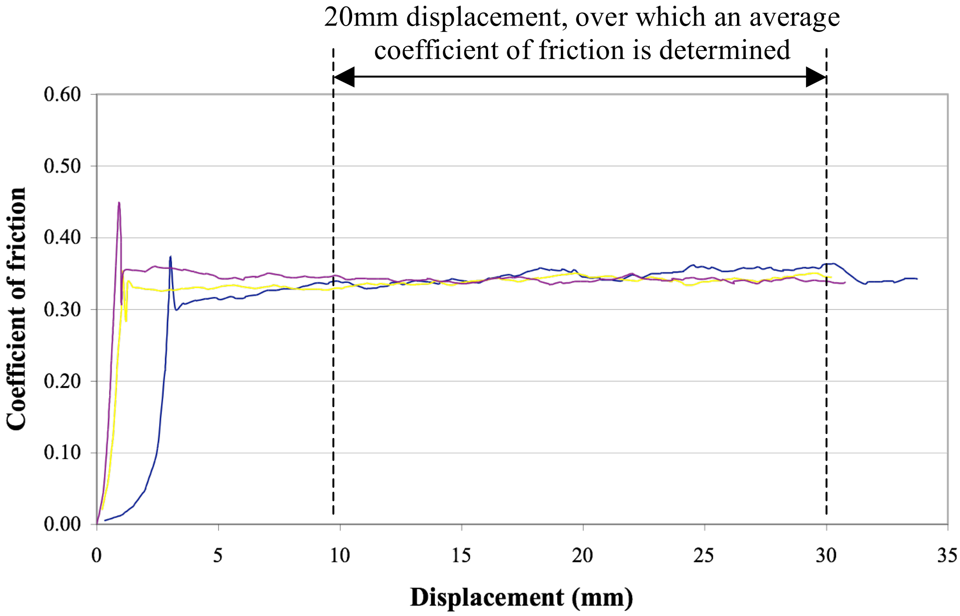

- Fabric draping assembly design specifications.

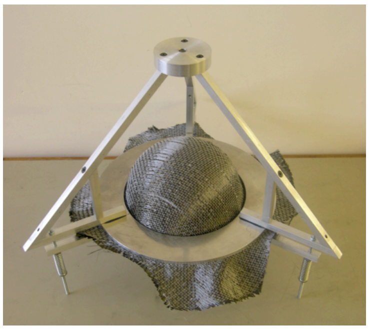

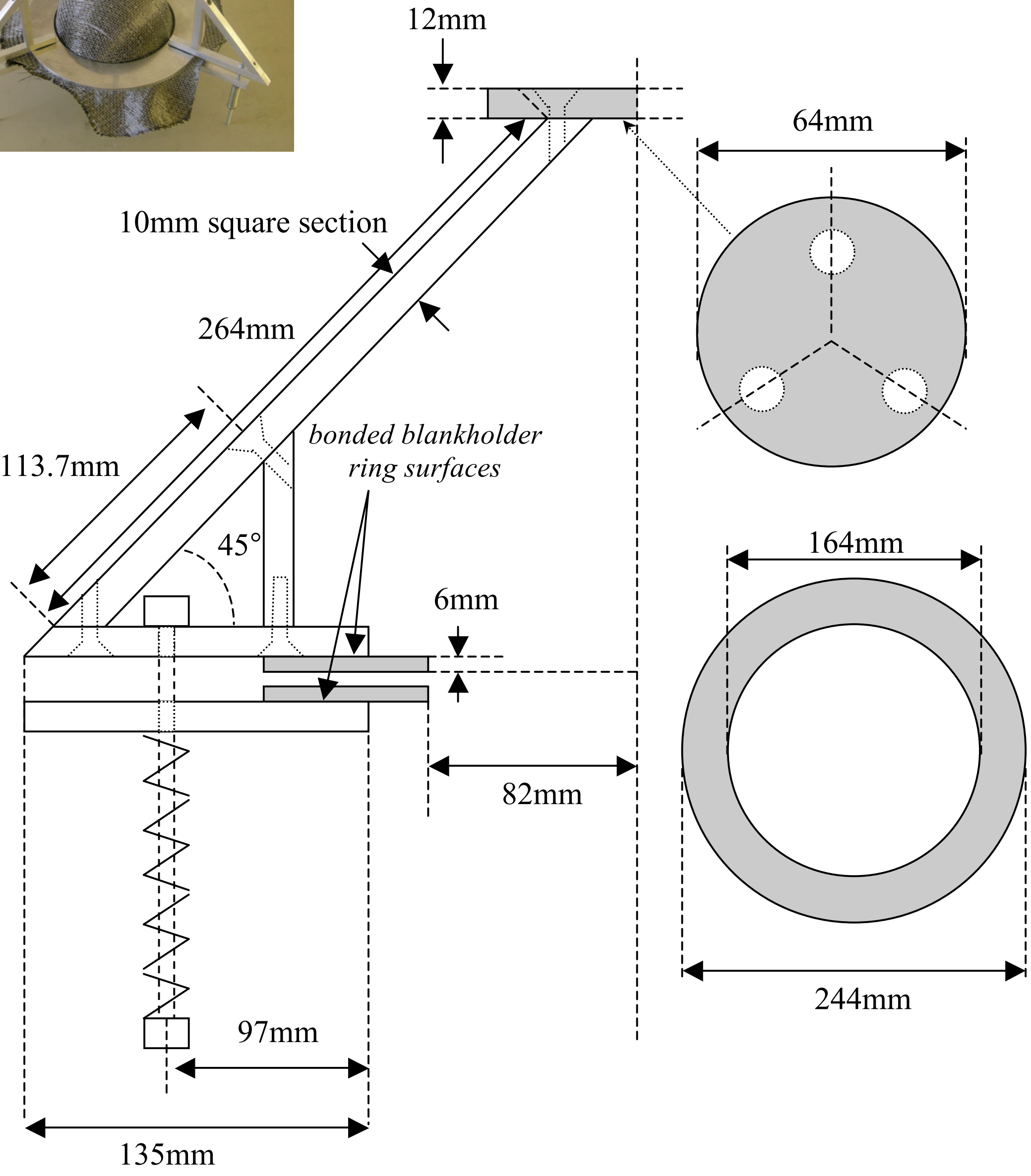

- ***Classical linear elastic bending theory used to obtain a first approximation of the tow axial stiffness***

Classical linear beam theory has been used for to determine a first approximation tow flexural stiffness, prior to calibration using FE simulation. As determined for a beam, uniformly loaded due to the mass of the beam only;

$$\frac{WL_b{}^3}{8\delta_b I} = E_{11} \qquad \text{Eq. (48)}$$

where, W is the mass of the tow, L_b is the experimentally measured tow length, δ_b is the vertical beam end deflection, and, for a beam of rectangular cross-section which bends through the central plane, I is calculated as follows,

$$I = \frac{bd^3}{12}. \qquad \text{Eq. (49)}$$